UNIVERSITY OF SOUTHAMPTON

FACULTY OF ENGINEERING AND THE ENVIRONMENT

Civil, Maritime, Environmental Engineering and Sciences Unit

BREAKAGE RESPONSE OF GLASS PANELS SUBJECT TO LONG-DURATION BLAST

Volume 1 of 1

by

Sarah Monk

Thesis for the degree of Doctor of Philosophy

August 2018

UNIVERSITY OF SOUTHAMPTON

ABSTRACT

FACULTY OF ENGINEERING AND THE ENVIRONMENT

Civil, Maritime, Environmental Engineering and Sciences Unit

Thesis for the degree of Doctor of Philosophy

BREAKAGE RESPONSE OF GLASS PANELS SUBJECT TO LONG-DURATION BLAST

By Sarah Monk

Glass windows are vulnerable building components and, in the event of a blast, give rise to a large damage radius. Many older buildings contain annealed glass which shatters instantly into angular shards, lacerating the skin on impact and causing significant injury. Up to 80% of injuries in an urban blast are caused by glass failure. In the far-field of large explosions, long-duration blast environments occur, typically defined by a positive phase duration greater than 40ms. Resulting impulses can cause window failure several kilometres away from the point of detonation. Data from long-duration blast events indicate window failure is highly dependent on glazing aspect ratio, area and other structural parameters. Inconsistency in window response has been attributed to material strength variation which can be in excess of ±25%. The Glazing Hazard Guide, the current UK design standard, indicates windows with matching dimensions respond consistently to blast loading, incorporates no extrapolation method to other glazing dimensions and has been demonstrated to be overly conservative.

In this thesis, influence of glazing aspect ratio, support conditions, material strength and the blast environment on window failure was investigated. Four phases of experimental testing and a comprehensively benchmarked parametric study enabled quantification of the influence of these parameters. Full-scale experimental testing of glazing response to long-duration blast was undertaken in the air blast tunnel (ABT) at MOD Shoeburyness, UK. Glazing response was dependent on complex interactions between structural and blast parameters. Experimental repeats importantly indicated significant data spread, demonstrating that glazing response should be measured as a probability of failure. Damage probability curves and pressure-impulse charts with contours of failure probability were produced for each parameter and were proposed as a new design method. These charts capture true glazing behaviour, are easy to interpret and highlight to the user that window response should be treated statistically. Findings indicated variation in material strength due to distribution of flaws produced the largest spread in failure pressure.

DECLARATION OF AUTHORSHIP

I, Sarah Monk declare that this thesis and the work presented in it is my own and have been generated by me as the result of my own original research.

BREAKAGE RESPONSE OF GLASS PANELS
SUBJECT TO LONG-DURATION BLAST

I confirm that:

1. This work was done wholly or mainly while in candidature for a research degree at this University;
2. Where any part of this thesis has previously been submitted for a degree or any other qualification at this University or any other institution, this has been clearly stated;
3. Where I have consulted the published work of others, this is always clearly attributed;
4. Where I have quoted from the work of others, the source is always given. With the exception of such quotations, this thesis is entirely my own work;
5. I have acknowledged all main sources of help;
6. Where the thesis is based on work done by myself jointly with others, I have made clear exactly what was done by others and what I have contributed myself;
7. Either none of this work has been published before submission, or parts of this work have been published as:

Monk, S. & Clubley, S.K., 2017a. Alternative methods of data capture for glass subjected to long-duration blast loading. In *2nd International Conference on Structural Safety Under Fire and Blast Loading*. London: ASRANet Ltd.

Monk, S. & Clubley, S.K., 2017b. Quantifying the influence of aspect ratio on window failure when subject to long-duration blast loading. In *17th International Symposium on Interaction of the Effects of Munitions with Structures*. Bad Neuenahr: Federal Office of Bundeswehr Infrastructure, Environmental Protection and Services.

Signed: Sarah Monk

Date: 28/08/2018

Acknowledgements

The author would like to express gratitude to Dr S.K. Clubley and Dr R. Johns for their guidance and encouragement through the course of this PhD. The advice and support of the sponsor team at AWE is gratefully acknowledged. The advice and assistance of Mr C. Tilbury and the Spurpark Ltd. trials division in facilitating experimental work for this thesis is gratefully appreciated. The author would also like to thank AWE and the MOD for use of experimental data and test facilities at MOD Shoeburyness. The support, encouragement and proof reading from the author's family throughout this research project is gladly acknowledged.

Contents

List of Figures

List of Tables

Nomenclature

General

ε	Strain	n.d.
ρ	Density	kg m^{-3}
σ	Standard deviation	n.d.
σ	Stress	Pa
E	Young's Modulus	Pa
F	Force	N
G	Shear modulus	Pa
t	Time	S
$\bar{x}$	Mean	n.d.

Blast Waves

γ	Specific heat ratio	n.d.
ρ_s	Density of the air behind the wave front	kg m^{-3}
A	Glazing area	m^2
A	Area of structure loaded by blast pressure	m^2
b	Parameter for Friedlander equation	n.d.
C_D	Drag coefficient	n.d.
C_r	Sound velocity in reflected region	m s^{-1}
F_D	Drag force	N
G	Larger clearing distance	m
I_r	Reflected positive phase impulse	Pa.s
I^-_s	Negative phase impulse	Pa.s
I_s	Positive phase impulse	Pa.s
K	Clark constant for shatter pressure calculation	n.d.
P	Overpressure	Pa
P_0	Atmospheric pressure in ambient conditions	Pa
P_{min}	Peak free-field static underpressure	Pa

P_r	Reflected overpressure	Pa
P_s	Peak free-field static overpressure	Pa
P_{stag}	Stagnation pressure	Pa
q_f	Glass static failure strength (Chilton, 1962)	Pa
q_s	Maximum dynamic pressure	Pa
R	Distance from point of charge detonation	m
R	Clark aspect ratio factor for shatter pressure calculation	n.d.
S	Clearing distance	m
t	Glass thickness	m
t'	Clearing time	s
t^-_d	Blast wave negative phase duration	s
t_a	Blast wave front arrival	s
t_d	Blast wave positive phase duration	s
t_m	Time to maximum element response	s
U_s	Blast wave front velocity	m s^{-1}
W	Charge mass expressed in TNT equivalence	kg
Z	Scaled distance from charge point of detonation	n.d.

Glass Material Properties

σ	Maximum tensile stress in glass	Pa
$\tilde{\sigma}_{t_d}$	Equivalent stress for specified load duration	Pa
A	Area of glass in Weibull equation	m^2
c	Weibull equation correction factor	n.d.
k	Weibull parameter	n.d.
m	Weibull parameter	n.d.
n	Static fatigue constant for Weibull equation	n.d.
P_f	Cumulative probability of glass failure	n.d.
t_d	Equivalent load duration for Weibull equation	s

The Applied Element Method

Δ	Displacement vector	m
d	Distance between spring groups	m
K_G	Global stiffness matrix	N m^{-1}
k_n	Normal spring stiffness	N m^{-1}
k_s	Shear spring stiffness	N m^{-1}
t	Element thickness	m

Glass Cracking

E	Sum of squares of errors	n.d.
r	Distance between crack and nearest piezo transducer	m
c	Speed of sound in glass	$m\ s^{-1}$
t_c	Time of glass failure	s
t_n	Calculated difference in time of arrival between first and n^{th} piezo transducer	s
T_n	Experimental difference in time of arrival between first and n^{th} piezo transducer	s
y_0	Y coordinate of crack	m
y_n	Y coordinate of n^{th} piezo transducer	m
x_0	X coordinate of crack	m
x_n	X coordinate of n^{th} piezo transducer	m

Chapter 1

Introduction

1.1 Introduction

On 19th April 1995, between 1800kg and 2300kg of ammonium nitrate and fuel oil (ANFO) detonated outside the Alfred P. Murrah Federal building, Oklahoma. Window failure occurred further than 1.6km away from the detonation. A large proportion of windows in the area were manufactured from monolithic annealed glass. This shatters instantaneously into angular shards that lacerate the skin on impact, causing significant injury. Such shards were thrown further than 3m into buildings close to the explosion, a dangerous and potentially life-threatening hazard. 167 deaths and 592 injuries were recorded, 39% of injuries were glass related. Victims generally suffered multiple soft tissue injuries like lacerations, contusions and abrasions (Norville *et al.*, 1999). Trawinski et al. (2004) estimated up to 80% of injuries in an urban blast are due to glass failure. In 1998 an estimated 90% of UK buildings contained annealed glazing (Claber, 1998). This would be highly dangerous in the event of an explosion.

In a short-duration explosion, the reaction generates gas at temperatures between 3000°C and 4000°C and pressures in the range of 10-30GPa. Hot gases expand quickly causing surrounding ambient air to be forced outwards, forming a blast wave in front of reaction products. The pressure increase from ambient conditions is called overpressure. Large explosions, like the Oklahoma event, produce a long-duration blast wave in the far-field, typically defined by a positive phase duration greater than 40ms (see section 2.2.2). This blast environment produces large impulses causing window failure several kilometres away despite low overpressure, a significant hazard radius. On 11th

December 2005, a vapour cloud of 240,000m^3 due to a leak of 300 tonnes of petrol, ignited at the Buncefield Oil Depot near Hemel Hempstead, UK. A report for the Health and Safety Executive by the Steel Construction Institute (2009) estimated the overpressure in the vapour cloud was approximately 200kPa. Overpressures of 5kPa were estimated up to 4km away, resulting in extensive damage. Windows were reported broken up to 7km away and the explosion was felt as far away as Lancashire and Powys, over 200km away (British Geological Survey, 2016).

1.2 Motivation and Scope

In August 2015, an estimated 800 tons (726 tonnes) of ammonium nitrate detonated over two explosions in Tianjin, China (Huang and Zhang, 2015) causing damage to windows up to five and a half kilometres away, affecting over 17,000 surrounding households. Buildings up to two kilometres away sustained "severe damage" (McGarry *et al.*, 2017). Window damage in a residential building near to the detonation is shown in Figure 1.1, capturing the motivation of this research project. It can be assumed that all windows received the same blast pressure due to the sufficiently large explosion. It is also a reasonable assumption that the glass was the same age, thickness, had the same framing and was monolithic annealed. Despite this, some glass failed and some survived. Analysis indicates a higher proportion of smaller windows survived compared to larger windows, indicating influence of area on window survival. From the same image it was determined that higher aspect ratio glazing had a higher failure probability than square glazing of a similar area. Material strength, which can vary by more than ±25% (Beason and Morgan, 1984), was the likely cause of inconsistent failure of windows with the same dimensions. The Tianjin explosion is analysed further in Chapters 2 and 3.

Figure 1.1: Damage to windows in a residential block near to the Tianjin explosion (BBC News, 2015).

The image of damage caused by the Tianjin explosion indicates window response to blast loading is highly variable, dependent on material strength and structural parameters like glazing area and aspect ratio. Current UK design standards are based on log-log pressure-impulse (PI) graphs (see Figure 1.2) published in the Glazing Hazard Guide in 1997 (Security Facilities Executive Special Services

Group - Explosion Protection, 1997). Based on a small number of experimental trials, these graphs indicate window hazard level for a given pressure and impulse combination. Hazard is defined by the throw distance of the shards produced (see Chapter 2 for more information). The lines indicate an absolute hazard rather than probability of failure, assuming all glass with specified dimensions will pose the same hazard, which is contradicted by Figure 1.1. PI graphs were produced for two window dimensions only with no guidance on extrapolation to other dimensions. Again the image of damage in Tianjin highlights the significance of window dimensions on glazing failure. This thesis demonstrates that the 21 year old Glazing Hazard Guide requires updating to implement a new failure probability method in place of current hazard levels. In this thesis, damage probability curves (shown in Figure 1.3) were produced to quantify variation in failure pressure due to structural parameters and material strength. In a long-duration blast environment, response is assumed impulse independent meaning structural response can be described in terms of overpressure only. This method was then extended to probability of failure contour plots on a PI graph to account for different blast environments. This statistical method acknowledges the complex and variable glazing behaviour and enables accurate damage prediction in the event of a large explosion, as seen in Tianjin and Oklahoma.

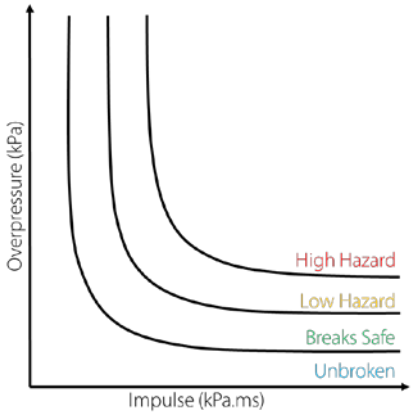

Figure 1.2: Example PI curve with hazard levels labelled.

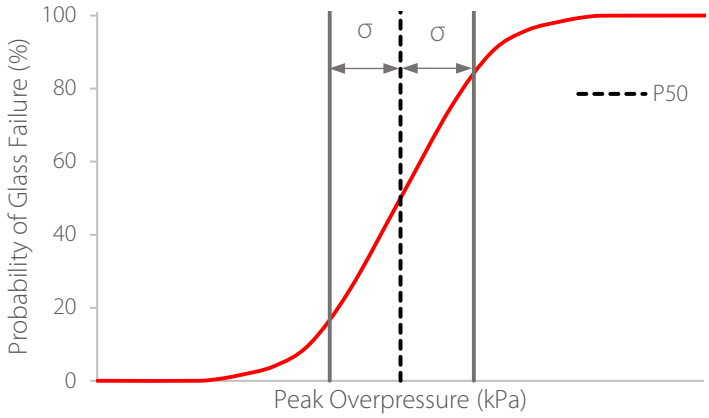

Figure 1.3: Diagram of a damage probability curve.

Recent research has focussed on short-duration blasts and the use of laminated glazing to mitigate damage. Laminated glass consists of two pieces of glass, usually annealed, bonded together using a polyvinyl butyral (PVB) interlayer. The interlayer transfers shear forces between glass layers and retains

shards in the frame in case of window failure, reducing risk of injury to building occupants. Due to the high cost involved, most researchers complete a limited series of explosive trials with few to no repeats and often only as a benchmark for computational analysis. The highly variable material strength, which is extremely difficult to model numerically, means rigorous experimental testing is necessary to understand the complex glazing response to blast loading. A review of current research demonstrated a lack of knowledge of structural parameter influence on glazing response to long-duration blast loading.

Modern long-duration blast trials require use of facilities such as the air blast tunnel (ABT) at MOD Shoeburyness (Figure 1.4). In a series of full-scale experimental trials, Johns (2016) investigated the effect of structural parameters on annealed glass resistance to long-duration blast. Johns varied glazing thickness, exposed area, aspect ratio and support conditions, concluding that influence of support conditions and aspect ratio was dependent on area, thickness and proximity to the glazing failure threshold. Elastically framed windows recorded a lower probability of failure compared to rigid framing which Johns argued was a result of stress reduction due to elastic framing. Peak window displacement was dependent on a complex interaction of area, aspect ratio and support conditions. Break time increased with glazing area and thickness. This resulted in an increased failure impulse due to longer break times. Fragmentation was strongly influenced by edge supports, significant cracking and small fragments were observed in rigidly framed windows compared to large angular shards from elastically supported glazing. Johns concluded that glazing response to long-duration blast was dependent on framing conditions, glazing area, thickness and aspect ratio.

Figure 1.4: The air blast tunnel (ABT) at MOD Shoeburyness (Clubley, 2014).

This thesis builds on Johns' research, quantifying influence of structural parameters on glazing response to long-duration blast loading. Annealed, 4mm thick glass represents the UK minimum window specification and therefore the worst case damage scenario in a blast event. As a result, it was the focus of this thesis. Initial computational modelling, using Johns' experimental data as a benchmark, highlighted aspect ratio, support conditions and peak overpressure as parameters requiring further research. A review of current research indicated variation in glass strength was a key parameter to quantify in order to produce window failure probability charts. Four experimental testing phases were undertaken for this thesis. Two phases of static testing provided cost-effective quantification of material variation with a large sample number. Static tests also trialled viability of an

innovative diagnostics method for accurate detection of glazing failure before use in expensive ABT trials. Influence of glazing aspect ratio, support conditions and peak overpressure was investigated in an extensive ABT trial schedule over two phases. The effect of each parameter on glazing response was analysed and ranked to determine its significance in governing glazing failure. Computational analysis, benchmarked using ABT trial data and an experimentally-based material model produced from static testing results, enabled a cost-effective data set extension to a blast overpressure range beyond the current scope of the ABT. A parametric study to find failure overpressures for a range of aspect ratios and support conditions enabled the significance of each parameter on glazing failure or survival be determined. Experimental and computational results facilitated production of failure probability curves for 4mm annealed glass subjected to long-duration blast loading.

1.2.1 Aims

This research project will investigate the significance of blast and structural parameters such as peak overpressure, aspect ratio and support conditions on annealed glazing response to long-duration blast loading. Full-scale experimental trials and an experimentally benchmarked parametric study will quantify parameter significance to glazing failure and facilitate production of annealed glass damage probability curves.

1.2.2 Objectives

1. Identify key parameters for quantification of glazing failure e.g. break time, failure displacement and crack patterns.
2. Analyse influence of structural parameters such as aspect ratio and support conditions on annealed glass failure.
3. Compare influence of structural and blast parameters on glazing failure and minimum failure pressure when subjected to long-duration blast loading. Determine which parameter had the greatest influence on glazing response.
4. Evaluate and test break detection options for use in dynamic trials. The preferred method should enable accurate and cost-effective capture of glazing failure in the aggressive ABT loading environment.
5. Produce damage probability curves for 4mm thick annealed glass subjected to varying peak overpressures.

1.3 Thesis Structure

The thesis structure is outlined below. A flow diagram of the work undertaken is outlined in Figure 1.5.

Chapter 2

An overview of blast wave theory and interaction with structures. Current research on glazing response to blast loading is evaluated, as well as current methods of determining and modelling

material strength variation. A review of numerical methods for modelling glazing response to blast is undertaken.

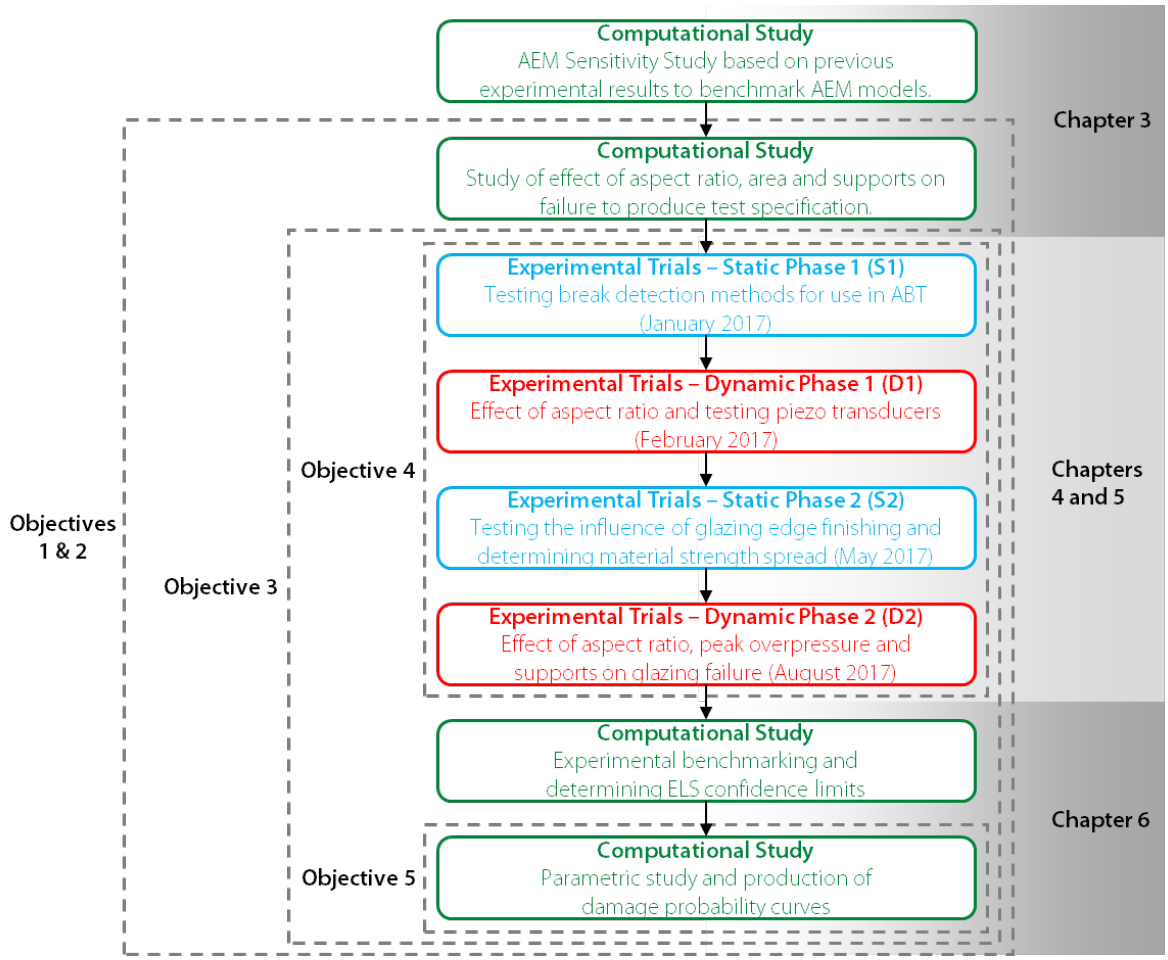

Figure 1.5: Workflow for this research project.

Chapter 3

Initial computational work culminating in experimental trial design is outlined in Chapter 3. This includes a numerical sensitivity study benchmarked using previous ABT trial data and an initial parametric study into the influence of glazing area and aspect ratio.

Chapter 4

Chapter 4 details experimental methodology for the static and dynamic testing. Development of a new data capture method is outlined in this chapter, the basis of a conference paper presented at Conference on Fire and Blast (CONFAB) 2017 and a journal paper submitted to Engineering Failure Analysis. Both papers can be found in the appendices. This work was also presented at the Group of Experts on Mitigation Systems (GEMS) 19th Annual Meeting in January 2018. Chapter 4 fulfils objective four of the research project. Analysis and quantification of the ABT blast environment is also undertaken in this chapter.

Chapter 5

In this chapter, analysis of glazing response and the influence of each structural parameter on window failure is quantified. Spread of material strength is calculated and a failure probability curve is

produced for material strength. Conclusions from this chapter partially meet objectives one, two and three of this thesis. Analysis of Dynamic Phase 1 was presented at the International Symposium on the Interaction of the Effects of Munitions with Structures (ISIEMS) 2017. The conference paper is located in the appendices.

Chapter 6

In Chapter 6, experimental benchmarking of numerical models is undertaken and software reliability limits are determined. Benchmarked models are used in a parametric study to produce probability of failure curves for annealed glazing subjected to long-duration blast loading. An alternative type of pressure-impulse graph is proposed to incorporate probability of failure into the Glazing Hazard Guide. Findings in this chapter meet objectives one, two, three and five.

Chapter 7

Chapter seven concludes this thesis and details recommended future work.

Chapter 2

Literature Review

2.1 Introduction

This chapter provides background theory of blast waves, glass fracture and computational methods in addition to analysis of current research into glazing behaviour in a blast environment. Some basic blast environment definitions and formulae are introduced as well as theory on blast wave-structure interaction. Glazing response to blast loading has been investigated in numerous studies, although recent research has focussed on short-duration blasts and laminated glazing. This work is summarised in section 2.3. Current methods of modelling glass strength and glazing response to blast loading are analysed in sections 2.4 and 2.5.

2.2 Blast Waves

Explosions can be divided into three categories: physical, nuclear and chemical. A physical explosion could be the sudden failure of a container of compressed gas. A nuclear event is caused by production of different atomic nuclei due to movement of nucleons. A chemical explosion is the result of rapid oxidisation (combustion) of explosive compounds. Combustion can be divided into two categories, deflagration and detonation. Deflagration has a reaction rate lower than the speed of sound in the material and is propagated by heat transfer. Detonation is a high intensity reaction with high pressure and temperature gradients. The reaction rate is faster than speed of sound in the material and is propagated by the shock wave produced.

In a conventional explosion, gas is generated at temperatures between 3000°C and 4000°C with pressures in the range of 10-30GPa. Hot gases expand quickly causing surrounding ambient air to be forced outwards, forming the blast wave in front of reaction products. During gas expansion, pressure and temperature fall and expansion rate slows, causing pressure in the blast wave front to decrease with distance. Due to molecular momentum the gases expand beyond ambient conditions producing a negative overpressure. This over-expansion causes a gas flow reversal along a pressure differential before pressure eventually returns to ambient, forming the negative phase of the blast wave (Smith and Hetherington, 1994). For an ideal blast wave in air, as the blast wave arrives at a specified distance away from point of detonation, pressure rises instantaneously from ambient pressure, P_0, to $P=P_0+P_s$ where P_s is peak overpressure. Overpressure then decays exponentially to below ambient pressure before asymptotically rising to ambient conditions (Figure 2.1). No interaction has occurred with an object so the blast wave profile is 'free-field'. Overpressure is the difference between ambient pressure and pressure as a result of the blast wave. Static overpressure is the peak overpressure caused by the discontinuity in air temperature and density at the propagating shock front.

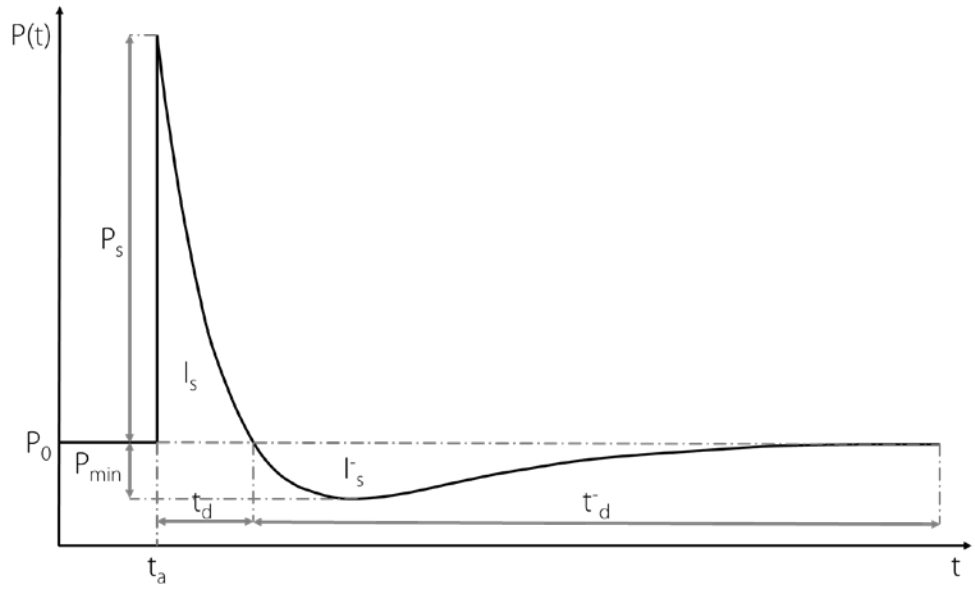

Figure 2.1: Blast wave profile.

- P_0 Atmospheric pressure in ambient conditions
- P_s Peak free-field static overpressure
- P_{min} Peak free-field static underpressure
- t_a Blast wave front arrival time
- t_d Blast wave positive phase duration
- t^-_d Blast wave negative phase duration
- I_s Positive phase impulse
- I^-_s Negative phase impulse

Exponential decay of overpressure can be described by the Friedlander equation (Friedlander, 1946):

$$P(t) = P_s\left[1 - \frac{t}{t_d}\right] exp\left(-\frac{bt}{t_d}\right) \quad 2.1$$

Larcher (2007) estimated the waveform parameter, b, using the positive phase. He determined that b could be approximated by the following equation.

$$b = 5.2777(\ Z^{-1.1975}) \quad 2.2$$

Scaled distance, Z (m/kg$^{1/3}$), can be calculated using the equation below. Blast wave parameters are dependent on distance from the point of detonation (R) and charge mass expressed as TNT equivalence (W). The scaled distance takes account of both parameters, enabling comparison of blast events produced by different combinations of charge mass and standoff distance.

$$Z = \frac{R}{W^{\frac{1}{3}}} \quad 2.3$$

Empirical equations for estimating P_s have been produced using numerical analysis (Henrych, 1979; Brode, 1995). Examples of such equations are outlined in Table 2.1. Both methods equate P_s in terms of scaled distance, Z. Henrych categorised his equations in terms of Z. In comparison Brode categorised location within the blast event in terms of P_s which is usually unknown, making the process to determine the correct equation iterative. Rearranging the equations enables calculation of charge size from measured P_s values. Forensic blast engineers frequently use damage of objects such as windows or bins, for which damage pressure guidelines exist, and these equations to estimate charge size.

Table 2.1: Equations for estimating P_s.

Henrych (1979)	Brode (1995)
Near-field ($0.05 \leq Z < 0.3$) $P_s = \frac{14.072}{Z} + \frac{5.540}{Z^2} + \frac{0.357}{Z^3} + \frac{0.00625}{Z^4}$ bar	Near-field ($P_s > 10$ bar) $P_s = \frac{6.7}{Z^3} + 1$ bar
Mid-field ($0.3 \leq Z < 1$) $P_s = \frac{6.194}{Z} - \frac{0.326}{Z^2} + \frac{2.132}{Z^3}$ bar	Far-field ($0.1 < P_s < 10$ bar) $P_s = \frac{0.975}{Z} + \frac{1.455}{Z^2} + \frac{5.85}{Z^3} - 0.0019$ bar
Far-field ($1 \leq Z < 10$) $P_s = \frac{0.662}{Z} + \frac{4.05}{Z^2} + \frac{3.288}{Z^3}$ bar	

Impulse of the blast wave is equal to the area under the pressure-time curve. Positive phase impulse, I_s, is described by the equation below. For modelling simplicity the blast wave is often approximated by a triangular pulse, where only the positive phase is modelled and overpressure decreases linearly to atmospheric pressure.

$$I_s = \int_{t_a}^{t_a + t_d} P(t)\, dt \quad 2.4$$

2.2.1 Blast Wave Interaction with Structures

When a blast wave hits a solid surface it reflects. By Newton's Third Law, air particles in the incident blast wave exert a pressure on the surface and the surface exerts an equal and opposite pressure on the air particles. At a point exactly on the surface, for an infinitely large perfectly rigid flat plane, reflected pressure, P_r, is twice the free-field pressure. In reality some energy is transferred to the structure. Clearing effects due to finite object dimensions reduce reflected overpressure further. When the blast wave reaches an infinitely large surface with a zero angle of incidence reflected overpressure is described by equation 2.5.

$$P_r = 2P_s + (\gamma + 1)q_s \qquad 2.5$$

- γ Specific heat ratio (1.4 in air)
- q_s Dynamic pressure

Blast wave dynamic pressure is kinetic energy of the air molecules and can be written in the form:

$$q_s = \frac{1}{2}\rho_s {U_s}^2 \qquad 2.6$$

- ρ_s Density of air behind the wave front
- U_s Blast wave front velocity

In air, equation 2.5 can be rearranged into the equation below. For small overpressures, P_r tends to $2P_s$ and for large overpressures to $8P_s$. Reflected overpressure can be between two and eight times greater than static free-field overpressure. For blast wave reflection off the ground, the P_r multiplying factor is approximately 1.8 due to energy transferral to the ground as shock or absorption in crater production.

$$P_r = 2P_s \frac{7P_0 + 4P_s}{7P_0 + P_s} \qquad 2.7$$

When the blast wave angle of incidence is 90° no reflection occurs and the surface is loaded by the static free-field overpressure. For angles of incidence between 0° and 90° either regular reflection or Mach reflection occurs, depending on the angle. In air Mach reflection occurs if angle of incidence is larger than ~40°. The blast wave expands and angle of incidence with the ground increases with increasing distance from point of detonation. When the incidence angle reaches the critical value the blast waves enters a region of Mach reflection (Figure 2.2). The reflected wave travels faster through hot air behind the incident wave, catching up and merging with the incident wave to form a single wave called the Mach stem, shown in the final part of Figure 2.2. A triple point forms at the top of the Mach stem and above this regular reflection occurs. As the reflected wave continues to catch up with the incident wave, the triple point rises. Mach stem formation corresponds with a pressure increase in the wave front. The stem is perpendicular to the ground so associated pressures act parallel to the ground, loading structures with a zero angle of incidence. Mach stems form when the charge is detonated at a particular height above ground, depending on charge mass. Mach reflection can also

occur inside structures where angle of incidence on internal surfaces varies over a wide range, as in the air blast tunnel (ABT) (Glasstone and Dolan, 1977).

For a building with finite dimensions diffraction and drag loading will occur. Diffraction loading is a normal squashing force caused by overpressure and acts on every surface (Figure 2.3a). Drag loading causes a push on the front face then suction on the rear surface and is caused by air molecules travelling past the object (Figure 2.3b).

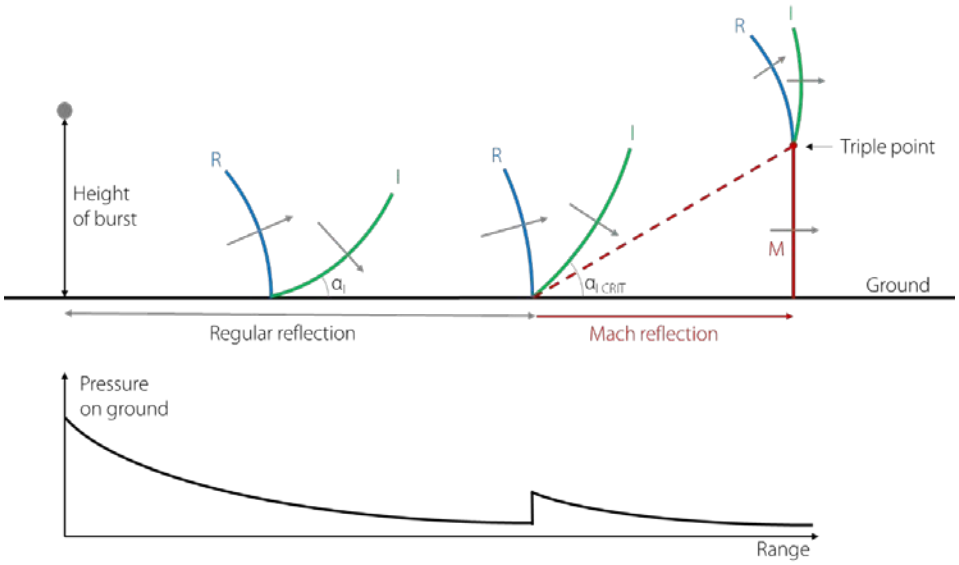

Figure 2.2: Mach stem formation and corresponding ground pressure (R: reflected, I: incident).

(a) Diffraction loading. (b) Drag loading.

Figure 2.3: Diagrams of drag and diffraction loading on a structure.

Blast wave interaction with a simple rectangular structure is demonstrated in Figure 2.4. Diffraction loading is indicated in Figure 2.4a. An overpressure history acting on the front surface is plotted in Figure 2.4b. At time t_2, blast wave arrival and reflection occurs. The pressure acting on the front face is reflected pressure, P_r. This decays from P_r to the stagnation pressure P_{stag} during clearing time, t'. The decay results from a pressure differential caused by stagnation pressure acting on the top and side faces. The stagnation pressure is described by equation 2.8. Clearing time can be estimated using empirical equation 2.9 (UFC 3-340-02, 2008).

$$P_{stag}(t) = P_s(t) + q_s(t) \quad 2.8$$

$$t' = \frac{4S}{(1+R)C_r} \quad 2.9$$

$$\text{where } R = \frac{S}{G} \quad 2.10$$

S is the smaller clearing distance (smaller of B/2 or H in Figure 2.5) and G is the larger of these two values. C_r is the speed of sound in the reflected overpressure region, determined from Figure 2.6. Pressure acting on the top and side surfaces of the object, equal to the stagnation pressure, is shown

in Figure 2.4c. Initial deviation from this pressure is due to vortices forming at the object edges. A rise time to peak stagnation pressure is observed on the rear face (Figure 2.4d) representing time taken for the blast wave to fully travel around the object. The Tianjin case study (Figure 1.1) described in Chapter 1 is unlikely to have been affected by clearing. Windows shown in the image are not on the building edge and previous long-duration trials indicate annealed glass fails within the first 6ms of blast wave arrival (Johns, 2016). The clearing time would have been much greater than 6ms so the wall can be considered infinite for this scenario.

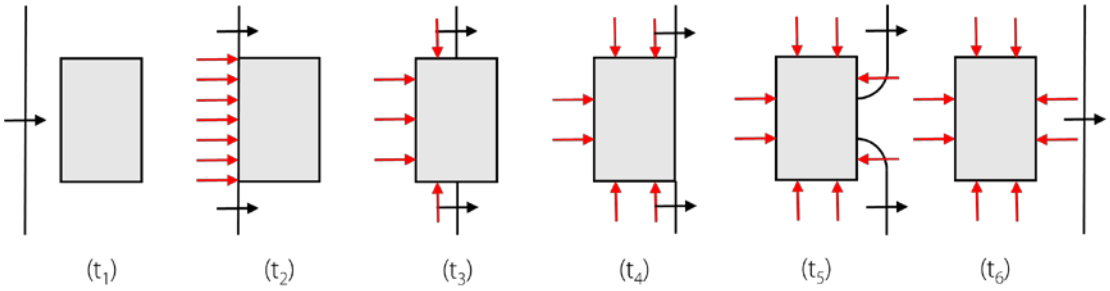

(a) Diffraction around an object.

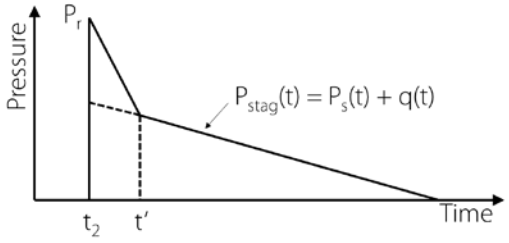

(b) Diffraction loading on front face.

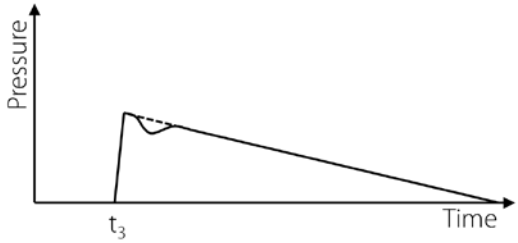

(c) Diffraction loading on side and top faces.

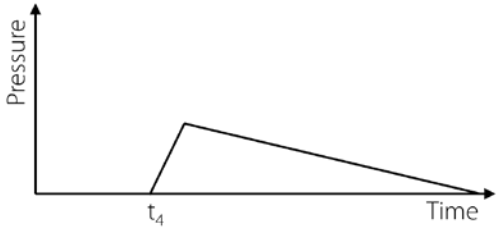

(d) Diffraction loading on rear face.

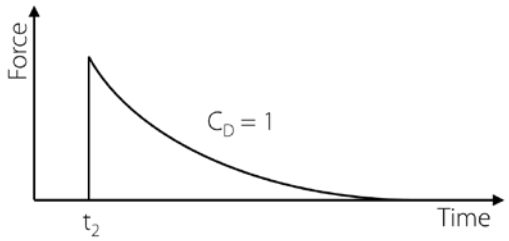

(e) Drag loading on front face.

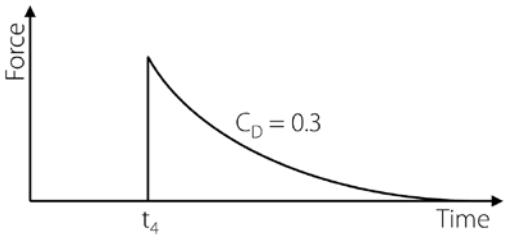

(f) Drag loading on rear face.

Figure 2.4: Diffraction and drag loading histories on each face of a rectangular object.

The drag force acting on the front and rear surfaces is outlined in Figure 2.4e and Figure 2.4f respectively. Drag force, F_D, is calculated using equation 2.11 where C_D is the drag coefficient of the object and A is the area exposed to the force.

$$F_D = C_D . q_s(t) . A \qquad 2.11$$

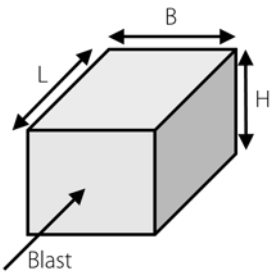

Figure 2.5: Dimensions of diffraction object.

Figure 2.6: Velocity of sound in reflected overpressure region versus peak incident overpressure (UFC 3-340-02, 2008).

2.2.2 Long-Duration Blast

As the blast wave moves away from the point of detonation, static overpressure decreases and the blast wave lengthens, increasing duration of the positive phase and length of the blast wave. For a blast wave to be classified as long-duration, the blast wave should be sufficiently long to engulf a structure. Large explosions can produce a long-duration blast wave in the far-field which is typically classified by a scaled distance, Z, greater than or equal to 1 m/kg$^{1/3}$ (Henrych, 1979). The resulting planar wave produces uniform loading on the front face of the structure, generating a global response. For this thesis, long-duration blast was defined by a positive phase duration greater than 40ms. Assuming the blast wave travels at the speed of sound, the positive phase would be 14m long, sufficiently large to engulf a small house. A positive phase duration of 40ms represents the lower bound of long-duration blast but produces large impulses in excess of 200kPa.ms (see Figure 2.7) causing window failure several kilometres away, despite low overpressure.

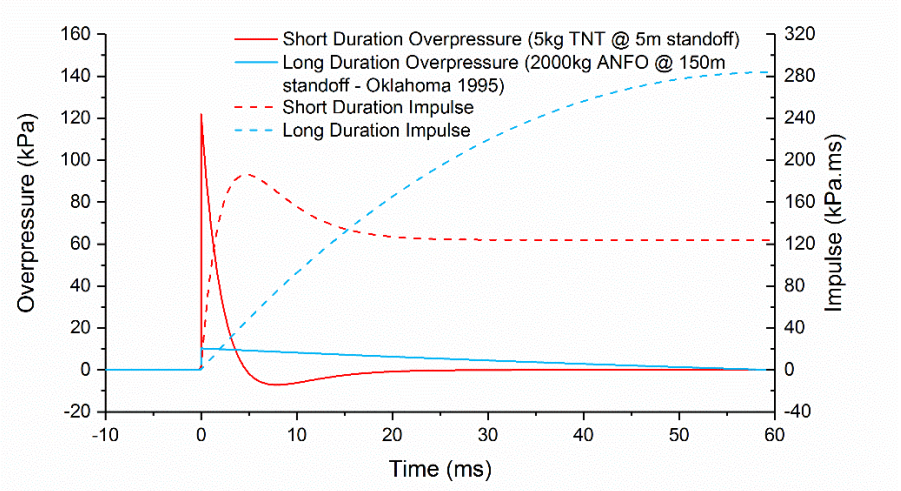

Figure 2.7: Long-duration and short-duration overpressure and impulse histories.

A number of historic large explosions have produced long-duration blast environments, resulting in extensive damage (Table 2.2). In 1917 a collision between two ships, one carrying munitions, occurred in Halifax Harbour causing the largest man-made explosion up to that date. The event's TNT

equivalence was approximately 2,712 tonnes. All structures within one mile were levelled and windows were reported broken 50 miles away. Approximately 2,000 people were killed and a further 9,000 injured (Lilley, 2013). In 1947, a fire caused 2,300 tons (2,087 tonnes) of ammonium nitrate being loaded onto a ship in the Port of Texas City to detonate. The resulting explosion flattened the entire dock area and approximately 1000 nearby buildings. A second ship carrying 961 tons (872 tonnes) of ammonium nitrate detonated 16 hours later causing further damage. Windows were broken up to 10 miles away. An estimated 600 people were killed and a further 2,000, up to 2km away from the blasts, were injured (Fire Prevention and Engineering Bureau of Texas and The National Board of Fire Underwriters, 1947). On 11th December 2005, a vapour cloud of 240,000m^3 due to a leak of 300 tonnes of petrol, ignited at the Buncefield Oil Depot near Hemel Hempstead, UK. A report for the Health and Safety Executive by the Steel Construction Institute (2009) estimated that overpressure in the vapour cloud was in the region of 200kPa. Overpressures of approximately 5kPa were observed up to 4km away, resulting in extensive damage. Windows were reported broken up to 7km away and the explosion was felt over 200km away in Lancashire and Powys (British Geological Survey, 2016). In August 2015, an estimated 800 tons (726 tonnes) of ammonium nitrate detonated in Tianjin, China (Huang and Zhang, 2015) causing damage to windows up to five and a half kilometres away, affecting over 17,000 surrounding households. Buildings up to two kilometres away sustained "severe damage" (McGarry *et al.*, 2017). On 19th April 1995, between 1800 and 2300kg of an ammonium nitrate and fuel mixture (ANFO) detonated outside the Alfred P. Murrah Federal building, Oklahoma. Broken windows were recorded over 1.6km away. Norville (2006) analysed injuries requiring medical treatment, of the 508 injured persons interviewed, 39% suffered glass related injuries.

Table 2.2: Estimated window failure P_s for historic large explosions.

Event	Description	Glass Failure Distance (km)	Estimated P_s (kPa)
Halifax, 1917 (Lilley, 2013)	Collision of munitions ship containing 2366 tons picric acid, 250 tons TNT, 246 tons benzene, 62 tons guncotton.	80	0.1
Texas City Explosion, 1947 (Fire Prevention and Engineering Bureau of Texas and The National Board of Fire Underwriters, 1947)	Two explosions caused by ammonium nitrate aboard separate ships (ship 1: 2300 tons ammonium nitrate, ship 2: 961 tons ammonium nitrate).	16	0.5
Buncefield Disaster, 2005 (Steel Construction Institute, 2009)	Detonation of a 240,000m^3 vapour cloud of petrol. Estimated 105,000-205,000kg TNT from far-field damage.	7	0.5
Tianjin, 2015 (Fu, Wang and Mingwei, 2016)	Explosion of container storage in port: 800 tons ammonium nitrate.	5.5	1.0
Alfred P. Murrah Federal Building, Oklahoma, 1995 (Norville and Conrath, 2006)	Detonation of a truck of between 1800 and 2300kg ANFO.	1.6	0.5

N.B. 1 ton = 0.907 tonnes

Glass windows are vulnerable building components and produce a large damage radius in a blast event. For this reason, distance to the furthest broken window is often quoted in discussion of large

explosions. This distance and interpretation of the Glazing Hazard Guide (see section 2.3.2) are often used by forensic engineers to approximate an equivalent TNT charge mass. It should be noted that for incidents involving multiple explosions, the largest governs maximum glass failure distance. Free-field overpressures (P_s) causing window failure in five events are estimated in Table 2.2. These have been calculated using Henrych's equations (Henrych, 1979). Results for each blast event described indicates a minimum failure pressure of 0.5-1kPa. No information was available regarding the failed window dimensions. Failure pressure for the Halifax event was lower (0.1kPa) which can be attributed to poor glass quality in 1917 compared to modern glazing.

2.3 Experimental Research

2.3.1 Long-duration Blast

Very little long-duration blast testing has been conducted to determine glazing response to highly dynamic loading. Several tests were undertaken between 1950 and 1980, but data collected were limited to qualitative descriptions. Many windows consisted of a sash and muntin construction and no dimensions were quoted. In 1951, a building with windows on all sides was subjected to an estimated P_s 14kPa and P_r 29kPa. No details of positive phase duration and impulse were supplied. 21 of the 28 panes on the front of the building broke, the majority that failed were 3mm thick, double-strength windows. All 6mm thick tempered glass located on the building front remained undamaged. All windows on the sides of the building were broken, despite only being subjected to the free-field overpressure. All glass on the sides was 3mm thick double-strength. 17% of the 30 windows on the building rear failed. Frames containing thicker glass were more heavily damaged which was attributed to a longer break time, resulting in a higher load transferral to the frame (Clark, 1955). In 1953, a typical two-storey American townhouse was subjected to an estimated P_s of 13kPa, producing P_r of 28kPa (Byrnes, 1953). Traditional timber sash windows were used but no dimensions were recorded. Damage was analysed by visual inspection. All windows and frames were "blasted out of the walls or remained in place in badly damaged condition" with the exception of four windows at the rear of the house that remained intact. It was concluded that these windows had been sheltered from the blast wave entering the front of the house by partitions within the floor plan.

In 1954, Clark produced a formula for predicting shatter pressure for windows subjected to long-duration blast loads (Clark, 1954). This equation (below) was derived empirically from test data and assumes no frame damage. No derivation for constant K or aspect ratio factor R was provided. The trend for the aspect ratio factor contradicts observations from the Tianjin case study (Chapter 1) which indicated a decrease in shatter pressure at higher aspect ratios. Limited data and unbalanced units further decrease credibility of this equation.

$$Shatter\ pressure, P\ (psi) = \frac{K\ R\ t^2}{A} \qquad 2.12$$

– K Constant (10,500 for ordinary glass)
– R Aspect ratio factor (see Table 2.3)

– t Glass thickness (in)

– A Glass area (in^2)

Table 2.3: Aspect ratio factor for calculation of shatter pressure using equation 2.12.

Aspect Ratio	1:1	1:1.1	1:1.3	1:1.4	1:1.7	1:2	1:2.5	1:3.3	1:5	1:10
R	1	1.005	1.02	1.07	1.14	1.25	1.45	1.8	2.6	5.0

In 1955, three houses of different design were subjected to P_s 12kPa (Randall, 1961). No information on glazing dimensions was provided. In all three houses, glass in the front windows was destroyed. Most side windows were blown in and glass in the rear windows "suffered some damage". It is not indicated whether window damage referred to the glass or frames. Peak overpressure at the rear of the houses is likely to have been lower than in the free-field due to clearing effects, resulting in less damage compared to windows in other locations.

Chilton (1962) summarised results of these tests into five rules, categorising survival against glass static failure strength, q_f:

1. $P_s < q_f/4$ Front facing windows will "almost surely survive the blast"
2. $P_s > q_f$ Front facing windows will "almost surely fail"
3. Large variation in survival or failure between scenarios 1 and 2
4. $P_s < q_f/2$ Side windows have an "excellent chance of surviving"
5. Damage to rear windows can be reduced by allowing pressure equalization in the building

In the 1973 Eskimo II trials (Fletcher, Richmond and Jones, 1973), 26 windows with varying structural parameters were subjected to three different long-duration blast environments. Glazing aspect ratio ranged from 1:1 to 1:2.1 and area varied between 0.54m^2 and 2.8m^2. The 2-3mm thick annealed glass was supported using a range of different conditions. All ten windows subjected to P_s 3.7kPa and impulse of 292kPa.ms failed. Seven of the eight windows subjected to P_s 2.8kPa and impulse 252kPa.ms failed. In comparison all eight windows subjected to P_s 1.5kPa and impulse 152kPa.ms survived. Despite a large variation in structural parameters like aspect ratio and glazing area, the blast environment appeared to govern window failure or survival. Impulse was calculated from peak static overpressure and positive phase duration assuming an idealised triangular blast wave.

Recent long-duration blast testing utilises facilities such as the ABT. In a series of full-scale experimental trials in the ABT, Johns (2016) investigated the effect of structural parameters on annealed glass resistance to long-duration blast pressure P_s ~14kPa. Johns varied glazing thickness, exposed area, aspect ratio and support conditions, concluding that influence of support conditions and aspect ratio was dependent on area, thickness and proximity to the glazing failure threshold. Two framing options were tested, one imitating rigid support conditions and the other elastic support conditions. Two elastically framed windows survived compared to failure of all rigidly framed glazing. These windows recorded the same peak deflection indicating a stress reduction due to elastic framing. Peak deflection appeared independent of aspect ratio and support conditions for a small glazing area (0.25m^2), although Johns argued this could be a function of a 10% measurement error.

For larger glass panes (0.89m^2) peak deflection decreased with elastic support conditions and an increase in aspect ratio from 1:1 to 1:1.7. Break time increased with area and thickness. Failure impulse for 8mm glass was higher than 4mm thick windows due to longer break times. Fragmentation was strongly influenced by edge supports, significant cracking and small fragments were observed for rigidly framed windows compared to large angular shards for elastically supported glazing.

2.3.2 Short-duration Blast

Modern experimental research into glazing response to blast loading has mainly focussed on short-duration blasts. Recent research has investigated use of laminated glass and improving resistance to blast loading. Very little research has focussed on annealed glazing, despite its use in a large proportion of buildings and the increased hazard associated with it. Claber (1998) estimated that 90% of UK glazing was annealed in 1998. New constructions, especially in urban areas implement blast resistant glazing however the percentage of annealed glass remains high in pre-1998 buildings. The remainder of this section summarises modern short-duration experimental research conducted since the Glazing Hazard Guide was published in 1997.

The UK Glazing Hazard Guide is a classified document based on explosive tests using small to medium charges and 30 different glass configurations. Two panel sizes were used, 0.55m x 1.25m and 1.55m x 1.25m with the charge size and glass thickness and type varied. No procedure was provided for extrapolation of results to other arrangements with varying areas, aspect ratios or support conditions. A standard test procedure with a quantitative method of describing damage caused was produced (Claber, 1998). Dimensions of the test cubicle and hazard levels are outlined in Figure 2.8. Distances were based on shard velocity calculations required to cause skin penetration and eye injury. Skin penetration occurs at a specific energy of 0.1J/mm^2, resulting in an estimated shard velocity of 9m/s and approximately 3m of flight, the basis of the high hazard dimension. Data based on shard dimensions of 50 x 50 x 4mm indicate penetration at 15m/s for annealed glass and over 60m/s for toughened glass indicating the Glazing Hazard Guide may be conservative. The low hazard distance of 1m was determined from a shard velocity of 2m/s, thought to cause a 0.06J/mm^2 specific energy, resulting in eye injury (Marchand *et al.*, 2006).

From experimental results, log-log pressure-impulse (PI) curves were calculated for each arrangement producing pressure and impulse combinations for each hazard level. These curves were named the Iso-Damage Curves (Claber, 1998), an example is shown in Figure 2.9. The minimum impulse resulting in damage is indicated by the vertical asymptote and corresponds to impulsive loading. The horizontal asymptote indicates quasi-static loading and the minimum overpressure to produce damage. Horizontal asymptotes of hazard level indicate that in the quasi-static regime, glazing response is independent of impulse and hazard level is solely a function of peak overpressure. This was tested numerically and results are outlined in Chapter 6. The Glazing Hazard Guide has been indicated to be conservative for most combinations of impulse and overpressure and disregards the influence of shard mass and size (Meyer, Little and Conrath, 2004). Blast loading categories dependent

on positive phase duration (t_d) are defined in Table 2.4 (Cormie, Mays and Smith, 2009). Previous research found that 4mm annealed glass breaks within 2-4ms of blast wave arrival in the ABT (Johns, 2016). This response time is much shorter than the load duration (100ms) and therefore the blast load can be assumed quasi-static for this scenario.

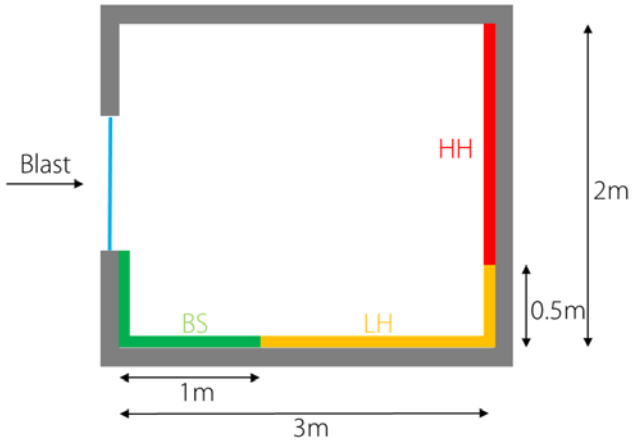

U – Uncracked.
BS – Breaks Safely. No glass found on the floor further than 1m away from the window.
LH – Low Hazard. Glass fragments found on the floor further than 1m away from the window but no higher than 0.5m on the rear wall.
HH – High Hazard. Glass fragments hit rear wall above the height of 0.5m.

Figure 2.8: Glazing hazard levels marked on the testing cubicle.

Table 2.4: Loading categories.

Impulsive	$3 < \frac{t_m}{t_d}$	Positive phase short compared to natural frequency.
Dynamic	$0.3 < \frac{t_m}{t_d} < 3$	Positive phase approximately equal to natural frequency.
Quasi-static	$\frac{t_m}{t_d} < 0.3$	Positive phase long compared to natural frequency.

Where t_m is time to maximum element response.

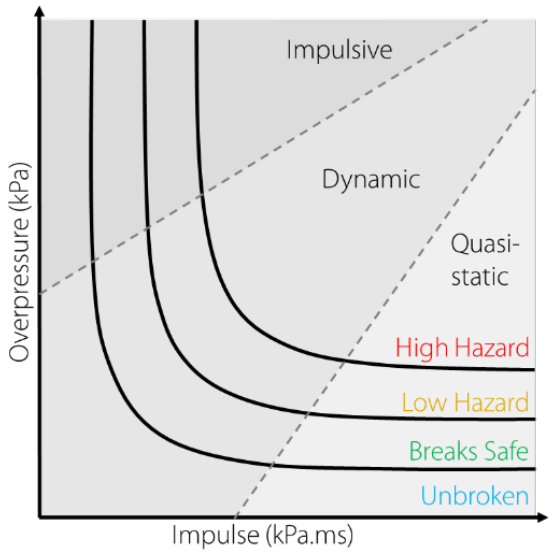

Figure 2.9: Example PI curve (hazard levels and loading categories labelled).

Norville et al. (1999) analysed glazing injuries resulting from the bombing of the Alfred P. Murrah Federal Building, Oklahoma in 1995. An estimated 1800-2300kg of ANFO was detonated causing glazing to fail over 1.6km away. Damage zones were allocated depending on structural and glazing damage (Figure 2.10), glazing damage occurred over an area larger than 2km^2. The majority of windows in these zones were manufactured from annealed monolithic glass. The Oklahoma State

Department of Health (OSDH) collected data to determine injury extent, their locations and causes immediately after the bombing and in surveys over the following two years. Initial data, reported by Mallonee et al. (1996), recorded 167 deaths and 592 injuries within the week following the bombing. Norville et al. disregarded injuries in the Alfred P. Murrah Federal Building for their glazing injury study, stating that glass presented a proportionally small hazard in this building. Glazing related injuries within 300m of the detonation are plotted in Figure 2.11 with corresponding approximate P_s values. This plot indicates that further than 60m from the detonation (due to the exclusion of data from the Alfred P. Murrah Federal Building) glazing injury decreased with P_s. Over 300m away P_s was estimated less than 5kPa but still resulted in 17 glazing related injuries.

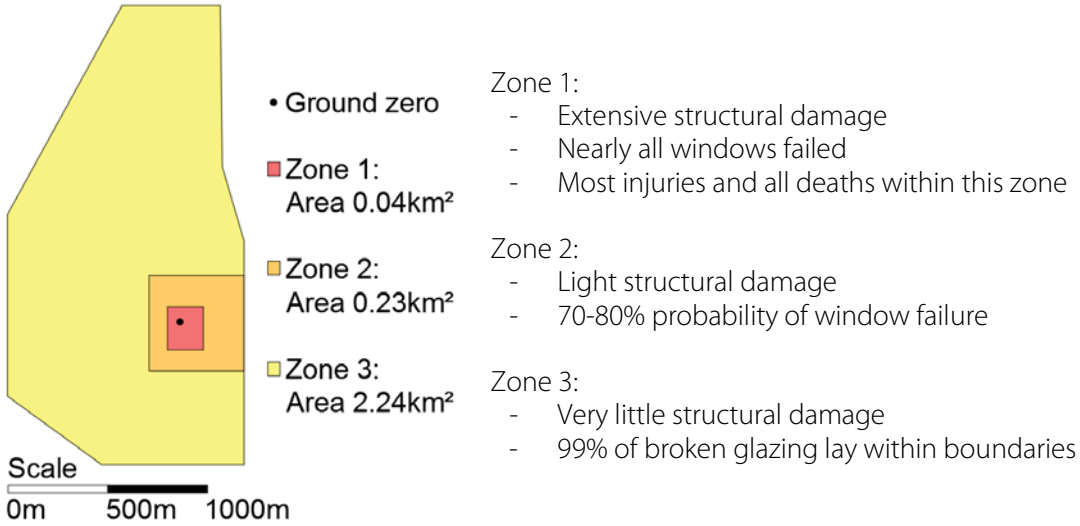

Figure 2.10: Allocated damage zones: Oklahoma Bombing (interpreted from Norville et al. (1999)).

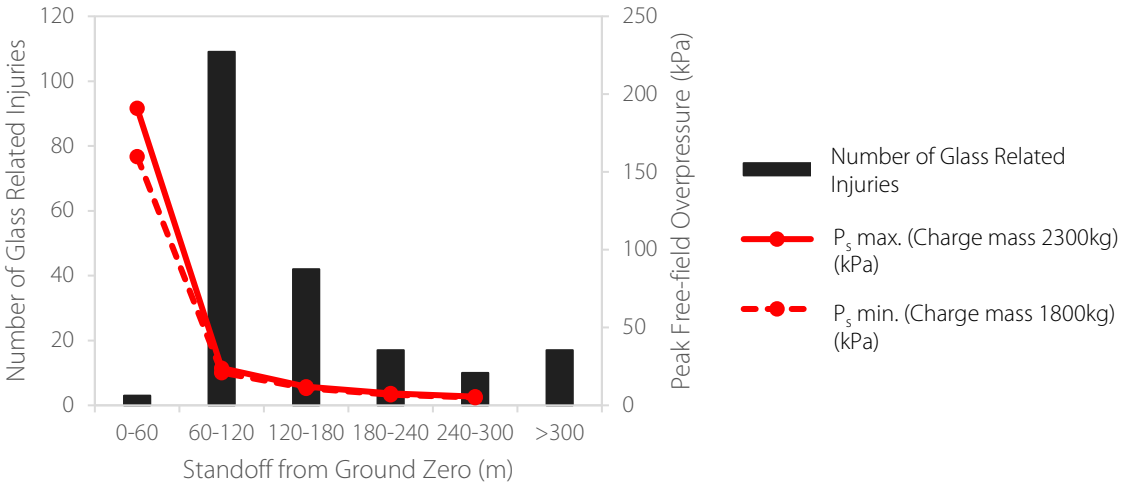

Figure 2.11: Glass related injuries with respect to standoff (interpreted from Norville et al. (1999)).

Injuries in two buildings near to the detonation were examined by Norville et al., the Water Resources Board, approximately a 30m standoff, and the Journal Record Building, approximately 60m away. Based on a charge size of 2050kg, the mean of the two predictions, P_s estimated at the nearest face of the Water Resources Board and the Journal Record Building was 176kPa and 44kPa respectively (see Table 2.5). A higher percentage of occupants in the Water Resources Board were injured (62%)

compared to the Journal Record Building, the percentage of glazing related injuries was also higher (59%). The percentage of occupants that suffered glass related injuries in the Water Resources Board and the Journal Record Building was 37% and 21% respectively. Victims with glass related injuries in the two buildings generally suffered multiple soft tissue injuries. Of these, 98% suffered lacerations, 56% suffered contusions and 23% abrasions. The authors observed that the majority of glass in both buildings was annealed. Laminated glass was installed in the entryway of the Journal Record Building and no glazing related injuries were reported in its proximity. In both buildings numerous glass related injuries were reported over 3m away from glazing indicating a High Hazard Level according to the Glazing Hazard Guide.

Table 2.5: Injuries in two buildings close to the detonation (data interpreted from Norville et al. (1999)).

	Water Resources Board	Journal Record Building
Approximate Standoff Distance (m)	30	60
Approximate P_s assuming charge size 2050kg (kPa)	176	44
Number of Occupants	63	296
% of Occupants Injured	62	43
% of Injuries that were Glass Related	59	48
% of Occupants with Glass Related Injuries	37	21

Kumar and Shukla (2011) simulated blast loading using a shock tube and applied the load to five different types of glass with dimensions 305mm x 305mm x 6.5mm. Annealed, tempered, wired, sandwiched and laminated sandwiched glass were tested. The laminated sandwiched panel was 7.5mm thick due to protective film on both sides. The shock tube diameter was 76.2mm and was centred on the panels. No blast parameter data were specified. In each trial, the glass broke in a circular pattern with a diameter consistent with shock tube dimensions. Glazing strain at initial fracture ranged from 0.01% for the annealed panel to 5% for the sandwich glass. The authors determined that the laminated sandwich glass panel sustained the least damage with no hole forming and a maximum of 6% strain before recovering to 3%. Protective film retained the shattered glass and the PVB interlayer increased panel flexural rigidity.

Three full-scale shock tube tests on 1.22m x 1.68mm laminated windows were performed by Lusk et al. (2011) and compared to numerical predictions produced in finite element analysis (FEA) software LS-DYNA. Each window had a different laminated glazing configuration with total thickness ranging from 7.4mm to 13.8mm. Windows were subjected to different blast pressures, indicating no test repeats. Peak pressure and impulse varied by 29-55kPa and 152-306kPa.ms respectively over the trial series, it was not specified whether reflected or free-field pressure was measured. One sample failed, displacing 140mm in 40ms. Both other windows remained within their frames reaching peak displacements of 51mm and 25mm. The 13.8mm thick sample deflected the least despite being subjected to the highest overpressure, indicating glazing thickness influenced displacement. Numerical simulations demonstrated good agreement with experimental trends in central deflection and reaction forces.

Wedding and Lusk (2012) investigated effectiveness of data capture methods for laminate glazing through 21 identical shock tube tests. Glazing area was 2.04m^2 with aspect ratio 1:1.3. Type and thickness of the laminated glass was not specified. The glass frame was bolted to the end of the shock tube at 20 discrete points as per manufacturers' instructions. No further support condition details were outlined. Deflection was measured using a laser gauge, white duct tape provided a reflective measurement surface on the glass. It is likely this had no effect on results as laminated glass was tested. Results for annealed 4mm thick glass, which is significantly weaker, could have been affected by the addition of duct tape to the surface. Pressure applied to the glass and the resulting reaction forces were also recorded. The window layout was designed to not fail and all samples survived testing. A mean peak overpressure of 34.0±2.5kPa was recorded by two gauges over the trial series. This corresponded to an impulse of 112.1±2.8kPa.ms. Whether the measured pressure was free-field or reflected was not specified. Peak deflection (31.1±0.5mm) was reached on average 9.27±0.25ms after blast wave arrival. The mean total peak reaction force was 35.0kN, average loading on the long side was 21% higher than on the shorter side.

Nawar et al. (2015) performed three shock tube tests on laminated glazing to benchmark an FEA numerical study. Glass dimensions were 1220mm x 1680mm, total thickness ranged between 7.4mm and 7.92mm (see Table 2.6 for glazing construction). Windows were attached to framing using structural silicone. Three different lamination combinations were tested in two blast environments, no repeats were completed. Pressure results and glazing response are summarised in Table 2.6. P_r ranged between 39kPa and 49kPa with a corresponding t_d range of 55-63ms, indicating a long-duration blast environment. The authors did not specify the type of pressure measured but calculations based on charge size and standoff indicate reflected pressure and impulse. All samples shattered but were retained within their frames. Window W3 tore slightly at the centre. This sample recorded the highest deflection (140mm) indicating the thinner interlayer was weaker resulting in a less stiff window arrangement. W2 with heat strengthened glass deflected the least (50mm) and recorded the smallest time to peak deflection, indicating a stiffer arrangement.

Table 2.6: Summary of shock tube test results (Nawar *et al.*, 2015).

No.	Glass Layout	P_r (kPa)	I_r (kPa.ms)	t_d (ms)	Peak deflection (mm)	Time of peak deflection (ms)
W1	3.2mm AN – 1.52 UVEKOL-S – 3.2 AN	48	305	55	120	30
W2	3.2mm HS – 1.52 UVEKOL-S – 3.2 HS	49	308	59	50	15
W3	3.2mm AN – 1.00 UVEKOL-A – 3.2 AN	39	152	63	140	45

AN – annealed glass HS – heat strengthened glass

Ge et al. (2012) produced an equation to predict initial velocity of glass fragments subjected to blast loading which was verified by four experimental trials. The basis of this equation was the principle that blast loading initially causes glass fracture by rapid propagation of micro-cracks then further loading is converted into fragment kinetic energy. Initial fragment velocity was expressed in terms of charge mass, standoff distance and glazing material properties (thickness, Young's modulus and 60

second failure strength). A correction factor of 2.3, obtained from experimental trials, accounted for loss of blast pressure during glass deformation and constant drag factor of 1.21×10^{-3} was taken from research by Gubinelli, Zanelli and Cozzani (2004). Fragment trajectory was predicted using Newton's second law and fluid dynamics. In the trials, windows with dimensions 1m x 1m x 8mm were subjected to short-duration blast loading with P_s between 60kPa and 90kPa and t_d of approximately 3ms. Windows were fixed to a masonry cubicle with an open end allowing pressure equalisation that may have affected results. Initial fragment velocity was recorded using high-speed cameras. Flight distance and fragment distribution were also measured. Initial fragment velocity plotted against charge mass approximately fit a Weibull distribution and good agreement with predicted values was observed.

Hooper et al. (2012) completed four full-scale short-duration blast tests on laminated glass and compared results to an FEA study. Recorded reflected peak overpressures were between 91.2kPa and 155kPa. Reflected impulse ranged from 284kPa.ms to 413kPa.ms. 1.5m x 1.2m windows were constructed from two 3mm thick annealed glass panels and a 1.52mm thick PVB interlayer. Digital image correlation (DIC) was implemented to calculate deflection and rear surface in-plane strain. Respective errors were ±0.1mm and ±0.05%. In three out of four trials, glazing failed by tearing of Dow Corning sealant in the frame and whole panel displacement. The deflected panel shape had a flat central region with little deformation and areas of high deformation near panel edges. Strain lines through the central region corresponded to later forming fracture lines. Deflection was not symmetrical, a larger deflection often occurred at the bottom outer corner of the panel. The author reasoned that this was due to a non-uniform pressure caused by blast wave reflection off the floor and formation of a Mach stem. Clearing was not considered. Cubicle design, with only 270mm between the glass edge and cubicle edge, resulted in a small clearing distance which is likely to have affected results.

Pelfrene et al. (2016) investigated adhesion properties of the PVB interlayer in a series of shock tube tests. Two 6mm thick annealed glass panels were connected by a 1.52mm thick PVB interlayer. Windows with dimensions 0.9m x 1.1m were subjected to overpressures between 47kPa and 155kPa with corresponding impulses of 350kPa.ms to 2000kPa.ms. Four different PVB materials with differing stiffness and adhesion properties were tested. The authors found that lower adhesion in the PVB interlayer produced a safer break, providing bond strength was high enough to retain glass fragments. Pelfrene et al. hypothesised this was due to energy absorption during delamination and viscoelastic deformation of the interlayer. The stiffer PVB acted in a more brittle fashion and either remained intact or completely failed, including PVB interlayer tearing.

Spiller et al. (2016) completed two series of short-duration, full-scale arena trials in 2012 and 2013. Annealed 1m x 1m x 12mm thick panels were fixed using silicone sealant in the first series and aluminium frames with neoprene gaskets in the second. Standoffs were 75m and 65m with a TNT equivalent charge mass of 410kg in series one. In series two, standoffs were 17.75m and 20m with charge masses of 51.25kg and 41kg. Break circuits were used to determine failure time of the glass. A

'wire' was painted onto the surface of the glass using conductive paint which broke with the glass. An error of 0.1ms was observed when the method was compared to high-speed camera footage. Time taken for crack propagation to meet the paint was determined to be the error source. In the initial series, five out of six panels failed to break. For two unbroken windows maximum deflections of 17mm and 13mm were observed 6ms after blast wave arrival. In series two, all 28 windows broke but few results were detailed. Two windows were described which broke with deflections of 17mm and 14mm and break times of 2.6ms and 3.3ms respectively.

Chen et al. (2016) completed nine full-scale blast tests on four-point supported laminated glazing. Four identical windows were tested in each trial, each consisting of two sheets of 1m x 1m tempered glass with a 1.14mm thick PVB interlayer. 8mm and 10mm thick glass sheets produced total window thicknesses of 17.14mm and 21.14mm respectively. Windows with 8mm thick sheets were subjected to four charge masses between 0.4kg and 1.0kg TNT, 10mm thick sheets were subjected to four charges between 0.6kg and 1.2kg TNT. All test standoffs were 5m. Glazing in these trials survived without visible damage. Maximum P_r was 58kPa for charge size 1.2kg. This was measured from a steel panel at an equivalent standoff, however no consideration of clearing distances was reported. Peak pressure was calculated as the mean pressure from two gauges placed 800mm apart vertically. Positive phase duration was "a few milliseconds". Five displacement transducers applied to the top left window recorded displacement histories. Windows subjected to charges smaller than 1kg showed no residual displacement, indicating elastic behaviour. Above 1kg TNT residual displacement, indicating non-linear behaviour, was recorded for both window thicknesses despite no visible damage. This could be attributed to PVB plastic deformation. Maximum displacement increased with charge size. Increasing window thickness from 8mm to 10mm decreased peak displacement by approximately 20%. In a second trial phase aiming to observe failure patterns, the same setup with 10mm thick panels and a 30kg TNT charge was implemented. Recorded P_r was 1064kPa. Windows failed by PVB tearing at supports. Glazing fragmented but was retained by the PVB. The authors hypothesised that fractured window speed was reduced due to energy dissipated via PVB tearing.

2.3.3 Summary

Long and short-duration experimental work is summarised in Table 2.7. Experimental research into long-duration blast interaction with glazing has been limited to a few trials between 1950 and 1980 in which limited qualitative data were recorded. Modern long-duration blast trials require use of facilities like the ABT but very limited data are available in the public domain. Modern research has focussed on short-duration blasts. Experimental testing of blast interaction with glazing is expensive and for this reason most experimental research consists of several trials to provide a computational analysis benchmark. Little work has been undertaken to experimentally investigate influence of structural parameters like aspect ratio, area and support conditions on glazing behaviour.

Table 2.7: Summary of experimental work.

Paper	Long/Short-Duration Blast	Glass Type	Research Focus
Clark, 1955	Long-duration	Tempered and double strength	Response of different glass types and thicknesses.
Byrnes, 1953	Long-duration	Not specified	Response of a typical American townhouse.
Randall 1955	Long-duration	Not specified	Response of three housing designs.
Fletcher, Richmond and Jones, 1973	Long-duration	Various	Whether blast or structural parameters have a larger effect on window failure.
Johns, 2016	Long-duration	Annealed	Effect of structural parameters (area, thickness, aspect ratio, supports) on glazing response.
Glazing Hazard Guide, 1997	Short- duration	Various	PI graphs for blast resistant glazing design.
Kumar and Shukla, 2011	Short-duration	Various	Shock tube trials to determine how glass type affected failure.
Lusk et al. 2011	Short-duration	Laminated	Shock tube trials to determine effect of varying peak overpressure and glazing thickness on peak displacement.
Wedding and Lusk, 2012	Short-duration	Laminated	Shock tube trials to determine repeatability of data capture methods including for peak deflection.
Nawar et al. 2015	Long-duration	Laminated	Shock tube trials for computational benchmarking.
Ge et al. 2012	Short-duration	Annealed	Determine relationship between initial fragment velocity and charge mass.
Hooper et al. 2012	Short-duration	Laminated	Computational benchmarking.
Pelfrene et al. 2016	Short-duration	Laminated	Shock tube trials to determine the effect of PVB interlayer stiffness on glazing response.
Spiller et al. 2016	Short-duration	Annealed	Computational benchmarking.
Chen et al. 2016	Short-duration	Laminated	Determine effect of charge mass and glass thickness on window displacement.

2.4 Glass Material Model

The fracture origin of a ceramic is defined in fractography as the "source from which brittle fracture begins" (Quinn, 2016). In experimental trials for this thesis, break time was recorded when the fracture origin was first observed. Cracking propagates away from the fracture origin initially as two single cracks travelling in opposite directions. Their directions are normal to the maximum local principal tensile stress in the glass, causing vertical cracking in windows of high aspect ratio. Cracks accelerate until terminal velocity is reached then split in two with an acute angle. This is called velocity branching and indicates direction of crack propagation, enabling cracks to be traced back to the fracture origin. Distance between branches is directly proportional to stored energy in the glass. The more energy stored (e.g. a longer break time in a blast experiment) the smaller the distance between branches, resulting in dense cracking and small fragments (Quinn, 2016). In their paper on glass debris hazards, Bewick et al. (2015) divided glazing response to blast into two categories. High overpressures produce

material level fragmentation due to immediate material overloading, causing smaller fragments. The window is described as being "punched" as failure occurs at low displacement. Low overpressures cause structural level fragmentation where large deflection causes fracture, resulting in fewer fragments. Long-duration blast environments produced in the ABT resulted in structural level fragmentation due to low overpressures.

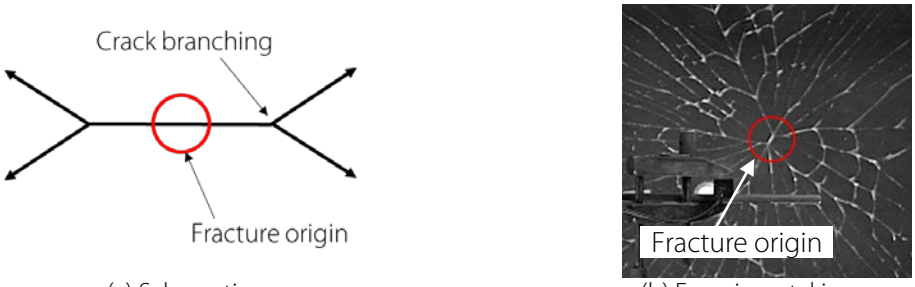

(a) Schematic. (b) Experimental image.

Figure 2.12: Velocity cracking occurs as cracks propagate away from fracture origin.

In his review of open literature, Pritchard (1981) highlighted the wide range of blast overpressures quoted for window failure, ranging from 1kPa (Brasie and Simpson, 1968) to 4-30kPa (Harris, Marshall and Moppett, 1977). Pritchard stated that extreme brittleness of glass was the most relevant property when subjected to blast loading as the window breaks suddenly, exhibiting no permanent deformation. He observed that windows fail in flexural tension, only in response to tensile stress. The maximum principal stress (MPS) model is the simplest method of predicting glass failure. In this approach, failure occurs when stress in any part exceeds the stated failure strength. prEN 13474-1 states that the failure strength of basic annealed glass is 45MPa, this is then adjusted to take into consideration effects of age and environment. Glass strength is also adjusted depending on strain rate. The design strength of annealed glass subjected to blast loading is 80MPa, an increase by a factor of 1.78 from the static design strength (British Standards Institution, 2012). While this method is simple and easy to use, the glass is treated as a homogeneous material, disregarding random flaws or local stress distributions (Spiller *et al.*, 2016).

Glass window design in the USA in the 1960s and early 1970s consisted of selecting a glass thickness from a single chart (see Figure 2.13). The empirically derived chart was based on new glass strength tests (Orr, 1957; Hershey, Higgins and Magrab, 1974) which were often not statistically significant. Orr produced his model from only 20 samples with 5 glass configurations. The chart was based on a 60s duration load and gave no consideration to aspect ratio or support conditions. Blast loading was not considered. Factors could be applied to adjust results for other glass types (Morse and Norville, 2010). In the late 1970s, PPG Industries Inc. (Pittsburgh Plate Glass Industries, 1979) released thickness selection charts based on a statistically large quantity of glass failure data and results of geometrically nonlinear FEA (Tsai and Stewart, 1976; Kraull *et al.*, 1981). The design stress was reduced to allow for in-service glass aging, typically resulting in thicker glass being specified compared to traditional charts. Individual charts were developed for each thickness and glass type. Glass thickness could be selected as a function of area, aspect ratio and glass type. Incorporating the PPG method into building

standards was resisted due to increased complexity and specification of thicker glass (Beason, Kohutek and Bracci, 1998).

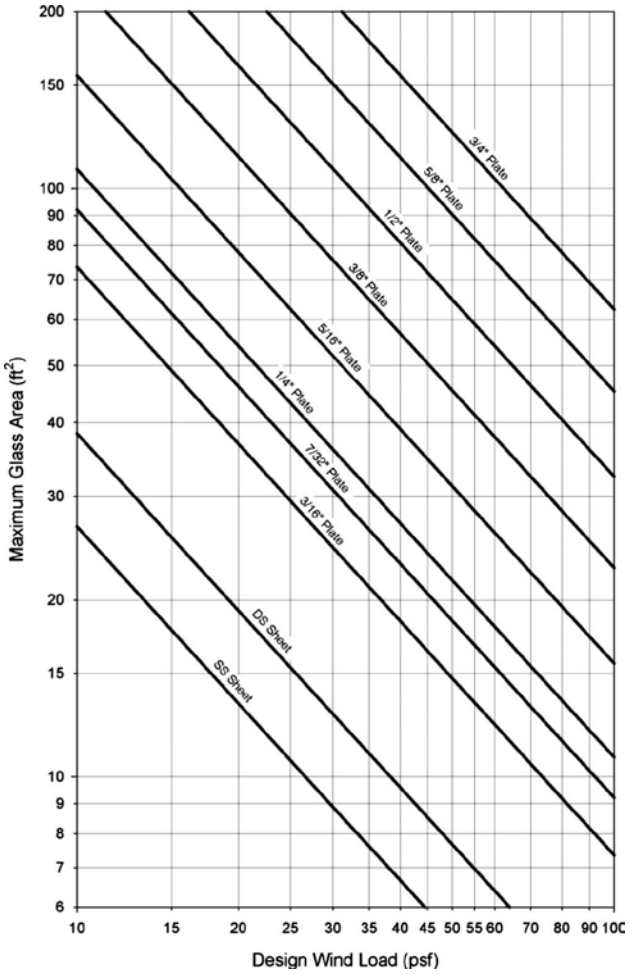

Figure 2.13: Traditional glass thickness selection chart (Morse and Norville, 2010).

Griffith (1921) used glass as an example to explain his theory of rupture in solids. Griffith observed experimentally that glass strength was less than one tenth of the theoretical strength when an isotropic material was assumed. He hypothesised that heating the glass rods resulted in thermal agitation of molecules causing them to become randomly oriented. After cooling, the molecules rotated to orient themselves with their maxima of attraction in line with each other, thus forming sheets and achieving a stable equilibrium. These sheets seed randomly causing an irregular arrangement. The new molecular configuration is accompanied by a very slight change in rod dimensions, causing internal stresses which, if sufficiently large, induce cracking. An increase in potential energy must occur when a crack forms due to the production of a new interior surface. This is due to work done against cohesive forces between attracting molecules which is balanced by the decrease in potential energy caused by molecular reorientation. He found that smaller diameter glass rods had higher material strengths, closer to the theoretical strength. Rod strength, while being dependent on size, was also controlled by maximum glass temperature, temperature during testing, presence of impurities and age of the fibre. Rod strength decreased with time after heat treatment due to molecular realignment.

From Griffith's theory, the surface of a glass pane is covered in flaws of varying sizes and shapes. Fracture will initiate from one flaw, the critical flaw and propagate outwards. This is referred to as a Griffith flaw and is not necessarily at the point of maximum stress but is the flaw with a combination of size, shape and orientation in the stress field that causes local stresses to reach yield. The random nature of a Griffith flaw can cause variation in strength data for annealed glass by as much as 25% (Beason, Kohutek and Bracci, 1998). As glass panel size increases, probability of the presence of a critical flaw increases and failure stress decreases. The main disadvantage of the Griffith flaw theory is that flaw distribution cannot be measured or calculated making the theory impractical to apply to modelling (Lam *et al.*, 2011).

Weibull used a statistical method to represent glazing failure strength. Cumulative probability of glass pane failure, P_f, is calculated using equations 2.13 and 2.14. This equation calculates the probability that glass with area A contains at least one critical flaw (Beason and Morgan, 1984). The Weibull function was adapted by Beason and Morgan (1984) to form the Glass Failure Prediction Model (GFPM). A correction factor, c, was added to equation 2.14 enabling the function to be applied to non-uniform and bidirectional flexural stresses (equation 2.15). A 60 second equivalent stress was introduced. This parameter, calculated using equation 2.16, converts the stress for a given load duration into an equivalent static stress lasting 60 seconds. Recently this value was changed to three seconds for a more realistic blast loading response. This parameter still does not portray the complexity of blast and is therefore a conservative design load (Seica *et al.*, 2011).

$$P_f = 1 - e^{-B} \quad 2.13$$

$$B = k\,A\,\sigma^m \quad 2.14$$

$$B = k\,A\,(c \cdot \sigma)^m \quad 2.15$$

$$\tilde{\sigma}_{t_d} = \left[\frac{\int_0^{t_d} \sigma(t)^n\,dt}{t_d}\right]^{\frac{1}{n}} \quad 2.16$$

- k Weibull parameter
- A Area of glass panel
- σ Maximum tensile stress
- m Weibull parameter
- t_d Equivalent load duration, usually 60 seconds
- n Static fatigue constant, normally taken to be 16

Beason and Morgan (1984) undertook an experiment in which old and new glass panes were tested to failure to determine values for m and k. Three different in-service windows from buildings in Texas and a new glass sample were tested. Results from Beason's experiments are outlined in Table 2.7 for reference. New glass was significantly stronger than old glass but a large variation in m and k was observed between samples. Glass accumulates flaws throughout its life via manufacturing, handling and in-service weathering. Older glass has a higher number of flaws with a higher probability of a critical flaw, reducing its strength compared to new glass. Linear scratches and pitting on 20 year old

glass are visible in Figure 2.14. Possible causes include installation, debris impact and biological attack (Overend and Zammit, 2012).

Table 2.8: Summary of m and k values from Beason's experiments.

Sample	Age	Dimensions (mm)	Sample No.	m	k
1	20 years	724x1540x5.56 724x724x5.56	20 each	6	6.33×10^{-15} mm^{10}/N^6
2	20 years	413x502x3.18	22	6	3.01×10^{-15} mm^{10}/N^6
3	25 years	356x921x3.18	132	5	9.60×10^{-14} mm^8/N^5
4	New	413x502x3.18	Not given	9	1.32×10^{-21} mm^{11}/N^9

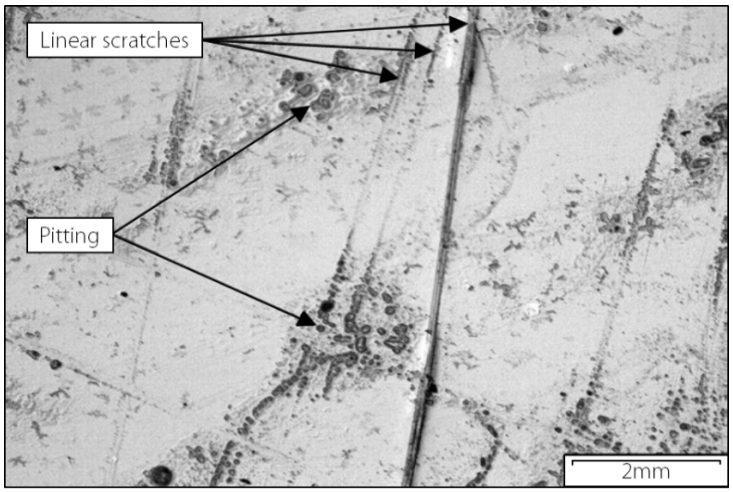

Figure 2.14: Surface flaws on 20 year old glass. Image taken with polarised light microscope (Overend and Zammit, 2012).

GFPM formed the basis of annealed thickness section charts quoted in ASTM E1300-89. Factors for chart application to other glass types were incorporated into the 1994 edition of ASTM E1300. Design loads are based on a 60s duration and probability of failure of 0.8% to ensure continuity from traditional and PPG charts (Beason, Kohutek and Bracci, 1998). In 1997 the load duration was changed to 3s to reflect current wind design standards (Morse and Norville, 2010) however this is still long compared to a blast wave. Area, aspect ratio and glass thickness can be used to read off a non-factored load (NFL) for a given configuration (see Figure 2.15). Weibull's material model with standard m and k values (m = 7, k = 2.86×10^{-53} N^{-7} m^{12}) was incorporated into the charts to ensure an accurate material model that considers normal in-service exposure. While GFPM is widely accepted and forms the basis of Canadian and American design standards, it is not without faults. Lam (2011) argued the method lacks formal mathematical proof or thorough experimental testing. Beason (1984) stated GFPM was based on the assumption that glass strength was controlled by interaction between flaws and tensile stresses but the method is semi-empirical. m and k have no physical representation and require calibration through rigorous experimental testing. Testing has shown m and k vary largely and cannot be assumed to be material constants (Nurhuda *et al.*, 2010).

Morse and Norville (2010) used Vallabhan and Wang's (1981) nonlinear finite difference model coupled with a Weibull (1939) distribution to query the cause of inflections in the ASTM non-factored load (NFL) charts (see Figure 2.15). Short and long glass lengths were increased from 50.8mm to

5080mm in increments of 50.8mm, disregarding aspect ratios larger than 1:10. While all glass thicknesses in ASTM charts (ranging from 2.5mm to 21mm) were modelled, only results from 6mm models are discussed in detail. A 1000 node mesh modelled a quarter of the glass. Values of m and k were taken from ASTM (7 and 2.86 $x10^{-53}$ N^{-7} m^{12}). Analysis converged to a NFL with probability of window failure 0.8%. Resulting stresses were plotted as contours on existing ASTM dimension plots. Normal bending stress in the y (shorter) direction increased with aspect ratio, consistent with one-way bending theory, with a large gradient between aspect ratios 1:1.5 and 1:3. Normal bending stress in the x (longer) direction was much smaller in magnitude and decreased above aspect ratio 1:3, also consistent with one-way spanning theory. Shear bending had a similar magnitude to normal bending in the y direction with a steep increase in magnitude for aspect ratios less than 1:1.5, consistent with two-way spanning theory. A steep gradient was observed for normal bending stress in the x direction and normal shear stress from aspect ratio 1:1.5 to 1:3. Membrane normal and shear stresses exhibited similar behaviour to bending stresses but magnitude was much smaller, indicating bending stresses governed contour shape. The single largest combined maximum principal stress (SLCMPS) was the sum of these stresses and was compared to NFL contour plots. In general, increasing dimensions decreased SLCMPS, consistent with the higher probability of a critical flaw in a larger glass plate. A transition region between aspect ratios 1.5 and 3 was identified where a significant gradient in SLCMPS occurred. This region indicated transition from two-way to one-way spanning regimes and corresponded to a significantly lower load resistance at aspect ratio 1:2.5. Morse and Norville concluded that inflections in ASTM NFL lines were due to switching from two to one-way spanning.

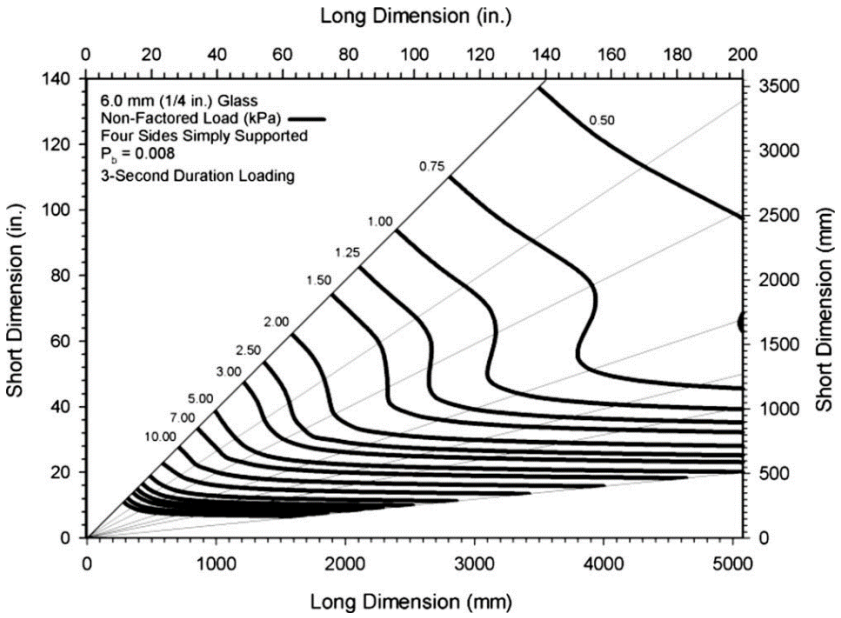

Figure 2.15: NFL values for 6mm thick glass from ASTM E1300 (Morse and Norville, 2010).

More recently the flaw distribution has been found to be more accurately modelled using a Log-Normal distribution instead of to the Weibull distribution. Nurhuda (2010) used FEA and experimental data to investigate accuracy of the Weibull function in predicting glass failure strength. 79 6mm thick specimens ranging from 2m x 0.4m to 2m x 2m were tested at different pressure rates. Weibull's m and k variables were determined for each arrangement and compared to ATSM standard values.

Results were highly variable. Nurhuda proposed an alternative Monte Carlo simulation to create a flaw distribution model where flaw size, density and locations were selected at random. No interaction between flaws was assumed. The glass was assumed elastic and only one quarter was modelled to decrease solver time. This model was verified by calibrating key variables against experimental data. Flaw size distribution modelled by a Log-Normal distribution agreed best with the experimental cumulative probability distribution (CPD). The effect of window size was investigated numerically. CPD curves produced for each panel size were matched to a Log-Normal distribution. Log-Normal parameters M and D, where M is the mean of the natural logarithm of strengths and D is the standard deviation of the natural logarithm of strengths, decreased as panel size increased, converging at 4.18 and 0.31 respectively for infinitely large windows.

Lam (2011) modelled the flaw distribution in a glass pane using a Monte Carlo technique. Number of flaws, their size and location were chosen using probabilistic methods and random seed numbers. Uniform, Normal, Log-Normal and Weibull distributions modelled flaw size. Stress distribution was modelled using FEA and stress at each flaw location was identified. Multiplying normalised stress at the flaw location by the square root of the normalised flaw size allowed the critical flaw to be identified. The process was repeated 100 times and a CPD was produced. Results for each distribution model were plotted against experimental results using new glass by Calderone (2000). A flaw density of 10 flaws per m^2 and a maximum flaw size of 278μm implementing a Log-Normal distribution for flaw size yielded results that were the closest match to experimental data.

Veer et al. (2005) performed four point bending tests on standing 10mm-thick annealed float glass using a Zwick Z 100 universal testing machine. 24 glass specimens were tested, half with dimensions 125mm x 1000mm and half with dimensions 250mm x 1000mm. Glass edges were ground and polished and the glass was supported at five points along its length. Failure stress for the 250mm wide and 125mm wide samples were 43.7±5.2MPa and 39.9±9.7MPa respectively. Veer noted that standing glass strength tends to be 40% less than the strength of lying glass. Measured failure stress from both sample sizes did not fit a Weibull function, especially near the bottom of the distribution. Number of cracks spreading from point of failure was recorded for each sample and good linear correlation was observed between number of cracks and failure stress. In some cases significantly lower cracking was recorded demonstrating that this relationship was not a reliable indicator of failure stress.

In four series of testing, Zhang et al. (2012) tested the compressive and tensile properties of annealed glass over a range of strain rates. 15mm thick annealed glass was cut then ground into 15mm diameter cylinders. Glass density was 2500kg/m^3. A Baldwin testing machine with a load cell and two strain gauges were used to perform three static compressive tests and three static split tensile tests to determine static material properties of the glass. All samples in compressive and tensile static tests broke with an approximately linear elastic stress-strain relationship and a very brittle failure. The average compressive strength was 265±9MPa and average tensile strength was 19.3±0.9MPa. Young's Moduli for compressive and tensile static testing were 65.8±4.5GPa and 57.8±2.5GPa respectively. The slightly higher compressive modulus was attributed to closure of micro-cracks

during compression. Split Hopkinson Pressure Bars (SHPB) with diameter 50mm were used for dynamic testing (36 compressive specimens and 30 tensile specimens). For compressive dynamic tests four strain rates between 129/s and 241/s were tested. All samples exhibited highly brittle fracture with a linear stress-strain relationship. The Young's Modulus remained consistent as strain rate was increased but compressive strength increased. Dynamic increase factors (DIF) were calculated based on the mean static compressive strength. Two regimes were observed when DIF was plotted against strain rate. DIF increased linearly at a low rate for strain rates below 100/s then at a much higher rate above 100/s. The SHPB machine was only able to achieve strain rates between 100/s and 400/s so a straight line was drawn between the data and static results. At a strain rate of 100/s the DIF was 30%, increasing to 200% at 400/s. A similar method was used for the dynamic tensile tests, with a similar trend in results. Young's modulus was constant and tensile strength increased with strain rate. At a strain rate of 300/s the DIF was 30%, for 900/s the DIF was 200%, indicating the compressive DIF was more significant than the tensile DIF. The authors suggested this was due to the number of fragments in tensile tests not changing as much as in compressive tests. In compressive tests, low strain rate specimens fractured into large shards whereas specimens subjected to high strain rates turned to dust at failure. The high number of fragments produced a large number of failure surfaces, absorbing more energy from the loading source and increasing compressive strength. Tensile tested specimens exhibited little change in fragment size as strain rate increased.

2.5 Computational Analysis

A number of computational methods have been used to analyse glazing response to blast loading. Spiller et al. (2016) modelled experimental results using three different software packages. While all predicted trial results with reasonable accuracy, software using a probabilistic failure criterion was more accurate than software using a deterministic failure criterion such as MPS. The authors concluded that choice of failure criterion was more important than type of analysis, for example single degree of freedom (SDOF) or FEA.

Krauthammer and Altenberg (2000) focussed on the negative phase of the blast wave and its effect on annealed glass panels. They found that in the far-field, magnitude of the positive and negative overpressures were very similar. The authors stated that if failure in the positive phase did not occur, the negative phase could enhance panel rebound, causing failure. Krauthammer used a linear SDOF model without damping to investigate response of a simply supported glass panel to 10kg and 100kg TNT charges at a range of stand-off distances. The blast wave was modelled linearly. Weibull's method, proposed by Beason (1984), was used to model window probability of failure. Two panels were tested, the first 1397mm x 1448mm x 9.63mm (approximately 1:1 aspect ratio) and the second 1524mm x 2438mm x 6.4mm (1:1.6 aspect ratio). Peak inward displacement (due to the positive phase) and peak outward displacement (due to the negative phase) were plotted against scaled distance, Z. In all cases outward deflection was greater than inward deflection when linear-elastic behaviour and no breakage was assumed. Peak displacement decreased with scaled distance Z and the rectangular

panel deflected further than the square panel. Probability of failure decreased with scaled distance Z. For larger values of Z, probability of failure was greater for the negative phase, especially in the square panel. The authors concluded that inclusion of the negative phase in analysis was key for small overpressures where the ratio of negative to positive overpressure is near one. They stated that glass panel behaviour was dependent on relative dynamic characteristics of the blast load. No mention was made of any experimental benchmark or the influence of impulse.

Morison (2010) developed SDOF models of laminated glazing response to blast loading. Previous SDOF coefficients were derived from reinforced concrete tests in the 1950s and 1960s and were highly inaccurate. Morison derived alternative coefficients for rectangular panels supported on all sides using non-linear FEA and yield line analysis. FEA produced deflection shape and reaction forces. Behaviour prior to glazing failure was modelled as an equivalent monolithic panel to simplify analysis. This method under-predicted deflection but was concluded to be acceptable for design purposes. Design resistance curves for laminated glass subjected to blast loading were produced from results of equivalent monolithic panels and PVB membranes with transitions depending on how the glass failed.

Wei (Wei and Dharani, 2005; Wei, Shetty and Dharani, 2006) used FEA (LS-DYNA) to simulate behaviour of old and new laminated and monolithic glazing subjected to a short-duration blast. The blast wave was approximated by a Friedlander curve with P_s of 27.5kPa and t_d 16.9ms. Cumulative failure probability curves were produced for each layout using a Weibull distribution. Values of m and k were taken from research by Norville (1985) and the glass and PVB interlayer were modelled as linear-elastic. A quarter of the glass pane was modelled using quadrilateral elements to save processing time. Wei found probability of failure was higher for older glass compared to new glass. Increasing impulse increased probability of failure but increasing glass thickness and decreasing area both decreased probability of failure. For new annealed glass, an aspect ratio of 1:1.4 provided the greatest blast resistance and a window of 1:2.8 aspect ratio the least.

Seica et al. (2011) used results from Wei's FEA analyses (2006) to benchmark their own FEA (ABAQUS) models. Charge mass was varied at a standoff of 25m. Windows were 1200mm wide with aspect ratios of 1:1 and 1:1.7. 12mm and 19mm thick glass was used in single and double glazed combinations. Windows with aspect ratio 1:1.7 broke earlier than 1:1 windows and with a lower deflection which was attributed to the 1:1.7 aspect ratio being a stiffer arrangement. In the double glazing, a delay was observed between outer panel and inner panel failure as a result of blast load transferral. In a second investigation, simply supported annealed glazing with aspect ratio 1:2 and thickness ranging from 6 to 22mm was subjected to a blast with P_s 34.8kPa and I_s 200kPa.ms. The smallest mean deflection was 13mm for 6mm thick glazing. The largest deflection (20mm) was observed for 12mm thick glass. The authors hypothesised this was due to the failure mechanism changing at 12mm from plate bending in thin glazing to shear in the thicker glass.

Lusk et al. (2011) used experimental results to benchmark their LS-DYNA FEA model of laminated glazing response to blast loading. Failure within glass layers was determined by a specified plastic strain. When exceeded, elements were not deleted but internal stresses were redistributed within remaining elements. The PVB interlayer was assumed to deform plastically without failure. Central deflection for all three samples demonstrated good agreement with experimental results despite deviation after 40ms for the two surviving samples. A contour plot of plastic strain from the model was comparable to observed failure patterns within the sample that broke. The authors concluded that their FEA model predicted glazing response well when subjected to blast loading. Hooper et al. (2012) also produced FEA models of their experimental trials. Initial results demonstrated good agreement with trial results but this reduced in the later stages of glass response. In the FEA model, panel edges were modelled with perfectly rigid restraints which the author acknowledged as a source of error.

Ataei and Anderson (2014) used explicit FEA solver ABAQUS to model failure patterns of annealed glass subjected to blast loading. Both homogeneous glazing and chipped glass were investigated. The 500mm x 750mm x 6mm window was modelled as a 3D shell comprising of 15,000 4-noded square elements. Crack patterns were produced using the element deletion technique with mesh regeneration after each time step. The maximum principal stress method was the implemented material model. A time interval of 0.0125ms was applied and two short-duration blast environments modelled as triangular pressure pulses were calculated using A.T. Blast (Applied Research Associates Inc., 2004) and "Defence Threat Reduction Agency Manuals". The "low intensity" blast event exhibited P_r of 38.9kPa and I_r of 250kPa.ms. The "medium intensity" blast had P_r of 165kPa and I_r of 1250kPa.ms. Glass failure mode was governed by load intensity not glass imperfections for bigger blast events. The panel subjected to the low intensity blast event cracked along the centreline after 4.750ms with total panel failure after 12.000ms. Cracking followed the predicted yield line pattern. When subjected to the medium intensity blast, the panel cracked after 3.750ms and failed after 5.850ms. Cracking followed yield line theory but crack density was higher compared to the low intensity event, with multiple initiation points. Two chips were introduced to the model along the glass edges. When the low intensity model was re-run, cracking occurred 0.388ms earlier and total panel failure occurred 3.275ms earlier. The crack pattern was less symmetrical and occurred faster. The chipped panel subjected to the medium intensity blast broke in a similar way however analysis terminated after 6.518ms due to large element rotation causing model instability. Chipping redistributed stresses causing cracking to pass through defects but cracking did not initiate from these imperfections. Defects caused crack patterns to form faster resulting in a quicker and less symmetrical panel failure.

Hidallana-Gamage et al. (2015) used FEA software LS-DYNA to investigate the effect of varying properties of a structural sealant supporting laminated glass subjected to blast loading. The authors highlighted the importance of not overdesigning the joint, resulting in high reaction forces transferred to the frame, or under-designing the joint causing sealant failure before panel capacity is reached and the entire window is thrown. No experimental data were used to benchmark or validate

the parametric study. A laminated glass panel with dimensions 1.1m x 0.9m x 7.52mm constructed from 3mm annealed glass sandwiching a 1.52mm thick PVB interlayer was modelled. No PVB delamination was assumed and the glass sealant boundary was assumed fully bonded. A 3D model of the glass and framing was produced. An 18kg TNT charge was modelled at 25m and 15m standoffs, producing two blast environments with P_r of 31kPa and 70kPa respectively. The blast pressure history was estimated using a Friedlander curve. Increasing width of the structural sealant joint from 7.5mm to 20mm reduced central deflection and energy absorption but increased framing reactions. The authors recommended a width of 10-12mm, agreeing with current ASTM standards but suggested a smaller joint width if capable of withstanding the design blast load. Joint thickness was varied between 4mm and 6mm. Thinner sealant resulted in a less flexible joint, reducing mid-span deflection and energy absorption while increasing reaction forces. Increasing thickness from 5mm to 6mm had little effect, resulting in the authors recommending a thickness of 5mm, agreeing with current ASTM guidelines. Young's modulus of the sealant was varied between 1.5MPa and 3.4MPa. A lower Young's modulus resulted in increased deflection and energy absorption with substantially reduced support reactions. The authors recommended minimising the sealant Young's modulus while ensuring the joint is capable of withstanding the design blast load.

Pelfrene et al. (2016) modelled their experimental trials using FEA package LS-DYNA. Good agreement was observed, however models did not accurately represent experimental set-up. The mesh was partially structured to encourage cracking similar to experimental observations. When failure stress was reached in an element, it was deleted to simulate cracking. A short plastic phase was introduced into the material model to stabilise analysis. Large crack widths due to element deletion caused strain in the PVB interlayer to remain low, preventing tearing. The authors were unable to produce a stable model where delamination occurred.

Chen et al. (2016) used FEA software LS-DYNA to model their experimental set-up investigating point support influence on laminated glazing. PVB delamination was assumed not to occur. The glass was modelled as an elastic-brittle material and the PVB as linear viscoelastic. An ultimate limit strain of 1.0 was set for the PVB and an idealised linear blast wave was applied to the glass. Comparisons to experimental displacements yielded a maximum difference of less than 35%. The authors commented that agreement was better for 8mm thick windows compared to 10mm thick. Failure of the window subjected to 30kg of TNT produced a failure pattern that demonstrated good agreement with experimental observations. The benchmarked numerical model was implemented in a parametric study to determine the effect of structural parameters such as thickness and area. Results demonstrating increasing glass thickness reduced maximum window deflection, in comparison increasing PVB thickness resulted in a slight deflection decrease and a reduction of glazing stress. Increasing glazing area caused an increase in peak deflection attributed by the authors to a decrease in global bending stiffness as a result of a span increase. Movement of the point supports closer to the window edges resulted in the same trend for the same reason. Increasing aspect ratio above 1:1

produced a changing failure pattern around the point support. Cracking angle varied from 45° at aspect ratio 1:1 to a much narrower shape with cracking parallel to the shorter glass edge.

2.5.1 The Applied Element Method

Thus far, all numerical analysis of glazing response to blast loading described in this literature review has been undertaken using FEA. This Continuum Method technique divides the structure into discrete elements connected by common nodes. FEA assumes the material is continuous so modelling separation of elements is difficult unless the crack location is known (Gohel, Patel and Joshi, 2013). The applied element method (AEM) was developed by Meguro and Tagel-Din (2002) as an explicit displacement-based alternative that combines features of FEA and the Discrete Element Method (DEM) (Lupoae and Bucur, 2009). The concept of AEM is outlined in Figure 2.16. The structure is divided into small elements connected at discrete points by groups of springs. This has similarities with DEM, in which the structure is divided into small interacting particles. For a three dimensional problem, three springs are located at each contact point, two shear and one normal. These springs fully describe stresses, strains and displacements of the elements. In FEA these same parameters are calculated at nodes shared between elements, meaning separation is impossible unless predefined. The equations in Figure 2.16 describe the axial stiffness of each spring. Each element has six degrees of freedom representing rigid body movement around its centroid. Spring deformation can be geometrically related to these degrees of freedom using a spring set stiffness matrix. Summing stiffness matrices for each spring set produces the element global stiffness matrix K_G.

AEM enables complicated non-linear behaviour to be tracked, so predicting crack locations is unnecessary. Stress and strain at each connection point is calculated throughout loading. The maximum force a spring can resist is calculated from material properties. Once this force is reached in any spring within the model it is simply removed from analysis, allowing cracking to occur at any location. When a spring is removed, stored energy is redistributed amongst remaining springs and converted into kinetic energy of the detached element group. Once all springs surrounding an element or group of elements have been removed, it is able to separate from the model. This enables full structural response to be modelled, through elastic behaviour, cracking and element collision with the ground or other elements (Gohel, Patel and Joshi, 2013). In comparison, separation in FEA cannot be automated (Applied Science International LLC., 2010). A number of researchers have combated this problem using the element deletion technique in which elements are deleted as they fail. This leads to large cracks appearing instantaneously and model instability as Pelfrene (2016) found.

Meguro and Tagel-Din (2002) used a number of scenarios to test AEM accuracy when large deformation occurs under static loading. AEM was highly accurate when compared to theoretical displacement values for beams, buckling columns, a two-member truss and an elastic frame undergoing large deformations. No comparison to experimental data was made. AEM has been used in previous University of Southampton blast research and has been found to model building response to blast loading well when element separation occurs (Johns, 2016; Keys, 2016). Johns (2016) used

AEM software Extreme Loading for Structures (ELS) to evaluate AEM capability of modelling glazing response to blast loading. An initial series of short-duration blast trials provided experimental validation. AEM calculated break time, failure impulse and leading fragment velocity with reasonable agreement to experimental results. Mean percentage difference between AEM and experimental data was 9%, 15% and 12% respectively for each parameter. Comparisons to long-duration trials in the ABT yielded mean percentage differences of 11% for peak deflection, 11% for break time and 12% for failure impulse across eleven glazing arrangements. Fragmentation analysis of rigid and elastic support conditions indicated fewer and larger fragments for elastically framed windows compared to rigid framing. This matched trends highlighted in Johns' analysis of the experimental data. Reasonable agreement with experimental data indicates AEM is capable of modelling glazing response to short and long-duration blast environments. Lupoae and Bucar (2009) used ELS to design explosive locations and predict collapse shape of a building due for demolition. Comparison of results indicated that AEM was capable of predicting structural response to the explosive layout. Collapse trajectory and final damage state demonstrated good agreement with those for the existing building.

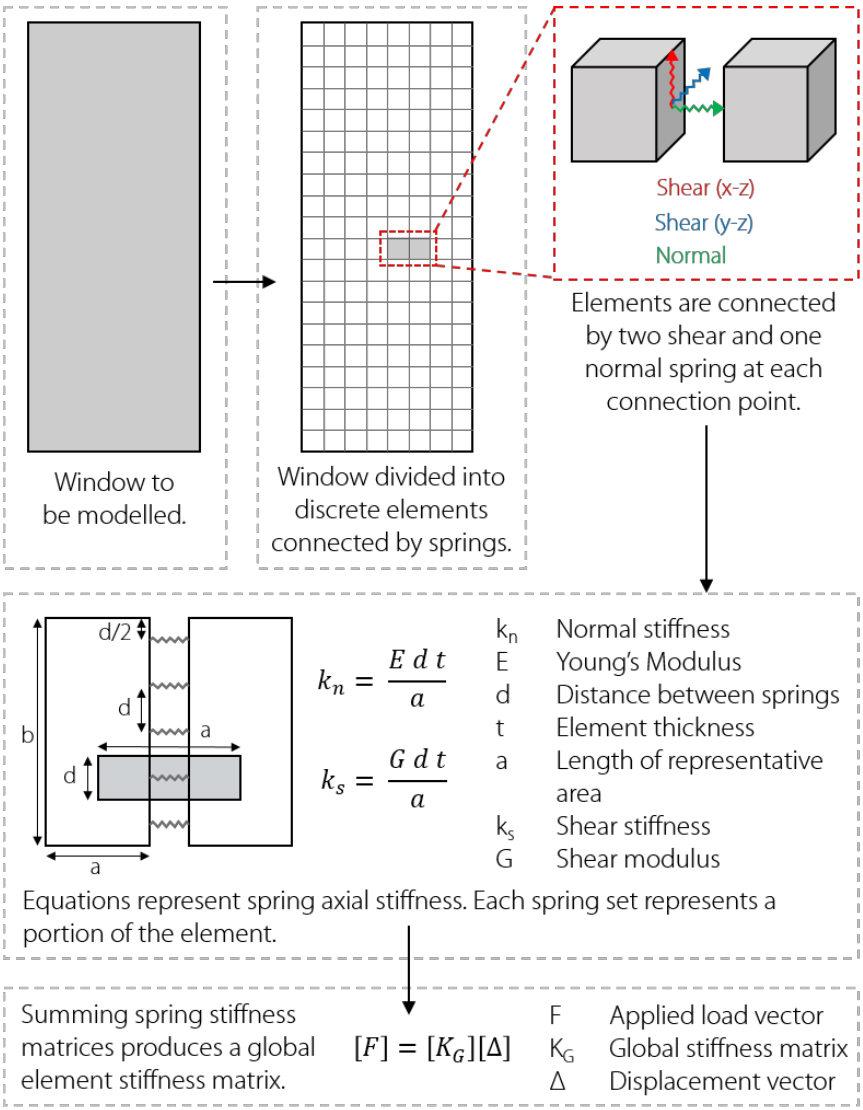

Figure 2.16: AEM concept and methodology.

The medical implications of the bombing of the Alfred P. Murray Building in 1995 were discussed in a previous section. Tagel-Din and Rahman (2006) modelled the event using AEM to determine if the technique was capable of accurately predicting progressive collapse. The authors found that the modelled blast caused an exterior column near to the point of detonation to lose its strength. A transfer girder supported by this column then failed causing the girders above to fail in bending. This series of events and the final collapse shape closely matched investigator descriptions. A secondary 2D model of the front line of columns indicated the girder made contact with the ground 1.6 seconds after detonation and full collapse occurred after 4.5 seconds. This agreed with a sound recording from the building indicating ground contact of the girder at 1.5 seconds and total collapse after 4.5 seconds. The final collapsed shape demonstrated good agreement with the actual building indicating that AEM can accurately model structural response to blast load and the resulting structural collapse. The transition from a continuum to discrete elements during building collapse was accurately modelled by AEM, something that FEA would be incapable of replicating.

2.6 Summary

Experimental research into long-duration blast interaction with glazing has been limited to a few trials between 1950 and 1980 in which limited qualitative data were recorded. An estimation of peak static overpressure was made but no other blast environment data were available. Various window sizes were tested as well as fixings and thicknesses. Structural parameters were found to have a smaller effect on glass survival than peak overpressure. In all trials with P_s 2.8kPa or higher, nearly all front-facing windows failed. All windows survived P_s 1.5kPa. Only 17% of rear-facing windows subjected to P_s 14kPa failed, indicating clearing substantially reduced overpressure at the building rear. Impulse was not recorded and might account for window failure inconsistency between these trials. Modern long-duration blast trials require use of facilities like the ABT. Johns (2016) determined, through rigorous testing in the ABT, that support conditions, glazing area and thickness influenced annealed glazing response to a long-duration blast environment.

Modern research has focussed on short-duration blasts. The Glazing Hazard Guide was produced from trials using small to medium sized charges and two different glazing arrangements. No guidance was given for data extrapolation to other arrangements and long-duration sections were not benchmarked against experimental data. This research project provides experimental data in this region. Influence of structural parameters like aspect ratio and support conditions, investigated to meet aims two and three of this research project, could aid extrapolation of the Glazing Hazard Guide to other dimensions. Experimental testing of blast interaction with glazing is expensive and for this reason most experimental research consists of several trials to provide a computational analysis benchmark. The lack of experimental repetition is of concern due to the highly variable material strength of glass which could result in skewed data. Due to the large expense, little work has been undertaken to experimentally investigate influence of structural parameters like aspect ratio, area and support conditions on glazing behaviour.

Glass strength is highly variable due to the presence of many defects which are random size, shape and location. The Griffith Flaw is the flaw that causes failure and its inconsistency causes variability in glass strength of ±30%. Weibull quantified the glass strength distribution as a probability of failure, but required two constants dependent on experimental testing. Variation in the values of these constants has been demonstrated by several researchers. Static tests in the Spurpark laboratory enabled material strength variation to be quantified and used to produce damage probability curves, aim five of this research project.

Most computational modelling of glazing response has implemented FEA. This technique is unable to model element separation resulting in some researchers employing element deletion methods to force cracking. Experimental validation demonstrated the competency of FEA in modelling parameters such as peak deflection and break time. These have been used to identify relationships between glass failure and structural parameters such as area and aspect ratio. AEM has been successfully used in previous University of Southampton research to model element separation. Discrete springs connecting rigid elements enable cracking to be modelled easily. Good agreement has been observed between experimental results and AEM modelling of masonry and glass subjected to long-duration blast loading. AEM was selected for use in this research project to model glazing response. The method was used in an experimentally benchmarked parametric study to produce damage probability curves of glazing response to long-duration blast loading, aim five of this thesis.

This literature review has highlighted the lack of experimental or computational data on annealed glazing response to long-duration blast loading. Modern research in this field has focussed on short-duration blast and the response of laminated glazing, despite the large proportion of annealed glazing present in older buildings that poses an increased risk in an explosion. Due to the high cost involved, most researchers complete a limited blast trial series with few to no repeats and often only as a benchmark for computational analysis. The highly variable material strength of glass means rigorous experimental testing is necessary and ensures computational modelling is highly complex. This review of current research has demonstrated a lack of understanding of structural parameter influence on glazing response to long-duration blast loading which was investigated to fulfil aims two and three of this research project. The effect of material strength variability on glazing behaviour was addressed in the production of damage probability curves, aim five of this research project.

Chapter 3

Initial Computational Modelling

3.1 Introduction

The next four chapters cover experimental and computational work for this thesis, their structure is outlined in Figure 3.1. Experimental work in the ABT is very expensive. Initial computational work benchmarked against previous experimental trials identified key glazing arrangements, reducing the number of trials required. Using the 2015 Tianjin chemical explosion as a case study, area and aspect ratio were identified as structural parameters key to glazing response. The effect of these parameters was investigated numerically and the experimental test specification was designed based on outcomes. Glazing response was modelled using AEM software Extreme Loading for Structures (ELS) version 5.0 (Applied Science International LLC., 2010). AEM was used in preference to finite element analysis (FEA) as it can model element separation, allowing crack patterns to be produced. Previous research at the University of Southampton demonstrated good agreement between AEM and experimental results for glazing and masonry response to long-duration blast (Johns, 2016; Keys, 2016). All computational analyses were undertaken using a dedicated Intel i7-2600 3.4GHz (quad-core with hyper-threading) system with 16GB RAM. Run time was 20 minutes for initial models (approximately 1500 elements) and 14 hours for final models (approximately 40,000 elements). Each model ran 10ms after blast wave arrival, mean glass failure occurred after 3.4ms.

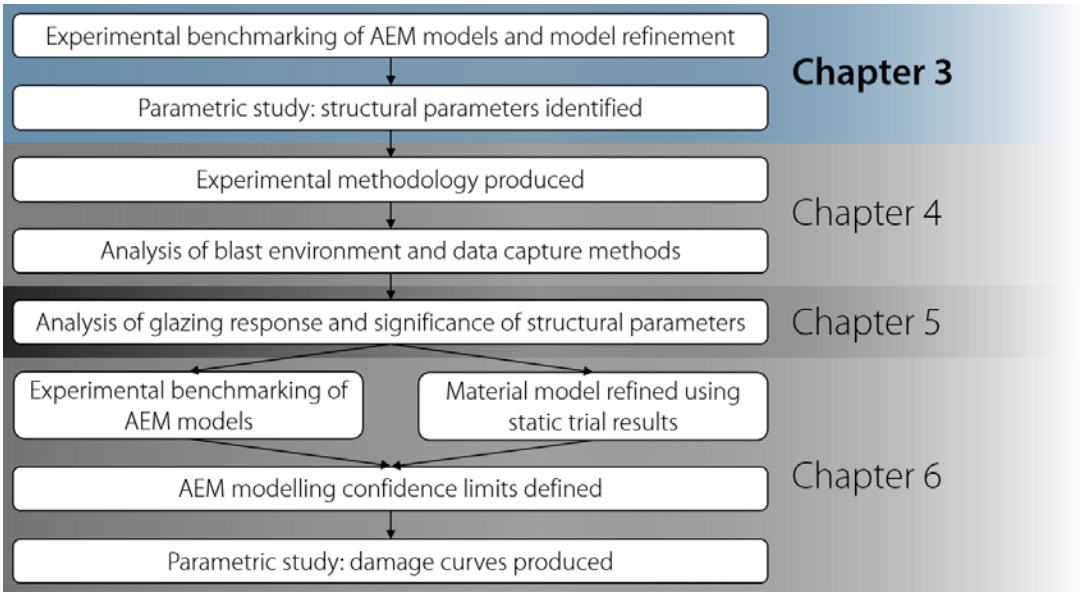

Figure 3.1: Numerical modelling and experimental work outline.

3.2 AEM Model Benchmarking

Data from previous ABT trials (Appendix A) provided an experimental benchmark for the initial parametric study. All experimental glazing arrangements were modelled in ELS with both rigid and elastic support conditions (Table 3.1). Two 10mm thick steel frames bolted together provided rigid support conditions to the glass (Figure 3.2a). Rigid boundary conditions were applied to the rear frame outer elements simulating connection to the test container. For elastic framing Dow Corning 993 silicone sealant connected a single steel frame to the window rear surface allowing some out-of-plane glass rotation (Figure 3.2b).

Table 3.1: Glazing arrangements used for benchmarking.

Arrangement	1	2	3	4	5	6
Glass thickness (mm)	4	4	8	8	4	4
Aspect ratio	1:1	1:1.75	1:1	1:1.7	1:1	1:1.7
Glazing area (m^2)	0.25	0.25	0.89	0.89	0.89	0.89

Glass and Dow Corning 993 material properties (Table 3.2) were taken from literature (European Organisation for Technical Approvals, 2006; Johns, 2016). Separation strain of 1 was implemented for the Dow Corning 993 to ensure separation did not occur. Framing implemented the ELS default steel material model as it was not critical to glazing response (see Table 3.2). Separation strain defines when springs are removed after failure. As tensile strength is reached within a spring its strength reduces to zero but remains intact until its strain reaches the specified separation strain. The spring is then removed from the model and the elements are allowed to separate. For brittle materials like glass separation strain is very low, for structural sealant Dow Corning 993 separation strain is much higher. Post-failure shear stiffness factor governs the rate at which shear strength reduces to zero after spring failure. The parameter ranges between 0 (shear strength reduces to zero instantaneously) and 1 (shear strength remains at value specified). A similar parameter for normal strength exists but was not critical

for glazing where deflection is out-of-plane. In lieu of experimental data, ELS recommended values for separation strain and post-failure shear stiffness were used. These parameters are investigated in Chapter 6. Glazing was meshed into triangular elements using the Delaunay triangulation method to approximate realistic crack patterns (Figure 3.3).

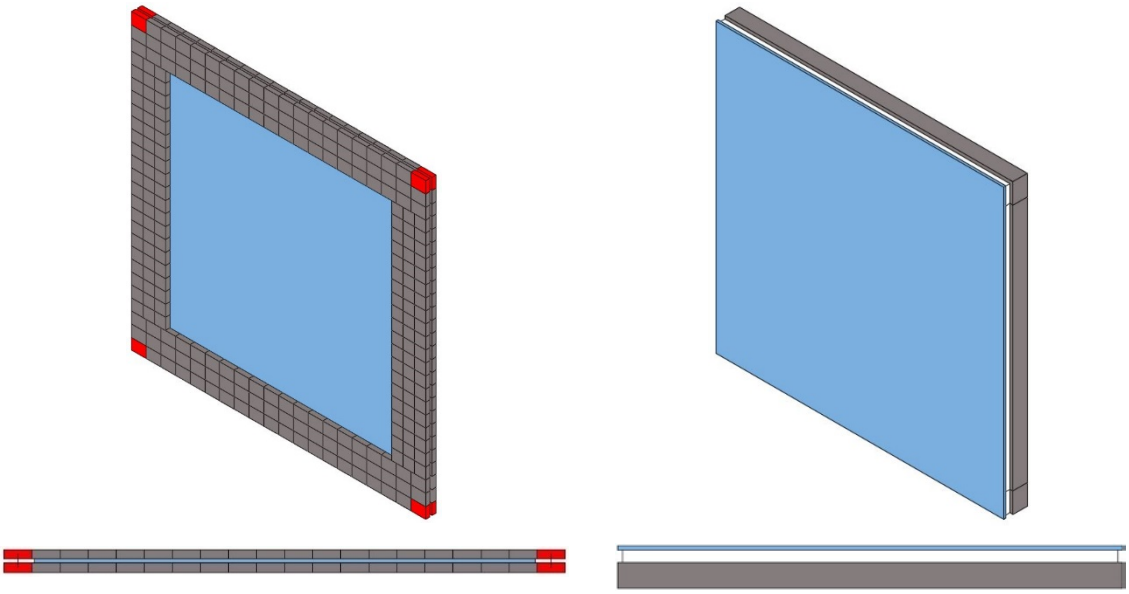

(a) Rigid frame. (b) Elastic frame.

Figure 3.2: Isometric view and section for rigid and elastic frames.

Table 3.2: Material properties used in AEM glazing response models.

	Annealed Glass	Dow Corning 993	Steel
Young's Modulus, E	68 GPa	1.4 MPa	200 GPa *
Shear Modulus, G	20 GPa	470 kPa	80 GPa *
Tensile strength	41 MPa	140 kPa	NA
Compressive strength	NA	1.4 MPa	NA
Shear strength	116 MPa	110 kPa	NA
Density, ρ	2,440 kg/m^3	1,320 kg/m^3	7,840 kg/m^3 *
Separation strain	0.005 *	1	0.2 *
Post-failure shear stiffness factor	0.01 *	NA	NA
Yield Stress	NA	NA	588 MPa *
Ultimate strain	NA	NA	0.1 *

Annealed glass reference: Johns, 2016
Dow Corning 993 reference: European Organisation for Technical Approvals, 2006
* indicates default ELS values.

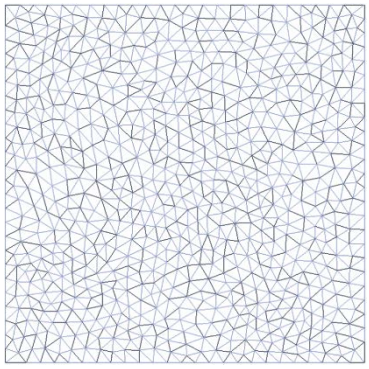

Figure 3.3: Delaunay triangulation of mesh with 1500 elements.

A reflected overpressure (P_r) history from previous ABT trials (Johns, 2016) was applied uniformly to the glass as a pressure history. Data were smoothed using a fast Fourier transform, low pass smoothing algorithm rationalising a 200 data point sweep. The full pressure history, corresponding to a 25 tonne (TNT equivalent) charge at a 250m standoff, is shown in Figure 3.4. The initial 10ms, the AEM pressure input, is inset. Time of glass failure, impulse received before break and maximum window displacement were used to quantify glazing response. Separation of all springs on one side of an element defined glass failure. Central displacement and reflected impulse received by the glass were recorded at break time. Crack patterns were analysed and compared to high-speed video footage from experimental trials.

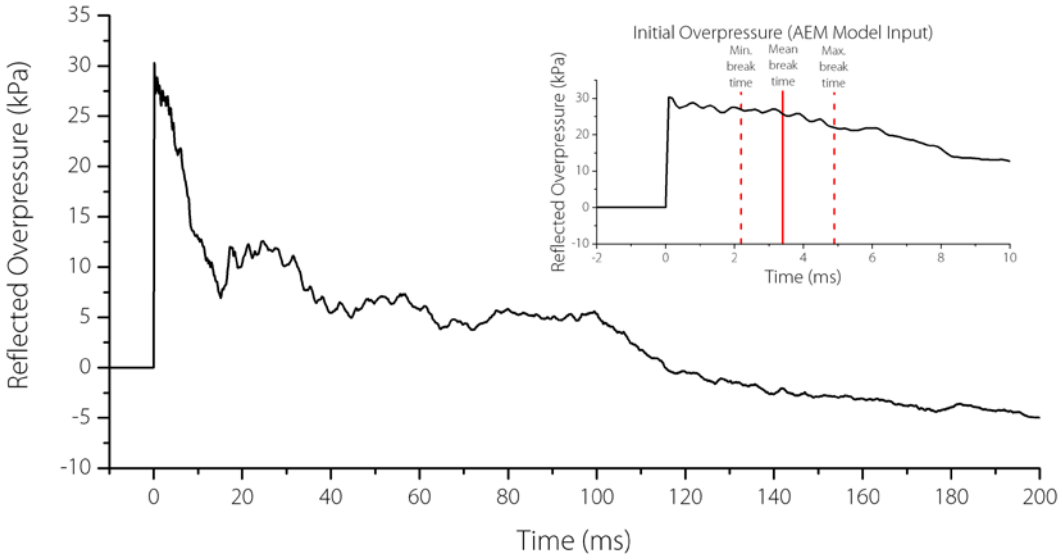

Figure 3.4: Pressure input for AEM models. Data from previous ABT trials (Johns, 2016).

Total element count and number of element layers in the glass model were refined in a sensitivity study. Arrangement 1 (see Table 3.1) with rigid support conditions was used for this analysis. Initially the element count in a single layer was increased from 1,500 to 11,000 (Table 3.3). Failure impulse and displacement decreased as the number of elements increased, indicating earlier glass failure. Below 5,000 elements failure impulse was close to the experimental value. With 10,000 elements failure impulse was 20% lower than the experimental result and displacement was 40% lower suggesting an inherent model stiffness with a high element count. Shard separation groups showed meshing and major shards indicating crack patterns (Figure 3.5). Models with under 5,000 elements exhibited unsymmetrical cracking suggesting mesh dependency. Models with 10,000 or more elements broke centrally with a higher degree of symmetry. Further increasing element number did not significantly affect the crack pattern, suggesting cracking was mesh independent for models implementing 10,000 elements.

Table 3.3: Effect of element number on glazing response.

Element No.	Trial data	1,500	3,000	5,000	10,000	11,000
Failure Impulse (kPa.ms)	63	68	70	68	54	54
Failure Displacement (mm)	10	8	8	8	6	6

Significance of layer count was investigated using 10,000 elements per layer (Table 3.4). A model with 10 layers of 1,500 elements was also tested. Increasing layer count from one to two caused an 11kPa.ms increase in failure impulse and 2mm failure displacement decrease. Further increasing number of layers had no effect on break parameters. Each element edge contained five sets of springs in each direction. With one element layer 25 sets of springs were positioned on each element edge. With fewer than four layers, areas of multiple cracks formed suggesting an out-of-plane spring deficit. With four layers of elements and 100 sets of springs in the out-of-plane direction, a clear crack pattern was produced. Further increasing number of elements was prevented by ELS licensing. The refined mesh with 40,000 elements (4 layers of 10,000 elements) produced results independent of meshing. Additional increase of element count or number of layers made no significant difference to results but caused a substantial increase to model run-time.

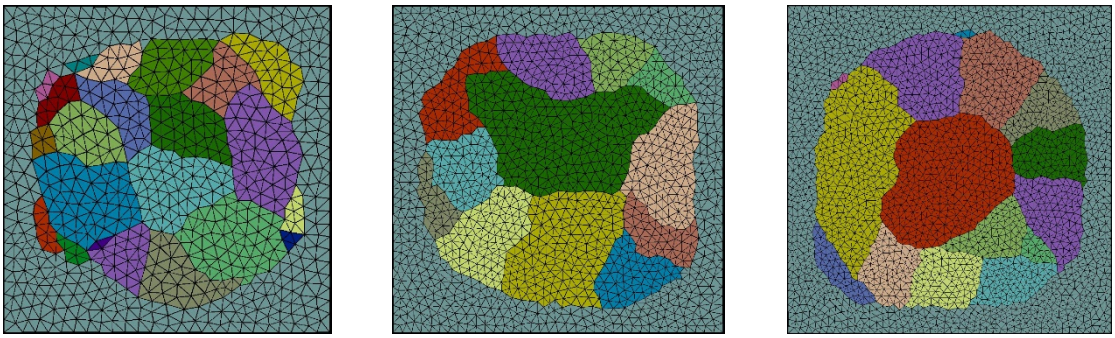

(a) 1,500 elements. (b) 3,000 elements. (c) 5,000 elements.

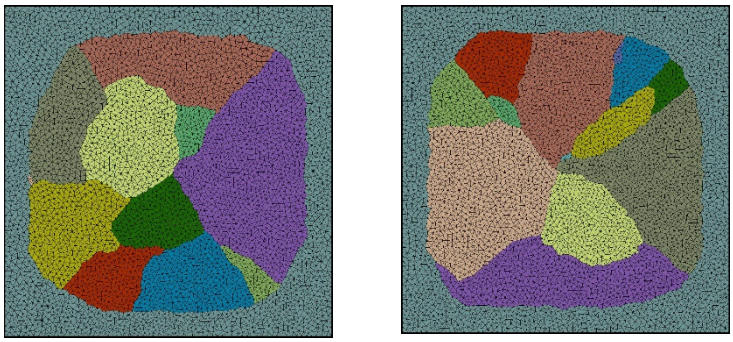

(d) 10,000 elements. (e) 11,000 elements.

Figure 3.5: Effect of element number on crack patterns.

Table 3.4: Effect of layer number on break parameters.

Layer No. (Elements per Layer	Trial data	1 (10,000)	2 (10,000)	3 (10,000)	4 (10,000)	10 (10,000)
Failure Impulse (kPa.ms)	63	59	70	70	70	70
Failure Displacement (mm)	10	8	6	6	6	6

AEM assumes small time intervals and small deformations between model iterations (Meguro and Tagel-Din, 2002). Initial models implemented a 0.1ms time step, using only 25 frames before failure of Arrangement 1. This averaged 0.2mm of central displacement per time step, too large for the small deformations assumption. Time step sensitivity was investigated using Arrangement 1 with rigid supports. Break time and AEM model run time were plotted against log of the time step (Figure 3.6).

Run times were based on calculating model response 10ms after blast wave arrival. Decreasing time step converged break time to 0.89ms (time step 0.005ms) from 1.1ms (time step 0.1ms). Time step was further decreased to 0.001ms but a predicted run time of 285hours meant it was unfeasible to complete the analysis. Predicted break time for this model is marked with a dotted line in Figure 3.6. Sufficient convergence was achieved at 0.005ms however the high run time was inefficient for large batches of models. Models with time step 0.05ms demonstrated passable accuracy with reasonable run-time for quick analysis. For more thorough analyses, a time step of 0.01ms exhibited increased accuracy but an increased run time of 23hours. The parametric study detailed in Chapter 6 required models to be run for 100ms producing a model run time of 54hours for time step 0.05ms. A smaller time step would have resulted in impractical run times on the computer used.

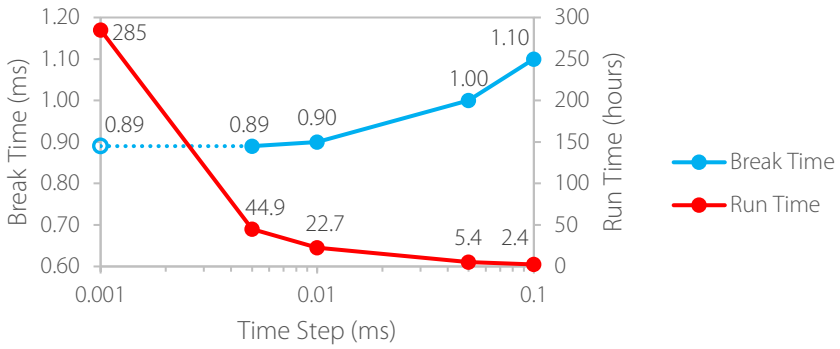

Figure 3.6: Break time convergence and AEM model runtime as time step was decreased.

Each glazing arrangement outlined in Table 3.1 was modelled using the refined AEM model. Break parameters for rigidly supported arrangements were compared to experimental values in Table 3.5 and plotted in Figure 3.7. AEM results were normalised against experimental results to enable comparison. If an AEM value exactly matched the experimental result, its normalised value would be 1.00. Normalised 90% confidence intervals calculated from previous experimental data allowed comparison to experimental data spread. For all arrangements, numerically calculated failure impulse lay within the experimental 90% confidence interval demonstrating good consistency. Failure impulse was under-predicted by AEM, all results were 1.00 or below. Arrangement 3 [8mm, 1:1, 0.25m^2] exhibited the smallest normalised impulse (0.62). Despite the large percentage difference, the AEM value was within 90% confidence limits due to a wide experimental data spread for this arrangement. AEM displacements were consistently lower than experimental values. Only Arrangement 5 lay within 90% confidence limits. All normalised displacements fell between 0.50 and 0.60. Despite severely under-predicting displacement this indicated AEM was capable of modelling window response trends for different structural parameters.

Break parameters from elastically supported arrangements are compared to experimental results in Table 3.6 and plotted in Figure 3.8. For failure impulse only Arrangement 5 fitted within experimental 90% confidence bounds, despite recording the smallest normalised impulse (0.63). Although AEM under-predicted failure impulse consistently, it demonstrated capability to follow experimental trends. AEM displacement values were all lower than experimental data. Good agreement was observed for Arrangements 1 to 4 (minimum normalised displacement 0.80 for Arrangement 2). For

Arrangements 3 and 4 [8mm, 0.89m^2] normalised displacements were between 0.91 and 1.00. Normalised displacements calculated for Arrangements 5 and 6 [4mm, 0.89m^2] were significantly lower, 0.43 and 0.45 respectively implying AEM modelling of large, thin windows produced a stiffer response than observed experimentally. This was despite calculated failure impulse being consistent with other arrangements. Reduced failure displacement can be attributed to AEM modelling glass membrane forces incorrectly, errors in material parameters or support conditions that were inconsistent with the experimental set-up.

Table 3.5: Comparison of experimental and numerical glazing response: rigid framing.

Arrangement No. Arrangement Layout		1 4mm, 1:1, 0.25m^2	2 4mm, 1:1.75, 0.25m^2	3 8mm, 1:1, 0.89m^2	4 8mm, 1:1.7, 0.89m^2	5 4mm, 1:1, 0.89m^2
Failure Impulse (kPa.ms)	Trial	63	76	149	124	90
	AEM	62	76	92	109	65
	Norm.	0.98	1.00	0.62	0.88	0.72
Failure Displacement (mm)	Trial	10	10	18	15	18
	AEM	6	6	10	8	9
	Norm.	0.60	0.60	0.56	0.53	0.50

Norm. – AEM result normalised against experimental result.

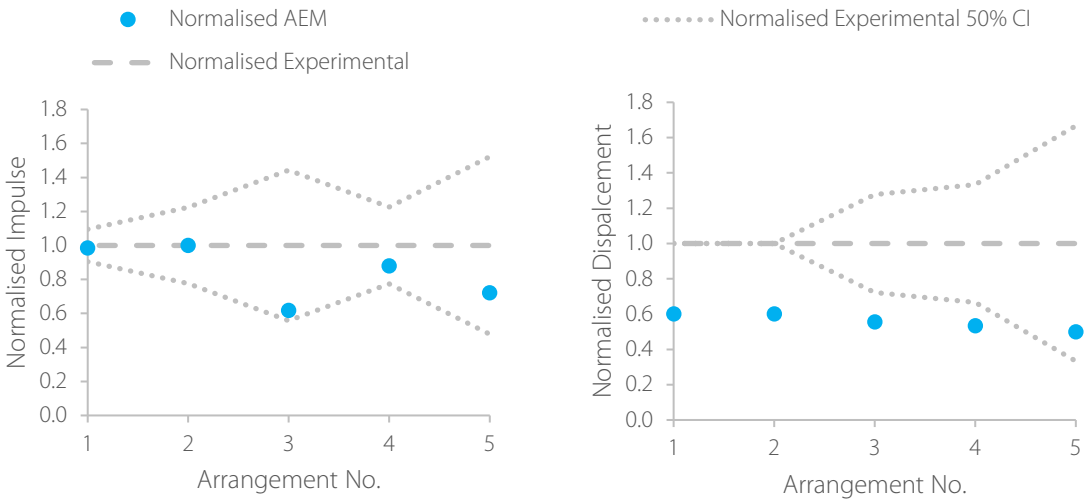

(a) Failure impulse.

(b) Failure displacement.

Figure 3.7: Normalised break parameters from rigid AEM models.

Table 3.6: Comparison of experimental and numerical glazing response: elastic framing.

Arrangement No. Arrangement Layout		1 4mm, 1:1, 0.25m^2	2 4mm, 1:1.75, 0.25m^2	3 8mm, 1:1, 0.89m^2	4 8mm, 1:1.7, 0.89m^2	5 4mm, 1:1, 0.89m^2	6 4mm, 1:1.7, 0.89m^2
Failure Impulse (kPa.ms)	Trial	86	87	127	109	98	85
	AEM	57	57	97	92	62	62
	Norm.	0.66	0.66	0.76	0.84	0.63	0.73
Failure Displacement (mm)	Trial	10	10	13	11	21	20
	AEM	8	7	12	10	9	9
	Norm.	0.80	0.70	0.92	0.91	0.43	0.45

Norm. – AEM result normalised against experimental result.

For both framing conditions numerically calculated impulse and displacement were lower than the experimental mean for all arrangements. Rigid framing produced better agreement than elastic framing. Failure impulse for all arrangements lay within experimental 90% confidence intervals and normalised displacements were very consistent indicating AEM was highly capable of modelling displacement trends. Failure impulse calculated for elastic frames was consistently lower than experimental impulses. Good displacement agreement was recorded for smaller area and thicker glass arrangements (Arrangements 1 to 4). AEM significantly under-predicted displacement for large, thin windows (Arrangements 5 and 6). Additional experimental data are required to determine if this trend is consistent for other aspect ratios at this window size.

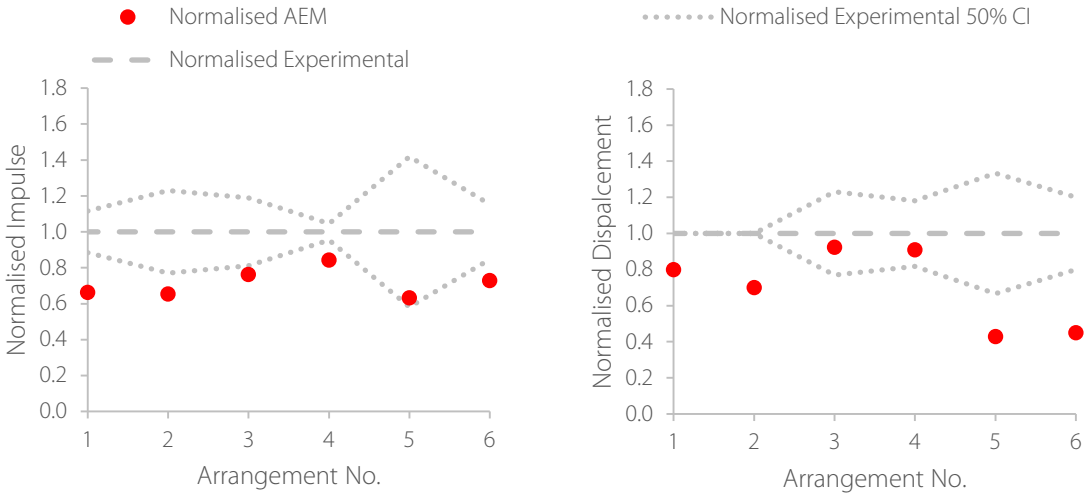

(a) Failure impulse.

(b) Failure displacement.

Figure 3.8: Normalised break parameters from elastic AEM models.

3.3 Choosing Structural Parameters

Damage probability curves for 4mm thick annealed glass were the main objective of this research project (Figure 3.9). Probability of glazing failure was plotted against overpressure for long-duration blast environments. Blast parameters to be implemented in the damage curves are discussed in section 5.8. P50 is the peak overpressure for which 50% of windows are expected to fail. Standard deviation of the curve (σ) is a function of glass structural parameters. A normal distribution has been assumed for simplicity due to limited experimental trials. For identical pieces of glass σ would be zero and the solution would be binary, below failure overpressure no windows would fail and above 100% failure would occur.

The structural parameters that σ is dependent on are:

- $\sigma_{thickness}$ Glass thickness
- σ_{area} Glazing area
- σ_{AR} Glazing aspect ratio
- $\sigma_{supports}$ Glass support conditions

– $\sigma_{material}$ Glass material strength variability

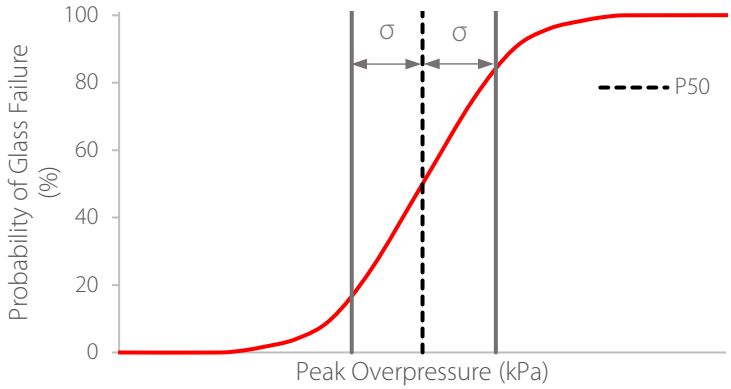

Figure 3.9: Diagram of a damage probability curve.

Aspect ratio, support conditions and material strength variability were investigated through experimental and computational studies. Individual damage probability curves were produced for each structural parameter (see Chapter 6). Thickness and area were outside the scope of this research project. Effect of positive phase duration (t_d) was also investigated numerically. For the long-duration section of PI graphs (see section 2.3.2) damage lines are horizontal indicating an impulse increase for the same peak overpressure (P_s) has no effect on glazing response. Investigating the effect of t_d determined the validity of this assumption. For this research project 4mm thick glass was used in all subsequent experimental and numerical work. As the minimum specification for annealed glass in the UK it is the worst case damage scenario for window failure. Support conditions benchmarked in section 3.2 were used throughout this research project. While not common in architecture they represent outer boundaries of the support condition range meaning $\sigma_{supports}$ corresponds to the worst case. Aspect ratio and area were analysed computationally to determine which to investigate further experimentally. Material strength variation was determined from static trials.

3.3.1 Case Study - Tianjin

In 2015, 800tons (726tonnes) of ammonium nitrate detonated in the port of Tianjin, China (for more information see section 2.2.2). Windows in a residential block within 5.5km of the explosion are shown in Figure 3.10. A window combination repeated in the photograph nine times is highlighted by a yellow box. This combination exhibited a range of window areas and aspect ratios, providing a useful case study. Other window arrangements were ignored due to a low repeat number or frame failure. It was assumed that all windows experienced the same blast environment and had the same support conditions and thicknesses. A consistent blast environment is a reasonable assumption as a long-duration blast wave is planar and the windows are not on the building edge. The selected window combination appears to have exact repeats in the image but windows may have been replaced leading to inconsistency in glass age, thickness and supports. This case study is only an estimation using available data therefore failure variation was assumed to be due to area, aspect ratio and material strength variability only.

Figure 3.10: Windows damage near to the Tianjin explosion (BBC News, 2015).

Window dimensions were measured from the photograph assuming a storey height of 3.1m (Figure 3.11). Broken windows were counted and their probability calculated. The highest failure probability was 89% for the window with area 1.5m^2. No 0.5m^2 windows failed, implying windows with a smaller area have a higher resistance to blast loading. 56% of the 0.8m^2 window failed compared to 33% with area 1m^2 despite a smaller area. The 0.8m^2 window had a higher aspect ratio (1:2 compared to 1:1.5) suggesting larger aspect ratios increase failure probability. All windows, apart from area 0.5m^2, exhibited non-binary failure probabilities (all failed or all survived) despite each window appearing identical, implying glass strength variation. The Tianjin case study demonstrated aspect ratio, area and material strength influence window survival in a blast environment. Area and aspect ratio were identified for investigation in a parametric study prior to experimental trial design. Glass strength variability was intrinsic to all experimental work, trial repeats demonstrated influence of this parameter.

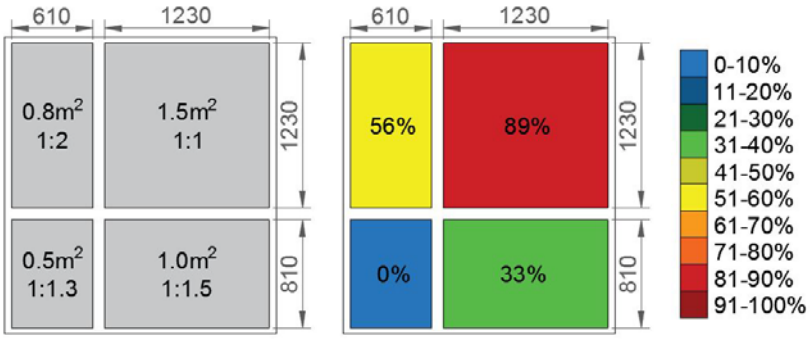

Figure 3.11: Window failure probability from Figure 3.10.

3.3.2 Area and Aspect Ratio Study

Influence of area and aspect ratio on break parameters was investigated using benchmarked AEM models. All rigidly framed 4mm thick windows were subjected to an ABT pressure history with P_s 14kPa and t_d 100ms. For the area study, exposed glass area with aspect ratio 1:1 was increased from 0.14m^2 to 3.5m^2, corresponding to glass sizes of 0.25m^2 to 4m^2. The corresponding failure displacements and impulses are shown in Figure 3.12. All windows failed and failure displacement increased by 90% between exposed areas of 0.14m^2 and 1.2m^2. The largest displacement was

recorded for exposed area 1.2m^2. A 3% decrease in failure displacement was observed when exposed area was increased from 1.2m^2 to 3.5m^2. A similar trend was observed for failure impulse with a 45% increase between exposed areas of 0.14m^2 and 1.2m^2. For exposed areas greater than 1.2m^2, no change in failure impulse was observed. Failure displacement and impulse exhibited similar trends implying parameters were closely related. Break time trends were consistent with failure impulse due to a constant pressure history applied to all models. For this reason break times are not shown.

The effect of aspect ratio was tested using windows with area 0.89m^2. Glazing aspect ratio was varied from 1:1 to 1:4, resulting in break parameters shown in Figure 3.13. Failure displacement for aspect ratio 1:1 was 6.7mm, maximum displacement was 9mm for aspect ratio 1:1.3, a 34% increase. Aspect ratio increase from 1:1.3 to 1:4 instigated a failure displacement decrease of 49% to 4.6mm. Maximum failure impulse for 1:1.3 was 63.1kPa.ms. Failure impulse exhibited a similar trend to displacement, increasing12% from aspect ratio of 1:1 to 1:1.3 and decreasing by 26% from 1:1.3 to 1:4. Crack patterns from windows with aspect ratios 1:1 to 1:4 are shown in Figure 3.14. Higher aspect ratio windows broke with a central crack whereas lower aspect ratios produced a central shard. These patterns follow yield line patterns for a homogeneous material and are very different to failure mechanisms observed in trial videos where failure occurred from a single point following Griffith's theory of brittle materials (Griffith, 1921). AEM modelling was unable to add a Griffith flaw to the glass, instead using the maximum principal stress failure criterion and limiting the crack pattern accuracy.

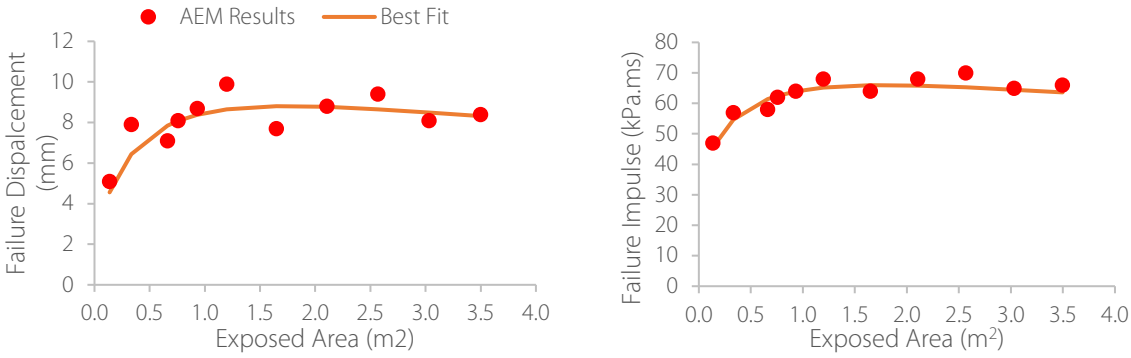

(a) Failure displacement. (b) Failure impulse.

Figure 3.12: Effect of glazing area on break parameters.

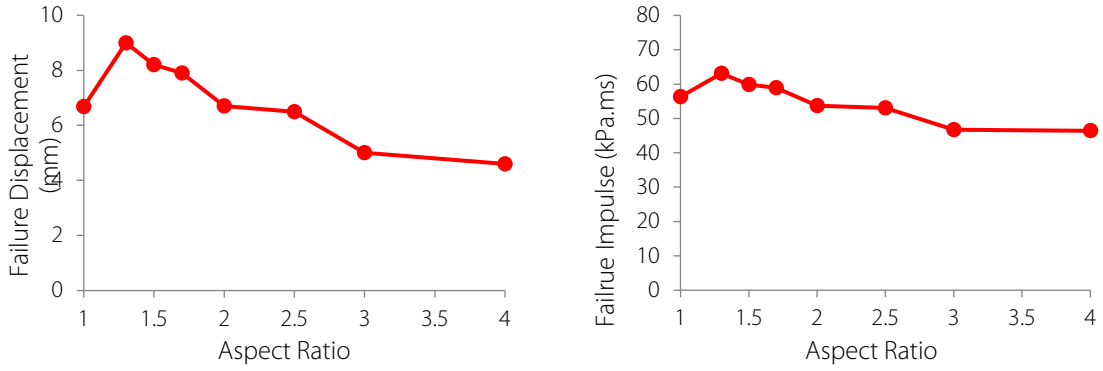

(a) Failure displacement. (b) Failure impulse.

Figure 3.13: Effect of aspect ratio on break parameters for rigidly supported glass.

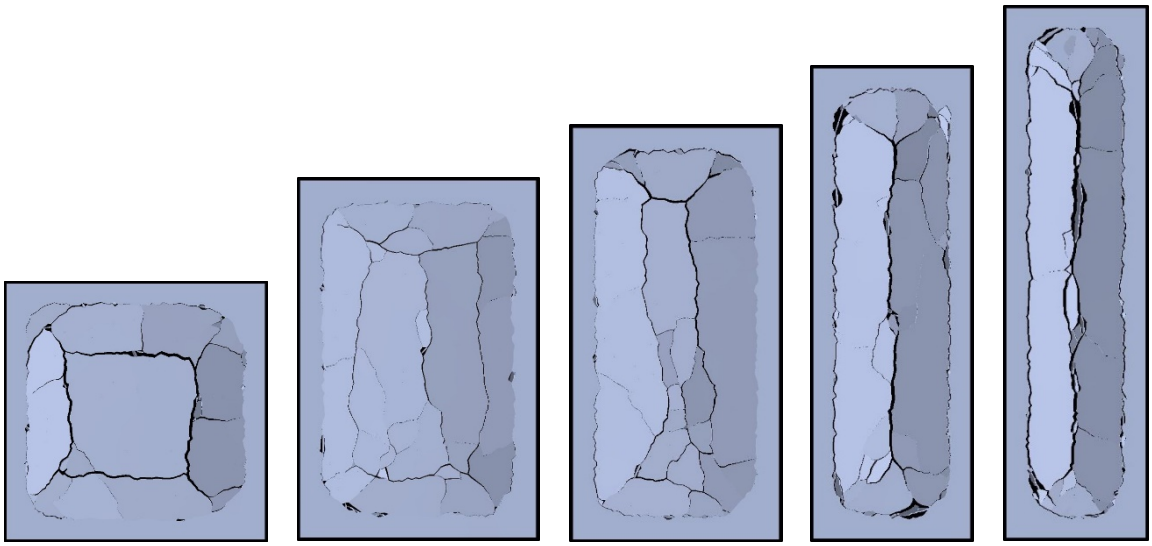

(a) Aspect ratio 1:1. (b) Aspect ratio 1:1.5. (c) Aspect ratio 1:2. (d) Aspect ratio 1:3. (e) Aspect ratio 1:4.

Figure 3.14: Numerically produced crack patterns by varying aspect ratios.

3.4 Conclusions

AEM models benchmarked against previous experimental data demonstrated generally good agreement with experimental results. Elastically supported, large, thin windows broke with much lower displacements than was recorded experimentally. Further benchmarking was required meaning this arrangement was highlighted for experimental testing. While AEM accurately calculated break parameters, crack patterns followed yield line theory and were not comparable to experimental results. An element count of 40,000 and time step of 0.05ms demonstrated adequate accuracy, which could be further increased with additional computational resources.

Five structural parameters influencing glazing failure were identified: aspect ratio, area, thickness, support conditions and material strength. Area and aspect ratio were investigated in an initial parametric study to aid experimental trial design. Failure impulse and displacement increased with exposed glass area increase from 0.14m^2 to 1.2m^2. Above this area no significant change in impulse and a small decrease in failure displacement were observed. Failure impulse and displacement were higher for aspect ratio 1:1.3 compared to 1:1. A decrease in both parameters was observed for aspect ratios higher than 1:1.3. Aspect ratio was identified for experimental investigation to determine if the break parameter peak at 1:1.3 was a function of AEM modelling or the glass. Aspect ratios 1:1, 1:1.3, 1:1.7 and 1:2 were selected. Further increase in aspect ratio was restricted by dimensions of testing cubicles.

Initial numerical work implemented a consistent blast environment: P_s 14kPa and t_d 100ms. Production of damage probability curves required benchmarking over a range of blast environments. Rapid glass failure in the current blast environment resulted in two lower blast pressures being identified for investigation (P_s 5kPa and 10kPa). P_s 5kPa was the minimum the ABT could consistently produce at the time of experimental trials for this research project. For experimental work, all glass was 4mm thick with area 0.89m^2. Rigid and elastic support conditions benchmarked in this chapter were implemented in all trials. Full experimental methodology and results are detailed in Chapter 4.

Chapter 4
Experimental Methodology and Diagnostics

4.1 Introduction

Experimental work for this thesis consisted of dynamic testing in the air blast tunnel (ABT) complemented by static loading tests. Dynamic trials provided further benchmarking for computational analysis while investigating the effect of aspect ratio, support conditions and peak overpressure on behaviour of 4mm thick annealed glass subjected to long-duration blast loading. Two phases of static testing informed the design of dynamic trials, including testing a new glass failure detection method, and provided material strength variability data. The schedule and phase aims are outlined in Table 4.1. Static and dynamic trial methodology and the piezo transducer triangulation analysis method are outlined in section 4.2. The dynamic trial blast environment is evaluated in section 4.3 and evolution of the triangulation method is outlined in section 4.4. Analysis of glazing response and the significance of structural parameters are addressed in Chapter 5. Full trial specifications can be found in Appendix B for reference.

Trials were undertaken in collaboration with industrial sponsor, AWE, and the Foulness Trials Group, Spurpark Ltd. Trial design and production of the test specification were undertaken by the author. Construction of experimental set-up was carried out by Spurpark Ltd. and supervised by the author. ABT firing was required to be executed by qualified personnel from MOD Shoeburyness. All data analysis and interpretation was performed by the author. The ABT at MOD Shoeburyness, UK, is one of a small number of facilities worldwide capable of testing full-scale structural response to long-duration blast waves (Figure 4.1). Constructed in 1964, the 200m long explosively-driven shock tube

has been used successfully in prior glazing blast trials (Johns and Clubley, 2015, 2016, 2017). Blast waves are simulated using a diesel-filled acrylic cylinder ignited by lengths of Davycord in the 1.8m diameter driver section. The conical shock tube shapes the short-duration blast wave to produce a planar long-duration blast wave in the test sections. The 10.2m diameter test section was used for all trials in this PhD. A rarefaction wave eliminator (RWE) is attached to the downstream end of the ABT to minimise unwanted reflections moving upstream due to clearing which can reduce the positive phase length. Damage to nearby buildings on Foulness Island is also prevented by the RWE.

Table 4.1: Schedule of experimental work.

Phase	Key	Aims	Date
Static 1	S1	Testing break detection methods for use in the ABT.	Jan 2017
Dynamic 1	D1	Effect of aspect ratio at P_s 14kPa, ABT testing of piezo transducers.	Feb 2017
Static 2	S2	Testing effect of edge finishing on glass failure and quantifying variation in material strength.	May 2017
Dynamic 2	D2	Effect of aspect ratio and edge supports at P_s 5kPa and 10kPa.	Aug 2017

Figure 4.1: The air blast tunnel (ABT) at MOD Shoeburyness (Clubley, 2014).

4.2 Methodology

4.2.1 Phases S1 and S2

Static testing enabled cost-effective assessment of new experimental techniques and aided dynamic trial design. In all phases, glass samples were fitted to an air-tight steel container. Pressure within the container was reduced at a constant rate by vacuum pump until glazing failure. Phase S1 consisted of five static tests to assess two break detection methods under static loading conditions. Phase S2 tested reliability of piezo triangulation and quantified annealed glass material strength variation over 20 samples.

With advances in instrumentation technology, experimental data capture is no longer limited to qualitative and binary descriptions of survival or failure (Byrnes, 1953; Clark, 1955; Fletcher, Richmond and Jones, 1973). Modern glazing trials use high-speed photography to determine location and time of glass failure. Typical frame rates range from 2,000 to 75,000fps (frames per second) (Ge, Li and Chen, 2012; Johns, 2016; Pelfrene *et al.*, 2016; Spiller *et al.*, 2016). This method is susceptible to camera shake and reduced accuracy. Camera availability can be a limiting factor on trial scheduling and data precision can be restricted by frame rate. Spiller et al. (2016) used break circuits to determine failure

time of the glass. A 'wire' was painted onto the surface of the glass using conductive paint which breaks with the glass. Spiller found that this method was accurate to 0.1ms when compared to high-speed camera footage (Spiller *et al.*, 2016). For this research project, two methods of determining glass failure were tested and compared to results from high-speed video. Glass failure time was measured at the instance when the crack was first observed. The location of this crack was recorded as the crack origin. Break circuits tested previously by Spiller and triangulation of piezo transducers were tested in laboratory conditions. Piezoelectric (piezo) transducers consist of two electrodes either side of a piezoelectric crystal. The piezoelectric effect states that when a force is applied to a piezoelectric material it produces an electrical potential. Pressure exerted on the crystal causes separation of charge gravity centres in the molecules, generating dipoles within the material. These dipoles cause polarisation of the material producing an electrical field (Vives, 2008), proportional to the imposed mechanical strain (Cady, 1964). When measuring acoustics, the sound wave travelling in the medium reaches the confinement structure (sensor) and produces a standing wave inducing the piezoelectric effect in the crystal. Piezo transducers in known locations on the glass surface record the sound of the glass cracking. Crack locations can be determined via triangulation using the difference in signal arrival times.

The static testing rig consisted of a 10mm thick airtight steel container supporting the framed glass specimen (Figure 4.2). Pressure in the container was reduced linearly at a rate of 0.44kPas^{-1} until glass failure. 700mm x 700mm x 4mm annealed glass was used in all tests in Phase S1. Frame aperture was 620mm x 620mm and samples were restrained in the frame by four clamps on each edge, providing rigid support conditions. In Phase S2, 20 samples with dimensions 600mm x 600mm x 4mm were tested in a modified test rig with frame aperture 520mm x 520mm (Figure 4.3) which closer represented support conditions produced in dynamic testing (see Figure 4.4 for modification detail).

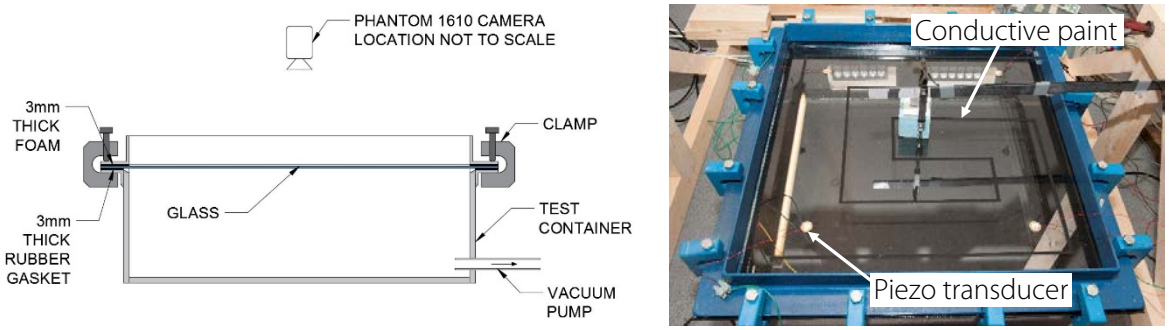

(a) Schematic of experimental set-up (cross section). (b) Test 2 instrumentation.

Figure 4.2: Experimental set-up of testing rig for Phase S1.

Phase S1 instrumentation is shown in Figure 4.5. Test 1 validated the two methods were capable of recording break time. Two Murata 7BB piezo transducers, 20mm in diameter, were fixed to the glass using Loctite 496 superglue. Piezo transducer locations were not recorded. A single strip of carbon-based conductive paint was applied to the midline of the glass, 5mm wide. In Test 2, four piezo transducers were adhered to the glass, 100mm from the edges, in each corner. Conductive paint was applied to the glass in a geometric pattern to ensure cracking met the circuit quickly (Figure 4.2b and

Figure 4.5). In Tests 3 to 5, repeatability of piezo transducer method was examined. Four piezo transducers were applied to the glass, one in each corner, 50mm from the edges. Conductive paint was not tested further. Signals from piezo transducers and conductive paint were sampled at a rate of 1MHz. A Phantom 1610 camera with a frame rate of 52,000fps provided an independent data set for comparison. Pressure within the container was recorded using an Endevco 8510C-50 gauge and window deflection was measured by a spring-loaded Contelec deflection gauge in the window centre. Both gauges were sampled at a rate of 1MHz. The instrumentation set-up used in Tests 3-5 was used in Phase S2 with a fifth piezo transducer applied to the centre of the glass. Camera frame rate in Phase S2 was increased to 75,000fps by changing to a Phantom 2512 camera.

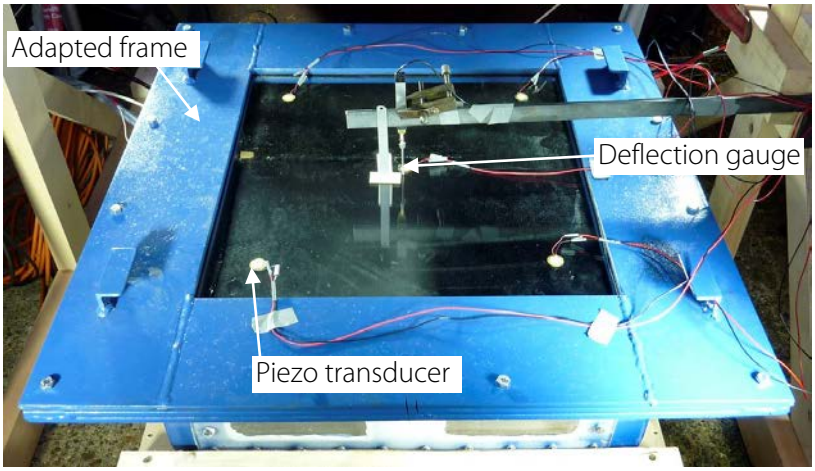

Figure 4.3: Phase S2 experimental set-up.

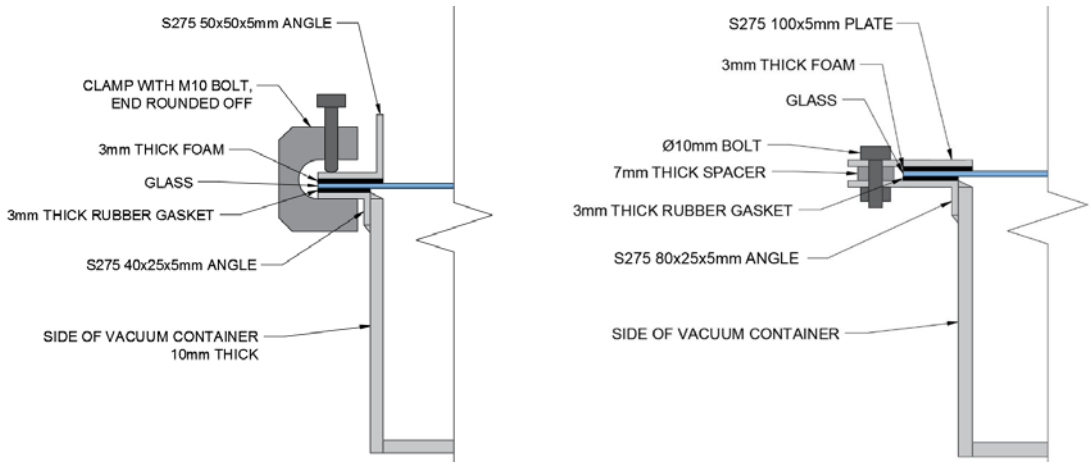

(a) Phase S1. (b) Phase S2.

Figure 4.4: Framing details for static test Phases S1 and S2.

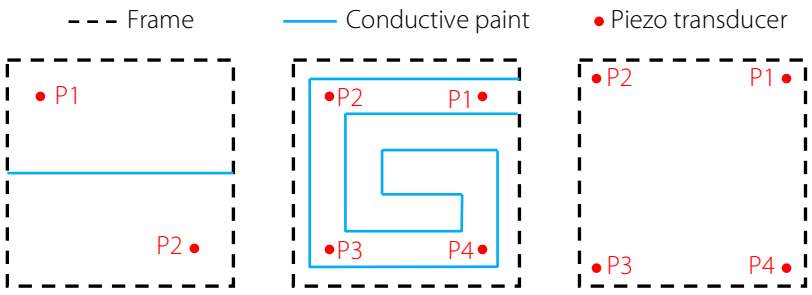

Figure 4.5: Instrumentation layout on surface of the glass for Phase S1.

4.2.2 Phases D1 and D2

Dynamic trials in the ABT embodied the majority of experimental work for this thesis. Two identical glass samples were tested per trial, 40 windows were tested over 20 trials (Table 4.2). In all trials 4mm thick annealed glass with area 0.89m^2 was used. Phase D1, consisting of eight full-scale blast trials, investigated the relationship between aspect ratio and glass failure in a blast environment with peak free-field overpressure (P_s) 14kPa and tested piezo transducer effectiveness in the aggressive ABT environment. Four aspect ratios were tested, 1:1, 1:1.3, 1:1.7 and 1:2, with four repeats for each arrangement. In Phase D1 only rigid support conditions were implemented. In Phase D2 24 glass samples were tested at two lower blast environments. Aspect ratios 1:1, 1:1.3 and 1:2 with both rigid and elastic support conditions were subjected to blast environments of 10kPa and 5kPa P_s.

Table 4.2: Dynamic trials specifications

Phase	Trial No.	Design P_s (kPa)	Aspect Ratio	Glass Dimensions [x:y] (mm)	Support Conditions
D1	1	14	1:1	[945:945]	Rigid
	2	14	1:1.3	[827:1075]	Rigid
	3	14	1:1.7	[725:1230]	Rigid
	4	14	1:2	[667:1334]	Rigid
	5	14	1:1	[945:945]	Rigid
	6	14	1:1.3	[827:1075]	Rigid
	7	14	1:1.7	[725:1230]	Rigid
	8	14	1:2	[667:1334]	Rigid
D2	9	10	1:1	[945:945]	Rigid
	10	10	1:1	[945:945]	Elastic
	11	10	1:1.3	[827:1075]	Rigid
	12	10	1:1.3	[827:1075]	Elastic
	13	10	1:2	[667:1334]	Rigid
	14	10	1:2	[667:1334]	Elastic
	15	5	1:1	[945:945]	Rigid
	16	5	1:1	[945:945]	Elastic
	17	5	1:1.3	[827:1075]	Rigid
	18	5	1:1.3	[827:1075]	Elastic
	19	5	1:2	[667:1334]	Rigid
	20	5	1:2	[667:1334]	Elastic

Steel test cubicles, used successfully in Johns' experimental trials (Johns, 2016), were installed in the 10.2m diameter section of the ABT, normal to the blast wave (Figure 4.6 and Figure 4.7). Modular sub-frames allowed frames to be constructed separately then quickly fitted to test cubicles warranting a quick trial turnaround. Sub-frames were rigidly connected to the test cubicle using bolts torqued to 40Nm. Sufficient bolts were implemented to ensure they were not a limiting factor. Glazing area of 0.89m^2 allowed data comparison to previous ABT trials. Glass and frame dimensions are detailed for reference in Table 4.3. The rigid frame (Figure 4.8a) was designed to represent a perfectly rigid support condition. Glass was restrained by steel frames bolted together against 7mm thick spacers to ensure uniform restraint. 3mm thick foam, compressed to 1.5mm, was adhered to both sides of the glass to prevent stress concentrations due to uneven frame surfaces. Elastic framing used structural sealant Sika SG500 to allow out-of-plane glass rotation representing pinned support conditions (Figure 4.8b).

These support conditions are not commonly used in industry but were selected as they represent outer bounds of commonly used frames and would therefore encapsulate behaviour of industry framing.

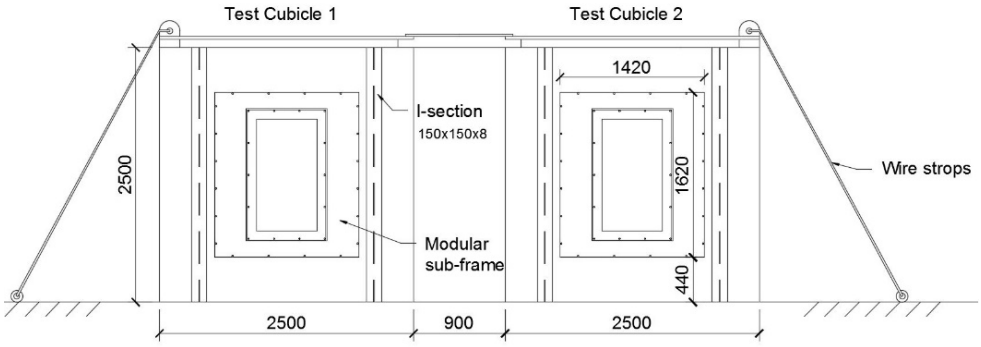

Figure 4.6: Front elevation (drawing) of test cubicles. View towards ABT RWE.

Figure 4.7: Front elevation (photograph) of test cubicles. View towards ABT RWE.

Table 4.3: Glass dimensions corresponding to Figure 4.8.

Trial No.	D1: 1-2 D2: 9-12	D1: 3-4 D2: 13-16	D1: 5-6	D1: 7-8 D2: 17-20
Aspect Ratio	1:1	1:1.3	1:1.7	1:2
Area (m^2)	0.89	0.89	0.89	0.89
X (mm)	945	827	725	667
Y (mm)	945	1075	1230	1334
B_x (mm)	815	697	595	537
B_y (mm)	815	945	1100	1204

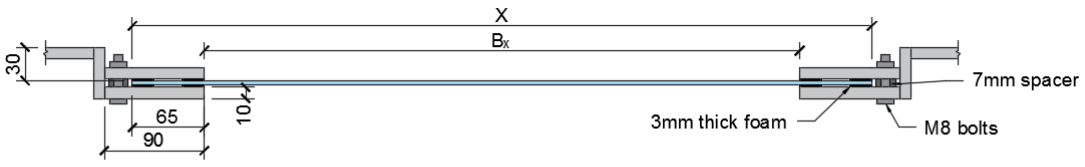

(a) Rigid frame.

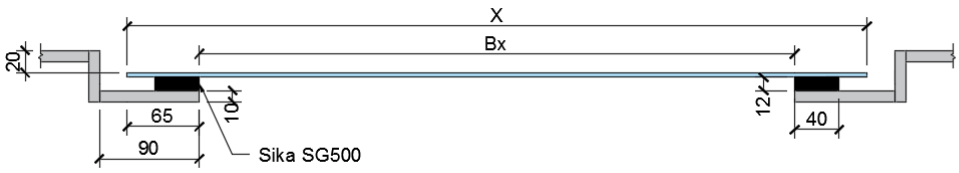

(b) Elastic frame.

Figure 4.8: Horizontal section through rigid and elastic frames used in dynamic testing.

A full pressure history was recorded using Endevco 8510-50 static pressure gauges and Endevco 8515C-50 reflected gauges (gauge locations shown in Figure 4.9). Three P_s gauges were located at 1m intervals upstream of test cubicles and a fourth in line with the test cubicle front surface. Two reflected pressure (P_r) gauges were attached to the test cubicle front surface in line with window centres. All pressure gauges were analysed at a 1MHz sample rate. Three high-speed cameras in each test container captured glazing response. Phantom 2512 cameras (C1 and C2) recorded crack location and break time at a frame rate of 75,000fps. Phantom V3.3 cameras with frame rate 5,000fps provided an overview of window displacement (C3 and C4). Phantom V711 cameras with frame rate 75,000fps tracked displacement gauge movement (shown in Figure 4.10) allowing central displacement to be measured (C5 and C6). For peak overpressure 5kPa trials Phantom V3.3 cameras were used in locations C5 and C6 due to Phantom V711 cameras being unavailable. These operated at frame rates of 15,000fps. LEDs in camera view illuminated at blast wave arrival to allow gauge and camera synchronisation. Cameras used satellite communication to maintain synchronised timing within approximately 10µs. Five 20mm Murata 7BB diameter piezo transducers, sample rate of 1MHz, were adhered to the rear side of each window (see Figure 4.11). The piezo transducer numbering system shown is used in all analysis. All instrumentation was triggered by fibre optic at driver detonation to ensure a common time scale.

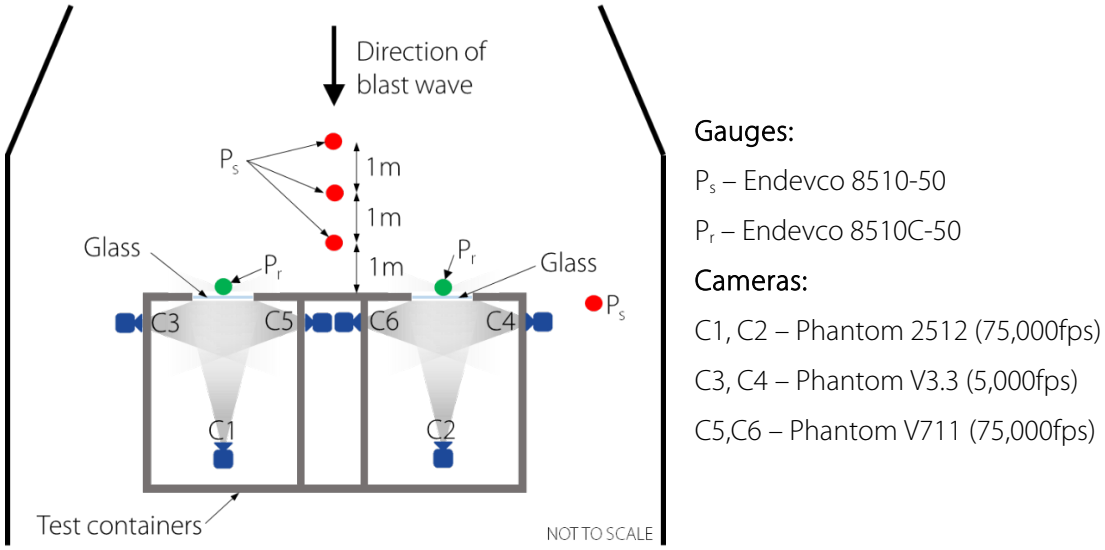

Figure 4.9: Plan view of experimental setup for Phases D1 and D2.

Figure 4.10: Deflection gauge tracked by cameras.

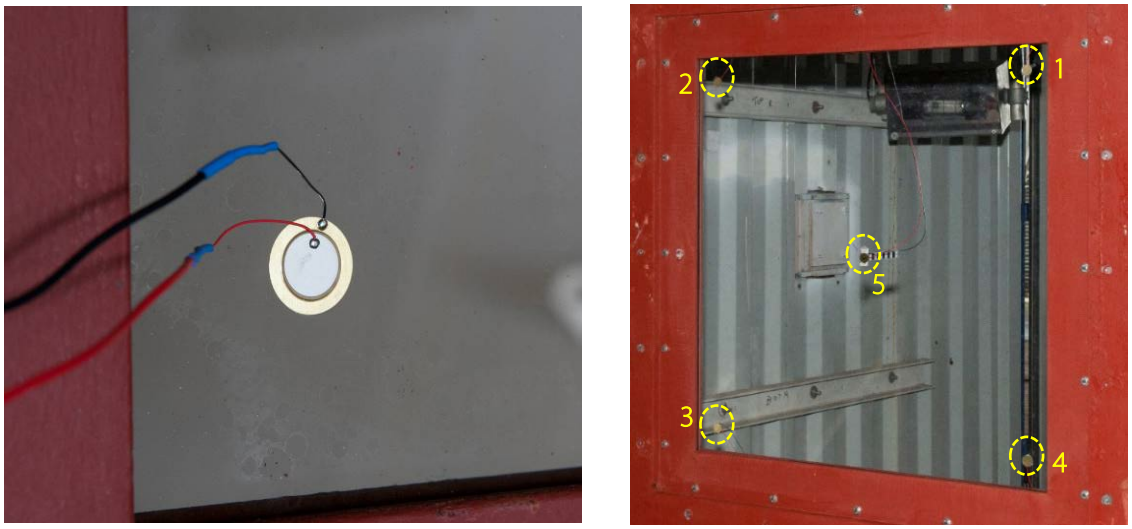

(a) Piezo transducer close-up. (b) Piezo transducers numbering.

Figure 4.11: Piezo transducer numbering for dynamic trials.

4.2.3 Finding the Crack Location from Piezo Transducers

In Phase S1, four piezo transducers were located on the glass samples as shown in Figure 4.12. In all other experimental work an additional piezo transducer was added to the centre point of the window. The fifth sensor has been omitted from this explanation but the method can be expanded to include it. Additional piezo transducers can be analysed in an analogous manner. The coordinate system adopted for analysis is depicted in Figure 4.12. The origin was defined at the bottom left corner, nearest to piezo 3. When glass cracks, the sound propagates outwards from the original point of failure. For this analysis it was assumed that speed of sound in glass, c, was constant with time and direction. When the sound wave reached the nearest piezo transducer, time of arrival was recorded. In Figure 4.12 the nearest piezo transducer to the example crack location is P4. The distance the sound wave travels to reach P4 can be described by equation 4.1. Piezo transducer 4 coordinates are x_4 and y_4, r is the distance from the crack to the nearest piezo transducer, in this case P4.

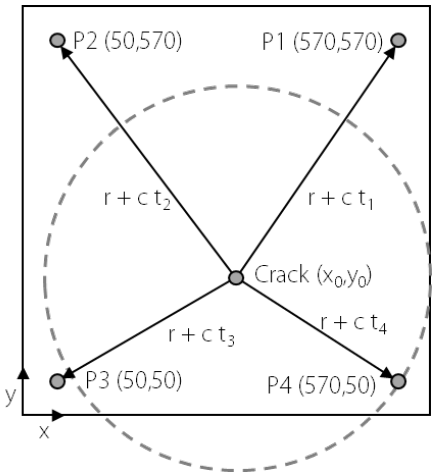

Figure 4.12: Coordinate system for piezo transducer analysis.

$$(x_4 - x_0)^2 + (y_4 - y_0)^2 = (r)^2 \quad 4.1$$

The difference in time of arrival for piezo transducer n, t_n, was defined as the time between the sound wave reaching the first piezo transducer, in the case above P4, and the piezo transducer being

analysed, n. As P4 was closest to the crack its difference in time of arrival, t_4, was zero. When the sound wave reached the next piezo transducer (piezo 3 in Figure 4.12) it had travelled r plus an additional distance during time t_3, the difference in time of arrival for piezo transducer 3. Assuming speed of the sound wave was constant, distance from the crack origin to P3 was equal to $(\mathbf{r + c\,t_3})$. The equation for P3 is shown below.

$$(x_3 - x_0)^2 + (y_3 - y_0)^2 = (r + c\,t_3)^2 \quad 4.2$$

Using the same method for the remaining piezo transducers, similar equations can be formulated. These can be used in the general case when the crack can be anywhere in the glass.

$$(x_1 - x_0)^2 + (y_1 - y_0)^2 = (r + c\,t_1)^2 \quad 4.3$$

$$(x_2 - x_0)^2 + (y_2 - y_0)^2 = (r + c\,t_2)^2 \quad 4.4$$

$$(x_4 - x_0)^2 + (y_4 - y_0)^2 = (r + c\,t_4)^2 \quad 4.5$$

In these equations, location and difference in time of arrival for each piezo transducer were known. The unknowns were coordinates of the crack (x_0 and y_0), speed of sound (c) and distance to the nearest piezo transducer (r). While this provided four unknowns and four equations, therefore an analytic solution was possible, experimental error meant that an iterative method for solving was more practical. The crack location was found by systematically testing each x_0, y_0 and c value using a Matlab® algorithm. Each possible set of x, y coordinates for the crack location was stepped through systematically over a range of possible values for speed of sound. The calculated time of arrival (t_n) at each piezo transducer was compared to the experimental value (T_n). Sum-of squares of errors, E, was calculated for each combination using equation 4.6.

$$E = \sum_{n=1}^{4} (T_n - t_n)^2 \quad 4.6$$

Values of x_0, y_0 and c corresponding to the minimum error, E, were stored as the best fit to the experimental data. The algorithm was executed initially with a precision of 1mm and 500m/s then a second time with a refined search criteria, using results from the first pass to calculate crack location to the nearest 0.5mm and speed of sound to the nearest 5m/s. Error for the crack location was multiplied by the calculated speed of sound to give an error in millimetres. Potential sources of error included location of piezo transducers, sample rate of piezo transducers, size of the piezo transducer and recording time of arrival at each piezo transducer. Use of more than four piezo transducers provided redundancy, ensuring triangulation could be undertaken in the case of piezo transducer failure. Speed of sound in the glass was assumed constant but is likely to vary as the glass is stressed. Results indicated this error was not critical to triangulation. Additional data points increased triangulation accuracy and reduced error. These errors are discussed in more detail in section 4.4.

4.3 Blast Environment

The blast environment was recorded using Endevco 8510-50 P_s gauges and Endevco 8515C-50 P_r gauges. P_s and free-field impulse (I_s) were recorded 3m upstream of the test containers. Very good consistency was observed for both overpressure and impulse, specifically in the initial part of the blast

wave. Slight variation in impulse in the later part of the overpressure history can be attributed to gauge noise or flow field turbulence behind the blast wave front. Free-field pressure and impulse histories for trials at 14kPa, 10kPa and 5kPa P_s are shown in Figure 4.13 to Figure 4.15.

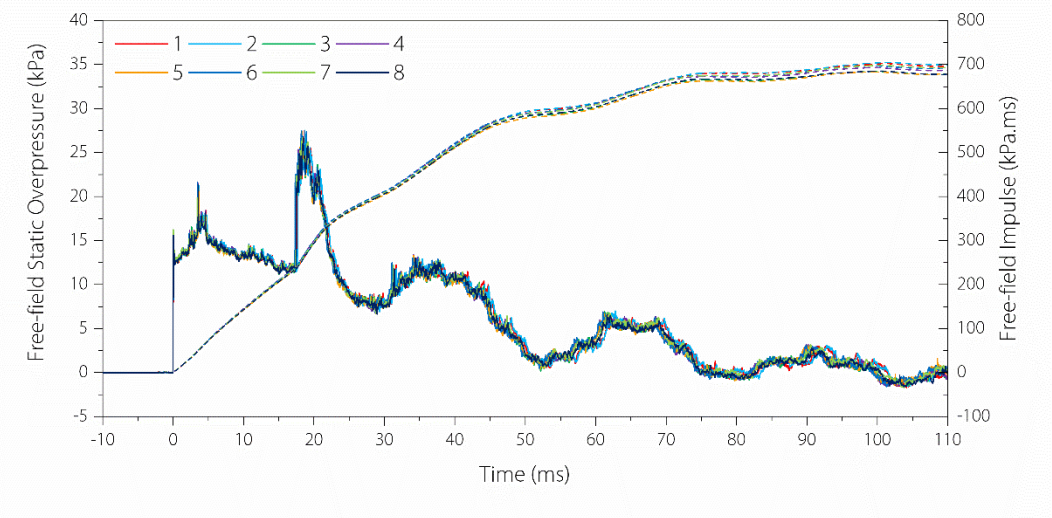

Figure 4.13: Free-field pressure histories (3m upstream) for P_s 14kPa trials.

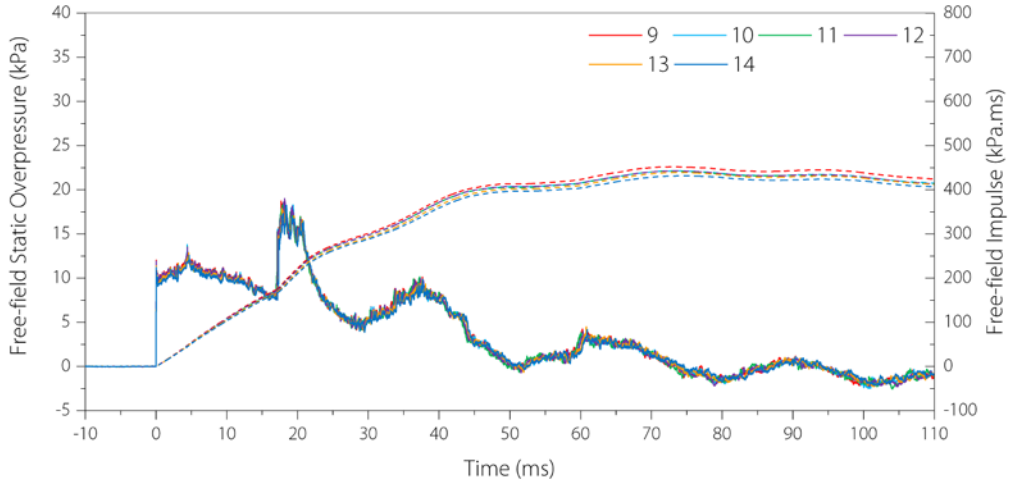

Figure 4.14: Free-field pressure histories (3m upstream) for P_s 10kPa trials.

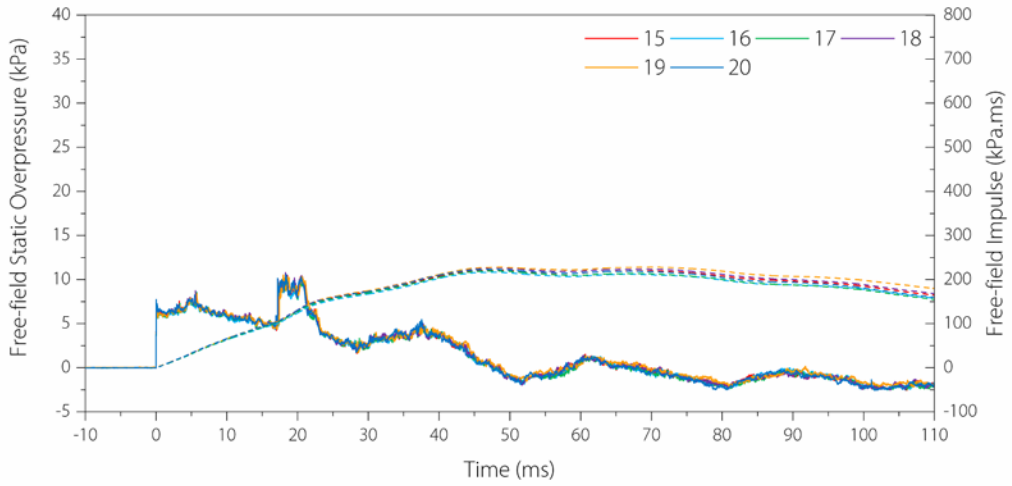

Figure 4.15: Free-field pressure histories (3m upstream) for P_s 5kPa trials.

P_s, I_s and positive phase duration (t_d) were recorded for each trial. Endevco 8510-50 gauges are prone to "ringing" at blast wave arrival causing noise in the initial signal. P_s was recorded as the average of this noise (see Figure 4.16) to be consistent with the convention used in all ABT trials. I_s was recorded as the maximum impulse value. Overpressure oscillations caused by reflections off test containers and flow field turbulence caused by ABT expansion made determining t_d difficult. To ensure consistency t_d was recorded at time of maximum impulse. Values of P_s, I_s and t_d for each trial and are detailed in Table 4.4 to Table 4.6. High consistency was observed for all blast parameters. Highest repeatability was recorded for P_s 14kPa trials with mean P_s 13.4±0.1kPa, t_d 100±1ms and I_s 690±7kPa.ms. P_s 10kPa trial break parameters were 10.1±0.2kPa, 74±1ms and 442±6kPa.ms respectively. P_s 5kPa trials exhibited reduced consistency in P_s compared to 14kPa trials (6.3±0.3kPa). Recorded t_d (48±1ms) and I_s (223±4kPa.ms) were highly consistent. This higher P_s variation (standard deviation of 5%) can be attributed to blast wave front perturbations due to turbulence at a low P_s.

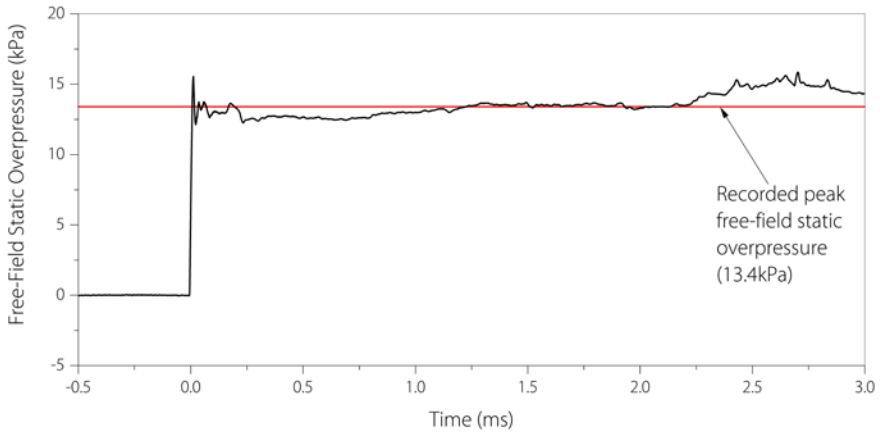

Figure 4.16: Free-field overpressure history showing the recorded peak.

Table 4.4: Free-field blast parameters for P_s 14kPa trials.

Trial No.	1	2	3	4	5	6	7	8	$\bar{x}$	σ
P_s (kPa)	13.4	13.3	13.5	13.5	13.4	13.5	13.5	13.1	13.4	0.1
t_d (ms)	101	102	100	99	100	99	101	100	100	1
I_s (kPa.ms)	701	693	681	691	681	694	697	683	690	7

Table 4.5: Free-field blast parameters for P_s 10kPa trials.

Trial No.	9	10	11	12	13	14	$\bar{x}$	σ
P_s (kPa)	10.4	10.3	10.2	10.3	9.9	9.7	10.1	0.2
t_d (ms)	74	74	73	74	74	75	74	1
I_s (kPa.ms)	452	443	442	443	439	431	442	6

Table 4.6: Free-field blast parameters for P_s 5kPa trials.

Trial No.	15	16	17	18	19	20	$\bar{x}$	σ
P_s (kPa)	6.1	6.0	6.1	6.6	6.0	6.7	6.3	0.3
t_d (ms)	49	48	48	49	49	47	48	1
I_s (kPa.ms)	222	217	220	226	228	223	223	4

Recorded P_s for all 14kPa trials was lower than specified (13.4kPa) however consistency between trials was of higher importance than achieving P_s 14kPa. P_s 5kPa trials measured a mean P_s of 6.3kPa, 1.3kPa

above specified. With minimal calibration shots at this new overpressure, consistency rather than an accurate P_s was more important. I_s and t_d increased approximately linearly with P_s, a function of the ABT. Large reflections produced by the test containers meant recording the true free-field overpressure history was impossible and measured I_s was larger than the true free-field value. The initial overpressure rise after the peak was a function of Endevco 8510-50 gauges which were very sensitive to intense light and heat. Windows in the side of the ABT allowed sunlight onto gauges, offsetting readings. At detonation all gauges were zeroed to remove this offset. The resulting dust cloud caused a light level decrease on the gauges and a subsequent rise in recorded overpressure after the initial peak. This behaviour has been observed in multiple ABT trials. The second overpressure peak was caused by particles reflecting off the container front surface travelling upstream. Overlaying overpressure histories from upstream static gauges 1m apart showed a staggered time of arrival (Figure 4.17). Time between blast wave arrival at each gauge was measured and used to calculate speed of the incident and reflected blast waves (Table 4.7). The incident blast wave was travelling on average at 352m/s and the reflected blast wave 335m/s, demonstrating the second peaks were a result of reflections off the testing cubicles. Wave speed was calculated as 351m/s and 348m/s for 10kPa and 5kPa trials respectively. Subsequent peaks in the free-field pressure history can be attributed to characteristics of the ABT and charge. The ABT diameter does not increase linearly but in steps. These steps cause decreases in air density and pressure causing peaks and troughs in the pressure trace. Reflections off the ABT sides can also cause this behaviour. The charge was very long and thin. The initial pressure peak was formed by the blast wave propagating away from the charge end furthest downstream. A secondary peak could be due to superposition of the blast pressure from the charge end furthest upstream over this. Another peak much later in the blast wave profile could be due to reflections off the RWE travelling back upstream.

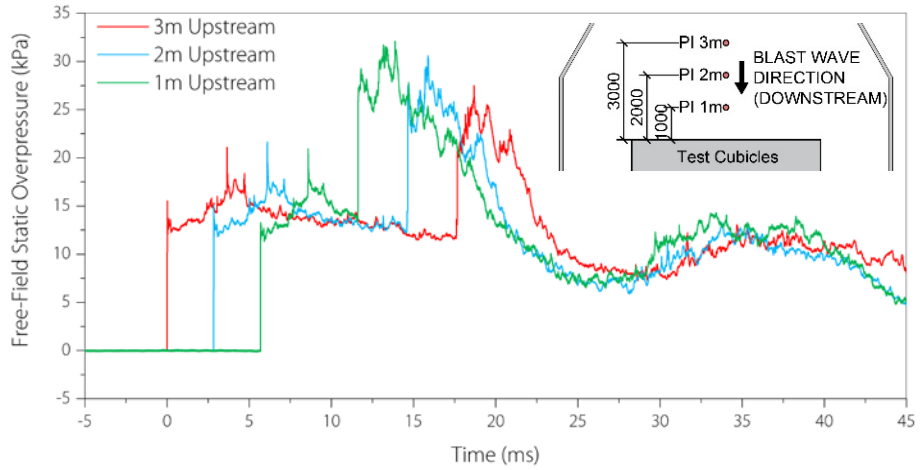

Figure 4.17: P_s histories for gauges 3m, 2m and 1m upstream of test cubicles (P_s 14kPa Trial 1).

Reflected overpressure was measured by Endevco 8515C-50 gauges on the test cubicle below the window frame, along the vertical centreline of each sample. It was assumed this was representative of pressure exerted on windows as the blast wave was uniform. Attaching P_r gauges to the glass surface was trialled unsuccessfully in previous ABT tests (Johns, 2016). Clearing distances were affected slightly in the vertical direction, this is discussed below. Reflected overpressure histories for

all trials (shown in Figure 4.18 to Figure 4.20) were highly consistent between trials and for both containers, indicating a uniform pressure wave. P_r and I_r for each trial are detailed in Table 4.8 to Table 4.10. These values were calculated using the same method as for free-field pressure data. Mean P_r values for 14kPa, 10kPa and 5kPa blast environments were 27.2±0.9kPa, 20.1±1.0kPa and 12.4±0.7kPa respectively. The largest standard deviation was 6% of the mean for the 5kPa blast environment. Total reflected impulse (I_r) was equally consistent with a maximum standard deviation 2%. The initial 7ms of reflected overpressure histories are shown in Figure 4.21 to Figure 4.23. The peak value was recorded from the average overpressure in the first 0.5ms, removing gauge noise. An increase in reflected overpressure between 0.5ms and 1.5ms after blast wave arrival was due to pressure build up and reflections within steelwork on the front of test containers. It cannot be assumed the glass experienced the same reflections so the initial peak was used to characterise the reflected blast wave. These graphs indicate loading applied to the glass before failure. Variation in the pressure history is clearer at this timescale and there was no significant difference in impulse applied before failure, indicating an extremely repeatable blast environment for all peak overpressures.

Table 4.7: Blast wave velocity from observed P_s peaks in Figure 4.17.

Direction of Blast Wave Movement	Gauge	Normalised Time of Blast Arrival (ms)	Distance Travelled (m)	Speed of Blast Wave (m/s)
Downstream	3m	0.00	0	
Downstream	2m	2.83	1	353
Downstream	1m	5.68	2	351
Upstream	1m	11.64	4	336
Upstream	2m	14.59	5	339
Upstream	3m	17.62	6	330
Mean				342

Table 4.8: Reflected blast parameters for P_s 14kPa trials.

Trial No.	Cubicle	1	2	3	4	5	6	7	8	$\bar{x}$	σ
P_r (kPa)	A	26.1	25.9	26.7	26.6	26.3	26.7	27.5	26.1	27.2	0.9
	B	26.8	26.9	28.2	28.6	27.7	28.7	28.8	27.5		
I_r (kPa.ms)	A	734	738	716	725	715	729	728	717	724	8
	B	734	735	715	723	712	726	727	716		

Table 4.9: Reflected blast parameters for P_s 10kPa trials.

Trial No.	Cubicle	9	10	11	12	13	14	$\bar{x}$	σ
P_r (kPa)	A	20.5	20.4	20.2	20.3	18.9	18.0	20.1	1.0
	B	21.2	21.2	20.7	20.9	19.4	19.2		
I_r (kPa.ms)	A	450	441	439	440	437	429	435	7
	B	441	432	431	434	427	423		

Table 4.10: Reflected blast parameters for P_s 5kPa trials.

Trial No.	Cubicle	15	16	17	18	19	20	$\bar{x}$	σ
P_r (kPa)	A	12.4	12.0	11.9	13.1	11.4	13.5	12.4	0.7
	B	12.1	11.9	11.8	13.5	11.7	13.5		
I_r (kPa.ms)	A	222	212	215	225	228	220	219	5
	B	220	213	212	220	226	217		

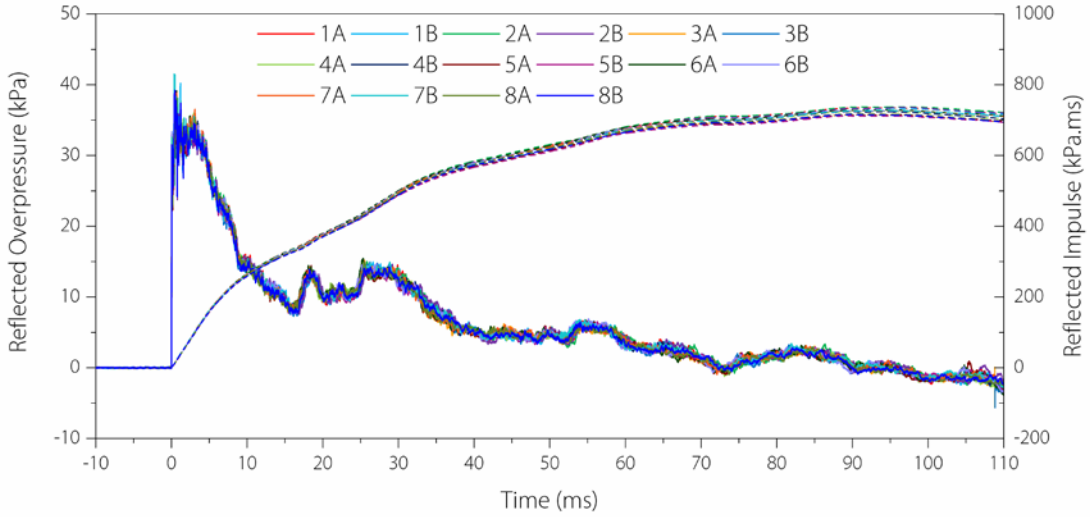

Figure 4.18: P_r and I_r from P_s 14kPa trials.

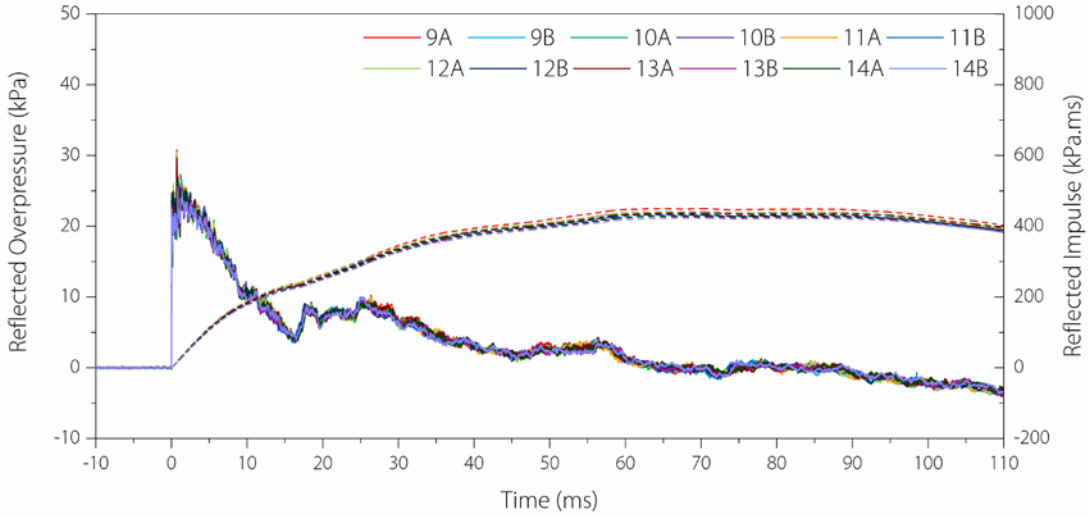

Figure 4.19: P_r and I_r from P_s 10kPa trials.

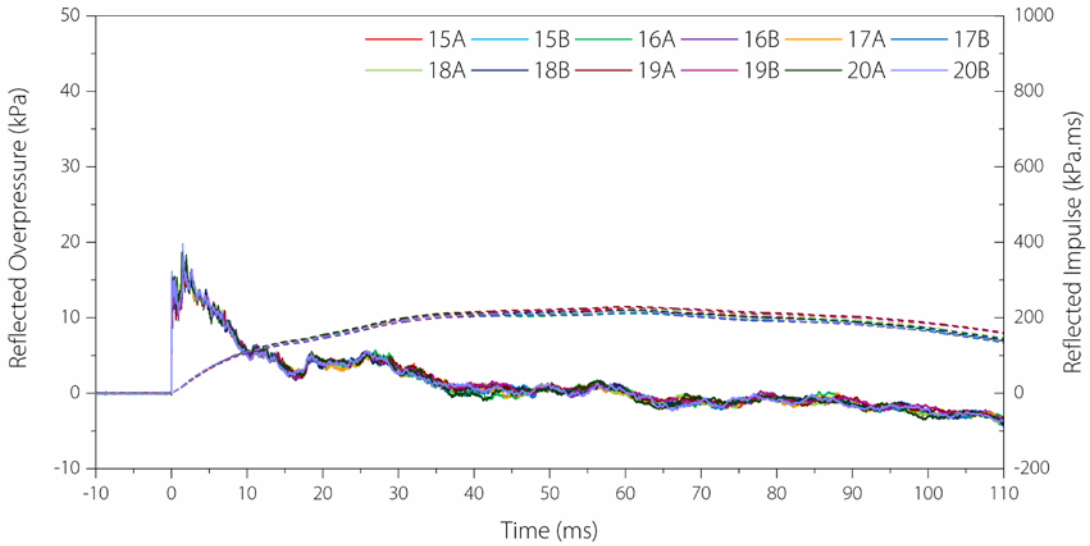

Figure 4.20: P_r and I_r from P_s 5kPa trials.

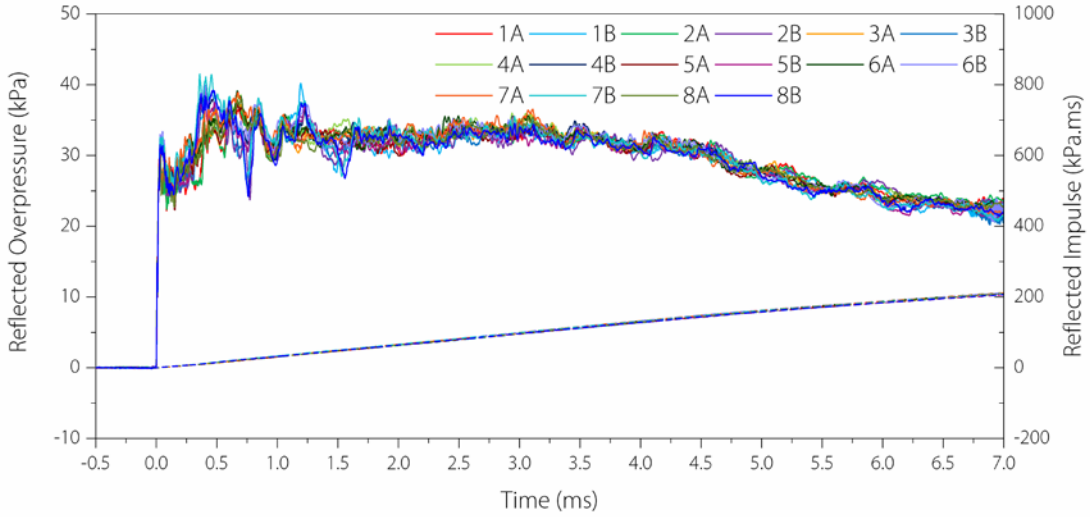

Figure 4.21: P_r and I_r from P_s 14kPa trials (initial 7ms).

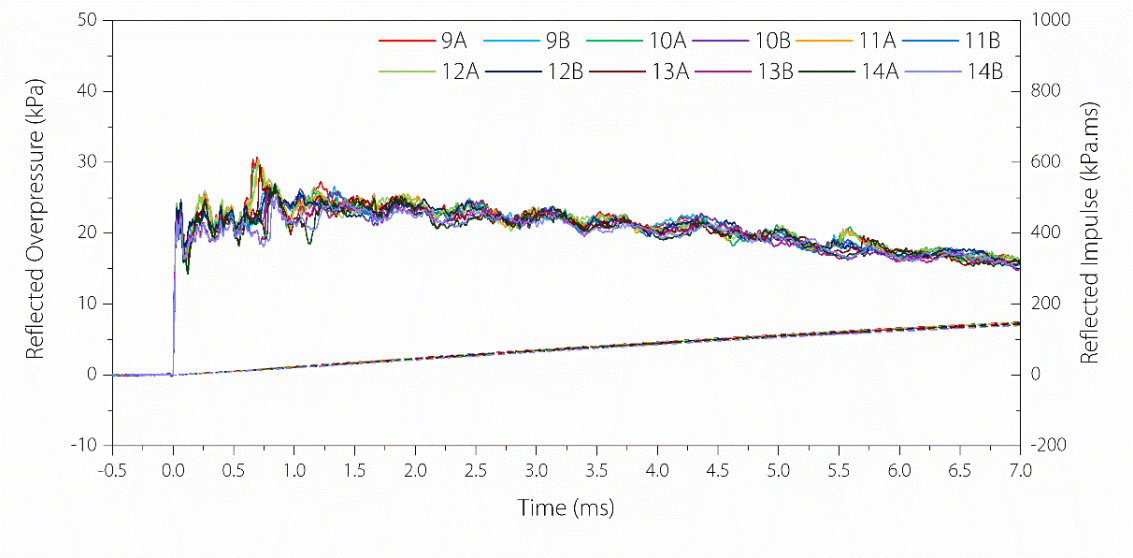

Figure 4.22: P_r and I_r from P_s 10kPa trials (initial 7ms).

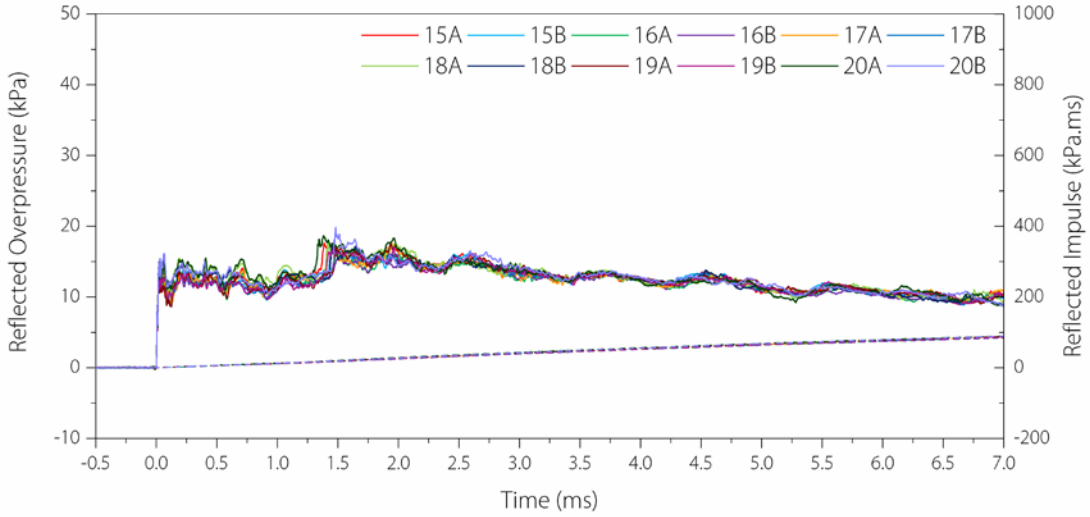

Figure 4.23: P_r and I_r from P_s 5kPa trials (initial 7ms).

Clearing time around the test cubicles was calculated using equation 2.9. Location of a P_r gauge on the test cubicles and its clearing distances are shown in Figure 4.24. The calculated clearing time was 9ms. C_r value from Figure 2.6 matched the blast wave speed calculated in Table 4.7, verifying that Figure 2.6 was applicable for long-duration blasts produced in the ABT. C_r for P_s 10kPa was 347 m/s and for P_s 5kPa was 343 m/s. For all blast environments the clearing time was 9ms. An example of a reflected overpressure history from each blast environment is shown in Figure 4.25. The calculated clearing time and minimum, maximum and mean glass failure times for all trials are labelled. The calculated clearing time fits the transition from reflected overpressure (P_r) to stagnation pressure (P_{stag}) on the graph. All glass failed before the end of the clearing time within the reflected overpressure regime. Latest glass failure occurred while P_r was approximately at its peak value, for this configuration loading can be assumed quasi-static if window failure occurs. If the gauge was located in the centre of the glass, clearing time would have been 7ms based on the same calculations. All windows that failed broke within 7ms meaning all failures occurred in the reflected pressure regime.

$$t' = \frac{4S}{(1+R)C_r} = \frac{4 \times 1.25}{(1+0.57) \times 0.35} = 9ms$$

$$S = 1.25m$$

$$G = 2.2m$$

$$R = \frac{S}{G} = \frac{1.25}{2.2} = 0.57$$

$$C_r = 350\ m/s$$

(C_r from Figure 2.6)

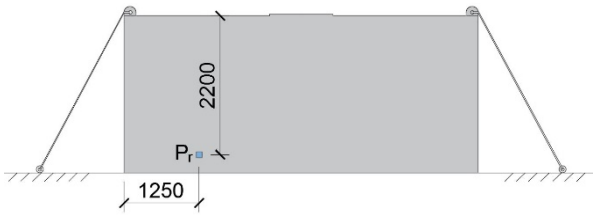

Figure 4.24: P_r gauge location (mm).

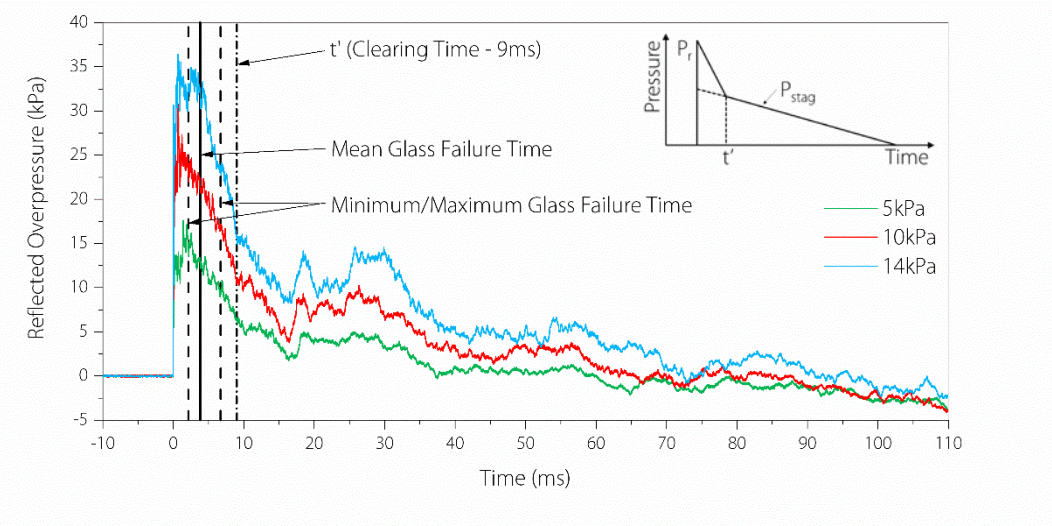

Figure 4.25: Reflected overpressure: glass failure times and clearing time labelled.

4.4 Detecting Cracking

Phase S1 consisted of five static tests to assess break circuits and triangulation of piezo transducers under static loading conditions. Phase D1, consisting of eight full-scale blast trials, considered effectiveness of piezo transducers in the aggressive loading environment of the ABT. In Phase S2 20

static trials were undertaken to test piezo transducer reliability. In Phase D2 a further 24 glass samples were tested over 12 trials at two lower blast environments.

4.4.1 Method Refinement (Phases S1 and D1)

Five glass specimens were tested to failure by linearly reducing vacuum chamber pressure at a rate of 0.44±0.03kPa/s. Crack development in Sample 4 from Phase S1 is shown in Figure 4.26. Failure occurred from a single point referred to in literature as the Griffith Flaw (Griffith, 1921). Cracks propagated outwards radially until reaching frame edges. Circumferential secondary cracks further developed between radial cracks. For Tests 2 to 5, initial crack location was calculated from piezo transducers using triangulation. Crack locations varied significantly between tests (Figure 4.27) as location of the Griffith Flaw was random. Good agreement was observed between piezo transducers and camera with an average difference of 23±21mm across four tests, and a maximum of 55mm in Test 3 (Table 4.11). Calculated speed of sound in the glass was 5375±1025m/s. Independent triggers were used for the camera and gauges so comparison of break times was not possible. Triangulation accurately located cracking in each test allowing the original crack time to be calculated. In Test 2, arrival time delay was 0.035ms for an individual piezo transducer, whilst the conductive paint exhibited a response time of 0.312ms (Figure 4.28a). Cracking in the sample at each of these response times is shown in Figure 4.28b and c. Very minor cracking was visible before piezo transducer response, whereas significant fracturing had occurred during the paint response time despite cracks crossing several parts of the wire. Piezo transducer delay can be attributed to the time for the sound to reach the piezo transducer. By locating the crack origin, failure time could be calculated, eliminating this error.

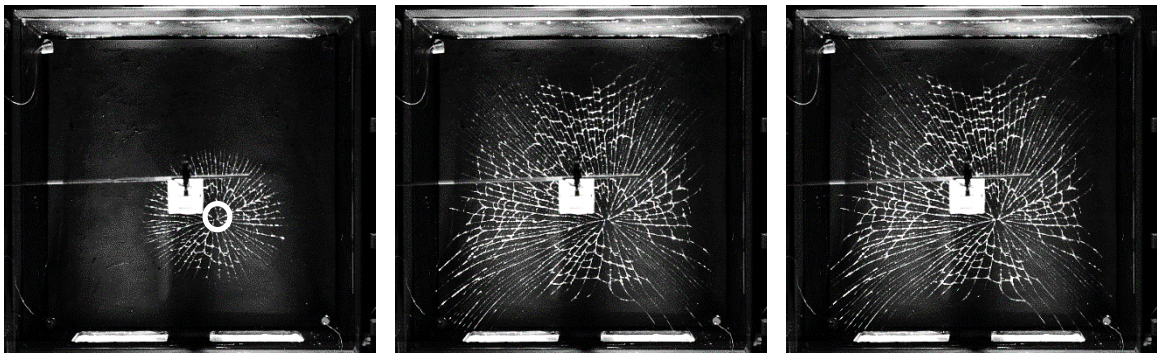

(a) $t = t_c + 77$ µs (b) $t = t_c + 230$ µs (c) $t = t_c + 384$ µs

Figure 4.26: Crack propagation for Test 4, Phase S1.

Break circuits measured break time but not crack location. Conductive paint recorded a response time of 0.3ms, despite cracks propagating across several parts of the circuit. With break times of approximately 3ms in the ABT, this corresponded to a 10% error in break time. This delay can be attributed to high resistivity of carbon-based paint which could have been resolved by using silver-based paint. Break circuits required significant time to prepare the geometric pattern and dry the paint. In comparison triangulation of piezo transducers accurately calculated break time and crack location. Piezo transducers were quick and inexpensive to install making them the preferred method.

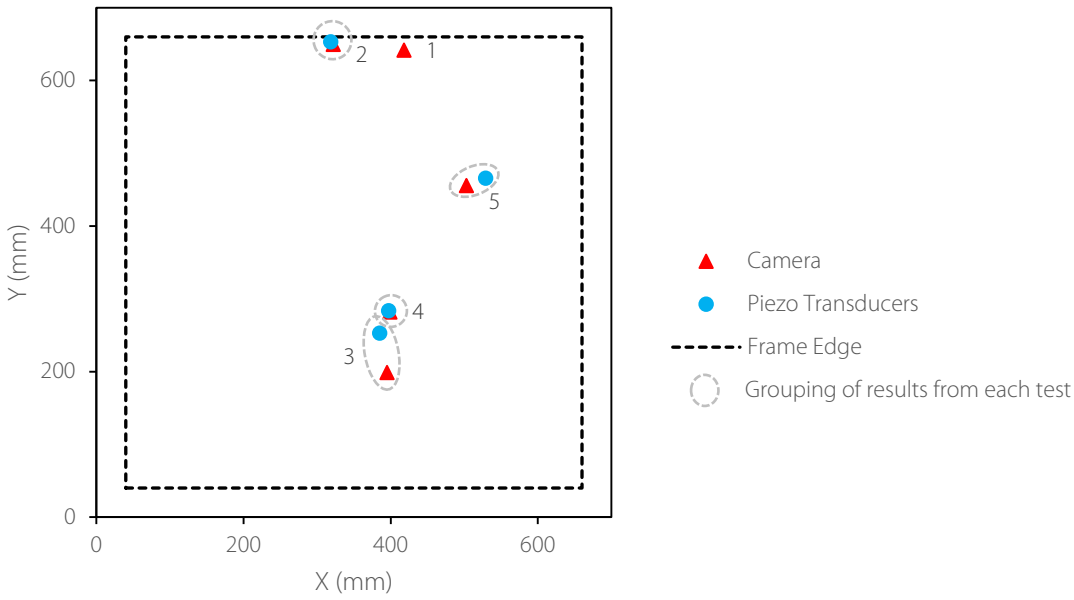

Figure 4.27: Initial crack locations for each S1 test from cameras and piezo transducers.

Table 4.11: Summary of crack locations from cameras and piezo transducers.

Test		1	2	3	4	5	$\bar{x}$	σ
Camera (mm)	x	418	322	395	399	503		
	y	642	650	199	282	456		
Piezo Transducers (mm)	x	-	319	385	397	529		
	y	-	654	253	284	466		
Difference (mm)		-	5	55	3	28	23	21

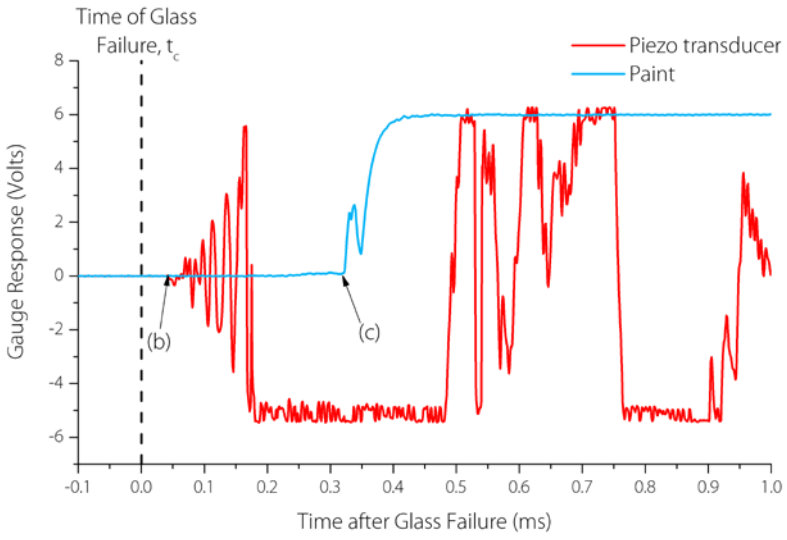

(a) Gauge signal after glass failure for Test 2.

(b) Time of piezo transducer response ($t = t_c + 0.038$ ms).

(c) Time of conductive paint response ($t = t_c + 0.304$ ms).

Figure 4.28: Comparison of gauge response time using Test 2, Phase S2

Piezo transducer data from three different trials are shown for reference in Figure 4.29. Piezo transducer amplitude sensitivity used in Phase S1 was maintained for Trial 1, Phase D1 (Figure 4.29a). Low frequency signals were observed before blast wave arrival at the containers, corresponding to

blast wave arrival in the 10.2m section which could be attributed to shock transmission through the ABT ground slab. Blast wave arrival at the containers was consistent with a high-amplitude, high-frequency response, greater than the amplitude sensitivity of the piezo transducers, resulting in data loss. Triangulation was not possible for this trace profile. Piezo transducer amplitude sensitivity was subsequently reduced by a factor of 100 (Figure 4.29b) removing noise attributed to ground shock. Piezo transducer 5 reached maximum amplitude 1.49ms before glass failure, piezo transducers 1 to 4 lost data 0.4ms before cracking occurred. Triangulation could be compensated using minor signal changes with camera data for reference. Piezo transducer amplitude sensitivity was further reduced by a factor of 10, 1000 times less than in Phase S1, and the full response was recorded for all glass samples (Figure 4.29c). A low frequency signal was recorded between blast wave arrival and glass failure; cracking was identified by a discontinuity in gauge signal followed by a high frequency response. This discontinuity was used for triangulation.

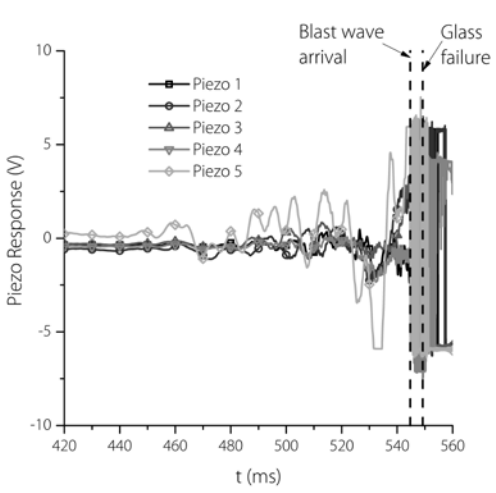

(a) Phase S1 sensitivity (Trial 1).

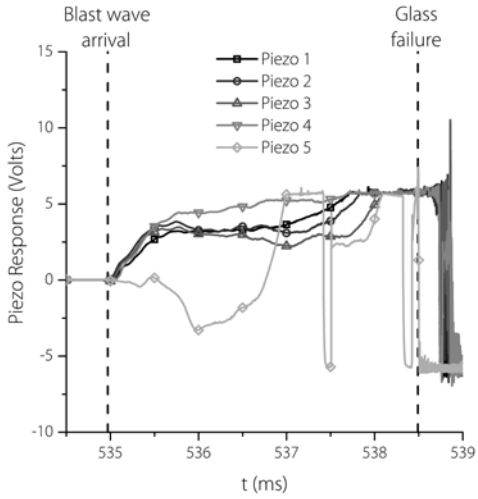

(b) Reduced by factor of 100 (Trial 3).

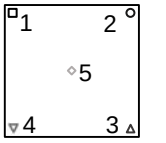

Piezo transducer locations

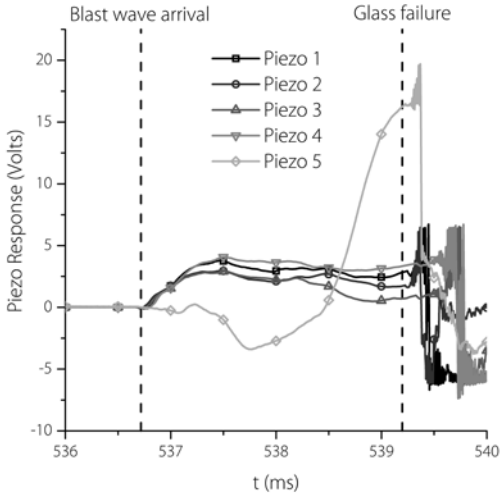

(c) Reduced by factor of 1000 (Trial 8).

Figure 4.29: Piezo transducer response to reduced sensitivity.

Triangulation was not possible for windows 1 and 2 for aspect ratios 1:1 and 1:1.3 due to data loss. For all other glass arrangements, crack locations from piezo transducers and cameras were plotted (shown in Figure 4.30). Calculation errors (see equation 4.6) from each sample are detailed in Table 4.13. Good agreement was observed between the two methods with a mean difference of 33±44mm (Table 4.13) despite the difference for 1:1.3 Sample 3 being significantly higher due to cracking within the frame. The calculated sound velocity for Phase D1 was 4484±1719m/s. The large standard deviation indicates error in triangulation calculations. While the trend suggests a higher calculation error was associated with lower aspect ratios, a larger error can be attributed to glass failure within the frame where accurate measurement was difficult. Reduced piezo transducer sensitivity filtered out sound travelling through the frame in Sample 4 for aspect ratio 1:1.7, allowing accurate location calculation. Measurement errors from piezo transducers and cameras are outlined in Table 4.12. For triangulation piezo transducers were assumed explicit points despite a diameter of 20mm, introducing a 10mm error. Piezo transducers were sampled at a rate of 1MHz, the resulting precision was 0.5µs or 2mm. Camera measurement of crack location required calibration against a scale in the image subsequently using Pythagoras to define coordinates. Calibration resulted in a pixel size of 2mm and a total camera measurement error of 2mm. Total error was calculated from the root square mean (RMS) of these errors. For cracks within the frame, location measurement using camera data assumed failure at the frame edge, a potential source of error. Camera frame rate did not contribute to the error due to crack location being determined from initial radial cracks visible a few frames after first fracture. Total error for comparison of detection methods was the sum of the piezo calculation error and RMS of measurement errors in Table 4.12. Difference in crack location measurements was larger than total error calculated for three samples. This can be attributed to an error in recorded break times from piezo transducer signals despite a solution with a low error being found. The first sample for aspect ratio 1:1.7 produced good agreement with the camera result despite a significantly lower speed of sound being calculated. This can also be attributed to an error in recorded break times, speed of sound should be used as an indication of the quality of the analysis.

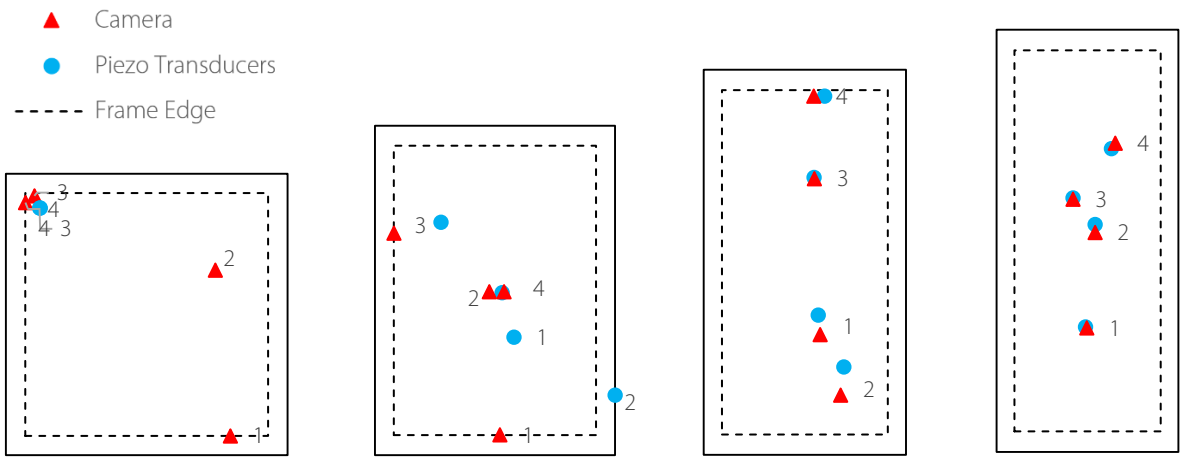

(a) Aspect ratio 1:1. (b) Aspect ratio 1:1.3. (c) Aspect ratio 1:1.7. (d) Aspect ratio 1:2.

Figure 4.30: Comparison of D1 crack locations: cameras and piezo transducers.

Table 4.12: Description of crack location errors.

Error Description	Error (mm)
Piezo transducer size	10
Piezo transducer precision (0.5μs)	3
Camera measurement error	2
RMS Total Measurement Error	11

Table 4.13: Crack location comparison and error summary: Phase D1.

Aspect Ratio	Glass Sample	Trial No.	Difference in Crack Locations (mm)	Piezo Calculation Error (mm)	Total Error: Piezo calculation error + total measurement error from Table 4.12 (mm)	Sound Velocity (m/s)
1:1	3	5	52	1047*	1058*	800
	4	5	17	7753*	7764*	4850
1:1.3	3	6	169	49568*	49579*	3600
	4	6	5	13	24	4650
1:1.7	1	3	18	8	19	1050
	2	3	41	8	19	3900
	3	7	3	9	20	3250
	4	7	34	9	20	3100
1:2	1	4	14	11	22	6000
	2	4	27	9	20	5400
	3	8	3	8	19	5650
	4	8	13	8	19	5500
$\bar{x}$			18	9	20	4280
σ			13	2	2	1520

Yellow highlighting indicates glass samples failed within the frame.
*These results were assumed anomalous due to errors > 1000mm and were omitted from calculation of mean and standard deviation.

4.4.2 Testing Repeatability (Phases S2 and D2)

Five piezo transducers were used on each glass sample in Phases S2 and D2. The additional data significantly improved the accuracy of triangulation calculations. For Phase S2, 20 glass samples of 600mm x 600mm x 4mm were tested statically and 19 failed. All piezo transducers were calibrated to the reduced sensitivity determined in Phase D1. Crack locations determined from camera and piezo transducer data are shown in Figure 4.31. All samples demonstrated good agreement. The largest difference was 18.6mm for sample 7, this sample failed within the frame which could have contributed to the higher difference. Crack locations from camera footage and triangulation (with associated errors) are compared in Table 4.14. The mean difference between crack locations was 10±12mm. Sample 7 recorded a large difference in locations and error compared to other samples indicating error in interpreting piezo response, despite speed of sound being within one standard deviation of the mean. Samples 8 and 18 recorded crack location differences over 25mm, contributing to a large standard deviation. If these three samples are set aside the mean difference reduces to 5±3mm, considerably lower than results from Phase D1 due to controlled laboratory conditions and a better choice of piezo transducer sensitivity. The mean piezo calculation error was 2±4mm, indicating analyses converged well and break time was accurately determined from piezo traces.

Consistent values of speed of sound (5615±148m/s, standard deviation 3% of mean) indicated accurate recording of break times from piezo transducer data.

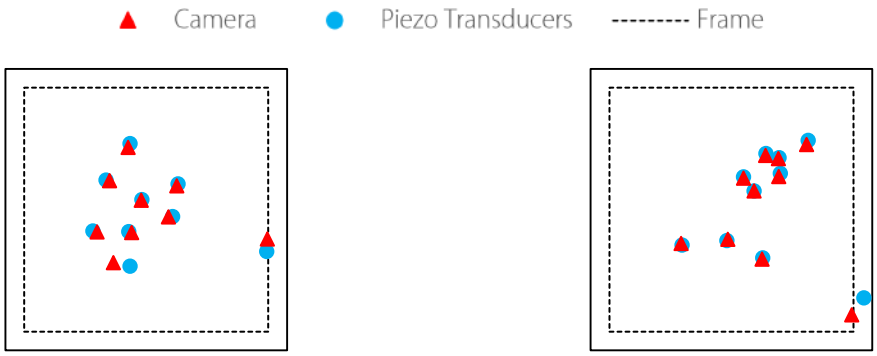

(a) Cut edges. (b) Ground edges.

Figure 4.31: Comparison of S2 crack locations: cameras and piezo transducers.

Table 4.14: Piezo transducer analysis: Phase S2.

Sample	Difference in Crack Locations (mm)	Piezo Calculation Error (mm)	Total Error: Piezo calculation error + total measurement error from Table 4.12 (mm)	Sound Velocity (m/s)
1	9	0.7	12	5240
2	-	-	-	-
3	9	0.8	12	5850
4	7	0.2	11	5950
5	5	3.6	15	5540
6	9	0.1	11	5630
7	36	18.6	30	5730
8	27	0.1	11	5635
9	8	0.6	12	5710
10	2	0.8	12	5580
11	1	0.3	11	5705
12	3	0.4	11	5675
13	4	0.7	12	5670
14	4	0.1	11	5575
15	3	1.5	12	5420
16	7	0.3	11	5560
17	3	0.2	11	5575
18	45	0.6	12	5540
19	10	0.4	11	5575
20	3	0.4	11	5515
$\bar{x}$	10	1.6	13	5615
σ	12	4.1	4	148

Phase D2 comprised 24 glass samples of various aspect ratios, half mounted in rigid and half using flexible mounting. All rigid frames in Phase D1 incorporated a strip of protective foam absent from frames in Phase D2 (shown in Figure 4.32). This foam tape prevented stress concentrations in the glass due to uneven frame surfaces and the glass striking the frame edge as it deflected. The missing foam

allowed the sample to collide with the frame, causing noise in the piezo transducer signal so piezo data could not be analysed. An example of the signal produced is shown in Figure 4.33. A sudden drop in voltage followed by low amplitude, higher frequency signals indicates the glass has struck the frame. A sudden drop in response, indicating glass failure, was hidden by this noise making triangulation impossible. Elastic samples could still be analysed as their framing did not produce such issues. Difference in crack locations and errors associated with the calculations are detailed in Table 4.15. Crack locations are plotted on each aspect ratio in Figure 4.34. Two samples survived and triangulation could not be performed on sample one from arrangement 10kPa, 1:1.3 due to differing time scales. The mean difference in crack locations (37±36mm) was much larger than in Phase S2 due to the harsh environment of the ABT. Mean calculation error (3±4mm) was consistent with results in Phase S2, in accordance with the calculated sound velocity (5625±241m/s), demonstrating well converging analyses. Highlighted samples failed within the frame but this did not affect accuracy as speed of sound in the silicone sealant is less than in glass.

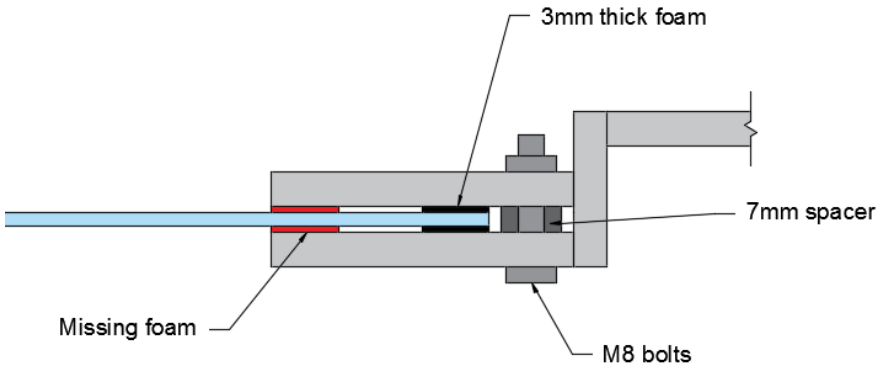

Figure 4.32: Cross section through rigid frame with missing foam.

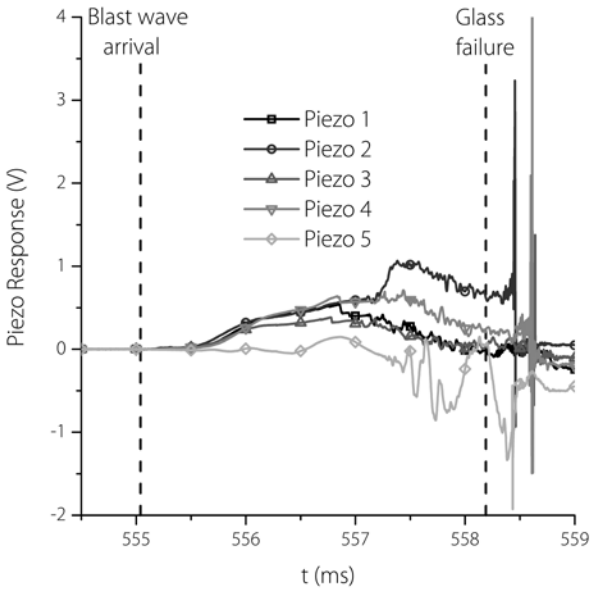

Figure 4.33: Example of piezo transducer response with frame noise.

Table 4.15: Summary of piezo transducer analysis from Phase D2.

Design P_s (kPa)	Aspect Ratio	Trial	Difference in Crack Locations (mm)	Piezo Calculation Error (mm)	Total Error: Piezo calculation error + total measurement error from Table 4.12 (mm)	Sound Velocity (m/s)
10	1:1	10A	4	1	12	5650
10	1:1	10B	21	1	12	5400
10	1:1.3	12A	-	-	-	-
10	1:1.3	12B	67	10	21	5650
10	1:2	14A	120	0	11	6150
10	1:2	14B	30	8	19	5300
5	1:1	16A	5	2	13	5600
5	1:1	16B	WINDOW SURVIVED			
5	1:1.3	18A	26	2	13	5750
5	1:1.3	18B	115*	130*	141*	3450*
5	1:2	20A	23	1	12	5500
5	1:2	20B	WINDOW SURVIVED			
$\bar{x}$			37	3	14	5625
σ			36	4	4	241

Yellow highlighting indicates glass samples that failed within the frame.
*These results were assumed anomalous due to a triangulation error > 100mm and were omitted from calculation of mean and standard deviation.

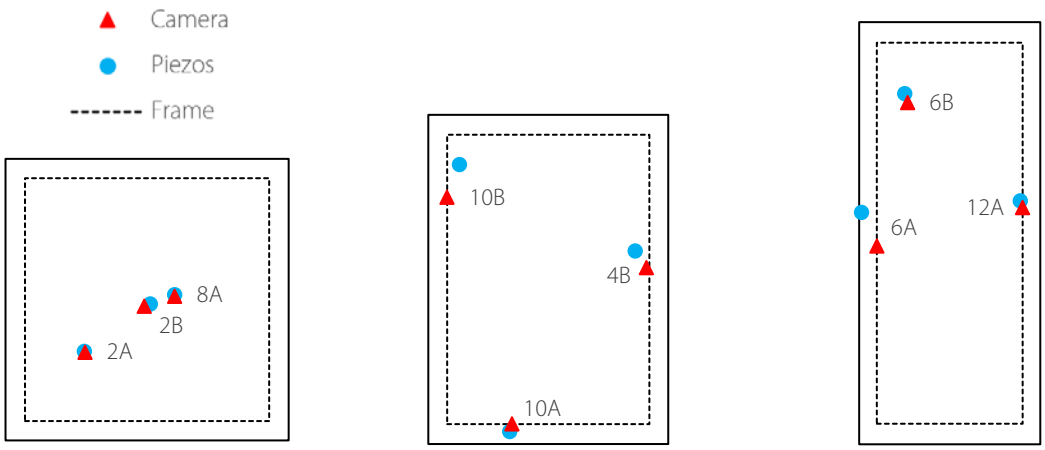

(a) Aspect ratio 1:1. (b) Aspect ratio 1:1.3. (c) Aspect ratio 1:2.

Figure 4.34: Comparison of crack locations from camera and piezo transducers from Phase D2.

4.4.3 Discussion and Summary

It is essential that the signal digitiser is able to record the piezo transducer response with sufficient resolution and without overload. It is recommended that piezo transducer amplitude sensitivity is tested and optimised using a method similar to that in Phases S1 and S2 before blast trials begin to prevent data loss. This is governed by the signal digitiser interpreting piezo transducer response. Sound velocity was consistently 5600m/s in Phases S2 and D2, providing good confidence in the data. Consistent values of sound velocity and small calculation errors (<20mm) indicated accurate solutions from triangulation. Large deviations can indicate convergence problems. Recorded break time for each piezo transducer should be checked to ensure the order is consistent with piezo transducer

layout. For example, if the first piezo transducer to respond is in the bottom left quadrant, and sound is only travelling through the glass, the piezo transducer in the top right corner cannot have a break time earlier than the piezo transducer in the centre of the glass. This initial sanity check can quickly highlight errors such as sound transmission through the frame or time of arrival recorded incorrectly. The use of more than four piezo transducers introduces redundancy in the data, so if one piezo transducer trace cannot be interpreted it may be removed from the triangulation analysis without loss of convergence. In all samples tested, failure occurred initially from a single flaw. In dynamic blast-based conditions in the ABT, some samples failed at a second Griffith Flaw soon after initial cracking. If multiple cracks occur almost instantaneously in opposite corners of the window, their acoustic emissions would interact making triangulation difficult. Increasing the number of piezo transducers would make identification of this case and triangulation easier. For all tests 20mm diameter piezo transducers were used, introducing a maximum positional error of 10mm. This could be reduced by decreasing piezo transducer size. Assumptions for triangulation include the glass remaining a flat plane and speed of sound being independent of time and direction. Speed of sound is likely to vary as the glass is stressed, however it did not appear critical to triangulation. In the ABT peak glass displacement was 36mm, nine times the sample thickness, corresponding to a 4° angle at the frame edges. Small triangulation errors and highly consistent calculated speed of sound indicate these assumptions are adequate for this application. Vibration of the glass against rigid frames in Phase D2 due to missing foam tape prevented triangulation. Any noise from framing should be minimised using foam tape or a similar material, or by increasing frame spacing. More tests with other framing types are recommended.

For future work it is recommended that at least six piezo transducers are used, one in each corner and two on the vertical centreline. If the glass fails at the centre with five piezo transducers, sound reaches the central piezo transducer instantaneously but can overload recording equipment and reach all corner piezos at the same time which can cause analysis convergence errors. Two piezo transducers at one third intervals along the vertical centreline can remove this error and additional sensors do not significantly increase analysis time. A degree of redundancy in case of piezo malfunction is also important in undeniably expensive blast experiments.

Triangulation of sound from piezo transducers is a cost-effective and accurate method of measuring annealed glazing response to long-duration blast representative of an extremely aggressive loading environment. Piezo transducers are quick to apply and break time and crack location can be calculated accurately using this method. Triangulation data capture was refined through four phases of testing involving 25 static and 40 dynamic tests; representing an impressive scientific repeat rigour. Accuracy was improved by adjusting piezo transducer amplitude sensitivity and increasing the number deployed from four to five. Speed of sound in annealed glass was consistently calculated at 5600m/s. This value was used to check analysis accuracy. Further testing is recommended to determine accuracy for short-duration blast events (t_d < 40ms) and different framing arrangements such as those found in the Glazing Hazard Guide.

4.5 Conclusions

In this chapter experimental methodology and results were presented and discussed. Four phases of experimental work, testing 65 windows, were executed in collaboration with industrial sponsor AWE and Spurpark Ltd. Trials were completed between January and August 2017 in the laboratories and ABT at MOD Shoeburyness. Two static phases informed cost-effective dynamic trial design. A highly repeatable testing rig was developed to facilitate material strength variation and the effect of glazing edge finish to be quantified. This method enabled viability of two data capture methods to be tested before use in the ABT. Over two dynamic phases, 40 windows were tested in 20 separate ABT trials. These trials quantified influence of aspect ratio, support conditions and blast environment on glazing failure and provided an excellent data set for comprehensive computational benchmarking. Glazing response is analysed in Chapter 5, benchmarking and the subsequent parametric study are detailed in Chapter 6.

Three blast overpressures were specified for dynamic trials; P_s 14kPa, 10kPa and 5kPa. Results yielded mean P_s of 13kPa, 10kPa and 6kPa. Corresponding mean t_d values were 100ms, 74ms and 48ms. A highly consistent blast environment was produced by the ABT for all specified blast pressures. Free-field pressures provided a reference and were measured upstream of testing cubicles. Overpressure oscillations due to reflections off the container front face and ABT expansion were observed. Changing light levels on light-sensitive gauges produced an artificial pressure increase after the initial peak. Reflected pressure data were used for glazing response analysis, the specified blast environments produced mean P_r values of 27kPa, 20kPa and 12kPa. Corresponding mean reflected impulses were 724kPa.ms, 435kPa.ms and 219kPa.ms. Reflected overpressure histories were highly consistent for all trials. The largest impulse standard deviation was 2% of the mean, indicating a very repeatable blast environment.

An innovative data capture technique, triangulating acoustic emissions recorded by piezo transducers to calculate glazing failure time and locate cracking origin, was trialled and refined during all experimental phases. Piezo transducers were quick to apply and offered a cost-effective and accurate alternative to high-speed photography in an aggressive loading environment. An iterative algorithm was developed to determine crack location from the difference in time of arrival of the acoustic emission at piezo transducers. Accuracy was improved by increasing the number of piezo transducers to five and optimising amplitude sensitivity. Speed of sound in the glass was consistently calculated as 5600m/s which provided an analysis accuracy check. The method was successfully tested in both static and blast loading environments, implying a wide range of possible applications in experimental testing of brittle materials.

Chapter 5

Analysis of Glazing Response

5.1 Introduction

The effect of aspect ratio, support conditions, peak overpressure and material variability on window failure was evaluated through experimental work. In this chapter each parameter is analysed and its effect on window failure quantified. Three long-duration blast environments were implemented in dynamic trials. These have been defined in Chapter 4 and will be referred to in terms of P_r from here on (see Table 5.1). The influence of varying P_r is explored in section 5.2. Aspect ratio was varied from 1:1 to 1:2, this variable is analysed in section 5.3. Two support conditions, rigid and elastic were tested in Phase D2, effect of these is evaluated in section 5.4. The significance of each parameter is compared in section 5.5. Finally, using 19 static trials, material variability is quantified in section 5.6 with the production of a damage curve.

Table 5.1: Mean P_r values used for reference to blast environments.

Design P_s (kPa)	5	10	14
Mean P_r (kPa)	12	20	27

Three break parameters quantified glazing failure: central displacement at failure, break time and reflected impulse received at break. Glass failure was defined by cracking identified using the front-facing camera. Blast wave arrival at the front of the containers was measured by two P_r gauges. Glass failure time was calculated as the difference between time of blast arrival (from P_r gauges) and time of glazing failure (from front-facing camera). Synchronisation of cameras and the data logger

recording all gauge readings was enabled by LEDs in view of side cameras that illuminated when blast arrival was detected by P_r gauges. All camera clocks were synchronised using IRIG satellite communication and were initially assumed perfectly synchronised. Initial calculation of break time was the difference between clock times of the side camera when the LED illuminated and the front-facing camera when cracking was observed. Later analyses used camera trigger times to refer each camera clock time back to the data logger, ensuring a common time base and removing the assumption of perfect clock synchronisation. This identified considerable IRIG synchronisation errors of up to 2ms resulting in all break parameters being reanalysed using this method. A timeline of trial trigger events is outlined in Figure 5.1. 100ms after trial initiation all gauges were triggered, then after a specified delay all cameras were triggered. Cameras recorded footage 300ms before and after trigger time. Camera trigger delay times ensured window failure was recorded and were a function of design P_s as lower overpressure blast waves travel slower. Trigger delay was 461ms for P_s 14kPa ranging to 483ms for P_s 5kPa. Displacement was measured by tracking a scaled gauge with a high-speed camera. Relative displacement was compared to the scale to calculate absolute displacement. Reflected impulse was measured at break time from P_r gauges for that trial. Errors associated with each break parameter are outlined in Table 5.2. Errors for impulse and displacement at failure take account of break time error. Break time and failure impulse errors were negligible compared to results. The failure displacement error was more significant (±1mm) with typical measurements between 10mm and 30mm. This error was due to the number of pixels used on the cameras and could not be improved without compromising the high frame rate which was required for a precise break time measurement. This error was insignificant when compared to variation in results due to material variability.

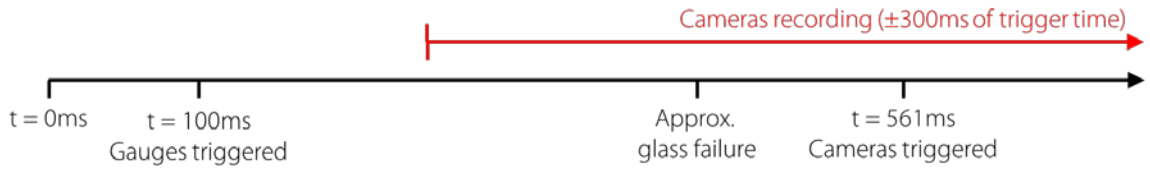

Figure 5.1: Timeline of trial events.

Table 5.2: Errors associated with calculation of break parameters.

Break Parameter	Error
Break time	± 0.01ms
Failure impulse	± 0.2 kPa.ms
Failure displacement	± 1 mm (3mm for wide view camera)

Raw break parameter data for each arrangement are detailed in Table 5.3 to Table 5.5. Four repeats were completed for arrangements subjected to P_r 27kPa, only two repeats were completed for other blast environments. Mean and standard deviation were calculated for each arrangement. For the remainder of this chapter arrangements will be referred to in the following format [P_r, aspect ratio, support conditions] e.g. [27kPa, 1:1, rigid]. Three samples remained unbroken in P_r 12kPa trials. All windows subjected to higher peak overpressures failed. Out of those that survived, two had elastic frames and one rigid. Each window had a different aspect ratio; 1:1, 1:1.3 and 1:2. The largest mean

displacement, 25mm, was recorded for the [27kPa, 1:1.3, Rigid] arrangement, the absolute largest displacement (36mm) recorded was for [27kPa, 1:1, rigid]. The lowest mean displacement was recorded for [20kPa, 1:1, rigid] and [12kPa, 1:1, rigid]. Both displaced 7mm on average. The absolute minimum displacement was 3mm for [12kPa, 1:2, rigid]. The largest standard deviation for displacement was 11mm, the smallest 0mm. Three arrangements with 0mm had a single data point due to one window surviving. One arrangement recorded identical displacements to the nearest millimetre. The longest mean break time was 7.97ms for arrangement [12kPa, 1:1.3, rigid]. One sample for this arrangement survived, causing a standard deviation of 0. It was also the absolute largest break time recorded. The lowest mean break time was 3.89ms for [20kPa, 1:1, rigid]. The lowest absolute break time was 3.15ms for [12kPa, 1:2, rigid]. The largest standard deviation was 1.86ms, the smallest 0ms. All arrangements with standard deviation 0 had a sample size of one. The largest mean impulse (153kPa.ms) was recorded for [27kPa, 1:1.3, rigid] with the largest absolute impulse (171kPa.ms) recorded for [27kPa, 1:1, rigid]. The minimum mean impulse (57kPa.ms) was recorded for [12kPa, 1:1, rigid]. The absolute smallest impulse recorded was 42kPa.ms for [12kPa, 1:2, rigid] which also recorded the largest standard deviation of 22kPa.ms. All arrangements with standard deviation 0 had a sample size of one.

Table 5.3: Displacement results summary: dynamic trials.

P_r (kPa)	Aspect Ratio	Support Conditions	Failure Displacement (mm)					
			1	2	3	4	$\bar{x}$	σ
27	1:1	Rigid	36	10	23	20	22	9
27	1:1.3	Rigid	20	28	26	27	25	3
27	1:1.7	Rigid	23	7	13	11	14	6
27	1:2	Rigid	13	23	18	11	16	4
20	1:1	Rigid	7	7			7	0
20	1:1	Elastic	24	21			23	1
20	1:1.3	Rigid	29	13			21	8
20	1:1.3	Elastic	19	27			23	4
20	1:2	Rigid	11	18			15	4
20	1:2	Elastic	18	8			13	5
12	1:1	Rigid	11	4			7	4
12	1:1	Elastic	13	X			13	-
12	1:1.3	Rigid	X	23			23	-
12	1:1.3	Elastic	17	18			17	1
12	1:2	Rigid	25	3			14	11
12	1:2	Elastic	16	X			16	-

X – Indicates unbroken sample.

5.2 Blast Environment

In this section the effect of blast environment on break parameters is analysed. Samples with aspect ratio 1:1.7 have been disregarded as they were only used in P_r 27kPa trials so no comparison was possible. All break parameters are plotted against P_r in Figure 5.2. Symbols differentiate between aspect ratios and colours between support conditions. Statistical analysis was not undertaken as data points represented different structural arrangements. Instead these plots provide an overview of data spread and general trends.

Table 5.4: Break time summary: dynamic trials.

P_r (kPa)	Aspect Ratio	Support Conditions	Break Time (ms)					
			1	2	3	4	$\bar{x}$	σ
27	1:1	Rigid	5.43	3.71	4.68	4.41	4.56	0.62
27	1:1.3	Rigid	4.48	5.03	4.72	4.80	4.76	0.19
27	1:1.7	Rigid	4.58	3.83	3.75	3.54	3.93	0.39
27	1:2	Rigid	3.76	4.59	4.24	3.56	4.04	0.40
20	1:1	Rigid	4.23	3.54			3.89	0.35
20	1:1	Elastic	5.70	4.81			5.26	0.45
20	1:1.3	Rigid	6.49	4.33			5.41	1.08
20	1:1.3	Elastic	4.77	5.54			5.15	0.38
20	1:2	Rigid	4.02	4.70			4.36	0.34
20	1:2	Elastic	4.99	3.52			4.25	0.73
12	1:1	Rigid	5.10	3.52			4.31	0.79
12	1:1	Elastic	5.29	X			5.29	-
12	1:1.3	Rigid	X	7.97			7.97	-
12	1:1.3	Elastic	5.73	6.83			6.28	0.55
12	1:2	Rigid	6.87	3.15			5.01	1.86
12	1:2	Elastic	5.89	X			5.89	-

X – Indicates unbroken sample.

Table 5.5: Failure impulse summary: dynamic trials.

P_r (kPa)	Aspect Ratio	Support Conditions	Failure Impulse (kPa.ms)					
			1	2	3	4	$\bar{x}$	σ
27	1:1	Rigid	171	118	149	141	145	19
27	1:1.3	Rigid	144	158	154	157	153	6
27	1:1.7	Rigid	147	124	124	117	128	11
27	1:2	Rigid	124	150	137	115	132	13
20	1:1	Rigid	98	81			90	9
20	1:1	Elastic	125	107			116	9
20	1:1.3	Rigid	139	96			118	22
20	1:1.3	Elastic	108	121			115	7
20	1:2	Rigid	90	101			96	6
20	1:2	Elastic	107	76			92	16
12	1:1	Rigid	67	47			57	10
12	1:1	Elastic	67	X			67	-
12	1:1.3	Rigid	X	95			95	-
12	1:1.3	Elastic	76	86			81	5
12	1:2	Rigid	85	42			64	22
12	1:2	Elastic	78	X			78	-

X – Indicates unbroken sample.

For failure displacement, results spread for each P_r was large (approx. 20mm) and was consistent between blast environments. The large spread indicated displacement dependency on other parameters (aspect ratio, support conditions and material strength). An apparent increase in displacement occurred as P_r increased however this was not observed when considering individual structural arrangements. Spread of break time data decreased and a small general decrease in break time occurred as P_r increased. A higher P_r caused a higher impulse rate causing earlier glass failure. Decrease in spread with increase of P_r can be attributed to the increase in impulse rate. For a higher impulse rate a small increase in break time caused a large impulse increase. Impulse spread was constant (approx. 60kPa.ms) for all blast environments, causing the decrease in break time spread.

Impulse received at failure increased significantly with P_r. Decrease in break time was not sufficient for failure impulse to be constant indicating a dependency of failure impulse on P_r.

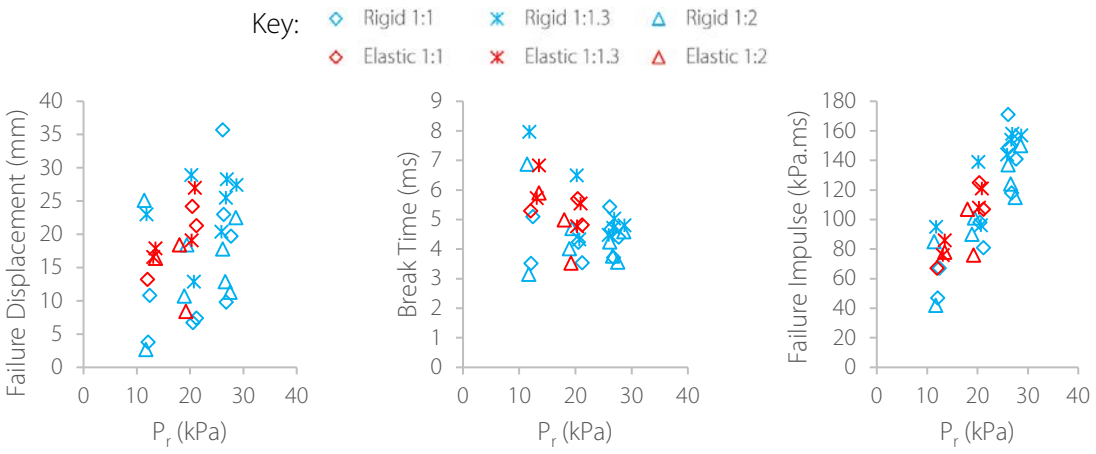

(a) Failure displacement. (b) Break time. (c) Failure impulse.

Figure 5.2: Break parameters as a function of P_r.

The data were broken down into six arrangements, aspect ratios 1:1, 1:1.3 and 1:2 with rigid and elastic support conditions. Elastic supports were only used in P_r 12kPa and 20kPa trials. Analysing individual arrangements allowed influence of blast environment to be quantified. Break parameter means and standard deviations are outlined in Table 5.6. Mean parameters were normalised against result for P_r 12kPa using equation 5.1 and were plotted in Figure 5.3 to Figure 5.5. Standard deviation calculation is omitted for single data points.

Table 5.6: Summary: break parameters as a function of P_r.

Aspect Ratio	Supports		Failure Displacement (mm)			Break Time (ms)			Failure Impulse (kPa.ms)		
			12kPa	20kPa	27kPa	12kPa	20kPa	27kPa	12kPa	20kPa	27kPa
1:1	Rigid	$\bar{x}$	7	7	22	4.31	3.89	4.56	57	90	145
		σ	4	0	9	0.79	0.35	0.62	10	9	19
		Norm	1.00	0.97	3.02	1.00	0.90	1.06	1.00	1.57	2.54
	Elastic	$\bar{x}$	13	23		5.29	5.26		67	116	
		σ	-	1		-	0.45		-	9	
		Norm	1.00	1.72		1.00	0.99		1.00	1.73	
1:1.3	Rigid	$\bar{x}$	23	21	25	7.97	5.41	4.76	95	118	153
		σ	-	8	3	-	1.08	0.19	-	22	6
		Norm	1.00	0.91	1.10	1.00	0.68	0.60	1.00	1.24	1.61
	Elastic	$\bar{x}$	17	23		6.28	5.15		81	115	
		σ	1	4		0.55	0.38		5	7	
		Norm	1.00	1.34		1.00	0.82		1.00	1.41	
1:2	Rigid	$\bar{x}$	14	15	16	5.01	4.36	4.04	64	96	132
		σ	11	4	4	1.86	0.34	0.40	22	6	13
		Norm	1.00	1.05	1.16	1.00	0.87	0.81	1.00	1.50	2.07
	Elastic	$\bar{x}$	16	13		5.89	4.25		78	92	
		σ	-	5		-	0.73		-	16	
		Norm	1.00	0.82		1.00	0.72		1.00	1.17	

Norm - Break parameter normalised against result for 12kPa.

$$Normalised\ break\ parameter = \frac{\bar{x}_{P_r}}{\bar{x}_{P_r=12kPa}} \qquad 5.1$$

The largest normalised displacement increase was for aspect ratio 1:1. A 72% displacement increase was recorded for [1:1, elastic] between P_r 12kPa and 20kPa. No significant change was measured for [1:1, rigid] between P_r 12kPa and 20kPa but an increase of 202% was recorded for P_r increase to 27kPa. P_r exhibited a smaller effect on displacement for all other arrangements. The largest displacement increase was +34% for [1:1.3, elastic] between P_r 12kPa and 20kPa. All other normalised displacements were less than 1.20 and deemed insignificant compared to standard deviations calculated for each arrangement.

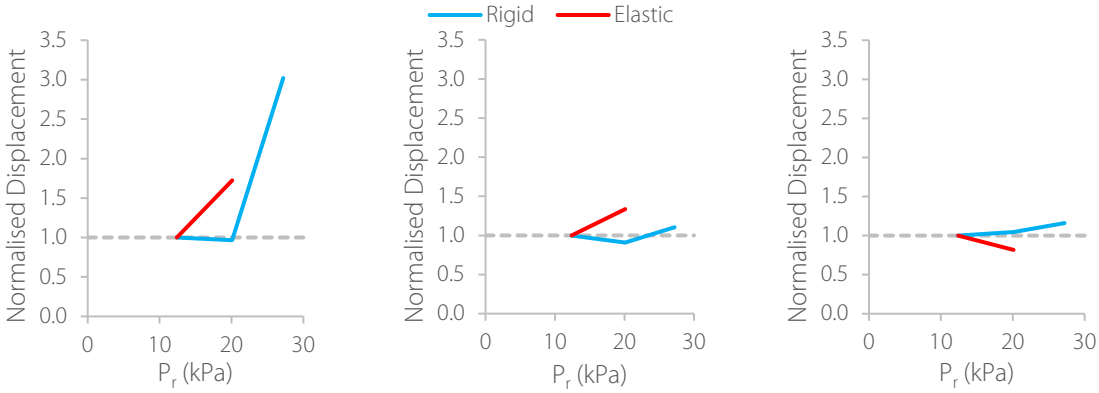

(a) Aspect ratio 1:1. (b) Aspect ratio 1:1.3. (c) Aspect ratio1:2.

Figure 5.3: Normalised failure displacement as a function of P_r.

In general normalised break times decreased with P_r increase. Magnitude of normalised break times was much smaller than displacements, the smallest normalised break time was 0.60 for [1:1.3, rigid] at P_r 27kPa. No significant effect was recorded for [1:1, rigid] or [1:1, elastic], normalised results were between 0.90 and 1.10. Decrease in normalised break time for [1:1.3, elastic] was much less than [1:1.3, rigid] at P_r 20kPa, respective normalised break times were 0.82 and 0.68. This indicated P_r had larger effect on rigid supports compared to elastic supports at aspect ratio 1:1.3. The opposite effect occurred for aspect ratio 1:2, normalised break time for elastic supports was 0.72 compared to 0.87 for rigid framing.

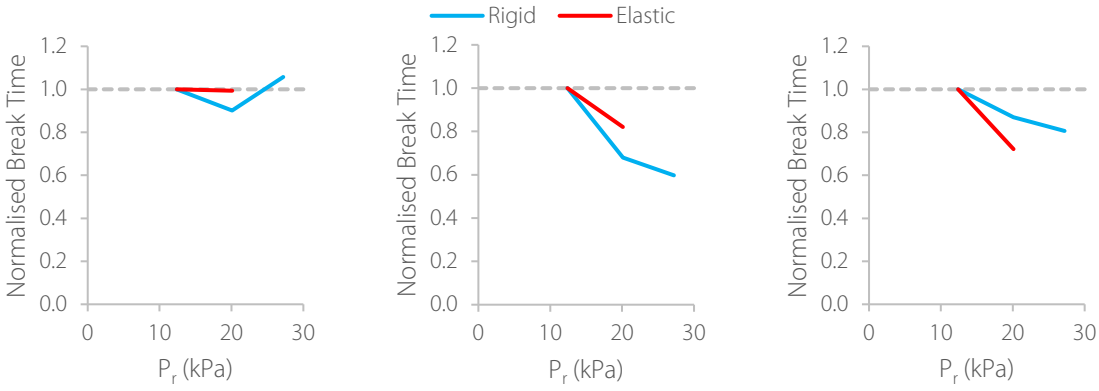

(a) Aspect ratio 1:1. (b) Aspect ratio 1:1.3. (c) Aspect ratio1:2.

Figure 5.4: Normalised break time as a function of Pr.

All normalised failure impulses increased as P_r increased. The largest normalised impulse was for aspect ratio 1:1. Elastically supported glass exhibited a larger normalised impulse for aspect ratios 1:1 and 1:1.3 but smaller for 1:2 when compared to rigid framing. For elastic supports subjected to P_r

20kPa, normalised impulse decreased from 1.73 to 1.17 when aspect ratio increased from 1:1 to 1:2. For rigidly supported glass the smallest normalised impulse at P_r 27kPa was 1.61 for aspect ratio 1:1.3, the largest 2.54 for aspect ratio 1:1. All normalised impulses except [1:2, elastic] were larger than 1.20 meaning trends were significant compared to standard deviations.

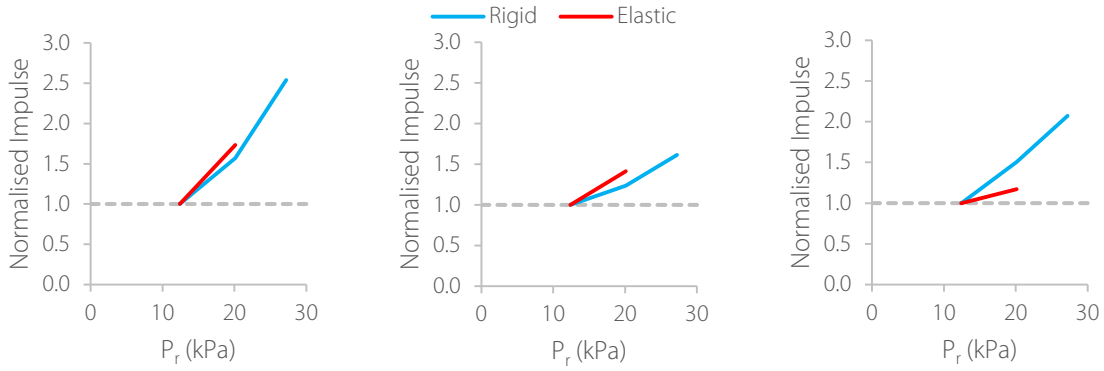

(a) Aspect ratio 1:1. (b) Aspect ratio 1:1.3. (c) Aspect ratio1:2.

Figure 5.5: Normalised failure impulse as a function of Pr.

Crack patterns caused by different blast environments are shown in Figure 5.6. Cracking varied highly due to the size and location of the Griffith flaw. Denser cracking was observed in glass subjected to P_r 27kPa compared to 12kPa due to increased impulse received at higher overpressures. More energy was stored by the glass resulting in denser crack branching to dissipate energy.

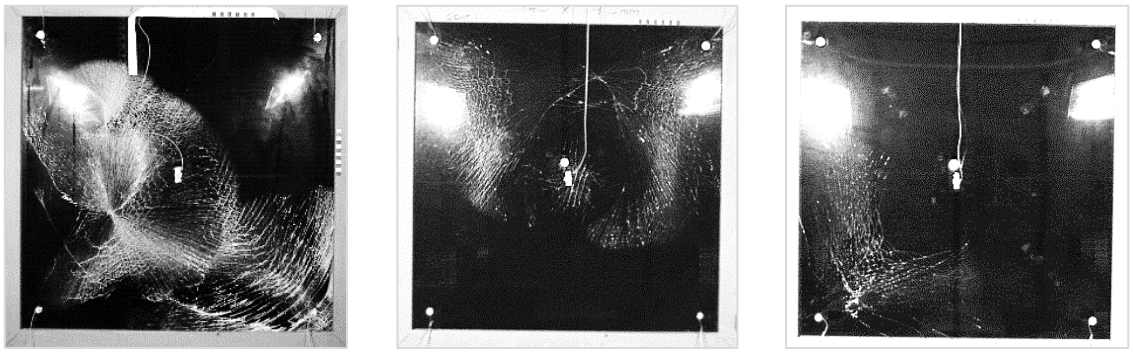

(a) P_r: 27kPa. (b) P_r: 20kPa. (c) P_r: 12kPa.

Figure 5.6: Crack patterns: effect of P_r.

5.3 Aspect Ratio

Four aspect ratios from 1:1 to 1:2 were investigated in blast environment P_r 27kPa, three were used in trials with P_r 20kPa and 12kPa. Aspect ratio 1:1.7 was not used in these trials. Elastic and rigid support conditions were used in trials with blast environment P_r 20kPa and 12kPa, only rigid supports were implemented in P_r 27kPa trials. Mean break parameters and corresponding standard deviations for each arrangement are outlined in Table 5.7. Mean values were normalised against the 1:1 value using equation 5.2 to determine the effect of aspect ratio.

$$Normalised\ break\ parameter = \frac{\bar{x}_{AR}}{\bar{x}_{AR\ 1:1}} \quad 5.2$$

Table 5.7: Summary: break parameters as a function of aspect ratio.

Supports	Design P_r (kPa)	Aspect Ratio	Failure Displacement (mm)			Break Time (ms)			Failure Impulse (kPa.ms)		
			$\bar{x}$	σ	Norm	$\bar{x}$	σ	Norm	$\bar{x}$	σ	Norm
Rigid	27	1	22	9	1.00	4.56	0.62	1.00	145	19	1.00
Rigid	27	1.3	25	3	1.15	4.76	0.19	1.04	153	6	1.06
Rigid	27	1.7	14	6	0.61	3.93	0.39	0.86	128	11	0.88
Rigid	27	2	16	4	0.73	4.04	0.40	0.89	132	13	0.91
Rigid	20	1	7	0	1.00	3.89	0.35	1.00	90	9	1.00
Rigid	20	1.3	21	8	2.96	5.41	1.08	1.39	118	22	1.31
Rigid	20	2	15	4	2.06	4.36	0.34	1.12	96	6	1.07
Rigid	12	1	7	4	1.00	4.31	0.79	1.00	57	10	1.00
Rigid	12	1.3	23	-	3.15	7.97	-	1.85	95	-	1.67
Rigid	12	2	14	11	1.90	5.01	1.86	1.16	64	22	1.11
Elastic	20	1	23	1	1.00	5.26	0.45	1.00	116	9	1.00
Elastic	20	1.3	23	4	1.01	5.15	0.38	0.98	115	7	0.99
Elastic	20	2	13	5	0.59	4.25	0.73	0.81	92	16	0.79
Elastic	12	1	13	-	1.00	5.29	-	1.00	67	-	1.00
Elastic	12	1.3	17	1	1.31	6.28	0.55	1.19	81	5	1.21
Elastic	12	2	16	-	1.24	5.89	-	1.11	78	-	1.16

Norm - Break parameter normalised against result for 1:1.

Individual displacement results and the arrangement displacement mean are plotted in Figure 5.7. The same key is used in all subsequent plots of break parameters against aspect ratio. For all arrangements aspect ratio 1:1.3 recorded the largest displacement. For [27kPa, rigid] displacement for aspect ratios 1:1 and 1:1.3 was much higher than 1:1.7 and 1:2. Different behaviour was observed in glass subjected to P_r 20kPa and 12kPa. In [20kPa, rigid] and [12kPa, rigid] displacement for aspect ratio 1:1.3 was much higher than 1:1 and 1:2. Aspect ratio 1:2 deflected 5.5mm more than 1:1 for [20kPa, rigid] and 7mm for [12kPa, rigid] indicating aspect ratio had a larger effect on displacement at lower overpressures. Aspect ratio had less of an effect on displacement of elastically supported windows. For [20kPa, elastic] no significant change was observed between mean displacements from aspect ratio 1:1 to 1:1.3. Displacement decreased by 10mm between 1:1.3 and 1:2. No significant effect was recorded for [12kPa, elastic]. Displacement increased by 3mm from 1:1 to 1:1.3 but no change was recorded between 1:1.3 and 1:2. Aspect ratio has less effect on displacement at lower overpressures for elastic framing than for rigid framing. Spread for each arrangement was large, the largest standard deviation was 11mm for [27kPa, 1:2, rigid]. For some arrangements, especially at P_r 27kPa, the spread was larger than the observed trend. More data are required to determine if observed trends were due to aspect ratio or spread of results.

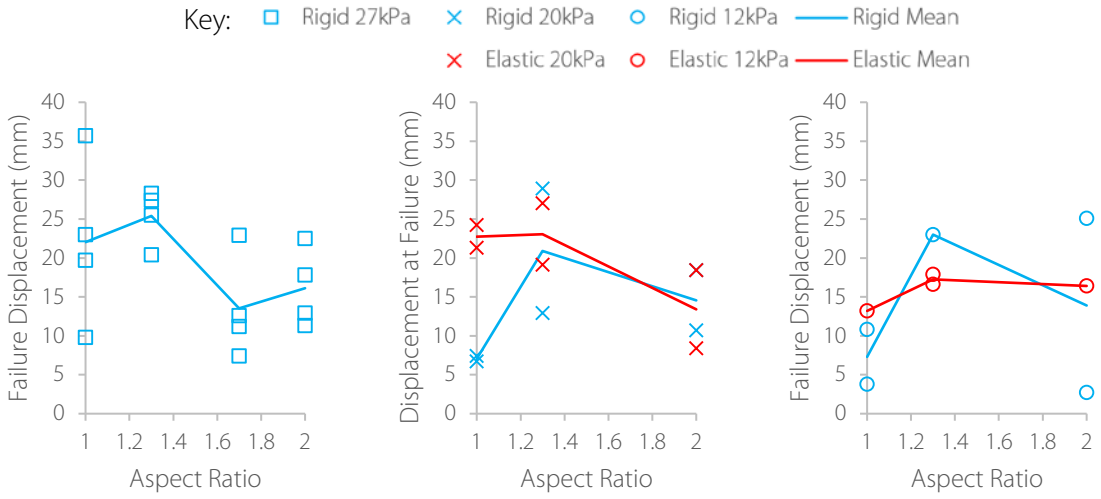

(a) P_r 27kPa. (b) P_r 20kPa. (c) P_r 12kPa.

Figure 5.7: Experimental data points and mean displacement versus aspect ratio.

Normalised failure displacements against the 1:1 result allowed aspect ratio trends to be quantified (see Figure 5.8). Arrangement [27kPa, rigid] recorded a 15% increase in displacement from 1:1 to 1:1.3 but reduced displacements for aspect ratios 1:1.7 and 1:2 (39% and 27% decreases from 1:1 result respectively). These normalised displacements for rigid framing were small compared to those from other blast environments. In comparison normalised displacements for [20kPa, 1:1.3, rigid] and [12kPa, 1:1.3, rigid] were 2.96 and 3.15 respectively. Normalised displacement for [1:1.3, rigid] arrangements increased as P_r decreased. For [20kPa, rigid] and [12kPa, rigid] normalised displacement for 1:2 was approximately 2.00 (2.06 for P_r 20kPa, 1.90 for P_r 12kPa). Normalised displacement was much lower for elastically supported windows. For [20kPa, elastic] normalised displacement was 1.01 for 1:1.3 windows and 0.59 for 1:2. For [12kPa, elastic] normalised displacements for 1:1.3 and 1:2 were 1.31 and 1.24 respectively.

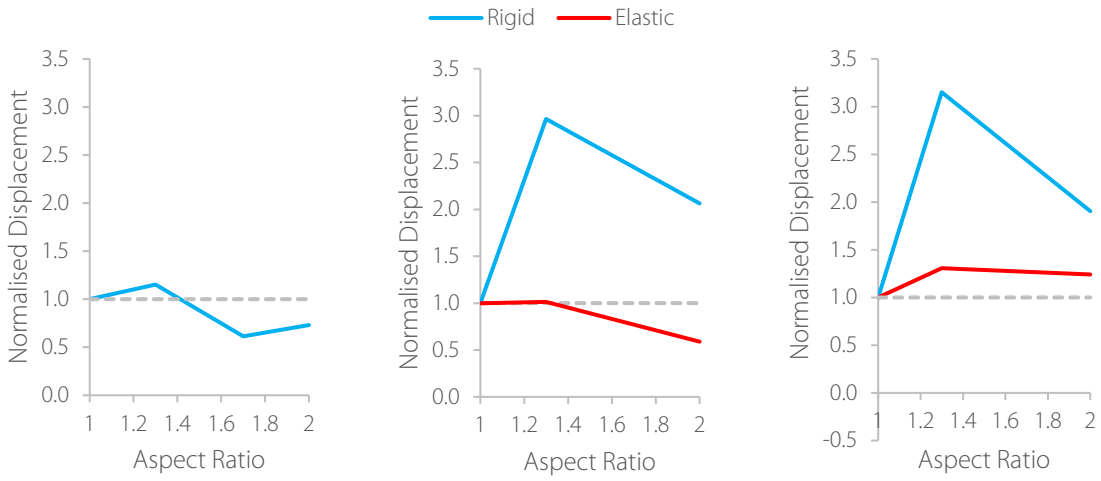

(a) Pr 27kPa. (b) Pr 20kPa. (c) Pr 12kPa.

Figure 5.8: Normalised displacement versus aspect ratio.

Individual and mean break times are plotted against aspect ratio in Figure 5.9. A similar trend to displacement was observed however the results range was smaller. The maximum mean break time

for [27kPa, rigid] was 4.76ms (aspect ratio 1:1.3) and the lowest 3.93ms (aspect ratio 1:1.7), a difference of 0.83ms. In general break time increased with P_r decrease. For all arrangements except [20kPa, elastic] the highest break time was recorded for aspect ratio 1:1.3. For rigid framing results for aspect ratios 1:1 and 1:2 were similar. Difference between minimum and maximum mean break time increased as P_r decreased indicating aspect ratio had greater impact on break time at lower overpressures.

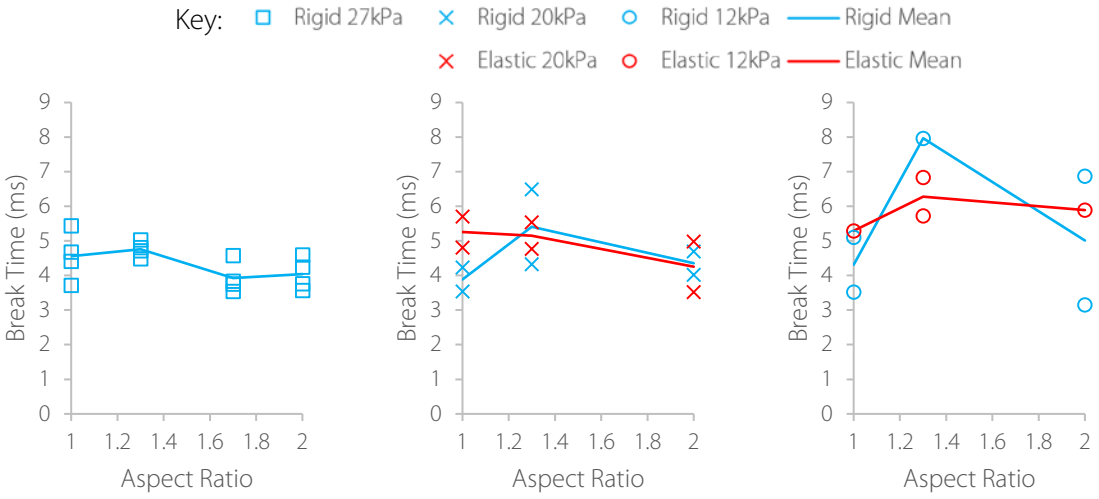

(a) P_r 27kPa. (b) P_r 20kPa. (c) P_r 12kPa.

Figure 5.9: Experimental data points and mean break time versus aspect ratio.

Normalised break times were much smaller than normalised displacements (Figure 5.10). The largest normalised break time was 1.85 compared to 3.15 for displacement. Both results were for arrangement [12kPa, 1:1.3, rigid]. Response was small for [27kPa, rigid], normalised break times were 1.06 for aspect ratio 1:1.3 and 0.86 and 0.89 for 1:1.7 and 1:2 respectively. This trend matched that for normalised displacement but was insignificant compared to the high standard deviation for this arrangement. Response for [1:1.3, rigid] increased with P_r decrease (1.39 for P_r 20kPa and 1.85 for P_r 12kPa). Normalised break time for [1:2, rigid] increased from 1.12 to 1.16 as P_r decreased from 20kPa to 12kPa. The magnitude of normalised break times for elastically supported windows was much lower than equivalent rigid results. Change in normalised break time for 1:1.3 from arrangement [20kPa, elastic] was not significant (0.98). A normalised break time of 0.81 was recorded for aspect ratio 1:2. For [12kPa, elastic] 1:1.3 exhibited a normalised break time of 1.19, and 1.11 for aspect ratio 1:2.

The failure impulse trend was similar to those for displacement and break time (Figure 5.11). A decrease in impulse as P_r decreased was observed. In general the largest failure impulse was recorded for aspect ratio 1:1.3. Results for aspect ratios 1:1 and 1:2 were similar for lower peak overpressures (P_r 20kPa and 12kPa). For [27kPa, rigid] failure impulse was 21kPa.ms higher for aspect ratio 1:1 than 1:2. For rigidly framed windows the response to aspect ratio 1:1.3 increased as P_r decreased. Mean values were similar for aspect ratios 1:1.3 and 1:2 for [20kPa, rigid] and [20kPa, elastic] but for [20kPa, elastic] impulse was 17kPa.ms higher for the 1:1 window.

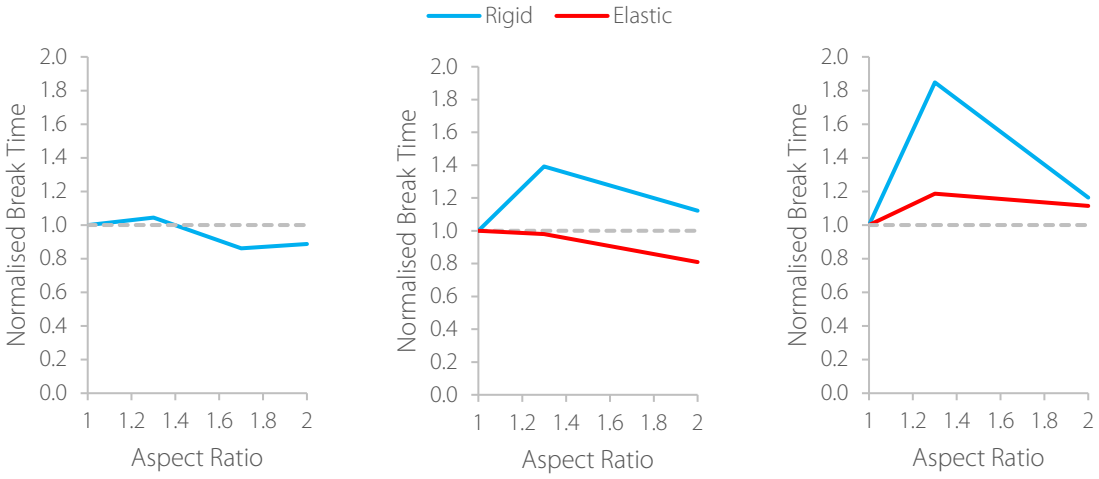

(a) P_r 27kPa. (b) P_r 20kPa. (c) P_r 12kPa.

Figure 5.10: Normalised break times in terms of aspect ratio.

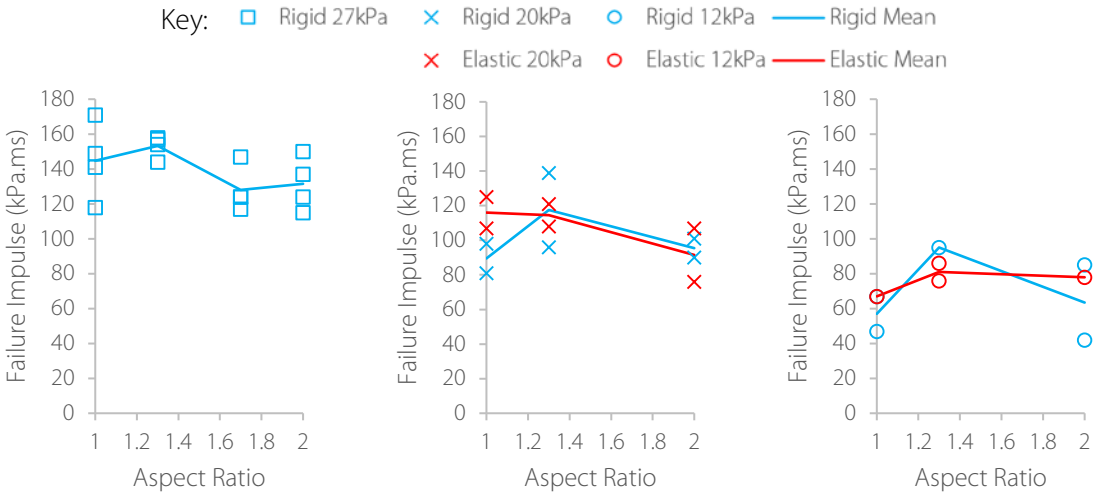

(a) P_r 27kPa. (b) P_r 20kPa. (c) P_r 12kPa.

Figure 5.11: Experimental data points and mean failure impulse versus aspect ratio.

Normalised failure impulses were lower than normalised break times and displacements (Figure 5.12). The maximum normalised impulse was 1.67 for [12kPa, 1:1.3, rigid] compared to 3.15 for displacement indicating aspect ratio was less significant with respect to failure impulse. Normalised impulse trends followed those for normalised displacement and break time. For all rigid arrangements maximum normalised impulse was recorded for aspect ratio 1:1.3 and increased as P_r decreased (1.06 at P_r 27kPa to 1.67 for P_r 12kPa). For arrangement [27kPa, rigid] aspect ratio 1:1.3 recorded the largest positive normalised impulse (1.06) with aspect ratio 1:2 measuring the largest negative normalised result (0.88). The largest normalised result for [27kPa, rigid] was 1.12 suggesting the trend was insignificant compared to standard deviations for this arrangement. For arrangements [20kPa, rigid] and [12kPa, rigid] the normalised impulse for aspect ratio 1:2 was less than for aspect ratio 1:1.3 (1.07 and 1.11 respectively). This matched the normalised displacement trend. [20kPa, elastic] exhibited normalised

impulses of 0.99 and 0.79 for aspect ratios 1:1.3 and 1:2 respectively. For [12kPa, elastic] normalised impulse was 1.21 for 1:1.3 but no significant change occurred between 1:1.3 and 1:2.

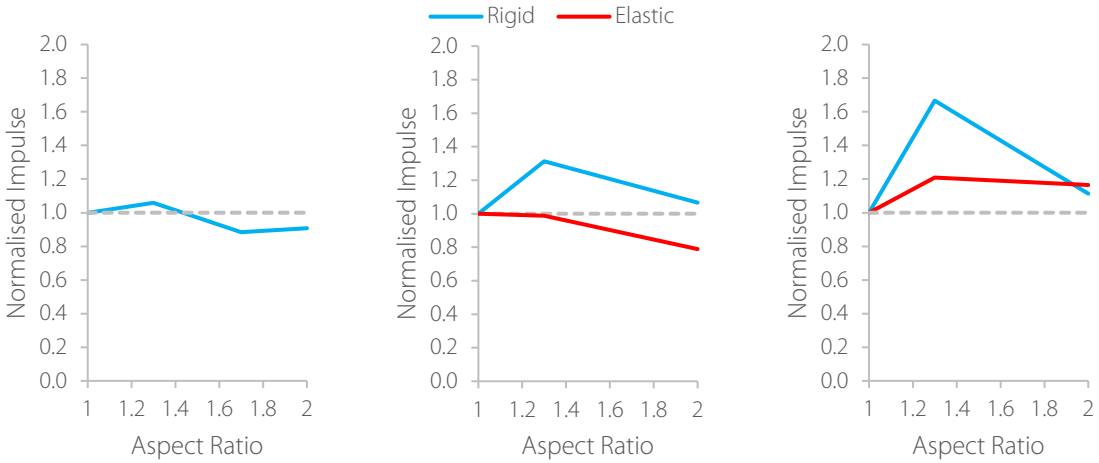

(a) P_r 27kPa. (b) P_r 20kPa. (c) P_r 12kPa.

Figure 5.12: Normalised impulse in terms of aspect ratio.

Cracking origins from all trials are shown in Figure 5.13. A high number of samples cracked along the centreline for higher aspect ratios. The highest proportion (73%) of samples to break within the frame was recorded for aspect ratio 1:1.3. This could be attributed to later break times and larger displacements allowing stress to build up where it was supported. For aspect ratio 1:1.3 all elastically supported glass broke within the frame and all but one for 1:2. In contrast all samples broke within the glass centre for aspect ratio 1:1. Proportion of rigid samples failing within the frame decreased with aspect ratio increase which could be attributed to a decrease in edge stresses. The absence of one strip of foam tape for rigid framing in Phase D2 could have caused local stresses to build up at the frame edge resulting in a higher proportion of these samples failing within the frame.

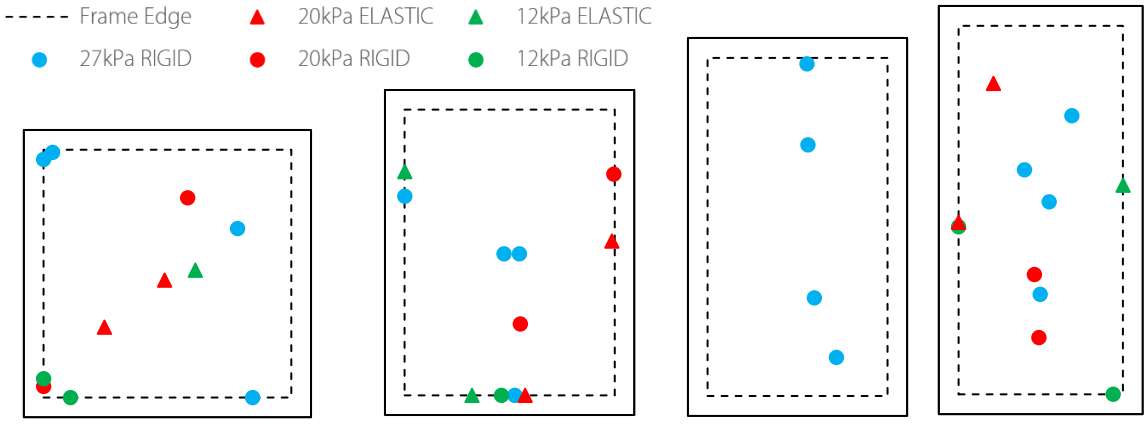

(a) Aspect ratio 1:1. (b) Aspect ratio 1:1.3. (c) Aspect ratio 1:1.7. (d) Aspect ratio 1:2.

Figure 5.13: Crack origins as a function of aspect ratio.

5.4 Support Conditions

Rigid and elastic framing conditions were implemented for 20kPa P_r and 12kPa P_r blast environments in Phase D2. Only rigid supports were implemented in Phase D1 trials so results were disregarded for

this section. All results are plotted against support conditions in Figure 5.14. Two out of six (33%) elastically supported windows survived when subjected to P_r 12kPa. Only one rigidly supported sample (17%) survived in the same blast environment. All samples failed when subjected to P_r 20kPa. A small increase in failure displacement was observed for elastically supported glass compared to rigid framing. Spread of results was smaller for elastic supports. For both support conditions spread was high, 3mm to 29mm for rigid supports and 8mm to 27mm for elastic supports. Spread of break times and impulses for elastic frames was smaller than rigid supports, indicating rigid framing introduced more inconsistency into results. This could be attributed to irregular stress concentrations in the glass caused by an uneven surface of the frame despite ensuring a smooth finish and applying foam tape to protect the glass. There was no significant difference between elastic and rigid mean results for break parameters indicating support conditions had little effect on the mean probability of glass failure.

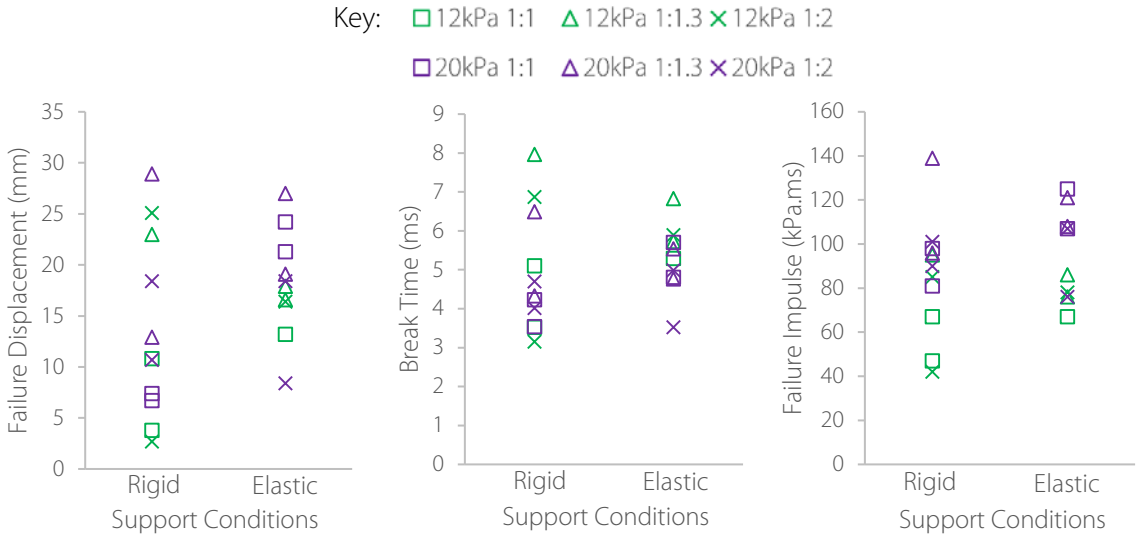

Figure 5.14: Break parameters versus support conditions.

Mean rigid and elastic results from each arrangement are compared Table 5.8. Mean break parameters for both framing options were normalised against rigid results and plotted in Figure 5.15. The largest normalised response was for displacement. The largest normalised displacement was 3.23 for [20kPa, 1:1]. Arrangement [12kPa, 1:1] also recorded a large normalised displacement of 1.81. Results from all other results were significantly smaller. Higher elastic displacements were recorded for arrangements [12kPa, 1:2] and [20kPa, 1:1.3] compared to equivalent rigid arrangements but normalised results were small, 1.18 and 1.10 respectively. Displacements recorded for elastic frames were lower than equivalent rigid support conditions for arrangements [12kPa, 1:1.3] and [20kPa, 1:2]. Normalised displacements for these arrangements were 0.75 and 0.92 respectively. Normalised responses for break time and impulse were much lower than displacement and exhibited the same trend. Arrangements [20kPa, 1:1], [12kPa, 1:1] and [12kPa, 1:2] recorded increased normalised break times and impulses for elastic framing. The largest was for [20kPa, 1:1], normalised break time was 1.35 and normalised impulse was 1.30. The smallest normalised break time and impulse was recorded for arrangement [12kPa, 1:1.3]. Normalised break time was 0.79 and normalised impulse was 0.85 for

elastic support conditions. Results from remaining arrangements ranged between 0.95 and 1.00, recording no significant change in break time or impulse between the two support conditions.

Table 5.8: Comparison of break parameters from rigid and elastic support conditions.

P_r (kPa)	Aspect Ratio	Supports	Failure Displacement (mm)			Break Time (ms)			Failure Impulse (kPa.ms)		
			$\bar{x}$	σ	Norm	$\bar{x}$	σ	Norm	$\bar{x}$	σ	Norm
12	1	Rigid	7	4	1.00	4.31	0.79	1.00	57	10	1.00
		Elastic	13	0	1.81	5.29	0.00	1.23	67	0	1.18
12	1.3	Rigid	23	0	1.00	7.97	0.00	1.00	95	0	1.00
		Elastic	17	1	0.75	6.28	0.55	0.79	81	5	0.85
12	2	Rigid	14	11	1.00	5.01	1.86	1.00	64	22	1.00
		Elastic	16	0	1.18	5.89	0.00	1.18	78	0	1.23
20	1	Rigid	7	0	1.00	3.89	0.35	1.00	90	9	1.00
		Elastic	23	1	3.23	5.26	0.45	1.35	116	9	1.30
20	1.3	Rigid	21	8	1.00	5.41	1.08	1.00	118	22	1.00
		Elastic	23	4	1.10	5.15	0.38	0.95	115	7	0.97
20	2	Rigid	15	4	1.00	4.36	0.34	1.00	96	6	1.00
		Elastic	13	5	0.92	4.25	0.73	0.98	92	16	0.96

Norm - Results normalised against rigid framing.

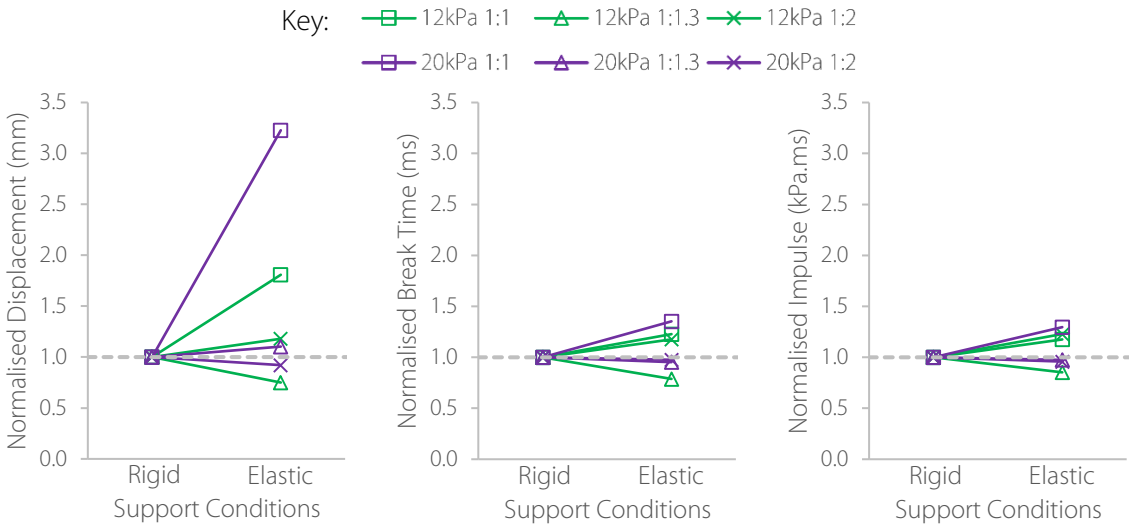

(a) Failure displacement. (b) Break time. (c) Failure impulse.

Figure 5.15: Break parameters for elastic supports normalised against rigid supports.

Crack patterns from rigid and elastic supports are shown in Figure 5.16. Images are of arrangement [20kPa, 1:1]. Crack locations were random and little difference was observed between rigid and elastic support conditions. Cracking was marginally denser for elastic supports due to an increased break time for elastic supports for this arrangement. A longer break time increased the amount of energy absorbed by the glass prior to failure. This was converted into denser cracking after the initial failure occurred.

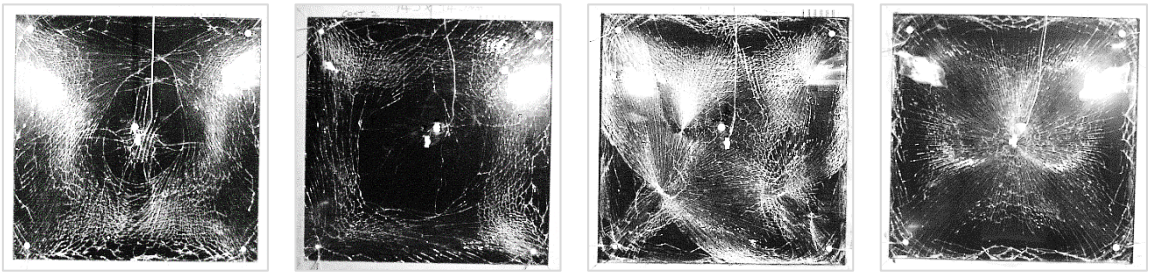

(a) Rigid 1. (b) Rigid 2. (c) Elastic 1. (d) Elastic 2.

Figure 5.16: Crack patterns: effect of supports.

5.5 Structural Parameter Significance

The significance of each structural parameter was determined from the magnitude of the range produced. Range was defined as the difference between maximum and minimum mean values for an arrangement (see Figure 5.17 for an example). In this example the effect of aspect ratio on failure displacement was quantified for arrangement [27kPa, rigid]. The largest mean value was 25mm and the smallest 14mm, producing a range of 11mm. Each displacement range for aspect ratio was plotted in Figure 5.19b. The largest value was highlighted in red. The process was repeated for support conditions and P_r. Mean values reduced the spread of results due to material variability. The significance of this intrinsic variability was determined by finding the range (e.g. displacement range) between repeats of the same arrangement, shown in red in Figure 5.17. This displacement range due to material variability was plotted for all arrangements with the maximum value coloured red (Figure 5.18). The process was repeated for each break parameter to determine the effect of P_r, aspect ratio and support conditions on glazing failure (Figure 5.18 to Figure 5.23). Maximum (red values) and mean for each structural parameter were compared in part (d) of the figure. This novel approach enabled the most significant structural parameter to be determined.

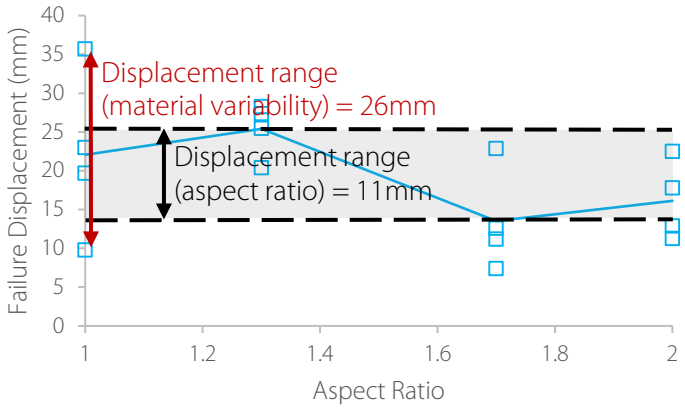

Figure 5.17: Displacement range and material variability for arrangement [27kPa, rigid].

Four repeats were completed for all arrangements subjected to P_r 27kPa but only two repeats for other blast environments. One window remained unbroken from arrangements [12kPa, 1:1, elastic], [12kPa, 1:1.3, rigid] and [12kPa, 1:2, elastic] causing material variation ranges to be zero. The largest displacement spread due to material variation was 26mm for [27kPa, 1:1, rigid]. Despite only two repeats, [12kPa, 1:2, rigid] exhibited a high displacement range (22mm) due to material variation.

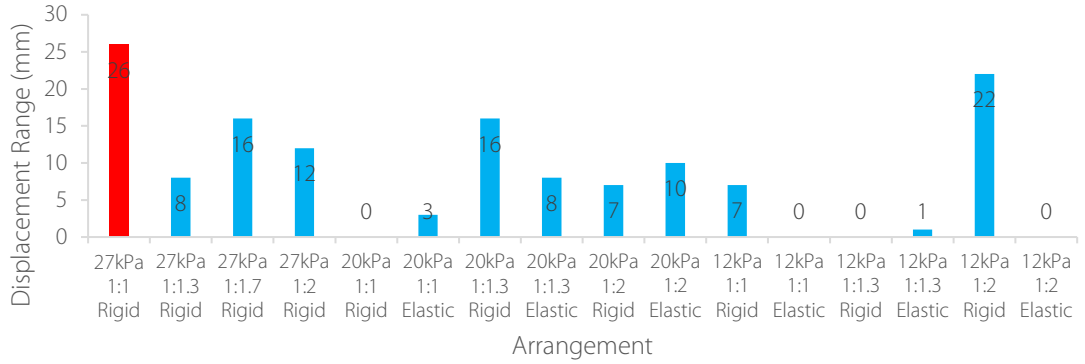

Figure 5.18: Displacement range due to material variability (red: maximum).

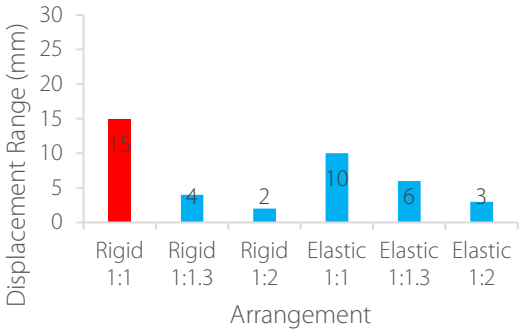

(a) P_r.

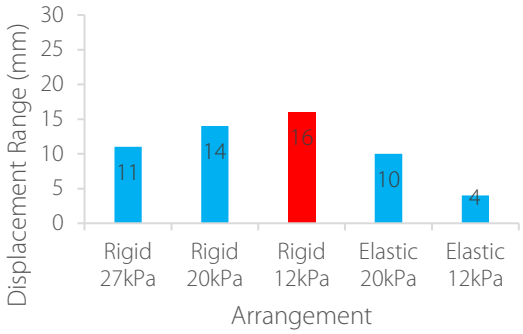

(b) Aspect ratio.

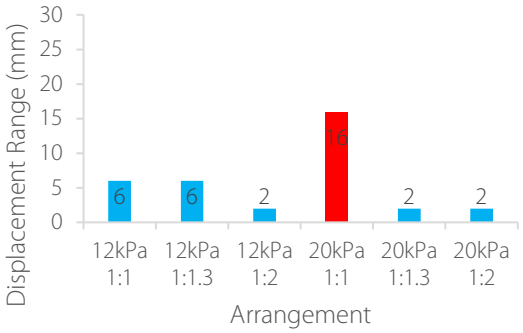

(c) Support conditions.

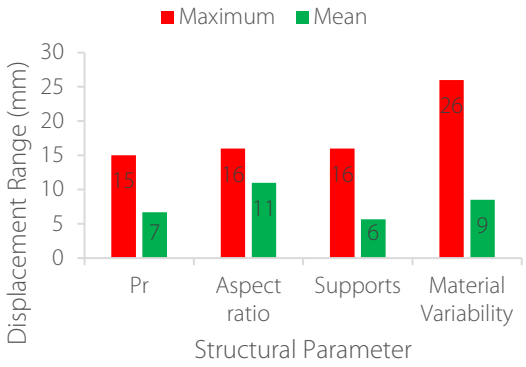

(d) Maximum and mean.

Figure 5.19: Displacement ranges due to structural parameters (red: maximum).

For rigid support conditions all blast environments were considered, elastic framing was only tested in blast environments P_r 20kPa and 12kPa (Figure 5.19a). The largest displacement range was 15mm for [1:1, rigid]. Displacement range for elastic supports was smaller than rigid which could be attributed to elastic supports not being tested at P_r 27kPa. Displacement range decreased as aspect ratio increased for both support conditions, implying P_r has less of an impact on displacement at higher aspect ratios. The largest displacement range for aspect ratio was 16mm for [12kPa, rigid]. Rigidly supported glass exhibited larger displacement ranges than equivalent elastic arrangements indicating aspect ratio had a larger effect on rigid framing. Aspect ratio displacement range increased as P_r decreased indicating higher sensitivity to aspect ratio at lower overpressures for rigid supports. Elastic framing recorded the opposite effect; displacement range decreased as P_r decreased. Displacement range for support conditions was significantly lower than aspect ratio or P_r. Maximum

displacement range was 16mm for [20kPa, 1:1]. Displacement ranges due to support conditions were 6mm for both [12kPa, 1:1] and [12kPa, 1:1.3] arrangements but lower for [12kPa, 1:2] (2mm). Despite a displacement range of 16mm recorded for [20kPa, 1:1] arrangements [20kPa, 1:1.3] and [20kPa, 1:2] logged displacement ranges of only 2mm, indicating support conditions had little effect. Maximum and mean displacement ranges for each parameter were plotted in Figure 5.19d. Little difference between maximum displacement ranges was observed. Material variation exhibited a higher maximum range (26mm). Considering mean values, aspect ratio had the largest influence on displacement (11mm), compared to material variability (9mm), P_r (7mm) and support conditions (6mm). Over the arrangements tested aspect ratio was the most significant parameter when considering glazing displacement at failure. Effect of material variation was also significant.

Break time range for material variation was less than 2ms for all but two arrangements (Figure 5.20). The largest break time range was 3.72ms for [12kPa, 1:2, rigid]. Arrangement [20kPa, 1:1.3, rigid] also recorded a break time range larger than 2ms (2.16ms). Break time ranges due to P_r, aspect ratio and support conditions are compared in Figure 5.21. The largest range due to P_r was 3.21ms for [1:1.3, rigid]. Break time ranges for elastic supports increased with aspect ratio, the opposite of displacement ranges. This indicated P_r was more significant to break time at higher aspect ratios for elastic support conditions. A similar trend for rigid support conditions did not exist. The largest break time range due aspect ratio was 3.66ms for [12kPa, rigid]. Range increased for rigid samples as P_r decreased indicating break time sensitivity to aspect ratio increased with decreasing P_r. No change was observed for elastic samples subjected to different P_r values indicating aspect ratio effect on elastic samples was independent of P_r. Support conditions exhibited lower break time ranges than other parameters. The maximum range was 1.69ms for [12kPa, 1:1.3]. Similar break time ranges were recorded for [12kPa, 1:1] and [12kPa, 1:2], 0.98ms and 0.88ms respectively. Break time range decreased as aspect ratio increased for P_r 20kPa indicating support conditions were less significant at higher aspect ratios. Comparing maximum and mean values in part (d), material variation recorded maximum range of 3.72ms. Aspect ratio exhibited a similar maximum break time range (3.66ms) and the highest mean range (1.60ms), making it the most significant parameter in terms of break time. P_r also had a large influence. Support conditions had the least effect on break time.

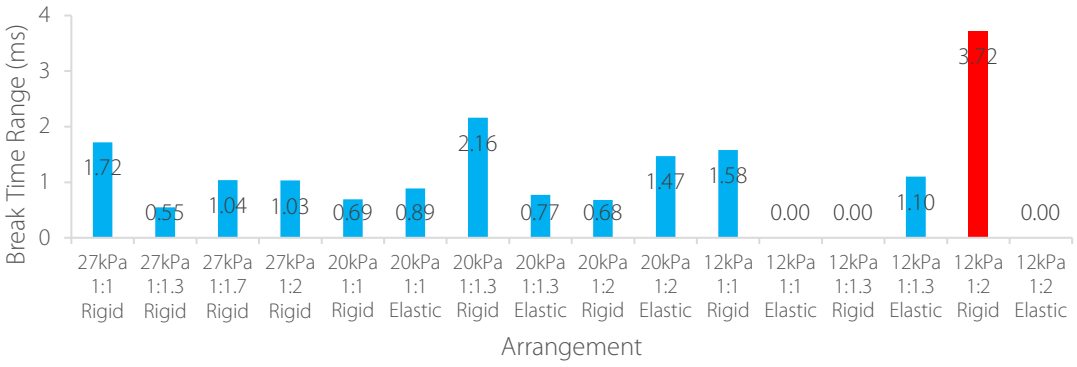

Figure 5.20: Break time range due to material variation (red: maximum).

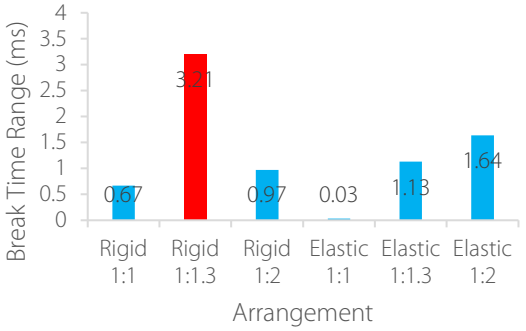

(a) P_r.

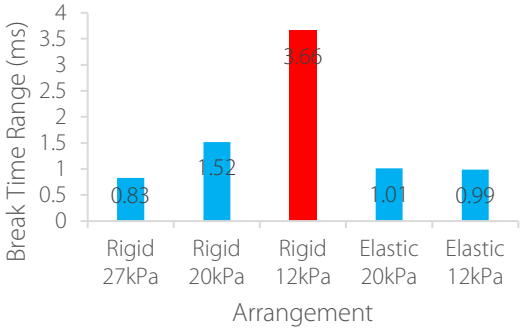

(b) Aspect ratio.

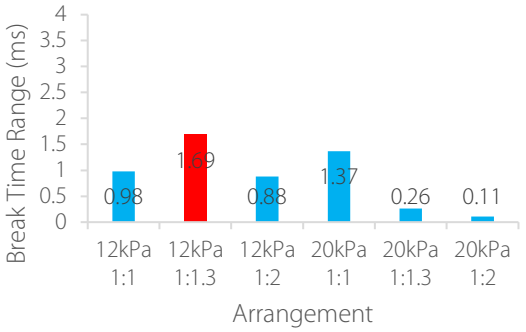

(c) Support conditions.

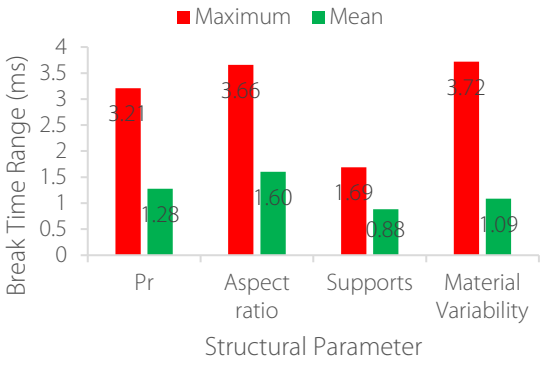

(d) Maximum and mean.

Figure 5.21: Break time ranges due to structural parameters (red: maximum).

The largest failure impulse range due to material variation was 53kPa.ms for [27kPa, 1:1, rigid] (Figure 5.22). Failure impulse ranges for each structural parameter were compared in Figure 5.23. The largest impulse range due to P_r was 88kPa.ms for [1:1, rigid]. All impulse ranges for rigid supports were larger than equivalent elastic samples. It should be noted that elastic supports were not used in trials with P_r 27kPa meaning P_r range was only 20kPa to 12kPa for these arrangements. Impulse range for elastic frames decreased as aspect ratio increased indicating P_r was less significant at higher aspect ratios for elastic support conditions. A similar trend was not observed for rigid supports. Failure impulse ranges due to aspect ratio were much smaller than those due to P_r. The largest range was 38kPa.ms for [12kPa, rigid]. For rigid framing, failure impulse range increased as P_r decreased. This indicated increased aspect ratio significance at lower P_r values. The opposite effect was recorded for elastic framing, impulse ranges decreased with P_r increase. Failure impulse ranges for support conditions were much smaller than other parameters (maximum 26kPa.ms for [20kPa, 1:1]). Support conditions had little effect on other aspect ratios in this blast environment (impulse ranges of 3kPa.ms and 4kPa.ms). Support condition influence on failure impulse was consistent for all aspect ratios subjected to P_r 12kPa (impulse ranges of 10kPa.ms, 14kPa.ms and 14kPa.ms). This indicated framing effect was independent of aspect ratio for P_r 12kPa. Looking at the data in part (d), P_r had the largest effect on failure impulse (maximum range 88kPa.ms and mean range 52kPa.ms). Material variability produced the second largest maximum range (53kPa.ms) but a smaller mean range (21kPa.ms). Support conditions were the least significant to failure impulse with a mean range of only 12kPa.ms.

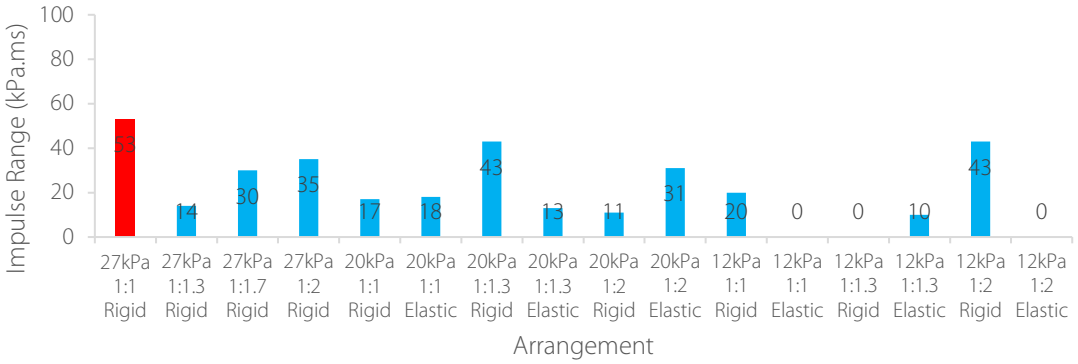

Figure 5.22: Range of failure impulse due to material variation (red: maximum).

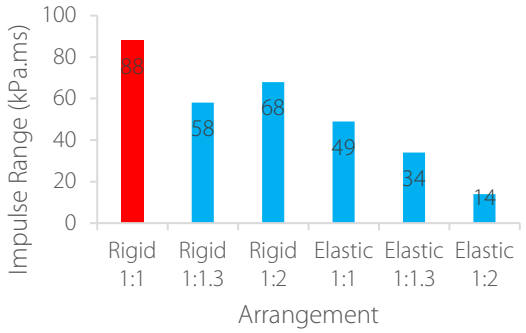

(a) P_r.

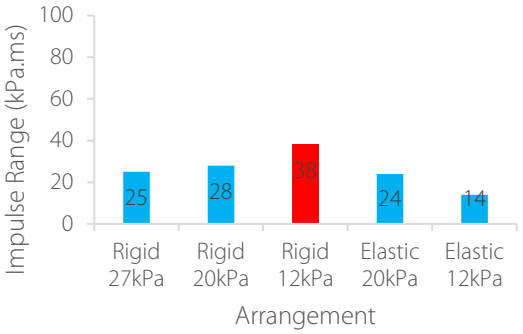

(b) Aspect ratio.

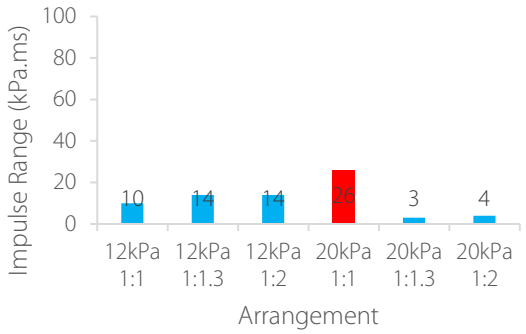

(c) Support conditions.

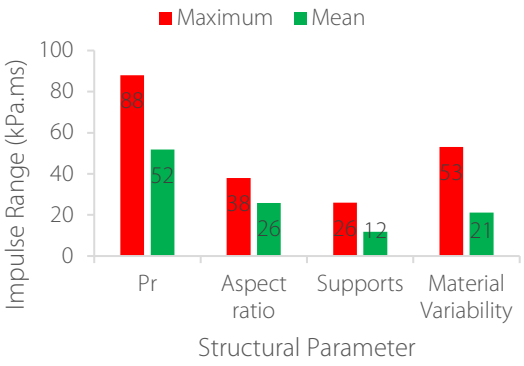

(d) Maximum ranges.

Figure 5.23: Failure impulse ranges due to structural parameters (red: maximum).

5.6 Material Variability – Static Testing

In Phase S2 20 samples were tested to failure using the modified testing rig to determine if edge finishing had an effect on failure. Half of the samples had cut edges which were left unfinished, on the other half all edges had been ground down to remove flaws caused by cutting. All samples failed except Sample 2 from the cut glass group. The seal on this test broke causing air to enter the testing container before sufficient pressure for glazing failure had developed. This sample was disregarded from results. Container pressure and central displacement were recorded at failure for each sample. Static failure pressures and displacements are summarised for reference in Table 5.9 and Table 5.10. No significant difference between results for polished and cut edge glass was observed. Failure pressure for all samples was 12.8±3.6kPa (standard deviation of 28%). Central displacement for all

samples was 8.2±1.3mm (standard deviation of 16%). The large failure pressure standard deviation, and to a lesser extent displacement, was due to variation in size and location of the Griffith Flaw between samples. Glass samples were small (600 x 600mm) so probability of a Griffith Flaw was small compared to a larger pane. Repeating tests with a larger window would reduce failure pressure standard deviation and mean due to the presence of a Griffith Flaw increasing. This research project aimed to find the worst case data spread so a small window pane was adequate. Location of failure origins for all samples are shown in Figure 5.24. Edge finish had no effect on crack locations. The high origin variation was due to the random nature of Griffith Flaws. All samples but two (one with each edge finish) broke near the glass centre. Two samples broke within the frame. Examples of crack patterns produced from two cut edge and two ground edge samples are shown in Figure 5.25. Glazing edge finishing did not have an effect on crack location or crack patterns.

Table 5.9: Summary: static failure pressures.

Finish	1	2	3	4	5	6	7	8	9	10	$\bar{x}$	σ
Cut	8.7	-	16.5	14.9	11.8	19.2	11.8	14.1	9.9	8.8	12.9	3.6
Ground	7.0	9.3	11.7	11.3	14.4	13.4	15.8	18.5	17.0	8.4	12.7	3.8
All											12.8	3.6

Table 5.10: Summary: static failure displacements.

Finish	1	2	3	4	5	6	7	8	9	10	$\bar{x}$	σ
Cut	6.8	-	9.6	9.3	8.1	10.5	8.0	8.8	6.9	6.8	8.3	1.3
Ground	6.4	6.9	8.3	7.9	9.2	8.5	9.2	-	10.1	6.6	8.1	1.3
All											8.2	1.3

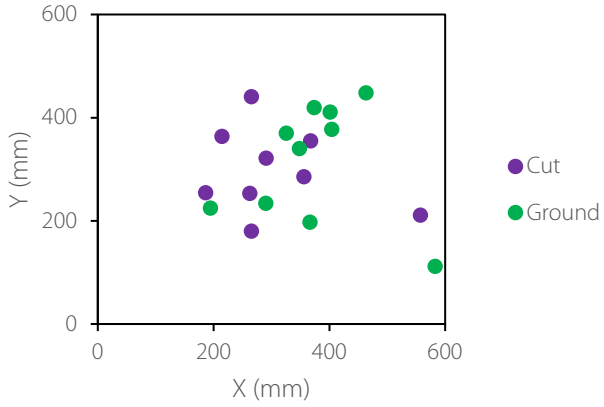

Figure 5.24: Fracture origins of all Phase S2 tests.

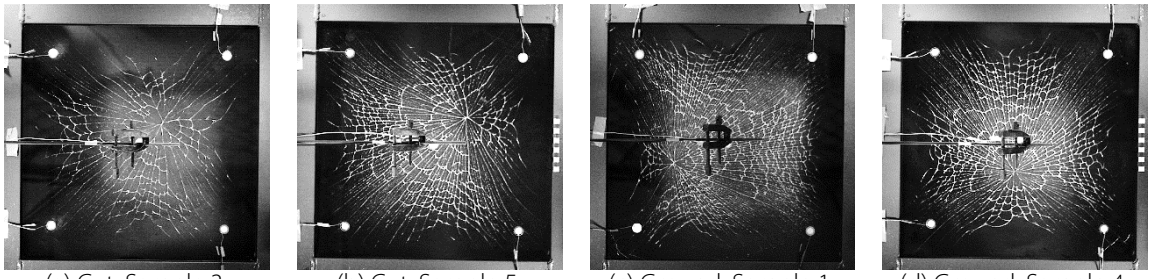

(a) Cut: Sample 3. (b) Cut: Sample 5. (c) Ground: Sample 1. (d) Ground: Sample 4.

Figure 5.25: Crack patterns: Phase S2.

A cumulative probability distribution (CPD) was produced from all failure pressures and a normal distribution was fitted (Figure 5.26). The normal distribution curve showed good agreement with experimental data points indicating failure pressure variation due to material strength can be assumed to be normally distributed. A dynamic increase factor (DIF) of 1.78 (British Standards Institution, 2012) was applied to the static load to produce a dynamic load failure distribution (blue CPD in Figure 5.27). The DIF was applied to each failure pressure individually. This meant the standard deviation was dependent on the mean and increased when the DIF was applied. The dynamic CPD was equivalent to P_r in the ABT and was converted to P_s using equation 2.7 (green CPD in Figure 5.27). The 600 x 600 x 4mm samples tested were comparable to previous ABT data (Appendix A). Out of 12 samples with area 0.25m^2 tested in the ABT, 2 survived P_s 12.2kPa (83%). This probability of failure corresponded to P_s 14.3kPa on the CPD produced. A higher P_s was expected due to smaller glass area but similar results indicated the DIF and static results were applicable. From the green CPD in Figure 5.27 a damage probability curve for material variability was produced (Figure 5.28), aim five of this thesis. For a window arrangement with area of 0.36m^2, aspect ratio 1:1 and rigid support conditions, P50 (P_s where 50% of windows are expected to break) was 10.8kPa and the damage sigma (one standard deviation) was 2.9kPa.

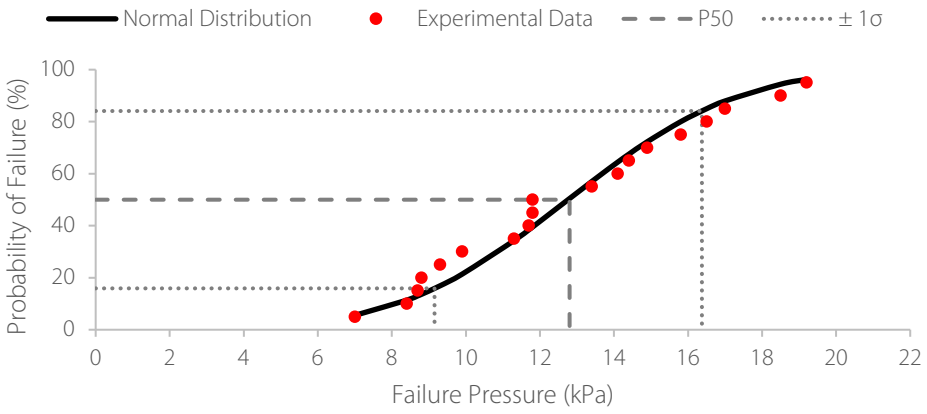

Figure 5.26: CPD of failure pressures from Phase S2.

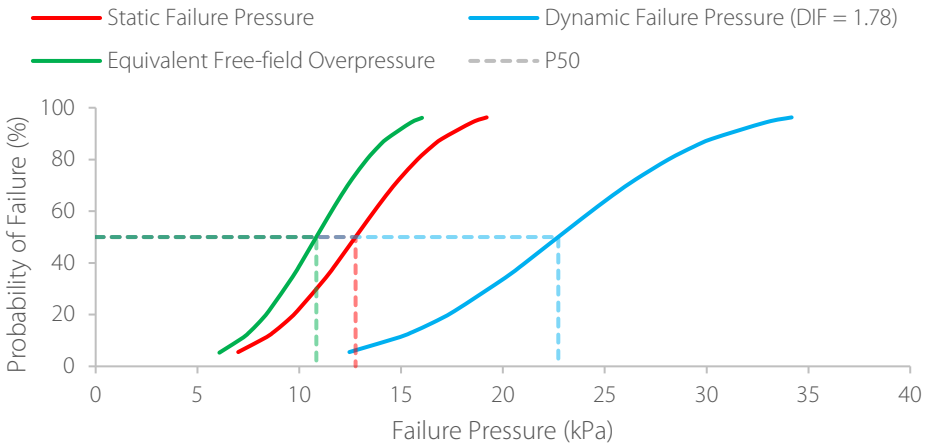

Figure 5.27: Conversion of static pressure CPD to equivalent blast pressures.

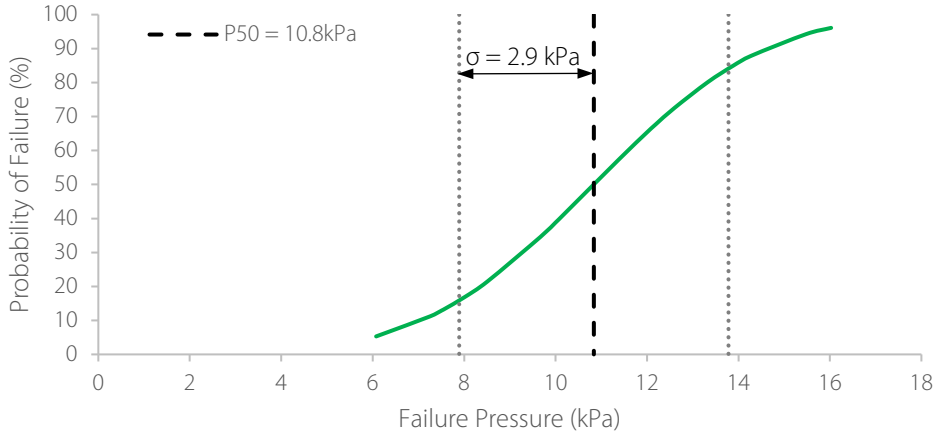

Figure 5.28: Damage probability curve with material variability sigma.

5.7 Discussion and Summary

In total, forty glass samples were subjected to three blast environments during dynamic testing. In blast environment P_r 12kPa, 3 out of 12 samples survived. Two were elastically supported, one had rigid framing. All samples had different aspect ratios and all were in different trials. This indicated P_r 12kPa was near the break/no break boundary for 4mm thick annealed glass with an area of 0.89m^2. Two surviving elastically framed samples compared to one rigid sample indicated support conditions had influenced glazing survival. Variation in material strength was the likely cause of some windows surviving and others failing. For instance in Phase D2, one sample failed and the other survived for three arrangements. All glass samples subjected to higher P_r blast environments failed. For the windows that broke, failure was quantified by central displacement at break, reflected failure impulse, break time and crack location. The effect of the blast environment, aspect ratio, support conditions and material variability are discussed and summarised in this section.

P_r was varied between 12kPa and 27kPa. Displacement at failure increased with P_r but spread of results was high indicating displacement was strongly dependent on other parameters. P_r had the largest influence on windows with aspect ratio 1:1, a large increase in failure displacement was observed for both framing conditions. Little change to failure displacement due to P_r was observed for other aspect ratios with either support condition. No significant trend was determined for these arrangements, change in displacement was attributed to material variation that was not fully removed from the mean due to the small number of repeats. The large response of windows with aspect ratio 1:1 can be attributed to the symmetrical 2-way spanning arrangement that resulted in a large span. This large span ensured the window was less stiff and more susceptible to increasing impulse rate due to P_r rising, causing a higher rate of displacement in turn. In general, break time decreased and spread of break times decreased as P_r increased. Decrease in break time spread was due to an increase in impulse rate as P_r increased. This meant a smaller increase in break time caused the same increase in failure impulse. The trends indicated impulse dependency in results. Normalised break times were considerably smaller than normalised displacements indicating a higher P_r influence on displacement than break time. No significant change in break time due to change in P_r was observed for aspect ratio 1:1 with either support condition. For aspect ratios 1:1.3 and 1:2 break time decreased with P_r for both

framing conditions. No change in displacement was observed for these arrangements as P_r increased indicating failure was governed by displacement. In contrast failure for aspect ratio 1:1 was governed by break time. Failure impulse increased with P_r for all arrangements but normalised values were smaller than observed for displacement. The largest increase was observed for aspect ratio 1:1. Spread of results was small compared to other break parameters indicating failure impulse was governed by P_r and structural parameters had less effect.

Three aspect ratios were considered for parameter analysis: 1:1, 1:1.3, 1:2. For all break parameters effect of aspect ratio was dependent on support conditions. Aspect ratio had greater influence on break parameters from rigid arrangements compared to elastic samples. Aspect ratio had little effect on displacement of rigidly supported glass subjected to P_r 27kPa. Displacement was highest for aspect ratio 1:1.3 and lowest for 1:1.7 and 1:2. Maximum displacement for all rigid framing was recorded for aspect ratio 1:1.3, for P_r 20kPa and 12kPa normalised displacement was approximately 3.00. Normalised displacement for aspect ratio 1:2 subjected to the same blast environments was approximately 2.00. A decrease in displacement with aspect ratio increase from 1:1.3 to 1:2 can be attributed to a decrease in the shortest glass dimension producing a stiffer one-way spanning arrangement. Aspect ratio 1:1 also exhibited a reduced displacement due to its stiffer two-way spanning set-up. Smaller normalised displacements recorded in the P_r 27kPa blast environment can be attributed to the higher blast pressure punching through the glass.

At lower overpressures the glass was able to deflect and broke due to displacement. This meant aspect ratio was able to affect glazing behaviour to a higher extent. Elastically supported windows exhibited much smaller normalised displacements, indicating aspect ratio as less influential. This can be attributed to reduced glass stresses due to elastic framing allowing some rotation making the effect of aspect ratio less severe than for a clamped rigid frame. The same trends were observed for break time and impulse indicating break parameters were closely linked. Aspect ratio 1:1.3 recorded the largest normalised break time and impulse for all rigid frames. This trend increased in magnitude as P_r decreased indicating aspect ratio was more significant at lower P_r values. At lower overpressures the glass took longer to deflect before failure meaning structural parameters such as aspect ratio acted over a longer time and became more significant to failure.

Comparing results from all arrangements, elastic frames generally induced higher displacements than rigid frames. Spread of results was large indicating influence of other parameters. Spread was larger for rigid framing which was attributed to local stresses induced by an uneven surface increasing variation between results. Structural sealant removed this effect in elastic framing. Normalised results for failure displacement were larger than other break parameters indicating support conditions influenced this most. Elastic framing induced the greatest increase in displacement in arrangements with aspect ratio 1:1. Response was greater for P_r 20kPa than 12kPa. Normalised displacement was low for other aspect ratios, normalised displacements were between 0.75 and 1.18 with an even number of results above and below 1.00 indicating support conditions had little influence. Break time and impulse followed the same trends identified for displacement. All normalised impulses lay

between 0.85 and 1.30. Windows with aspect ratio 1:1 recorded the largest normalised break time and impulse however this was small compared to normalised displacements.

Crack patterns and locations were highly varied between seemingly identical windows due to the random nature of the Griffith Flaw. Density of cracking was dependent on the amount of energy the glazing absorbed prior to failure, a larger failure impulse resulted in denser cracking. Failure impulse increased with P_r meaning cracking was denser for higher P_r blast environments. Framing conditions had little influence on crack patterns. Elastically framed windows with aspect ratio 1:1 exhibited denser cracking compared to equivalent rigid arrangements. This can be attributed to a longer break time causing a larger failure impulse. As aspect ratio increased a larger proportion of windows failed along the vertical centreline of the glass, indicating one-way spanning conditions with windows failing at the point of maximum stress. In comparison, glass failed in the central area at lower aspect ratios, in the area of maximum stress for two-way spanning. The highest number of failures within the frame occurred for aspect ratio 1:1.3, a longer break time could have allowed local stresses to build up due to irregularities in the frame. The proportion of rigidly supported windows failing within the frame decreased as aspect ratio increased which was attributed to edge stresses decreasing. In Phase D2, all rigid frames did not have a second line of foam tape which prevented frame irregularities causing local stresses building up in the glass. For all of these samples the glass struck the metal frame before failure (recorded by piezo transducers) which could have resulted in glass failure caused by frame contact rather than a Griffith Flaw.

Significance of each structural parameter was quantified by calculating break parameter ranges caused. Material variation caused the largest displacement range but maximum ranges from all structural parameters were similar. The highest mean result was for aspect ratio, showing this has a strong influence on displacement at fracture. The lowest mean displacement range was for support conditions indicating framing had the least effect on displacement at failure. Aspect ratio was the most significant parameter over the arrangements tested. A decrease in the P_r displacement range as aspect ratio increased was observed for elastic and rigid framing indicating P_r was less influential on displacement at high aspect ratios. Aspect ratio effect on displacement increased as P_r decreased for rigid frames but decreased with elastic support conditions. The maximum break time range was also caused by material variation, the aspect ratio result was also significant. Aspect ratio consistently produced high break time ranges across all arrangements, resulting in the highest mean range.

Support conditions produced the lowest mean range having the least effect on break time. For elastically supported glass the P_r induced break time range increased with aspect ratio, indicating P_r had a greater effect on break time for higher aspect ratios. A similar trend was not identified for rigid supports. Break time range due to aspect ratio for rigid frames increased as P_r decreased indicating that aspect ratio had a larger effect on break time at lower P_r values. P_r exhibited no significant effect on aspect ratio induced break time range for elastically framed windows indicating effect of aspect ratio was independent of P_r. failure impulse range due to P_r was substantially higher than any other parameter indicating failure impulse was governed by the blast environment. Maximum range

produced by material variability was second highest but was nearly half of that due to P_r. The mean range produced by aspect ratio was second to P_r but the impulse range was less than half of that produced by P_r. The smallest range was produced by support conditions, less than a quarter of P_r results indicating very little effect on failure impulse. Impulse ranges for support conditions were reasonably consistent across all arrangements indicating response was independent of aspect ratio and P_r. The aspect ratio induced impulse range increased slightly as P_r decreased for rigid framing, the opposite effect occurred for elastic frames. Impulse range due to P_r decreased as aspect ratio decreased when glazing was elastically supported.

From this analysis it was determined that break time and displacement were dependent on aspect ratio and material variability whereas impulse at failure was governed by the blast environment. Support conditions had little effect on failure behaviour. Trends within break parameter ranges indicated all parameters were interlinked and glazing behaviour was dependent on a complex combination of parameters.

Static testing of 20 glass samples enabled spread of failure pressures to be calculated. Edge finish had no significant effect on results. Mean failure pressure was 12.8kPa, standard deviation was 28% of the mean. Failure pressures fitted a normal distribution well. A CPD curve was produced and converted into equivalent ABT pressures. This damage curve partially fulfilled aim five of this thesis.

5.8 Defining the Blast Environment

Traditionally long-duration blast environments are defined by peak reflected overpressure. Long-duration blasts are located within the quasi-static region of pressure-impulse (PI) graphs meaning structural response is governed by P_r. Free-field and reflected PI graphs of data from this research project and previous ABT trials (Johns, 2016) are shown in Figure 5.29. Pressure and impulse increased linearly for this trial series, a function of the ABT driver. In comparison, the old ABT firing method produced a longer t_d, forming a larger impulse. The linear relationship between peak overpressure and impulse in the current trials meant determining the key blast parameter was difficult. Comparison of results from both trial series enabled the effect of peak overpressure and impulse on break parameters to be determined.

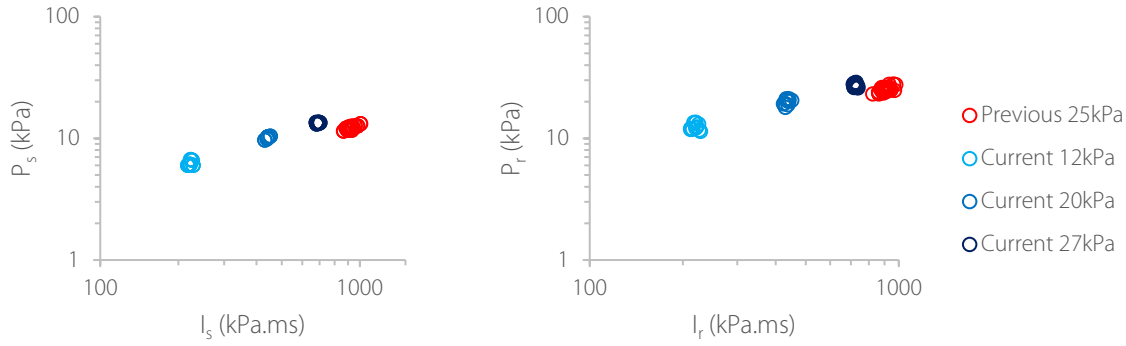

(a) Free-field. (b) Reflected.

Figure 5.29: PI graphs from this PhD and previous ABT trials.

Break parameters (failure displacement, break time and failure impulse) were plotted versus P_r in Figure 5.30. Blue data points indicated trials from this research project and red indicated previous trials. Many glazing arrangements were used in both trial series causing a large result spread. Previous trial data fitted the current trials trend of increasing displacement with P_r despite a lower spread. Previous break times were smaller than trends in the current data set. This can be attributed to a longer t_d in previous trials resulting in a reduced overpressure decrease rate. Previous failure impulse results fitted the trend from current trials very well when plotted against P_r. This indicated P_r quantified blast influence well when determining structural response.

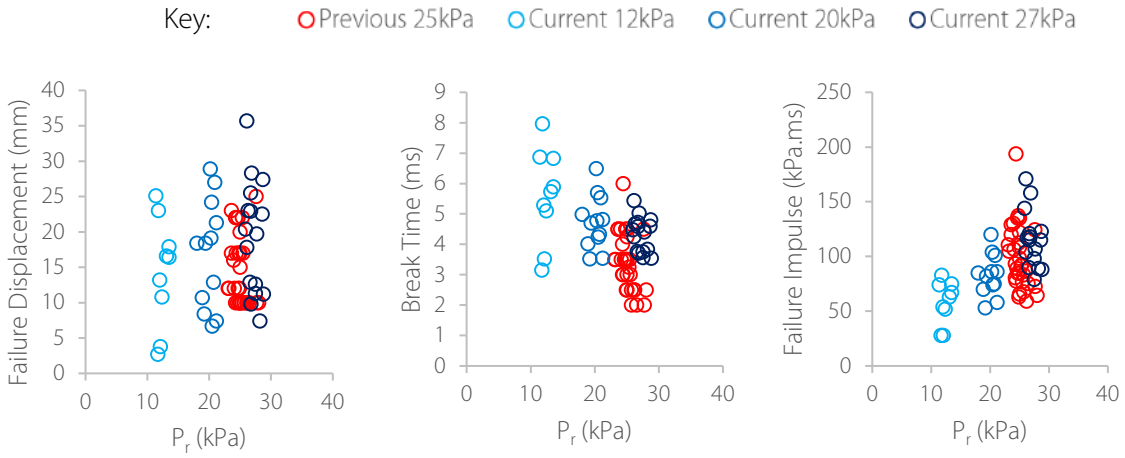

(a) Failure displacement. (b) Break time. (c) Failure impulse.

Figure 5.30: Break parameters versus P_r.

Each break parameter was plotted against total reflected impulse (I_r) in Figure 5.31. The previous data set (red) moved to the right of the current data set due to a larger impulse. This meant failure displacements and impulses measured from previous trials were below trends from the current trial series. Previous recorded break times were closer to the trend when plotted against I_r. Break time was a function of the variable blast environment so was the least advantageous break parameter for quantifying glazing response. Failure deflection and failure impulse demonstrated better agreement when plotted against P_r making it the best parameter for quantifying the blast environment.

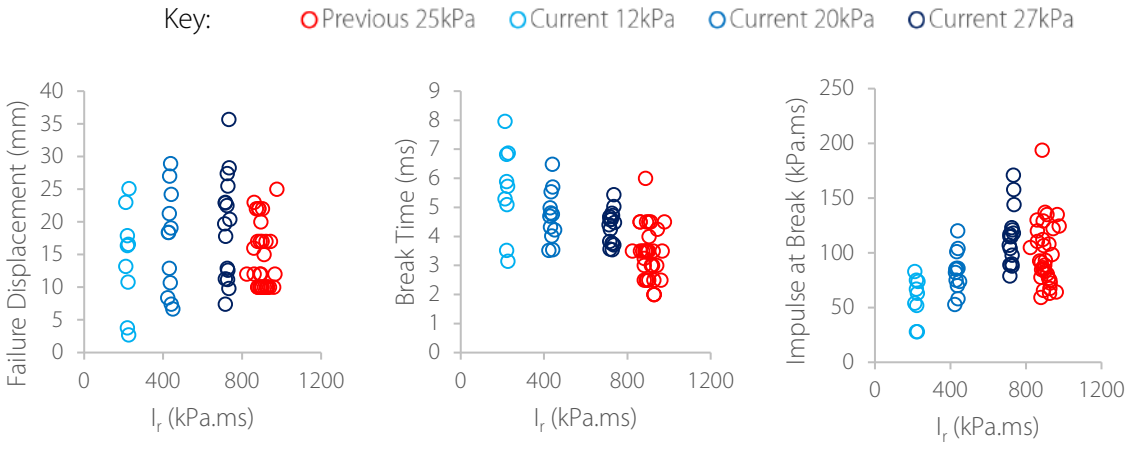

(a) Failure displacement. (b) Break time. (c) Failure impulse.

Figure 5.31: Break parameters versus I_r.

While P_r described the pressure the window was exposed to, it was dependent on location of the window within the structure, and how the blast wave interacts with the structure. For damage prediction when building characteristics are unknown, the use of P_s is preferable as damage can be quantified in a more general case. Therefore P_s was the blast parameter used in the production of damage curves in Chapter 6.

5.9 Conclusions

Over two dynamic trial phases 40 windows were subjected to three different long-duration blast environments. P_r varied from 12kPa to 27kPa. All glass was 4mm thick annealed with an area of 0.89m^2. Four aspect ratios between 1:1 and 1:2 were tested along with two framing options, rigid and elastic. Three glass samples out of 12 survived the P_r 12kPa blast environment but all glazing subjected to higher overpressures failed. No trend was observed between intact glazing and all windows were in separate trials indicating material variation caused the results range. It can be concluded that P_r 12kPa was near the survival/failure threshold for 4mm thick annealed glass with area 0.89m^2. Failure displacement increased with P_r but a large result spread indicated displacement was dependent on other structural parameters. The largest displacement increase was for aspect ratio 1:1, P_r had little effect on other arrangements. This can be attributed to a large span causing the arrangement to be more susceptible to change in P_r. Failure impulse increased with P_r increase, a low spread indicated failure impulse was governed by P_r.

Aspect ratio had little effect on arrangements with elastic framing. Effect on rigidly framed glazing increased as P_r decreased. Aspect ratio had little effect on windows subjected to P_r 27kPa indicating the high pressure 'punched' through the glass with little time for structural parameters to be significant. At lower overpressures failure displacement and break time decreased as aspect ratio increased above 1:1:3. This can be attributed to stiffer arrangements. The stiffer two-way spanning aspect ratio 1:1 recorded reduced break parameters compared to 1:1.3. Support conditions had minimal effect on window failure except for arrangements with aspect ratio 1:1. Again this can be attributed to the large span causing arrangement sensitivity to change in structural parameters.

Quantifying the significance of each structural parameter indicated aspect ratio had the largest effect on displacement and break time while failure impulse was most influenced by P_r. This indicated that increase in impulse rate with P_r was much greater than the effect of structural parameters. Support conditions exhibited little significance on arrangements tested. Structural parameter significance was dependent on interaction with other structural and blast parameters. Break time range due to aspect ratio increased as P_r decreased for rigid framing. P_r had little effect on the break time range due to aspect ratio for windows elastically framed. Break parameter trends indicated parameters were interlinked and glazing behaviour was dependent on a complex combination of all parameters.

Cracks radiated from the critical failure-inducing flaw, the location of which was random. Cracking density was governed by impulse received prior to failure. Larger impulses caused higher energy

release in the form of denser cracking. Static testing determined variation in material strength was responsible for a failure pressure standard deviation of 3.6kPa, 28% of the mean static failure pressure. A CPD curve was produced from 19 test samples and converted to equivalent P_s failure pressures. This damage curve partially fulfilled objective 5 of this thesis. Remaining curves were produced numerically and are discussed in Chapter 6.

Blast data from current trials were compared to previous ABT data with a longer t_d to determine whether impulse or P_r governed glazing response. Data from both trial series demonstrated better agreement with break parameter trends when plotted against P_r indicating this governed glazing response to a long-duration blast environment. P_s was the chosen parameter for damage curves as it is independent of structure interaction, providing a more general case. A damage curve for change in t_d determined if glazing response was impulse independent (see Chapter 6).

The key findings from experimental work were:

1. Triangulation of piezo transducers is a cost-effective and accurate method of recording glazing failure time and cracking location (discussed in Chapter 4).
2. For 4mm thick annealed glazing with area 0.89m^2, the survival/failure threshold is near P_r 12kPa.
3. Aspect ratio had the largest effect on failure time and displacement, failure impulse was governed by P_r.
4. Glazing response to blast loading is dependent on a complex interaction of structural parameters. Effects of structural parameters are not independent from one another.
5. Material strength variation was responsible for a failure strength standard deviation of 3.6kPa, 28% of the mean static failure pressure.

Chapter 6

Parametric Study and Damage Curves

6.1 Introduction

In this chapter two parametric studies are outlined. The schedule of computational and experimental work for this thesis is shown for reference in Figure 6.1. A new glazing material model, based on experimental data, is proposed in section 6.2. Two ELS-specific material parameters were investigated and pre-trial and post-trial material models were compared. Initial parametric study results validate the new glazing material model against experimental data to provide a benchmark. Results of this study, outlined in section 6.3, provided the basis of reliability limits determined in section 6.4. These reliability limits indicate boundaries of good performance and reliable results from ELS. The experimentally benchmarked AEM model was used to determine the effect of support conditions, aspect ratio and positive phase duration on glazing failure pressure. This parametric study, described in sections 6.5 and 6.6, fulfilled objectives two and three of this research project. Resulting data were used to produce damage probability curves for annealed glass subjected to long-duration blast, objective five of this research project. These curves and a proposed new method of plotting pressure-impulse (PI) curves are described in section 6.7. Section 6.8 concludes this chapter.

6.2 Material Model Sensitivity Study

Failure pressure and displacement results from experimental Phase S2 enabled production of an improved computational material model. In Chapter 5, glass edge finishing was proved insignificant to glazing response. This meant edge finishing was disregarded and the data were considered as a

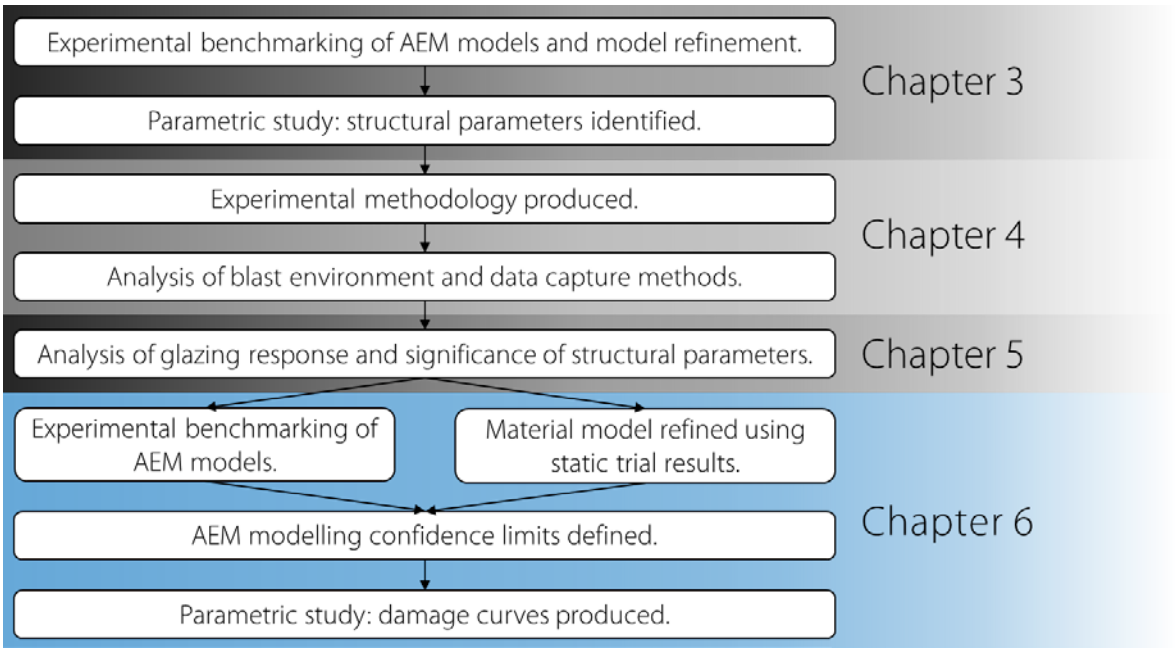

Figure 6.1: Layout of experimental and computational work.

single group. A static linear-elastic model of each test was created using FEA software Lusas Modeller. Glass was modelled as a thick shell surface with dimensions 520mm x 520mm, the testing frame aperture. Glass edges were fixed against rotation and translation in all directions, representing a rigid frame. A uniform pressure equal to the observed failure pressure was applied normal to the glass surface with gravity applied in the same direction. Initially the software's default annealed glass Young's Modulus of 61GPa was implemented. For each test maximum tensile stress was recorded (see Table 6.1). Homogeneity was assumed, resulting in maximum tensile stress observed at each edge midpoint in the top fibre. A contour plot of stress in the top glass fibres is shown in Figure 6.2, in this model the glass was subjected to the mean experimental failure pressure. Analysis yielded mean maximum static stress of 68MPa and standard deviation of 19MPa. To determine the mean Young's Modulus, failure pressure was plotted against experimental and numerical displacement s and the FEA Young's Modulus was adjusted until gradients of the linear relationships matched (see Figure 6.3). This yielded a Young's Modulus of 42.6MPa.

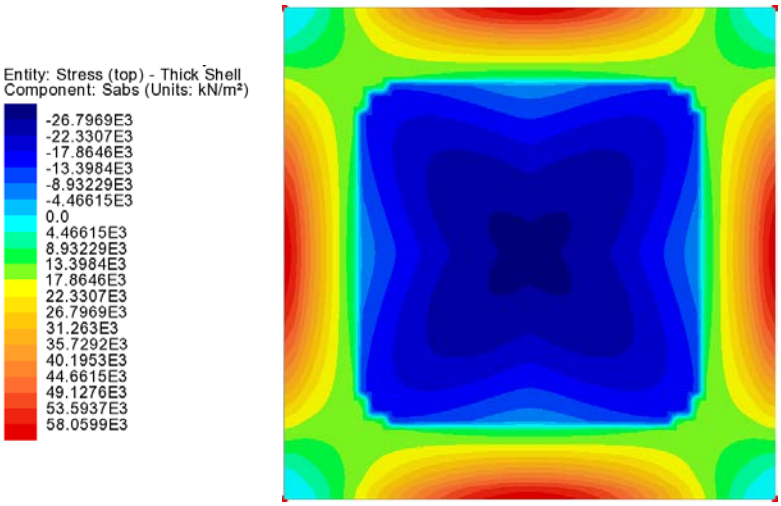

Figure 6.2: Contour plot of signed largest value of principal stress in the top fibre for mean test pressure.

Table 6.1: FEA results: modelling of Phase S2.

Sample No.	Experimental Results		Numerical Modelling Results	
	Failure Pressure (kPa)	Failure Displacement (mm)	Maximum Static Stress (MPa)	Failure Displacement (E= 42.6MPa) (mm)
C1	8.7	6.8	47	3.3
C3	16.5	9.6	88	6.3
C4	14.9	9.3	79	5.7
C5	11.8	8.1	63	4.5
C6	19.2	10.5	102	7.3
C7	11.8	8.0	63	4.5
C8	14.1	8.8	75	5.4
C9	9.9	6.9	53	3.8
C10	8.8	6.8	47	3.4
G1	7.0	6.4	38	2.7
G2	9.3	6.9	50	3.5
G3	11.7	8.3	62	4.5
G4	11.3	7.9	60	4.3
G5	14.4	9.2	77	5.5
G6	13.4	8.5	71	5.1
G7	15.8	9.2	84	6.0
G8	18.5	-	98	7.0
G9	17.0	10.1	91	6.5
G10	8.4	6.6	45	3.2
$\bar{x}$	12.8	8.2	68	4.9
σ	3.6	1.3	19	1.3

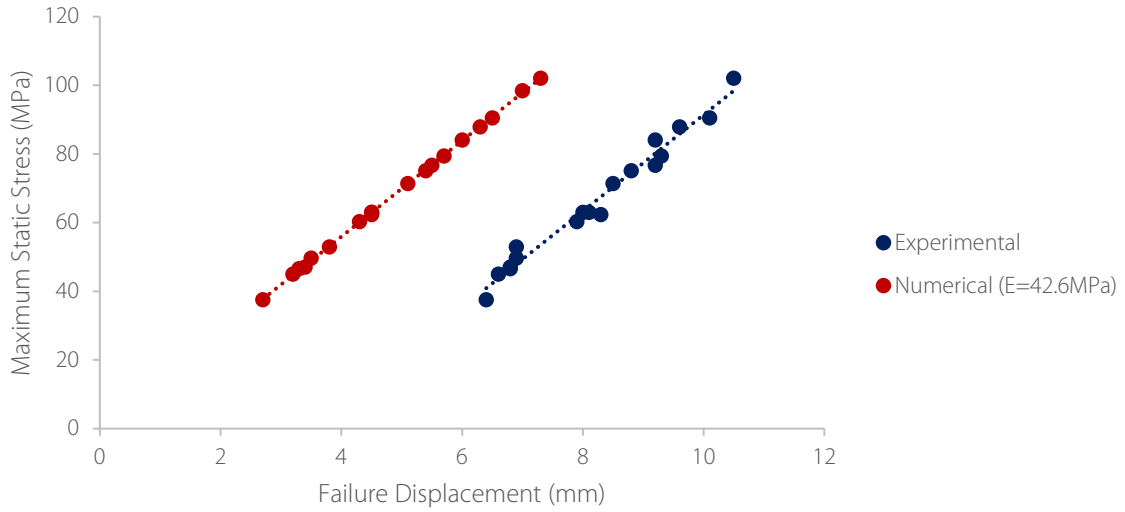

Figure 6.3: Comparison of experimental and numerical stress-displacement relationships.

Good agreement between experimental and numerical gradients was observed but experimental results indicated a consistent pre-test deflection of 3.5mm. This was a systematic measurement error caused by a deflection gauge that was not zeroed. Error consistency, indicated by good agreement with the linear trend line, meant it could be disregarded. The calculated Young's Modulus was considerably smaller than the default value which could be a glass property or due to support condition simplification in the FEA model. The glass was restrained against displacement and rotation along all edges, a severe restraint compared to what was achieved in testing. In experimental tests the outer 40mm of glass was clamped between steel frames and total glazing dimensions were 600

x 600 mm compared to the 520 x 520 mm modelled. For more accurate Young's Modulus and tensile strength measurements a sample should be sent to a material testing laboratory. In the next section, these material properties were implemented in dynamic trial models to provide a benchmark. It has been demonstrated throughout this thesis that glazing response to blast loading is highly variable due to variation of many parameters such as peak overpressure and material strength. Results of the benchmarking study indicated good agreement with experimental results and that the low Young's modulus was not critical to glazing response. It was concluded that the material model was adequate and could be used in the main parametric study.

Two material parameters unique to ELS were identified for investigation in Chapter 3, separation strain and post-failure shear stiffness factor. Separation strain defines when springs are removed after failure. As tensile strength is reached within a spring its strength reduces to zero but it remains intact until its strain reaches the specified separation strain. The spring is then removed from the model and element separation is allowed. The post-failure shear stiffness factor governs rate of shear strength reduction after spring failure. The parameter ranges between 0 (shear strength reduces to zero instantaneously) and 1 (shear strength remains at value specified). A similar parameter for normal strength exists but was not critical for out-of-plane deflection of glazing. A sensitivity study for each parameter was undertaken using an ABT trial glazing arrangement. Model set-up was unchanged from the initial computational study outlined in Chapter 3. Refer to this chapter for model construction and framing details.

Break time as opposed to failure impulse was compared due to experimental pressures being implemented in the model. The glazing arrangement used was [12kPa, 1:1.3, rigid]. Resulting break times from variation of each parameter is shown in Figure 6.4. Increasing separation strain from 0.005 to 0.007 yielded an increase in break time of 1.05ms. Further increasing separation strain to 0.008 increased break time by another 0.05ms, above this separation strain had no effect on break time. A separation strain of 0.007 was selected for analyses, the small value ensured brittle failure but produced a break time closer to the observed experimental value. Increasing separation strain aided modelling results where glazing survival occurred. With separation strain too low, springs were deleted quickly resulting in rapid cracking when experimental results indicated survival should have occurred. Varying the post-failure shear stiffness factor between 0 and 0.4 did not affect model break time. Break time reduced by 1.05ms between 0.4 and 0.5, above which no further change occurred. A number close to one indicates shear strength remained at the specified value after failure, not a characteristic of glass. Varying the parameter between 0 and 0.4, in the brittle region, had no effect on results so the default value of 0.01 was implemented in future analysis.

A comparison of glazing material models implemented in AEM modelling is outlined in Table 6.2. The Young's Modulus was reduced due to Phase S2 data analysis. The shear modulus reduced slightly to 17kPa, calculated from the Young's Modulus and an assumed Poisson's ratio of 0.23 (Pilkington North America Inc, 2013). Tensile strength increased considerably from the initially used design strength to the experimental mean strength (121MPa). The tensile strength value was implemented for shear

strength based on guidance by Feldmann and Kasper (2014). Glass density increased slightly to 2,460kg/m^3 established from experimental glazing measurements. Separation strain was increased from 0.005 to 0.007 based on sensitivity study results. Post-failure shear stiffness factor was unchanged as a result of the same study. The described material model was implemented in the benchmarking study described in the next section.

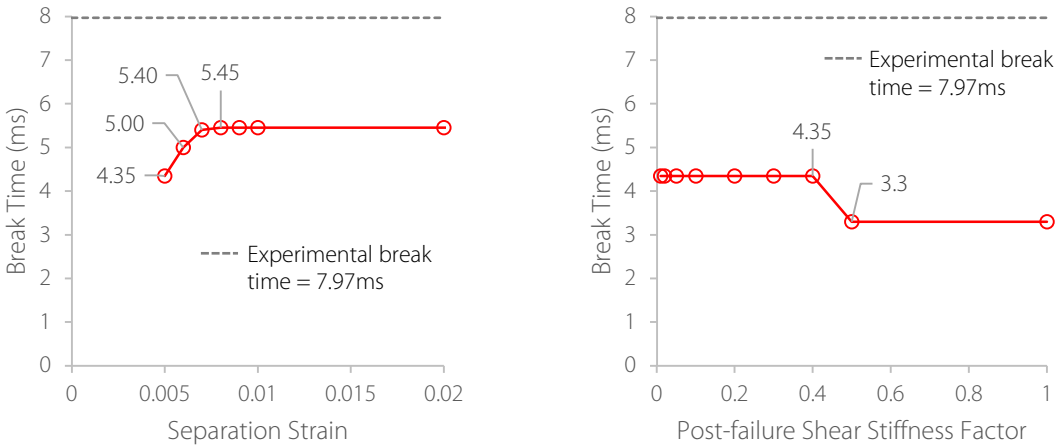

(a) Separation strain. (b) Post-failure shear stiffness factor.

Figure 6.4: Effect of ELS material properties on glazing break time.

Table 6.2: Comparison of glazing material models before and after experimental trials.

	Pre-trial values	Post-trial values
Young's Modulus, E	68 GPa	43 GPa
Shear Modulus, G	20 GPa	17 GPa
Tensile strength	41 MPa	121 MPa
Compressive strength	NA	NA
Shear strength	116 MPa	121 MPa
Density, ρ	2,440 kg/m^3	2,460 kg/m^3
Separation strain	0.005	0.007
Post-failure shear stiffness factor	0.01	0.01

6.3 Experimental Benchmarking

The AEM model, implementing the post-experimental material model, was experimentally benchmarked by verification of model behaviour against experimental results. Computational models of all experimental arrangements from this research project and Johns' thesis (Johns, 2016) (see Table 6.3) were built and results were compared to those observed. Rigid and elastic framing was modelled as detailed in Chapter 3. Elastic framing implemented structural sealant Dow Corning 993 in Johns' trials and Sika SG500 in trials from the current research project. Sealant and glazing material properties are outlined in Table 6.4. Each arrangement was tested with three tensile and shear strengths (shear strength = tensile strength (Feldmann and Kasper, 2014)). Glazing material strength standard deviation, determined from Phase S2 data, was 34MPa, 28% of the mean strength. To ensure consideration of material variation in the benchmarking study, the mean strength and mean ± two standard deviations were implemented for each arrangement. This meant 95% of possible material

strengths were represented (see Figure 6.5) and upper and lower bounds of calculated break parameters represented 95% of glazing behaviour. Experimental results located within these bounds indicated accurate modelling of glazing response. Material strength bounds are outlined in Table 6.5 for reference.

Table 6.3: Benchmarking study arrangements.

Research Project	Benchmarking Study Arrangement No.	P_r (kPa)	Aspect Ratio	Area (m^2)	Thickness (mm)	Support Conditions
Current	1	12	1:1	0.89	4	Rigid and elastic
Current	2	12	1:1.3	0.89	4	Rigid and elastic
Current	3	12	1:2	0.89	4	Rigid and elastic
Current	4	20	1:1	0.89	4	Rigid and elastic
Current	5	20	1:1.3	0.89	4	Rigid and elastic
Current	6	20	1:2	0.89	4	Rigid and elastic
Current	7	27	1:1	0.89	4	Rigid only
Current	8	27	1:1.3	0.89	4	Rigid only
Current	9	27	1:1.7	0.89	4	Rigid only
Current	10	27	1:2	0.89	4	Rigid only
Johns	11	27	1:1	0.25	4	Rigid and elastic
Johns	12	27	1:1.75	0.25	4	Rigid and elastic
Johns	13	27	1:1	0.89	4	Rigid and elastic
Johns	14	27	1:1.7	0.89	4	Elastic only
Johns	15	27	1:1	0.89	8	Rigid and elastic
Johns	16	27	1:1.7	0.89	8	Rigid and elastic

Table 6.4: Benchmarked material parameters.

	Annealed Glass	Dow Corning 993	Sika SG500
Young's Modulus, E	43 GPa	1.4 MPa	1.5 MPa
Shear Modulus, G	17 GPa	470 kPa	500 kPa
Tensile strength	121 MPa *	140 kPa	1.1 MPa
Compressive strength	NA	1.4 MPa	11 MPa
Shear strength	121 MPa *	110 kPa	804 kPa
Density, ρ	2,460 kg/m^3	1,320 kg/m^3	1,370 kg/m^3
Separation strain	0.007	1	1
Post-failure shear stiffness factor	0.01	NA	NA

* Strength varies as outlined in Table 6.5.

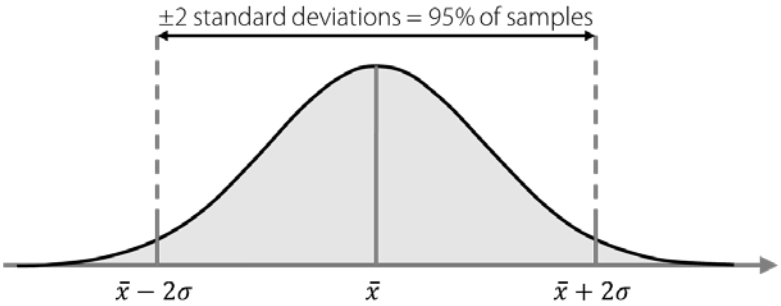

Figure 6.5: Normal distribution with ±2 standard deviations indicated.

Table 6.5: Tensile and shear strength variation.

	Tensile and Shear Strength (MPa)
$\bar{x} - 2\sigma$	53
$\bar{x}$	121
$\bar{x} + 2\sigma$	189

Results from rigidly framed models are initially discussed, results from elastic arrangements follow. Break parameters calculated by numerical modelling were normalised against mean experimental results for each arrangement (see equation 6.1). A normalised result of one indicated an exact match with experimental values. Results greater than one indicated a computational result larger than experimental results and vice versa. Analysis results from rigid arrangements are outlined in Table 6.6 and are colour coded for clarity. Blue indicates a normalised result less than 0.8, green indicates a normalised result between 0.8 and 1.2 and red, a normalised result greater than 1.2. Failure displacement and impulse at failure results are plotted in Figure 6.6 and Figure 6.7 respectively.

$$Normalised\ break\ parameter = \frac{Break\ parameter\ (AEM)}{Mean\ break\ parameter\ (experimental)} \qquad 6.1$$

Table 6.6: Normalised break parameters: rigid benchmarking.

	Failure Displacement (mm)			Failure Impulse (kPa)		
Arrangement Configuration	-2σ	$\bar{x}$	+2σ	-2σ	$\bar{x}$	+2σ
1: 12kPa; 1:1; 0.89m²; 4mm; R	0.58	1.45	2.12	0.57	0.85	1.19
2: 12kPa; 1:1.3; 0.89m²; 4mm; R	0.19	0.50	0.61	0.34	0.55	0.64
3: 12kPa; 1:2; 0.89m²; 4mm; R	0.34	0.55	0.67	0.53	0.72	0.93
4: 20kPa; 1:1; 0.89m²; 4mm; R	0.51	1.19	1.94	0.45	0.68	0.82
5: 20kPa; 1:1.3; 0.89m²; 4mm; R	0.19	0.43	0.77	0.34	0.52	0.68
6: 20kPa; 1:2; 0.89m²; 4mm; R	0.21	0.59	0.72	0.39	0.63	0.74
7: 27kPa; 1:1; 0.89m²; 4mm; R	0.14	0.36	0.54	0.30	0.47	0.60
8: 27kPa; 1:1.3; 0.89m²; 4mm; R	0.12	0.31	0.52	0.30	0.46	0.56
9: 27kPa; 1:1.7; 0.89m²; 4mm; R	0.22	0.55	0.92	0.34	0.51	0.66
10: 27kPa; 1:2; 0.89m²; 4mm; R	0.16	0.50	0.70	0.32	0.51	0.63
11: 27kPa; 1:1; 0.25m²; 4mm; R	0.20	0.50	0.60	0.52	0.82	1.08
12: 27kPa; 1:1.75; 0.25m²; 4mm; R	0.59	1.23	1.23*	0.70	1.18	- *
13: 27kPa; 1:1; 0.89m²; 4mm; R	0.19	0.45	0.74	0.46	0.69	0.87
15: 27kPa; 1:1; 0.89m²; 8mm; R	0.24	0.55	0.58*	0.40	0.66	- *
16: 27kPa; 1:1.7; 0.89m²; 8mm; R	0.27	0.45	0.53*	0.50	0.70	- *
*Model unbroken	Normalised value < 0.8		0.8 < Normalised value < 1.2		Normalised value > 1.2	

For most rigid arrangements all three material strengths yielded normalised break parameters less than 0.8, indicating result under-prediction. AEM models failed earlier than corresponding experimental arrangements and with a lower displacement. A large proportion of results were less than 0.5, indicating severe parameter under-prediction. Four arrangements, including 1:1 aspect ratio windows subjected to lower overpressures, produced normalised failure displacements greater than 0.8. Three of these produced normalised failure displacements greater than 1.2 when the upper bound material strength was used. This meant experimental values were bounded by numerical modelling results, indicating AEM had modelled glazing response well. Normalised failure impulses greater than 0.8 were recorded for five arrangements. Only two of these were greater than 1.0. Three arrangements from Johns' research survived when modelled with the upper bound material strength. All repeats of these arrangements broke in the experiments, indicating computational modelling with material strength variation was bounding the experimental response. Break time was disregarded in favour of impulse at failure due to a single blast pressure been implemented in all models, rather than

individual experimental pressure histories from each trial. Small differences between the implemented and experimental pressure histories could have resulted in a break time error.

Normalised break parameter graphs (Figure 6.6 and Figure 6.7) indicate highly consistent results. Consistency in normalised values indicated trends due to structural and blast parameters were modelled correctly in AEM. Variation between rigid arrangement results for upper and lower material strength models was small, indicating material strength had little effect on glazing failure. Using results from models implementing the mean material strength, mean normalised displacement was 0.64±0.34, reducing to 0.48±0.08 when disregarding arrangements 1, 4 and 12. These arrangements are discussed further below. This mean result indicated failure displacement produced by AEM models was approximately half the experimental values. This discrepancy in results can be attributed to modelling approximations. For rigidly framed arrangements only the glass and frame were modelled, with frame outer edges fixed against rotation and displacement in all directions. This conservative approximation assumed the front of the test containers were perfectly rigid. Deformation of the front face was observed by high-speed cameras during the blast, reducing rigidity of the window support conditions. The default high-strength steel material model was implemented in the AEM model but material strength of the steel frame was not tested. Framing conditions more rigid than in experimental trials induced higher stresses in the glass edges resulting in quicker failure with a lower displacement.

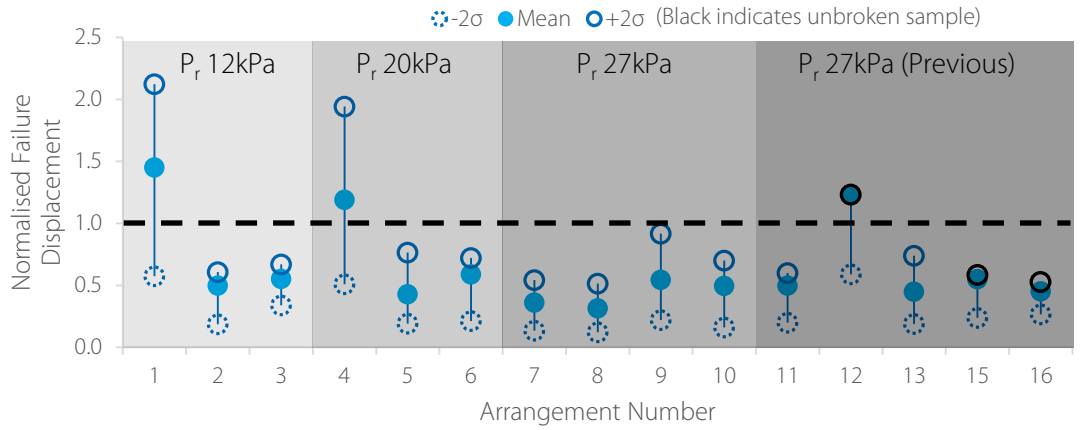

Figure 6.6: Normalised failure displacement: rigid results.

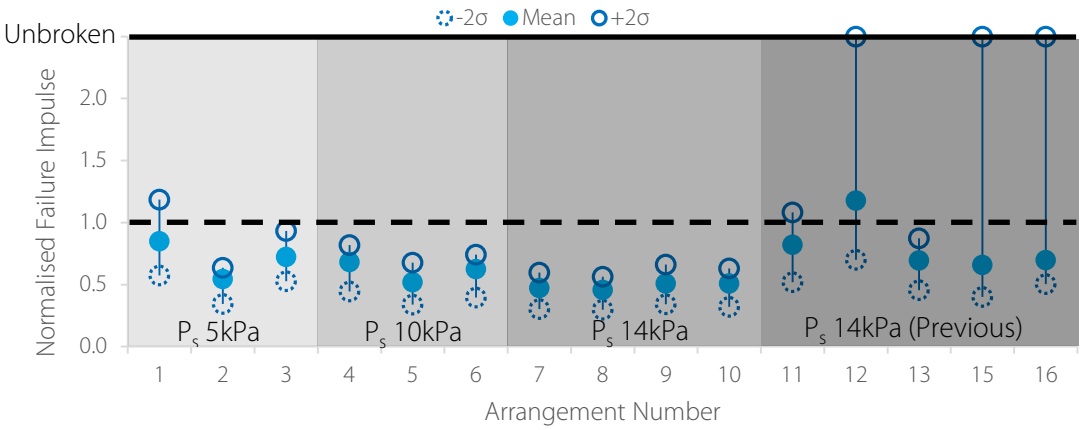

Figure 6.7: Normalised failure impulse: rigid results.

Normalised displacements produced by AEM models of arrangements 1 and 4 were greater than one indicating a result higher than experimental values. This can be attributed to large spans in the 1:1 aspect ratio. An increased span reduced stresses in the glass edges, minimising the effect of over-rigid support conditions. This behaviour was only observed for windows subjected to lower overpressures (P_r of 12kPa and 20kPa) that deflected further prior to failure. Windows subjected to P_r 27kPa did not exhibit the same behaviour as the higher overpressure punched through the glass before large displacements could occur. Arrangement 12 also recorded a normalised displacement above one. This arrangement had a small area and high aspect ratio, resulting in a small span. An arching effect could have occurred between supports, resulting in a longer break time and larger displacement.

A higher consistency was observed for normalised impulse at failure. The mean result for models implementing the mean material strength was 0.66±0.18 for all arrangements. This consistency across all arrangements indicated AEM models captured glazing response trends observed in experimental trials. The mean normalised impulse was higher than the mean normalised displacement, indicating better agreement with experimental results despite normalised failure impulses generally being lower than experimental results. This indicates higher rigidity in modelled support conditions compared to the trials. Arrangements 1 and 11 recorded normalised failure impulses greater than 1.0 when the upper bound material strength was implemented. Arrangement 12 also recorded a normalised failure impulse greater than 1.0 when the mean material strength was used. For three arrangements, when the upper bound material strength was employed, the AEM model did not fail. Although no glazing survived in these experimental trials, this indicated AEM was capable of modelling survival and that experimental results for these arrangements lay within the bounds of computational results. Arrangements 1 and 4, which recorded substantially larger normalised displacements than other arrangements did not produce the same trend in failure impulse. This can be attributed to a lower displacement rate in AEM models compared to experimental results.

Results from elastic arrangements are outlined in Table 6.7 and plotted in Figure 6.8 and Figure 6.9. Results spread was much higher between arrangements compared to rigid results. When the upper or mean material strength was implemented all normalised displacements were greater than 1.2, indicating displacements higher than experimental results. Two arrangements, 1 and 15, also produced normalised displacements larger than 1.2 when the lower bound material strength was used, indicating a displacement overestimation in AEM models. For all other arrangements, AEM models with the lower bound material strength produced normalised displacements less than 1.2. Arrangements 2 to 6 and 12 to 14 produced normalised displacements that bounded the experimental result, indicating good agreement from the AEM model. Two arrangements (11 and 15) employing the mean material strength survived and seven models implementing the upper limit material strength survived. Of these arrangements, four recorded some unbroken samples in experimental trials, indicating good agreement between AEM and experimental results for the survival/failure boundary. Consistency in normalised failure displacement (1.79±0.27 for all arrangements implementing the mean material strength) indicated good agreement between trends

modelled using AEM and those observed in experimental trials. Over-prediction of displacement by AEM was attributed to support conditions with higher elasticity than those in the trials. Elastic support conditions were determined by the structural sealant stiffness. Two different sealants were used, Sika SG500 for arrangements 1 to 6 and Dow Corning 993 for arrangements 11 to 16. No material testing was undertaken for either sealant meaning material properties were obtained from literature. Sealant Young's Moduli in experimental trials may have been higher than specified, resulting in an over-elastic support condition in the AEM model and a larger displacement.

Table 6.7: Normalised break parameters: elastic benchmarking.

	Failure Displacement (mm)			Failure Impulse (kPa)		
Arrangement Configuration	-2σ	$\bar{x}$	+2σ	-2σ	$\bar{x}$	+2σ
1: 12kPa; 1:1; 0.89m^2; 4mm; E	1.47	2.15	2.15*	0.96	1.33	-
2: 12kPa; 1:1.3; 0.89m^2; 4mm; E	1.01	1.63	1.66*	0.76	1.07	-
3: 12kPa; 1:2; 0.89m^2; 4mm; E	0.81	1.87	1.87*	0.70	1.27	-
4: 20kPa; 1:1; 0.89m^2; 4mm; E	0.58	1.57	1.62	0.64	1.00	1.14
5: 20kPa; 1:1.3; 0.89m^2; 4mm; E	0.48	1.47	1.61	0.60	0.96	1.13
6: 20kPa; 1:2; 0.89m^2; 4mm; E	0.97	2.16	3.06	0.77	1.12	1.60
11: 27kPa; 1:1; 0.25m^2; 4mm; E	1.08	1.65*	1.65*	0.78	-	-
12: 27kPa; 1:1.75; 0.25m^2; 4mm; E	0.84	1.43	1.67*	0.74	0.96	-
13: 27kPa; 1:1; 0.89m^2; 4mm; E	0.50	1.78	1.92	0.74	1.27	1.46
14: 27kPa; 1:1.7; 0.89m^2; 4mm; E	0.52	1.69	2.07	0.86	1.38	1.71
15: 27kPa; 1:1; 0.89m^2; 8mm; E	1.31	2.02*	2.02*	0.91	-	-
16: 27kPa; 1:1.7; 0.89m^2; 8mm; E	1.12	2.17	2.34*	0.96	1.39	-

*Model unbroken Normalised value < 0.8 0.8 < Normalised value < 1.2 Normalised value > 1.2

Normalised failure impulse for elastic arrangements bounded experimental results for all arrangements, demonstrating AEM predicted experimental behaviour well. AEM models employing the mean material strength produced a normalised failure impulse greater than 1.0 for all but two arrangements (5 and 12) indicating an over-prediction of failure impulses. The mean normalised failure impulse for all models implementing the mean material strength was 1.18±0.16. This mean result was within the green boundary, indicating good agreement with experimental results. The small standard deviation demonstrated consistency with observed experimental trends. Models of glazing subjected to P_r 20kPa (arrangements 4, 5 and 6) performed especially well with a mean normalised result of 1.03. For both break parameters, response of arrangements 2 and 5 was lower than other results. Both arrangements had aspect ratios of 1:1.3 which demonstrated increased displacement and failure impulse in experimental trials compared to other aspect ratios. The reduced normalised result indicated AEM modelling did not capture this behaviour to the same extent. Normalised failure impulse was closer to 1.0 for arrangements in this research project (arrangements 1 to 6) compared to results from Johns' research. This could be due to differing sealants and the accuracy of their material models implemented in AEM models.

Benchmarking results demonstrated rigid support conditions implemented in the AEM model were too severe. Normalised break parameters were consistently less than one, indicating under-prediction compared to experimental results. In comparison, arrangements modelled in AEM with elastic support conditions typically over-predicted experimental results. Over-prediction of failure

displacement was higher than failure impulse indicating structural sealant stiffness was too low. Consistency in normalised break parameters indicated AEM was capable of modelling experimental trends. A reduced trend due to aspect ratio was observed for elastically framed arrangements which should be considered in future parametric studies. Models with rigidly supported arrangements under-predicted results and elastically framed models slightly over-predicted break parameters, meaning damage probability curves produced in section 6.7 yielded a conservative standard deviation. Results higher and lower than experimental results for the same arrangement indicated the glass material model was representational of glass used in experiments, successfully benchmarking the material for future parametric studies.

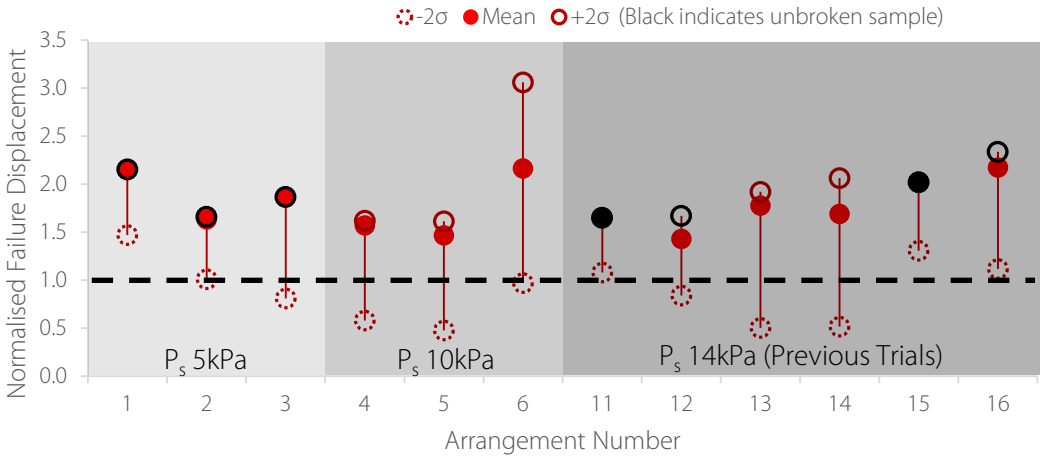

Figure 6.8: Normalised failure displacement: elastic results.

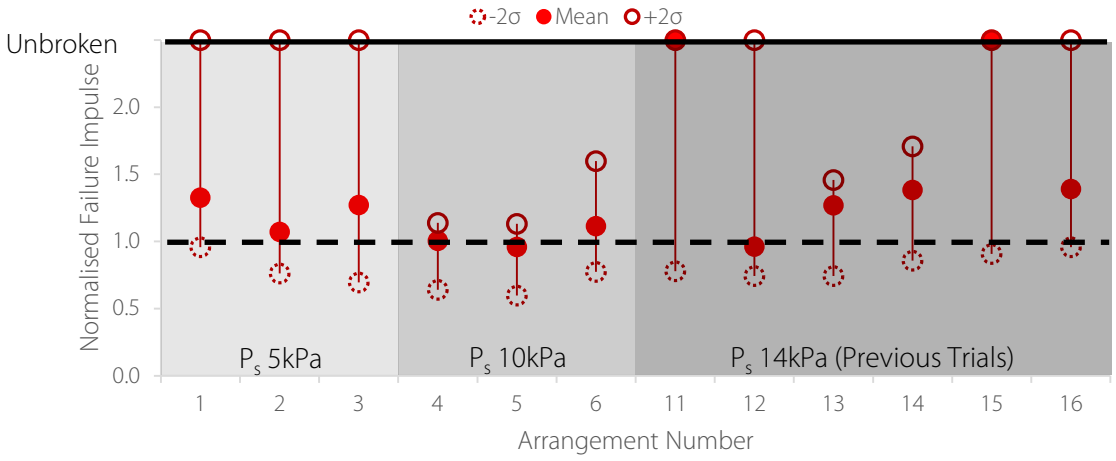

Figure 6.9: Normalised failure impulse: elastic results.

6.4 ELS Reliability Limits

Based on results from the benchmarking parametric study, a set of reliability limits were produced. These indicate the experimental benchmark extent and scope for extrapolating structural parameters before confidence in ELS ability to model glazing response reduces and further experimental data are recommended. Extents of both limits are outlined in Table 6.8. Linear plots of parameter limits are shown in Figure 6.10 and Figure 6.11 and each limit is discussed separately. Described reliability limits

formed the basis of the main parametric study described in following sections. Effect of aspect ratio, supports and the blast environment on glazing response was explored, matching experimental data analysis in Chapter 5.

Table 6.8: Experimental and reliability limits of structural and blast parameters.

Parameter	Experimental values	Experimental limits	Reliability limits
P_s (kPa)	6, 10, 13	6 – 13	0 – 20
Aspect ratio	1:1, 1:1.3, 1:1.7, 1:2	1:1 – 1:2	1:1 – 1:4
Support conditions	Rigid and elastic	Rigid and elastic	Rigid and elastic

In the previous chapter peak overpressure was determined as the blast parameter governing response to the long-duration blast environments tested. Three free-field overpressures were tested: 6kPa, 10kPa and 14kPa. These, and corresponding experimental and reliability limits, are outlined in Figure 6.10. Reliability limits of 0kPa and 20kPa were selected for this parameter. The benchmarking parametric study indicated good agreement for window survival between AEM and experimental results. It was therefore assumed AEM was capable of modelling response to overpressures below 6kPa with confidence. An upper limit of 20kPa was selected, above this it was believed failure would occur due to material overloading as a result of high peak overpressure instead of deflection which was observed at lower overpressures. This failure mechanism was not experimentally benchmarked so could not be modelled with confidence.

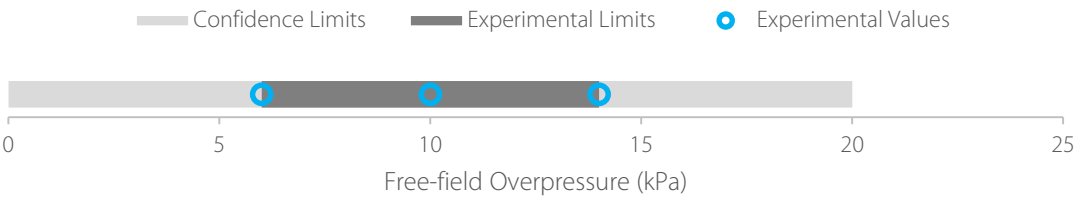

Figure 6.10: Reliability limits: P_s.

Experimental and reliability limits for aspect ratio are detailed in Figure 6.11. Four aspect ratios were tested experimentally, 1:1, 1:1.3, 1:1.7 and 1:2. Due to small increments between experimentally benchmarked aspect ratios, interpolation between values can be undertaken with confidence. It was determined in Chapter 5 that transition from two-way to one-way spanning behaviour occurred within experimental limits and by aspect ratio 1:2 the glass was acting as a one-way spanning plate. Aspect ratio 1:4 was selected for the upper extrapolation bound before further benchmarking was required. It can be assumed that between 1:2 and 1:4 the glass acts as a one-way spanning plate in the same manner as the 1:2 aspect ratio arrangement. At higher aspect ratios, the short span may sufficiently diminish to result in new behaviour such as arching to supports. In the absence of an experimental benchmark, it is recommended experimental work is undertaken to verify glazing behaviour for aspect ratios above 1:4.

No reliability limit was produced for support conditions. Two distinct framing conditions were tested, represented rigid and elastic bounds of window framing. Most frames implemented in buildings should lie within these limits but not on a linear scale. Frames used in industry come in many different

designs and it cannot be assumed that benchmarking outer limits of framing conditions means a completely different frame like a spider connection can be modelled with confidence. Each frame to be modelled should be experimentally benchmarked to ensure model accuracy. The two experimentally benchmarked frames in this research project can be varied slightly, for example the Sika SG500 sealant stiffness could be modified to change elastic support conditions.

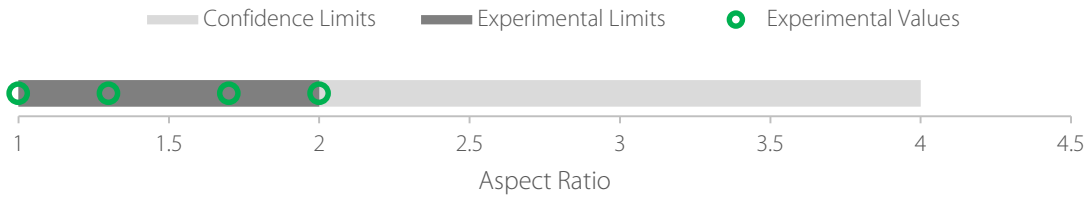

Figure 6.11: Reliability limits: aspect ratio.

6.5 Main Parametric Study Methodology

The second parametric study in this chapter implemented ELS reliability limits and the benchmarked material model. This parametric study, discussed in the remainder of this chapter, determined the effect of blast environment, aspect ratio and support conditions on the minimum failure overpressure for annealed glazing. Study results enabled production of damage probability curves for these parameters, fulfilling objective five of this thesis. For this investigation a base configuration was selected. This window had an area of 0.89m^2 and thickness of 4mm, consistent with experimental work for this research project. Elastic support conditions were implemented due to better agreement with experimental results during benchmarking. An aspect ratio of 1:1 was selected for the base model. The benchmarked material models for glazing and structural sealant Sika SG500 were implemented. The mean glass material strength was used in all models.

The applied blast pressure was simplified to a Friedlander curve of the positive phase only (see Figure 6.12). The negative phase was not modelled to restrict calculation time, an approximate run time with t_d 100ms was 50 hours. Reflected overpressure was applied to the glass, assuming no clearing effects. This parametric study aimed to calculate probability of failure for a generic window. This meant dimensions of the associated structure not be known so assuming an infinite wall, where no clearing was possible, was the conservative approach. To determine minimum overpressure resulting in failure of a particular arrangement, models were run with an initial P_s of 6kPa. If glazing failed before completion of the positive phase, the calculation was terminated and a lower overpressure was selected for the next model pass. If the glass was intact at the end of the positive phase, the window was deemed unbroken and a higher overpressure was selected for the following pass. This was continued until a minimum failure pressure was found to the nearest 0.1kPa. Further increasing precision was impractical due to long run times and uncertainty of peak overpressure and other parameters, such as material strength, in application of produced damage curve.

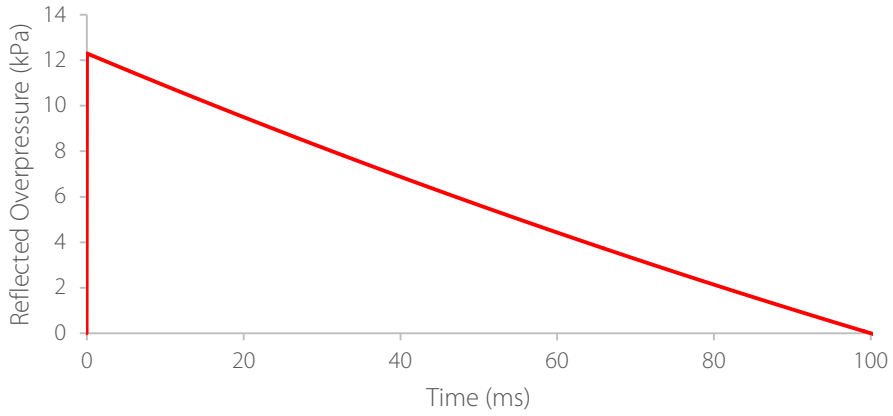

Figure 6.12: Pressure input for failure P_s 6kPa.

The blast parameter varied was peak overpressure, determined in Chapter 5 to be the governing parameter in blast environments tested. In current Glazing Hazard Guide pressure-impulse (PI) graphs, see Figure 6.13, P_r is assumed to be the only parameter influencing window failure in a long-duration blast. Horizontal damage state lines indicate glazing failure is impulse-independent in this regime. A positive phase duration of 100ms was maintained for the base model, reducing number of blast parameters to vary. This meant all modelled blast environments lay along a straight line on the PI graph as impulse increased linearly with overpressure. Parameter t_d was then investigated in the parametric study. Modelling three different t_d values, 40ms, 100ms and 500ms, determined whether the current assumption of impulse-independence in a long-duration blast regime was correct. It was predicted that a negative slope, resulting in decreased failure pressure as impulse increased, would be found. This would indicate failure was impulse dependent in a long-duration regime.

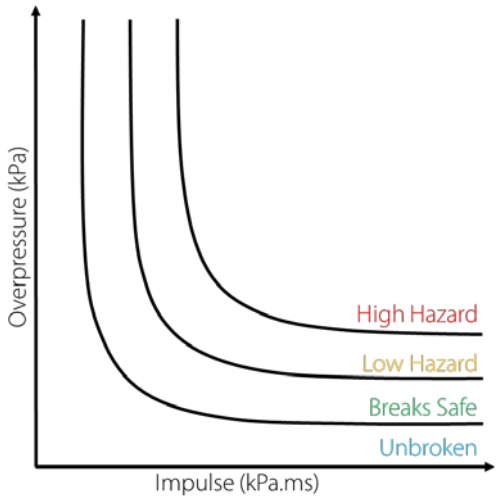

Figure 6.13: Diagram of a PI graph with current Glazing Hazard Guide damage states.

Eight aspect ratios were modelled to determine minimum failure pressures. Four experimentally tested aspect ratios, 1:1, 1:1.3, 1:1.7 and 1:2, were selected in addition to aspect ratios in 0.5 increments between 1:2 and 1:4, the extent of ELS reliability limits. Five support conditions were modelled, experimentally benchmarked elastic and rigid frames and three variations between these bounds. It was stated in the previous section that minor variations of benchmarked frame could be modelled

with confidence. Modification of the elastic frame involved increasing structural sealant stiffness (see Figure 6.14). Rigid frame variation required extension of the existing frame to add a dummy stiffness element. This additional frame, labelled as a stiffness element in Figure 6.15b, enabled a spring stiffness boundary condition to be applied to the existing frame, reducing its rigidity. This method was adopted as ELS did not allow boundary conditions with a specified spring stiffness. A study of the rigid frame stiffness element and elastic frame structural sealant was undertaken using arrangement 2 from the benchmarking study. This was a 1:1.3 aspect ratio window with area of 0.89m^2 and thickness of 4mm. The glass was subjected to P_r 12kPa.

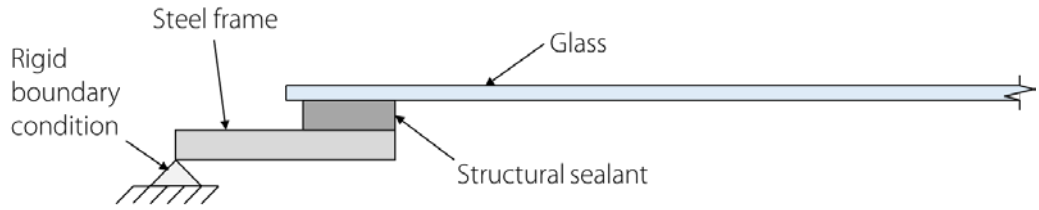

Figure 6.14: Section through elastic framing in AEM models.

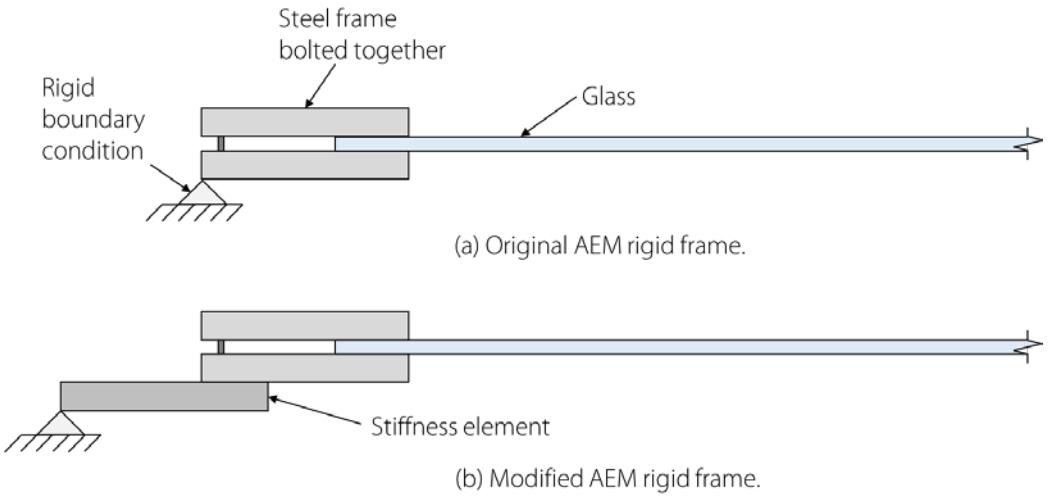

Figure 6.15: Modification of AEM rigid frame to reduce rigidity (section).

Young's Modulus of the structural sealant was varied between 2MPa (value for Sika SG500 used in elastic frames) and 50MPa (see Figure 6.16). Increasing sealant stiffness had a significant effect on break time and failure displacement. Increasing stiffness from 2MPa to 10MPa resulted in a break time decrease of 1.05ms and a decrease in failure displacement of 5.6mm. Further increasing stiffness to 50MPa resulted in a break time decrease of 1.4ms and displacement of 5.5mm. As sealant stiffness increased, effect on break parameters reduced as values tended towards rigid framing results.

Young's Modulus of the rigid stiffness element was varied between 200GPa and 0.1MPa, results of this study are shown in Figure 6.17. Decreasing element stiffness from 200GPa to 10GPa had no significant effect on break parameters. Further decreasing stiffness from 10GPa to 100MPa, resulted in an increase in break time of 0.7ms and increase in displacement of 3.7mm. Decreasing the stiffness below 10MPa had no further effect on break parameters.

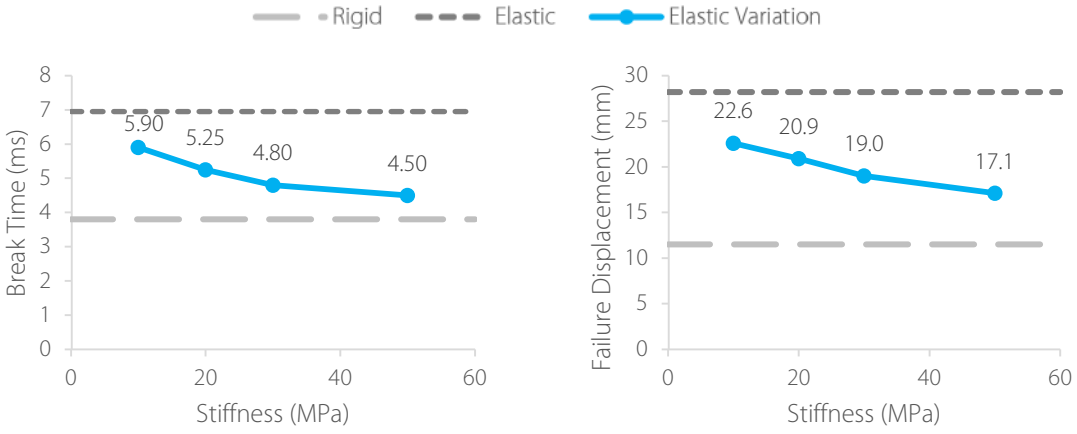

(a) Break time. (b) Failure displacement.

Figure 6.16: AEM results: variation of elastic support stiffness.

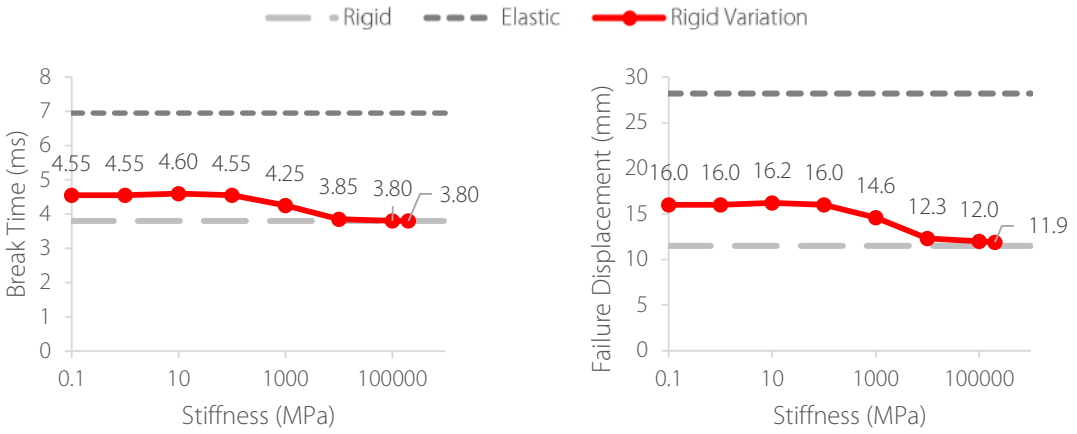

(a) Break time. (b) Failure displacement.

Figure 6.17: AEM results from variation of rigid support stiffness.

Three variations of elastic and rigid frames were selected to provide intermediate support conditions in the parametric study. A modified rigid frame with stiffness element Young's Modulus of 100MPa was chosen. Two elastic frames, with sealant stiffness of 10MPa and 20MPa, were also selected. Break parameter results, compared to original elastic and rigid frame results for arrangement 2 are shown in Figure 6.18. Frame variations provided a balanced data spread between bounding support conditions, implying a representative spread of minimum failure pressures in the parametric study. A summary of these framing conditions, as well as selected aspect ratio and t_d values are outlined for reference in Table 6.9.

Table 6.9: Summary selected values for structural and blast parameters.

Parameter	Values tested							
t_d (ms)	40	100	500					
Aspect Ratio	1:1	1:1.3	1:1.7	1:2	1:2.5	1:3	1:3.5	1:4
Support conditions	rigid	rigid (100MPa)	elastic (20MPa)	elastic (10MPa)	elastic			

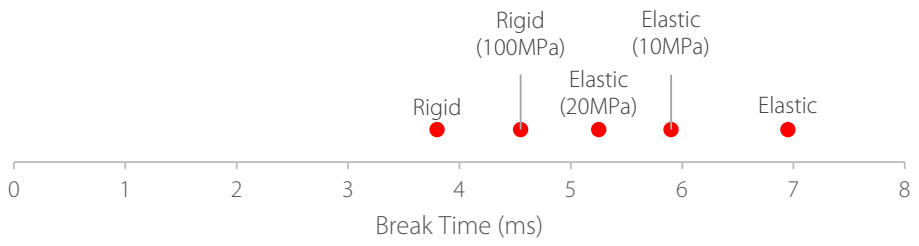

(a) Break time.

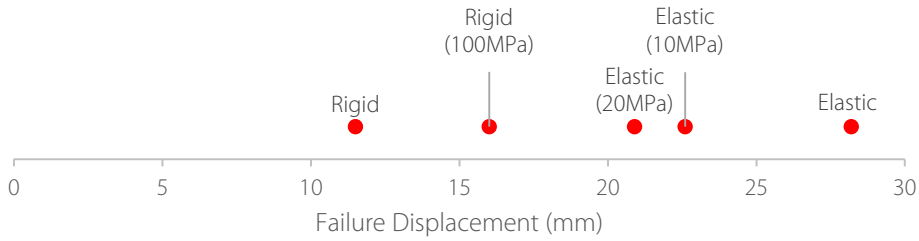

(b) Failure displacement.

Figure 6.18: Break parameter result spread from support condition variation.

6.6 Parametric Study Results

The parametric study base model was initially modelled with varying positive phase duration to determine the effect of t_d on the minimum overpressure resulting in window failure. Three values of t_d were tested, 40ms, 100ms and 500ms. A reflected PI plot of broken and unbroken windows subjected to each t_d value is shown in Figure 6.19. A minimum failure pressure line was plotted at the survival/failure boundary. Minimum failure pressure decreased as positive phase duration and impulse increased. Minimum free-field overpressure resulting in failure reduced from 5.8kPa to 4.9kPa with t_d increase from 40ms to 500ms, indicating impulse dependency. A summary of results is outlined in Table 6.10.

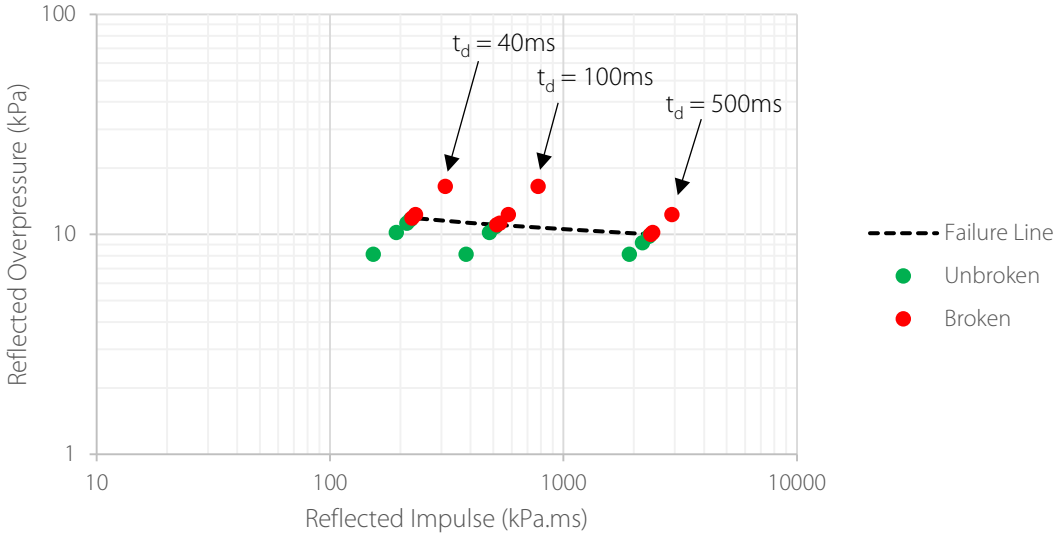

Figure 6.19: PI graph of broken and unbroken windows in t_d study.

Table 6.10: Results summary: t_d.

	Minimum blast causing failure				Break parameters at minimum failure pressure		
t_d (ms)	P_s (kPa)	I_s (kPa.ms)	P_r (kPa)	I_r (kPa.ms)	Failure Displacement (mm)	Break Time (ms)	Failure Impulse (kPa.ms)
40	5.8	109	11.9	224	26	8.05	85
100	5.4	255	11.0	518	26	8.35	64
500	4.9	1158	10.0	2364	26	58.8	548
$\bar{x}$	5.4	507	11.0	1035	26	25.1	232
σ	0.4	464	0.8	947	0	23.9	224

Change in minimum free-field overpressure resulting in window failure and corresponding break parameters are plotted in Figure 6.20. Minimum failure P_s decreased approximately linearly as the logarithm of t_d increased. In contrast, failure displacement for each minimum failure P_s remained constant across all three t_d values, indicating glazing failure resulted from reaching maximum displacement. Mean displacement at failure was 26±0mm, rounded to the nearest millimetre. No significant change was recorded between break times and impulse at failure for t_d 40ms and 100ms. A large increase in both parameters occurred when t_d increased to 500ms. Impulse at failure increased from 63.5kPa.ms to 548kPa.ms which could be attributed to a lower peak overpressure that was not high enough to cause failure. High impulse resulting from the long positive phase duration caused window failure later in the glazing response once sufficient impulse had been received.

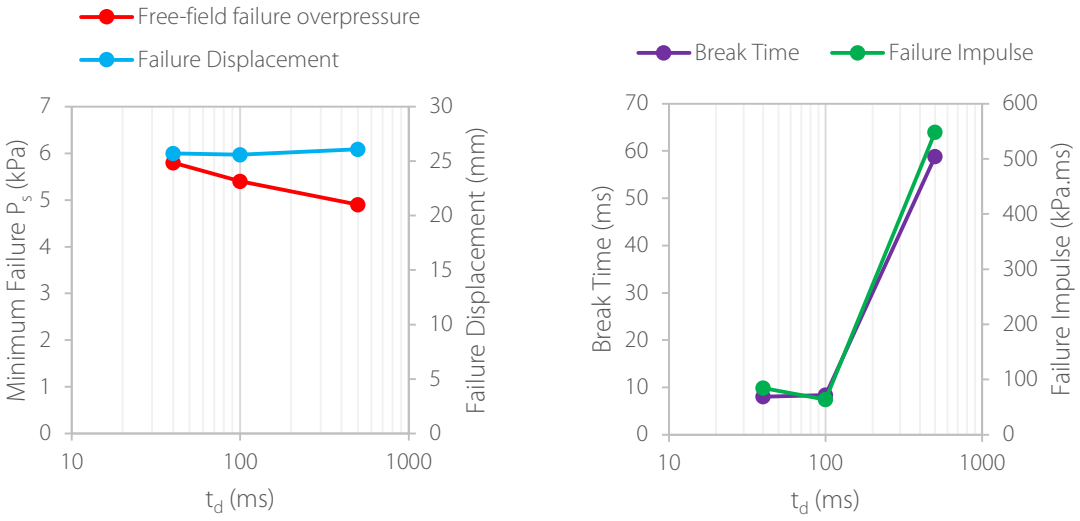

(a) Displacement at failure.

(b) Break time and failure impulse.

Figure 6.20: Minimum failure pressure and break parameters from t_d parameter study.

The minimum failure pressure line plotted in Figure 6.19 was replotted in Figure 6.21 with corresponding lines from the Glazing Hazard Guide (Security Facilities Executive Special Services Group - Explosion Protection, 1997). Lines plotted correspond to "no break" lines for 4mm thick annealed glass. The small window had area 0.69m^2 and aspect ratio 1:2.3, the large window parameters were 1.94m^2 and 1:1.2. From these dimensions, parametric study results (window parameters 0.89m^2 and 1:1) should lie between the two Glazing Hazard Guide lines. Numerical results indicate a much higher minimum failure pressure than specified in the Glazing Hazard Guide.

Experimental results indicated P_r 12kPa was near the survival threshold for 0.89m^2, 4mm thick annealed glass, demonstrating computational accuracy. This plot indicates, as stated by Meyer, Little and Conrath (2004), the Glazing Hazard Guide is overly conservative. Framing conditions could be responsible for this discrepancy as those implemented in the Guide are unknown. A frame with higher rigidity would produce a lower failure overpressure. Elastic frames with structural sealant to provide support flexibility were implemented in the numerical study.

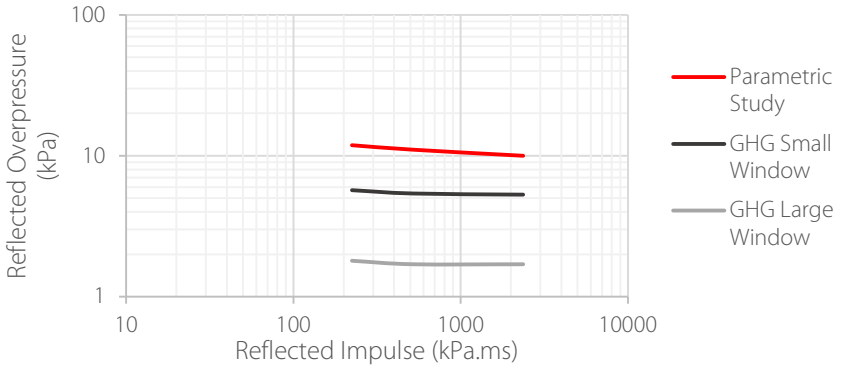

Figure 6.21: Comparison of results from t_d study to Glazing Hazard Guide (data interpreted from Security Facilities Executive Special Services Group - Explosion Protection (1997)).

Eight aspect ratios between 1:1 and 1:4 were originally tested in the parametric study. An additional aspect ratio of 1:2.1 was included after a large decrease in displacement at the minimum failure pressure was observed between 1:2 and 1:2.5. A plot of broken and unbroken models for each aspect ratio is shown in Figure 6.22. A line indicating minimum free-field overpressure resulting in failure at each aspect ratio has been drawn. This demonstrates that varying aspect ratio between 1:1 and 1:4 resulted in minimum failure P_s variation between 4.3kPa and 5.7kPa, a range of 1.4kPa. A summary of minimum failure pressures and corresponding break parameters for each aspect ratio is outlined in Table 6.11 for reference. These parameters are additionally plotted in Figure 6.23.

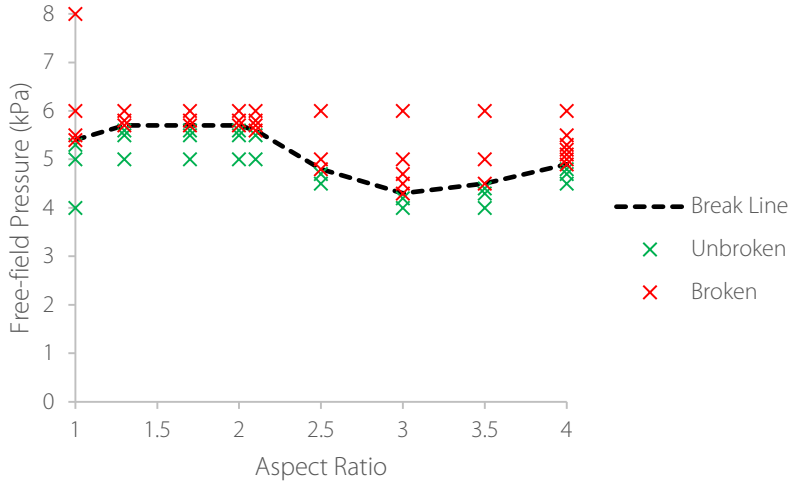

Figure 6.22: Plot of broken and unbroken models with varying aspect ratio.

The mean minimum failure P_s for aspect ratio was 5.2±0.6kPa, corresponding to a mean minimum failure P_r of 10.6±1.2kPa. The maximum value for minimum failure P_s was 5.7kPa, calculated for models with aspect ratios 1:1.3, 1:1.7 and 1:2. Aspect ratio 1:1 produced a lower minimum failure P_s of 5.4kPa.

For aspect ratios above 1:2, minimum failure P_s reduced to a minimum of 4.3kPa at aspect ratio 1:3, increasing to 4.9kPa for aspect ratio 1:4. An increase in minimum failure P_s above 1:3 indicates a stronger aspect ratio which could be attributed to the short span reducing sufficiently to enable arching to supports. Displacement at failure increased with aspect ratio from 26mm at aspect ratio 1:1 to 33mm at 1:2. This trend can be attributed to intermediate aspect ratios between two and one-way spanning arrangements decreasing window stiffness and enabling displacement to increase. Further increasing aspect ratio caused a rapid decrease in displacement at failure to 13mm at 1:4. This was attributed to the small span decreasing resulting in a stiffer arrangement.

Table 6.11: Results summary for aspect ratio study.

	Minimum blast causing failure				Break parameters at minimum failure pressure		
Aspect Ratio	P_s (kPa)	I_s (kPa.ms)	P_r (kPa)	I_r (kPa.ms)	Failure Displacement (mm)	Break Time (ms)	Failure Impulse (kPa.ms)
1:1	5.4	255	11.0	518	26	8.35	87
1:1.3	5.7	269	11.7	551	27	7.90	88
1:1.7	5.7	269	11.7	551	30	9.05	100
1:2	5.7	269	11.7	551	33	8.60	96
1:2.1	5.6	264	11.5	542	28	8.45	92
1:2.5	4.8	226	9.8	462	23	6.95	65
1:3	4.3	203	8.8	415	18	8.75	73
1:3.5	4.5	212	9.2	434	16	8.20	72
1:4	4.9	231	10.0	471	13	7.75	74
$\bar{x}$	5.2	244	10.6	499	24	8.22	83
σ	0.6	26	1.2	54	7	0.62	12

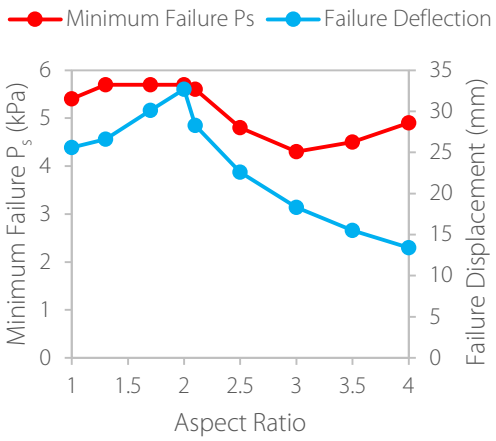

(a) Failure displacement.

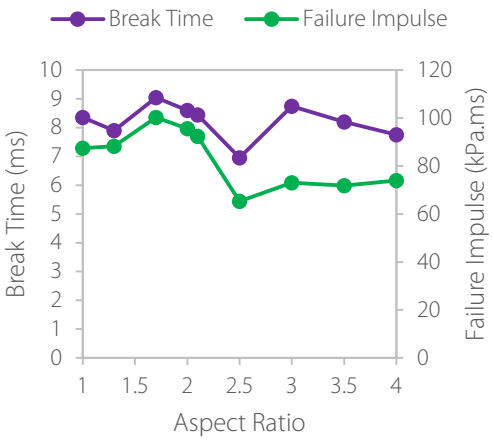

(b) Break time and failure impulse.

Figure 6.23: Minimum failure pressure and break parameters from aspect ratio study.

Break time and failure impulse did not follow the same trend as displacement, indicating that failure displacement at minimum failure pressure was independent of these parameters. The closely linked behaviour of failure displacement and minimum failure P_s with aspect ratio indicates minimum failure pressure was governed by failure displacement for each arrangement. Break time varied between 6.95ms and 9.05ms with a mean result of 8.22±0.62ms. Failure impulse closely matched the break time pattern as it was directly calculated from this parameter. Failure impulse varied between 65kPa.ms and 100kPa.ms with a mean of 83±12kPa.ms.

Five support conditions were tested in the parametric study, rigid and elastic frames that were experimentally benchmarked and three variations determined through a study discussed in section 6.5. A summary of results is outlined in Table 6.12, corresponding break parameters are plotted in Figure 6.24. Minimum failure P_s decreased as support condition rigidity increased. A decrease in minimum failure P_s from 5.4kPa to 3.2kPa was observed when framing varied from elastic to rigid supports. Intermediate support conditions yielded intermediate responses. Increasing elastic support stiffness by increasing Sika sealant stiffness from 2MPa to 10MPa resulted in an increase in minimum failure P_s to 5.6kPa. This was attributed to the stiffer sealant reducing glazing displacement and preventing failure displacement being reached at lower overpressures. Mean minimum failure P_s was 4.6±1.0kPa. The 22% standard deviation produced by support conditions was much higher than t_d and aspect ratio, indicating support conditions had the highest influence on minimum failure pressure.

Table 6.12: Results summary: support conditions parametric study.

	Minimum blast causing failure				Break parameters at minimum failure pressure		
Support Conditions	P_s (kPa)	I_s (kPa.ms)	P_r (kPa)	I_r (kPa.ms)	Failure Displacement (mm)	Break Time (ms)	Failure Impulse (kPa.ms)
Elastic	5.4	255	11.0	518	26	8.35	87
Elastic (10MPa)	5.6	264	11.5	542	21	7.35	81
Elastic (20MPa)	4.6	217	9.4	443	17	7.40	66
Rigid (100MPa)	4.2	198	8.5	401	14	7.35	60
Rigid	3.2	151	6.5	306	10	6.85	43
$\bar{x}$	4.6	217	9.4	442	18	7.46	68
σ	1.0	46	2.0	95	6	0.55	18

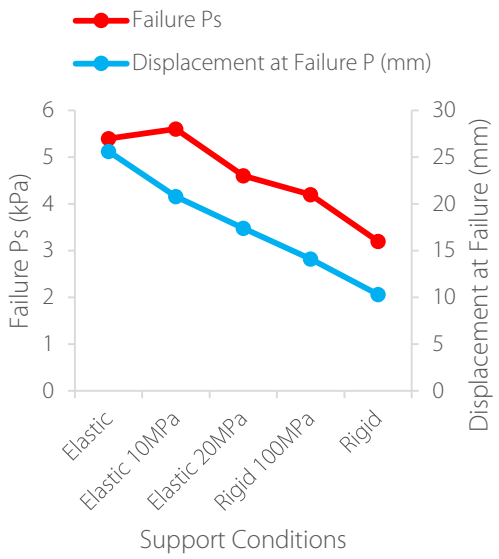

(a) Minimum failure P_s and failure displacement.

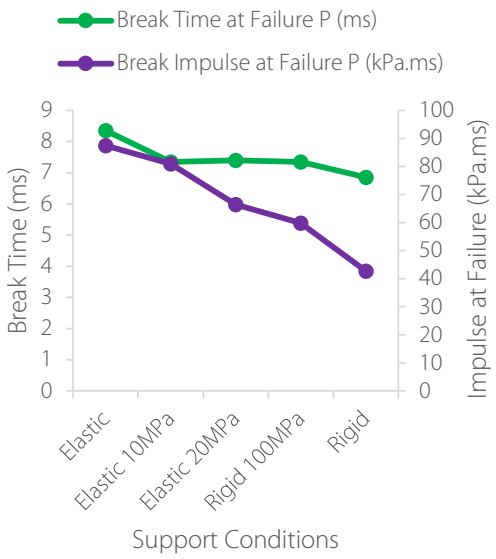

(b) Break time and impulse at failure.

Figure 6.24: Support conditions failure parameters.

Failure displacement decreased from 26mm for elastic supports to 10mm for rigid supports, yielding a mean failure displacement of 18±6mm. Break time and failure impulse also decreased as framing stiffness increased. Break time decreased from 8.35ms for elastic framing to 6.85ms for rigid framing, a decrease of 18%. Failure impulse decreased at a faster rate due to decrease in minimum failure pressure and break time, from which it was calculated. Failure impulse decreased from 87kPa.ms to 43kPa.ms, a decrease of 51%. All results indicated that increasing support condition stiffness resulted in a decreased minimum failure pressure and break parameters.

Increasing positive phase duration resulted in a slight decrease in minimum failure pressure, contradicting current thinking that in long-duration blasts window response is governed by peak overpressure only. This was tested between t_d values of 40ms and 500m corresponding to a reflected impulse range of 200kPa.ms to 2400kPa.ms. The data set should be extended further to incorporate other positive phase durations to determine if the trend continues. Failure appeared to be governed by displacement, which remained constant for all values of t_d tested. Comparing results to the Glazing Hazard Guide "no break" line indicated the Glazing Hazard Guide could be conservative, but unknown support conditions used in testing for the Guide could account for this discrepancy. The mean minimum failure P_s was 5.4±0.4kPa.

Aspect ratio varied between 1:1 and 1:4 produced a mean minimum failure P_s of 5.2±0.6kPa. Peak minimum failure pressure was recorded for aspect ratios between 1:1.3 and 1:2 with a minimum value at 1:3. This trend was dependent on failure displacement which increased to a maximum at 1:2 then decreased with shortest span decrease. An increase in minimum failure P_s above 1:3 was attributed to the glass span being sufficiently small to enable arching action to supports.

Support conditions were varied from elastic to rigid, with three variations between. Increasing support stiffness resulted in a decrease in minimum failure P_s. The exception was elastic supports with sealant stiffness of 10MPa which increased minimum P_s. This was attributed to reduced displacement preventing maximum displacement being reached at lower overpressures. Failure displacement, break time and failure impulse all decreased as frame stiffness increased.

6.7 Damage Curves

Aim five of this research project was production of damage probability curves where probability of window failure was plotted against peak free-field overpressure. Static experimental results analysed in Chapter 5 enabled construction of the damage probability curve in Figure 6.25. By conducting 19 repeats, spread of failure pressures due to material strength was found. An equivalent P_s spread was produced, resulting in a P50 (P_s that fails 50% of glass) of 10.8kPa. The standard deviation was 2.9kPa. In this section, results from the parametric study are interpreted to produce similar damage probability curves for each parameter investigated.

It was assumed that failure was dependent only on peak overpressure in the damage probability curve in Figure 6.25. While in Chapter 5 this was proved to be an adequate assumption for long-

duration blast environments tests, it cannot be transferred to short-duration blast environments. The Glazing Hazard Guide overcomes this by plotting damage states on a PI graph (Figure 6.26). Details of hazard levels can be found in Chapter 2. A PI graph plots damage against pressure and impulse, enabling one chart to be implemented for all blast environments. Contours of damage state were plotted on Glazing Hazard Guide PI graphs, however these could be exchanged for probability of failure contours. This would enable a probability of failure plot for all blast environments.

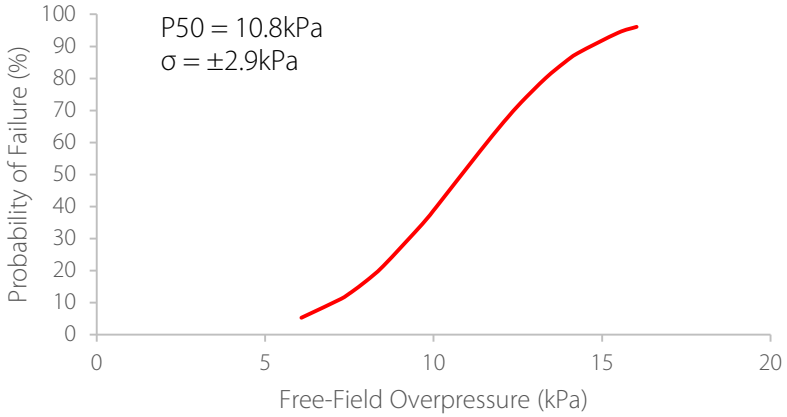

Figure 6.25: Damage probability curve for material strength.

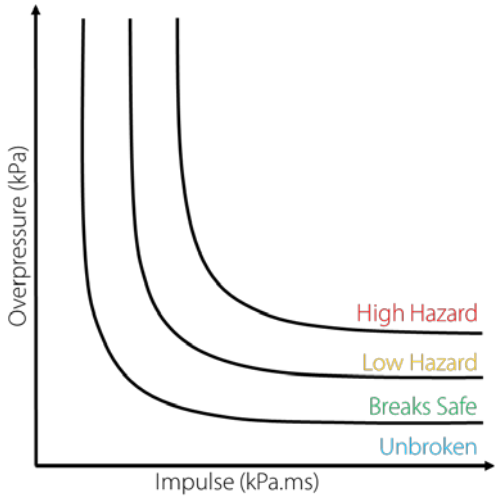

Figure 6.26: Diagram of a PI graph with current Glazing Hazard Guide damage states.

The parametric study was solely undertaken in a long-duration blast environment which can be simplified on a PI graph to horizontal asymptotes. A further study investigating probability of failure in short duration and transient graph regions is recommended as future work. This study would produce vertical asymptotes and connecting curves which are required to enable the PI graph to be used in all blast environments. In the previous section impulse was shown to affect minimum failure pressure, meaning the assumption of horizontal asymptotes was an over simplification. This will be addressed later in this section. Assuming horizontal asymptotes, the probability damage curve for material strength was replotted on a PI graph in Figure 6.27. 2% and 98% probability of failure contours represent ± two standard deviations, 16% and 84% represent ± one standard deviation of

the mean (50%). In design work this graph could be used to find a failure P_r for a required failure probability of 2% for example. In this graph, the corresponding P_r value would be 15.5kPa.

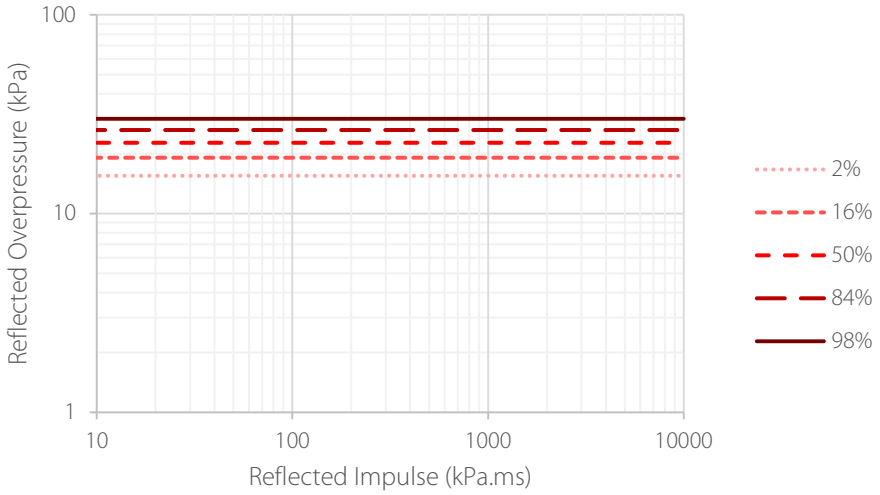

Figure 6.27: Proposed probabilistic PI chart for material strength (lines show asymptotic behaviour for long-duration case only).

In addition to material strength, influence of aspect ratio, positive phase duration and support conditions was investigated and similar plots were produced. A total standard deviation for all variables was calculated using the root mean square (RMS) (equation 6.2). This enabled a general case PI chart and damage probability curve to be produced, considering all structural parameter effects on probability of window failure. Other parameters that σ_{total} is dependent on but were not investigated in this research project are glazing thickness, age, area and type. It is recommended that these parameters are investigated in the future.

$$\sigma_{total} = \sqrt{\sigma_{thickness}{}^2 + \sigma_{AR}{}^2 + \sigma_{supports}{}^2 + \sigma_{material}{}^2 + \sigma_{t_d}{}^2 + \cdots} \qquad 6.2$$

- $\sigma_{thickness}$ Glass thickness
- σ_{AR} Glazing aspect ratio
- $\sigma_{supports}$ Glass support conditions
- $\sigma_{material}$ Glass material strength variability
- σ_{td} Positive phase duration

A summary of minimum failure P_r mean and standard deviation values for each parameter is outlined in Table 6.13. The mean minimum failure P_r for the "Total" column was 10.3kPa. This was the average of results for aspect ratio, t_d and support conditions. Material strength was disregarded due to a smaller glazing area, resulting in higher failure pressures. The material strength standard deviation was assumed transferable to the larger area because the smaller area was expected to produce a conservative larger standard deviation. This can be attributed to a lower critical flaw probability in a smaller pane. To account for the increased minimum failure P_r for material strength, standard deviations were converted into percentages of the mean (third row in table). All % standard deviations were then transformed to standard deviations of the total mean result (10.3kPa). The RMS of

converted standard deviations resulted in a total standard deviation of 3.9kPa. Using the total result for the mean, percentiles were calculated for ± one and two standard deviations. This was undertaken for each parameter and the total. Results for each individual parameter are plotted on reflected PI graphs in Figure 6.28. All plots implemented the same 50% P_r, the total result 10.3kPa.

Table 6.13: Summary of parameter study outcomes for P_r.

Minimum Failure P_r			Material Strength	Aspect Ratio	t_d	Support conditions	Total
$\bar{x}$ (kPa)			22.7	10.6	11.0	9.4	10.3
σ (kPa)			6.4	1.2	1.0	2.0	
σ (% of $\bar{x}$)			28.2	11.0	8.7	21.5	
σ applied to Total $\bar{x}$ (kPa)			**2.9**	**1.1**	**0.9**	**2.2**	**3.9**
Percentiles calculated from Total $\bar{x}$ and σ (kPa)	2%	($\bar{x}$ -2σ)	4.5	8.0	8.5	5.9	2.4
	16%	($\bar{x}$ -1σ)	7.4	9.2	9.4	8.1	6.4
	50%	($\bar{x}$)	10.3	10.3	10.3	10.3	10.3
	84%	($\bar{x}$ +1σ)	13.2	11.4	11.2	12.5	14.2
	98%	($\bar{x}$ +2σ)	16.1	12.6	12.1	14.7	18.2

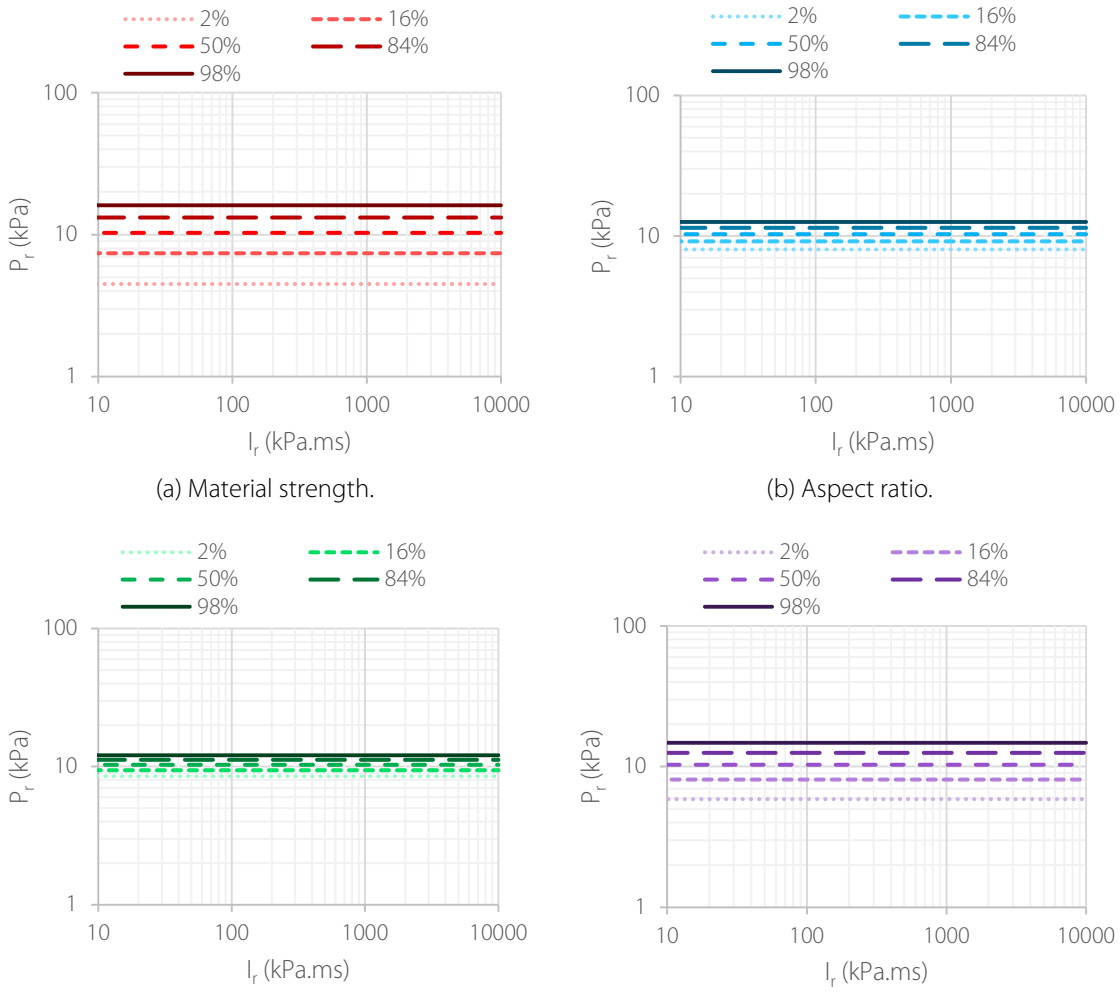

(a) Material strength.

(b) Aspect ratio.

(c) Positive phase duration.

(d) Support conditions.

Figure 6.28: Reflected PI graphs of probability of failure (lines show asymptotic behaviour for long-duration case only).

The largest standard deviation, and therefore largest spread in percentiles, was for material strength. The standard deviation was 2.9kPa, resulting in a 2% failure P_r of 4.5kPa and a 98% failure P_r of 16.1kPa. The second largest standard deviation was 2.2kPa for support conditions, resulting in a 2% failure P_r of 5.9kPa and 98% failure P_r of 14.7kPa. Aspect ratio had the third largest standard deviation of 1.1kPa. This produced 2% and 98% failure P_r values of 8.0kPa and 12.6kPa respectively. The parameter with the least effect on failure pressure was t_d. Standard deviation for positive phase duration was 0.9kPa, resulting in 2% and 98% failure P_r values of 8.5kPa and 12.1kPa. These plots clearly indicate material strength variation was accountable for the largest failure pressure spread, making it the parameter with the greatest effect on window failure pressure. Aspect ratio was the structural parameter with the least influence on failure pressure (t_d was considered a blast parameter not structural parameter) despite in Chapter 5 being identified for having the greatest influence on break time and failure displacement of broken windows. Positive phase duration was expected to have little effect in a long-duration blast regime, but a standard deviation of 0.9kPa indicate its influence should not be disregarded.

The total standard deviation was 3.9kPa and the resulting total reflected PI graph is shown in Figure 6.29. Damage probability curves for each parameter and total result are plotted in Figure 6.30 for reference. The total reflected PI graph indicates when considering material strength, aspect ratio, support conditions and positive phase duration, 2% failure P_r was 2.4kPa and 98% failure P_r was 18.2kPa. This PI graph represents new annealed glass with a 4mm thickness and area of 0.89m^2 only. Further studies into the effect of aging, other glass types, thickness and area should be undertaken to extend the PI graph to a more general case. The PI graph produced from this study is likely to be conservative. Applied blast loading was a Friedlander curve for an infinite wall, assuming no clearing. In reality clearing would reduce impulse applied, but this may have little effect as failure is likely to have occurred before clearing finishes.

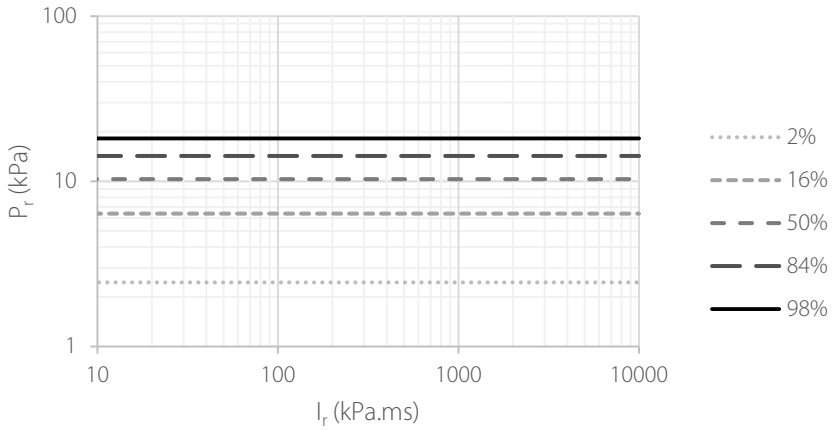

Figure 6.29: Reflected PI graph of probability of failure from all parameters (lines show asymptotic behaviour for long-duration case only).

The equivalent free-field damage probability curve was calculated from free-field results outlined in Table 6.14. The mean failure pressure when considering the influence of all four parameters was 5.0kPa, with a standard deviation of 1.9kPa. This resulted in a 2% failure P_s of 1.3kPa and a 98% failure P_s of 8.8kPa. Damage probability curves for each parameter and the total are plotted against P_s in

Figure 6.31. From Chapter 4, the mean P_s over six trials was 6.3kPa for trials designed to be P_s 5kPa. From the damage probability curve, the expected probability of failure would be 75%. Out of 12 windows tested at this overpressure, three survived meaning that 75% of windows failed as the curve predicted. The mean P_s for trials designed to have P_s 10kPa was 10.1kPa. All windows failed. A 98% failure probability was predicted at P_s 8.8kPa, indicating a strong probability that all windows would fail at 10.1kPa. With a low sample number, it is a coincidence that such good agreement has occurred. More experimental data are required to validate damage probability curves and PI graphs but good agreement between graphs and experimental data indicate these graphs produce sensible results.

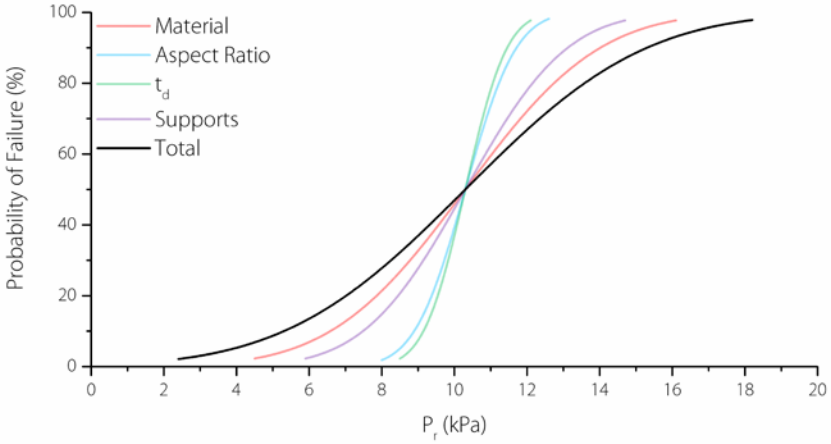

Figure 6.30: Damage probability curve of P_r for all parameters.

Table 6.14: Summary of parameter study outcomes for P_s.

Minimum Failure P_s			Material Strength	Aspect Ratio	t_d	Support conditions	Total
$\bar{x}$ (kPa)			10.8	5.2	5.4	4.6	5.0
σ (kPa)			2.9	0.6	0.5	1.0	
σ (% of $\bar{x}$)			27.2	10.8	8.4	21.1	
σ applied to Total $\bar{x}$ (kPa)			**1.4**	**0.5**	**0.4**	**1.1**	**1.9**
Percentiles calculated from Total $\bar{x}$ and σ (kPa)	2%	($\bar{x}$ -2σ)	2.3	4.0	4.2	2.9	1.3
	16%	($\bar{x}$ -1σ)	3.7	4.5	4.6	4.0	3.2
	50%	($\bar{x}$)	5.0	5.0	5.0	5.0	5.0
	84%	($\bar{x}$ +1σ)	6.4	5.6	5.5	6.1	6.9
	98%	($\bar{x}$ +2σ)	7.8	6.1	5.9	7.2	8.8

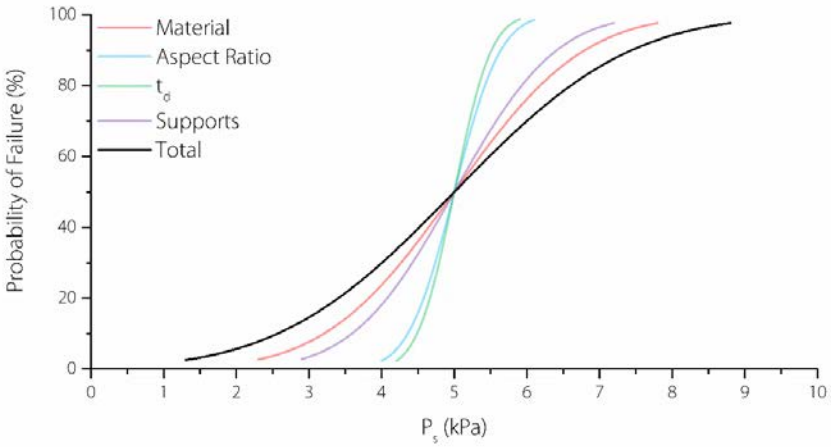

Figure 6.31: Damage probability curve of P_s for all parameters.

It was demonstrated earlier in this section that t_d and impulse influence failure pressure even in a long-duration environment. The minimum failure line for three t_d values tested is replotted in Figure 6.32 and an equation of a linear best fit line is stated adjacent to the plot. The negative gradient indicates failure pressure decreased as positive phase duration and impulse increased. This behaviour was only tested between impulses of 200kPa.ms and 2400kPa.ms, further investigation is required to extend the failure line. The linear trend line gradient in Figure 6.32 was applied to the total reflected PI graph. Circles represent the original contours plotted in Figure 6.29. The gradient was only applied between modelled impulses, above which a horizontal asymptote was assumed. No failure lines were drawn for impulses lower than 200kPa.ms as behaviour could not be assumed constant approaching the short-duration blast regime. This modification reduces the 2% failure P_r at I_r greater than 2400kPa.ms to 2.2kPa. The 50% probability of failure reduced to 9.2kPa and 98% failure P_r reduced to 16.3kPa. For smaller impulses the failure pressure increased, 50% probability of failure for an impulse of 200kPa.ms increased to 11.1kPa.

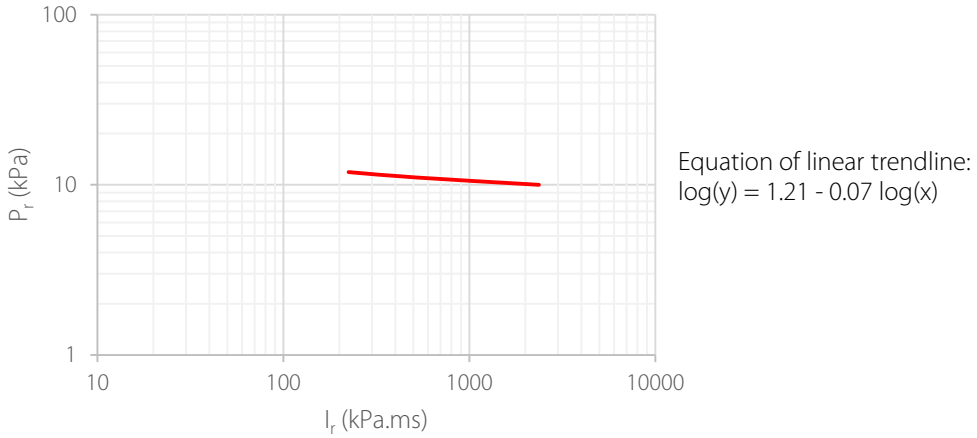

Figure 6.32: Minimum failure line from t_d parametric study.

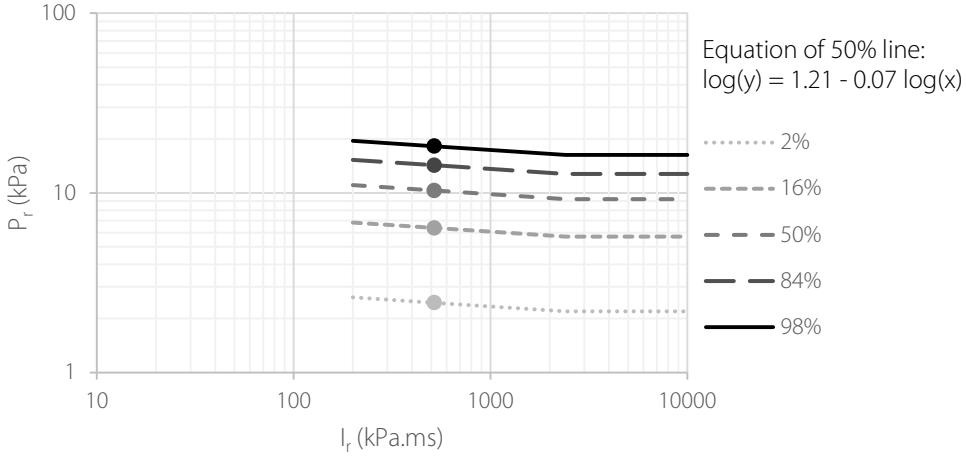

Figure 6.33: Reflected PI graph of probability of failure with t_d effects allowed for.

6.7.1 Proposed Design Method

Probability of damage contour plots developed in this section can be used for predicting damage and for blast resistant window design. For damage prediction, the specified pressure and impulse can

be used to read probability of window failure directly from the long-duration general graph (Figure 6.31). For example in the Tianjin image 43% of windows failed, excluding frame failure. This relates to a predicted peak free-field overpressure of 4.7kPa so the photographed building was approximately 2km away from the point of detonation based on Kingery-Bulmash calculations (UN SaferGuard, 2015). Peak free-field overpressure could be calculated using the existing Glazing Hazard Guide charts but would require additional fragment throw information not available from the image. The conservative nature of the Guide would also result in a much greater distance being calculated.

For window design, an acceptable probability of failure should be selected depending on building use. This would be used to determine allowable blast parameters from the general graph. Factors for specific aspect ratios and support conditions should be derived from Figure 6.22 and Figure 6.24a respectively. For example aspect ratio 1:3 produced a minimum reflected failure pressure of 8.8kPa. The general graph was based on an average failure pressure of 10.3kPa. A factor of 0.83 (specific failure pressure/average failure pressure) should be applied to the pressure read from the general window plot (Figure 6.29). These factors should be developed and tabulated as future work.

6.8 Conclusions

In this chapter, computational modelling and production of damage probability curves has been described. A material study was undertaken using FEA software Lusas Modeller to determine an accurate glass Young's Modulus and material strength from experimental results. A simplified model of the Phase S2 experimental set-up was produced. A Young's Modulus of 42.6MPa and material strength of 68MPa produced numerical results that best agreed with experimental data. Two software specific material parameters, separation strain and post-failure shear stiffness factor, were identified in Chapter 3 for investigation. A sensitivity study, using dynamic trial data for comparison, indicated that a separation strain of 0.007 and an unchanged value of 0.01 of for the post-failure shear stiffness factor resulted in the best agreement with experimental data.

Material model results were implemented in the benchmarking study. 27 unique glazing arrangements experimentally tested in this research project and previous research provided a benchmark for the computational model. Results indicated that modelled rigid support conditions were more severe than those tested in the ABT. As a result, numerical break times and failure displacements were consistently less than those observed experimentally. A comparably small over-prediction of break parameters was observed for elastically supported arrangements, indicating structural sealant stiffness could be a little low in the simulation. Normalised results for both support conditions were consistent, indicating AEM was capable of modelling structural and blast parameter trends well. Benchmarking results were converted to ELS reliability limits, outlining the extent that parameters could be varied before confidence in ELS reduced and further experimental data were required. Peak free-field overpressure limits were extrapolated to 0-20kPa. Above this it was assumed that material overloading would cause failure. Aspect ratio reliability limits were extended to 1:4,

above which behaviour could not be confidently predicted due to arching to supports. No reliability limits were produced for support conditions as a linear scale did not exist.

In the main parametric study, minimum overpressures resulting in window failure for various aspect ratios and support conditions were determined. Peak overpressure was decreased in each model until window survival occurred. Positive phase duration was maintained at 100ms in all models and was then investigated as a separate parameter. Rigid and elastic frame stiffness was modified to provide additional support conditions. Increasing positive phase duration slightly decreased the glazing minimum failure pressure, indicating impulse dependency in a long-duration blast. Comparison to the Glazing Hazard Guide indicated a higher failure pressure than specified in the Guide. Only three durations were selected between 40ms and 500ms and it is recommended this data set is extended further. Varying aspect ratio between 1:1 and 1:4 resulted in a maximum failure pressure between aspect ratios 1:1.3 and 1:2 and a minimum at 1:3. This result was determined to be displacement dependent. Generally minimum failure pressure decreased as support stiffness was increased. A small increase in failure pressure was observed for elastic supports with sealant stiffness of 10MPa, this was attributed to reduced displacements due to stiffer supports.

Results from the main parametric study were implemented in damage probability curves for annealed glass, objective five of this thesis. These curves were plotted against peak free-field overpressure only, meaning results were only relevant for a long-duration blast. An alternative method was proposed whereby results were plotted as contours of failure probability on a PI curve, in a similar layout to the Glazing Hazard Guide. As only long-duration blast was considered, these plots were simplified to horizontal contours. The gradient from the positive phase duration study was then applied to the plot to allow for impulse dependency. Further research in transient and short-duration blast regimes would complete the PI graphs, enabling them to be used in all blast environments. Individual plots were produced for material strength, support conditions, t_d and aspect ratio. Material strength was identified as the parameter with the largest data spread and therefore the greatest influence on failure pressure. The root mean square of failure pressure standard deviations produced a general plot for all windows. It was acknowledged that this plot did not incorporate glazing thickness, age, area or type and these were identified as further research areas.

This research project has highlighted the extent that window failure pressure varies due to structural parameters. Charts in the Glazing Hazard Guide only specify two glazing arrangements and no method of converting to other dimensions indicating that area and aspect ratio are not critical to failure pressure. This thesis has proven this assumption to be wrong: glazing dimensions can significantly influence window failure pressure. Current design methods, stated in the Glazing Hazard Guide, use damage states classified by fragment throw, assuming all windows with the same dimensions behave in exactly the same way. In this thesis a new method has been proposed, in which design should be instead based on probability of failure. Damage probability PI graphs produced in this research project enable this new method of design to be implemented.

Chapter 7

Conclusions and Future Work

7.1 Conclusions

The aim of this thesis was to investigate the significance of parameters such as peak overpressure, aspect ratio and support conditions on annealed glazing response to long-duration blast loading. Full-scale experimental trials and an experimentally benchmarked parametric study quantified parameter significance to glazing failure, facilitating production of annealed glass damage probability curves.

The key findings of this thesis are:

1. Computational modelling of annealed glass is too complex to undertake without comprehensive experimental benchmarking.
2. Triangulation of piezo transducers is a cost-effective and accurate method of recording glazing failure time and crack location.
3. Glazing response to blast loading is dependent on a complex interaction of structural parameters. Effects of structural parameters are not independent from one another.
4. Aspect ratio had the greatest effect on break parameters when window failure occurred.
5. Material strength variation produced the largest spread in window failure pressures.
6. The Glazing Hazard Guide could advantageously be updated to incorporate PI graphs with probability of window failure contours.

Forty windows were tested in twenty individual ABT trials over two dynamic trial series. The ABT blast environment was highly consistent across all trials, the largest total reflected impulse standard deviation was just 2% of the mean. Consistent reflected overpressure histories provided reliable loading and accurate impulse measurements. Three out of 12 windows subjected to peak reflected overpressure (P_r) 12kPa survived. It was concluded that P_r 12kPa was close to the survival threshold for 4mm thick annealed glass with area 0.89m^2. Peak overpressure had the greatest effect on windows with aspect ratio 1:1. This was attributed to the large glass span causing higher susceptibility to other parameters. Impulse received before failure increased with P_r. Data spread was low, indicating a strong relationship between the parameters. Aspect ratio had little effect on elastically supported windows and aspect ratio influence on rigidly framed windows decreased as P_r was increased. This was attributed to material overloading at higher overpressures resulting in a punching effect through the glass which minimised the effect of structural parameters. Peak failure displacement and impulse for rigidly framed windows was recorded at aspect ratio 1:1.3. Above this, the higher aspect ratio induced an increased arrangement stiffness, decreasing break time and displacement. Support condition influence was small except for arrangements with aspect ratio 1:1. The higher sensitivity to support conditions in these arrangements was attributed to a larger span. Aspect ratio had the largest influence on break time and failure displacement whereas impulse at failure was highly influenced by peak overpressure. It was concluded that the significance of each structural parameter was dependent on interaction with other structural parameters. Trends in break parameters indicated interlinkage of structural parameters and that glazing behaviour was dependent on a complex combination of all parameters.

A new method of capturing glazing failure based on triangulation of piezo transducer signals was trialled initially in static tests and refined through two dynamic test phases. This quick and cost-effective technique of capturing window failure was a reliable alternative to high-speed video which is limited by frame rate and camera-shake in the harsh blast environment of the ABT. The technique was successful in both dynamic and static testing, implying a wide range of possible applications in brittle material testing. This method was presented at Conference on Fire and Blast (CONFAB) 2017 and a journal paper was submitted to Engineering Failure Analysis. Both papers can be found in the appendices. The work was also presented at the Group of Experts on Mitigation Systems (GEMS) 19th Annual Meeting in January 2018.

Experimental data were used to comprehensively benchmark computational models. Results normalised against experimental data yielded good consistency, implying computational results agreed well with experimental trends. A numerical study into structural parameter influence on window failure pressure was undertaken. Increasing t_d resulted in a small decrease in failure pressure, indicating some impulse dependency in a long-duration blast event. It is recommended that this data set is increased to determine the full trend. Comparison to the Glazing Hazard Guide indicated, as concluded in literature, that the Guide was conservative for long-duration blast loading. The maximum failure pressure for aspect ratio was recorded for aspect ratios between 1:1.3 and 1:2. The

minimum failure pressure was at aspect ratio 1:3. This trend was concluded to be displacement dependent. Failure pressure decreased as support condition stiffness increased. The exception to this was the elastic frame with sealant stiffness 10MPa, which was attributed to increased sealant stiffness reducing displacement. Damage probability curves, objective five of this thesis, were produced from parametric study results. The largest spread in failure pressure was caused by material strength, indicating this parameter had the largest influence on window survival or failure. It was acknowledged that further damage curves were required for glazing area, thickness, type and age to produce a general curve for all windows.

The Glazing Hazard Guide is a 21 year old document that is still used for blast-resistant glazing design in 2018. Only two 4mm thick annealed glazing arrangements are accommodated in the Guide and material strength variation is not considered. Only one frame type was implemented in tests for the Guide. Contours on PI graphs are of fragment throw based hazard levels, assuming consistent responses from windows with the same dimensions and have been shown to be overly conservative. This thesis demonstrates there are significant trends between window failure pressure and structural parameters such as aspect ratio, area and support conditions. Material strength was responsible for failure pressure variation of ±28% of the mean in experimental work undertaken for this research project. Based on the findings of this thesis it is recommended that new PI charts are produced implementing probability of failure contours to account for window response variation. Individual PI graphs for each structural parameter and a general graph for all windows should be produced. The probabilistic method already has precedent in seismic and flood design practice where structures are designed to resist an event with a specified occurrence probability. Failure probability charts capture true glazing behaviour. Probability of window failure is a parameter that is easy to interpret and highlights to the user that window response is variable and should be treated statistically. The charts can be used to rapidly predict and assess damage at the scene or by analysing photographs. If failure probability contour graphs are made available for glazing, they would be very useful design tools for prediction of window failure and design of safer urban environments.

The aim of this thesis was to investigate significance of blast and structural parameters on annealed glazing response to long-duration blast loading. In four series of experimental trials, influence of aspect ratio, support conditions, material strength and peak overpressure on break parameters was investigated. Experimental results enabled comprehensive computational benchmarking prior to a parametric study. This study investigated influence of aspect ratio, support conditions and t_d on window failure pressure. Experimental and computational results enabled production of damage probability curves for 4mm thick new annealed glass with area 0.89m^2. Glazing area, thickness, type and age were identified as influential parameters that should be investigated in the future. Short-comings of the damage probability curves were identified and a new method was proposed whereby probability of failure contours are plotted on PI graphs, enabling one global chart to be used for all blast environments.

7.2 Future Work

Based on the conclusions of this thesis the following future work is recommended.

The importance of a high number of experimental repeats due to material strength variation was highlighted in this thesis. It is therefore recommended that Phase D2 trials are repeated to increase number of repeats for each arrangement to four. This will enable better standard deviations to be calculated, especially for arrangements with glass that survived.

Aspect ratio, support conditions, material strength and peak overpressure were investigated in this thesis. Glazing area, thickness, type and age were identified as further parameters that could influence glazing response to blast loading. It is recommended that these parameters are investigated and PI graphs are produced.

Further long-duration blast tests in the ABT should be undertaken at lower overpressures. P_s of 6kPa was the lowest that could be consistently tested at the time of trials for this thesis. 25% of windows subjected to this pressure survived, indicating the P50 pressure was lower than 6kPa. It is recommended that P_s values between 2kPa and 6kPa are investigated to determine the survival/failure threshold of this glazing arrangement.

Two support conditions were tested in this research project, rigid and elastic. Neither of these frames are regularly used in industry but were thought to represent outer bounds of support conditions typically used. It was highlighted that experimentally benchmarking these outer bounds did not mean that all possible frames were benchmarked. Recommended future work includes experimentally testing typical frames found in industry and verifying that break parameters lie within rigid and elastic bounds. The data could be used for benchmarking these frames, enabling their addition to support condition PI curves.

Triangulation of acoustic emissions recorded by piezo transducers was a cost-effective and accurate method of calculating break time and crack location in the glass. Further refining the method by increasing number of piezo transducers per window and testing the technique with other types of glass and brittle materials is recommended.

To further increase accuracy of material models implemented in ELS, glass and structural sealant samples should be sent to a material testing laboratory. Alternatively strain gauges should be applied to glass tested in the static testing box to experimentally determine a Young's Modulus. The numerical model should be extended to incorporate the container front wall. It was identified that the container walls moved during the blast and not modelling this could have caused over-estimation of stiffness in the rigid supports.

Probability of failure plots on PI graphs were simplified to horizontal asymptotes for the long-duration section. Further experimental testing and computational modelling should be undertaken for the whole range of impulses to determine the full shape of probability of failure contours. ELS reliability limits should be extended by further benchmarking structural parameters. For example experimental

testing of higher aspect ratios would extend the reliability limit above 1:4 and these new aspect ratios could be incorporated into the aspect ratio PI graph.

Applied element method software ELS was used for all numerical work in this research project. Benchmarking demonstrated that the material model in ELS was simplistic, relying on the MPS criterion rather than modelling a flaw distribution. While good agreement was found between break parameters modelled in ELS and experimental results, other software with better glazing material models could provide improved results. A review of other available software and their capabilities should be undertaken to determine if ELS should be retained or replaced by a more capable software.

The aim of this thesis has been to determine whether glazing failed, and to quantify the failure if this occurred. Parameters selected were break time, failure displacement and impulse at failure. Video footage from all trials is sufficient to also analyse leading fragment velocity and fragment mass distribution. These data could be used to predict fragment throw distance, enabling classification of window failure in accordance with the Glazing Hazard Guide or determination of skin penetration at different standoffs. This would provide not only data on how structural parameters influence probability of failure but also injury level. It is recommended that data from all ABT trials are reanalysed to determine leading fragment velocity and fragment mass distribution. These data could be used to design a trial series investigating shard penetration into gelatine, enabling conversion to maximum standoff behind a window where skin penetration would occur. This would mean structural data from glazing trials could be directly converted to an injury level that may be used to determine injury probability in the event of an explosion.

References

Applied Research Associates Inc. (2004) 'A.T.-Blast, version 2.2'. Alburquerque, NM USA: Applied Reserach Associates, Inc. Available at: http://www.ara.com/prod- ucts/AT-blast.htm.

Applied Science International LLC. (2010) *Extreme Loading for Structures - Theoretical Manual*. Durham, North Carolina.

Ataei, H. and Anderson, J. C. (2014) 'Computational Modeling of Glass Panels for Mitigating the Injuries Due to Air Blast', *Advances in Materials Science and Applications*, 3(3), pp. 109–119. doi: 10.5963/AMSA0303002.

BBC News (2015) *China explosions: What we know about what happened in Tianjin*. Available at: http://www.bbc.co.uk/news/world-asia-china-33844084 (Accessed: 2 February 2016).

Beason, W. L., Kohutek, T. L. and Bracci, J. M. (1998) 'Basis for ASTM E 1300 Annealed Glass Thickness Selection Charts', *Journal of Structural Engineering*, 124(2), pp. 216–221.

Beason, W. L. and Morgan, J. R. (1984) 'Glass Failure Prediction Model', *Journal of Structural Engineering*, 110(2), pp. 197–212.

Bewick, B., Rolater, G., Sanai, M. and Ziemba, A. (2015) 'Debris Hazards Due to Overloaded Conventional Construction Facades', in *16th International Symposium for the Interaction of the Effects of Munitions with Structures*. Destin, Florida: University of Florida. Available at: https://www.protection-consultants.com/wp-content/uploads/2016/01/Bewick-ISIEMS-2015-Debris-Hazards-Due-to-Overload-Conventional-Construction-Facades.pdf.

Brasie, W. C. and Simpson, D. W. (1968) 'Guidelines for estimating damage from chemical explosions',

in *Symposium on Loss Prevention in the Process Industries, 63rd National Meeting*. St Louis, MO, USA: Association of Industrial Chemical Engineers.

British Geological Survey (2016) *Analysis of the Buncefield Oil Depot Explosion 11 December 2005*, *Natural Environment Research Council*. Available at: http://earthquakes.bgs.ac.uk/research/events/buncefield_explosion.html (Accessed: 3 March 2016).

British Standards Institution (2012) *BS EN 572-1:2012: Glass in building – Basic soda lime silicate glass products – Part 1: Definitions and general physical and mechanical properties*. Available at: https://www.bsigroup.com/ (Accessed: 10 February 2018).

Brode, H. L. (1995) 'Numerical Solutions of Spherical Blast Waves', *Journal of Applied Physics*, 6(26), pp. 766–775.

Byrnes, J. (1953) *Effects of an atomic explosion on two typical two-storey-and-basement wood-frame houses (WT-792)*. Washington D.C. Available at: https://apps.dtic.mil/dtic/tr/fulltext/u2/611251.pdf (Accessed: 20 September 2017).

Cady, W. G. (1964) *Piezoelectricity: an introduction to the theory and applications of electromechanical phenomena in crystals*. New York: Dover Pubilcations Inc.

Calderone, I. (2000) *The equivalent wind loading for window glass design.* PhD Thesis. Monash University, Melbourne, Australia.

Chen, S., Zhu, C. G., Li, G. Q. and Lu, Y. (2016) 'Blast test and numerical simulation of point-supported glazing', *Advances in Structural Engineering*, 19(12), pp. 1841–1854. doi: 10.1177/1369433216649387.

Chilton, C. A. B. (1962) 'Resistance of Glass Windows to Atomic Blast', in Department Of the Navy (ed.) *Studies in Atomic Defence Engineering*. Washington D.C.: Department of the Navy, Bureau of Yards and Docks.

Claber, K. J. (1998) 'Designing Window Glazing for Explosive Loading', in *Proceedings IEEE 32nd Annual 1998 International Carnahan Conference on Security Technology*. Washington D.C.: IEEE, pp. 65–72. doi: 10.1109/CCST.1998.723768.

Clark, W. C. (1954) *Window and glass hazards under wartime conditions and recommended protective measures*. Washington D.C.: United States Department of Energy. Available at: https://catalog.hathitrust.org/Record/011572974 (Accessed: 18 December 2017).

Clark, W. C. (1955) *The effect of atomic weapons on glazing and window construction*. Washington D.C.: United States Atomic Energy Commission. Available at: https://catalog.hathitrust.org/Record/011571972 (Accessed: 5 December 2017).

Clubley, S. K. (2014) 'Non-linear long duration blast loading of cylindrical shell structures', *Engineering Structures*. Elsevier Ltd, 59, pp. 113–126. doi: 10.1016/j.engstruct.2013.10.030.

Cormie, D., Mays, G. C. and Smith, P. D. (2009) *Blast Effects on Buildings*. 2nd edn. London: ICE

Publishing.

European Organisation for Technical Approvals (2006) *EU Technical Approval: Dow Corning*. Brussels: European Organisation for Technical Approvals. Available at: http://www.eckelt.at/de/downloads/produkte/structural_glazing/ssg/eta_approval_dc993__dc895.pdf.

Feldmann, M. and Kasper, R. (2014) *Guidance for European Structural Design of Glass Components*. Ispra, Italy: European Commission. doi: 10.2788/5523.

Fire Prevention and Engineering Bureau of Texas and The National Board of Fire Underwriters (1947) *Texas City, Texas, Disaster: April 16, 17, 1947*. Available at: http://www.local1259iaff.org/report.htm (Accessed: 21 November 2017).

Fletcher, E. R., Richmond, D. R. and Jones, R. K. (1973) 'Air blast effects on windows in buildings and automobiles on the Eskimo II Event', in *Minutes of 15th Explosives Safety Seminar - Volume 1*. San Fransisco: Department of Defence Explosives Safety Board, pp. 251–275.

Friedlander, F. G. (1946) 'The Diffraction of a Sound Pulse. 1. Diffraction by a Semi-Infinite Plane', *Proceedings of the Royal Society of London*, 186, pp. 322–344.

Fu, G., Wang, J. and Mingwei, Y. (2016) 'Anatomy of Tianjin Port Fire and Explosion: Process and Causes', *Process Safety Progress*, 35(3), pp. 216–220.

Ge, J., Li, G. Q. and Chen, S. W. (2012) 'Theoretical and experimental investigation on fragment behavior of architectural glass panel under blast loading', *Engineering Failure Analysis*, 26, pp. 293–303.

Glasstone, S. and Dolan, P. J. (1977) *The Effects of Nuclear Weapons*. Third Ed. Washington D.C.: United States Department of Defense and the Energy Research and Development Administration.

Gohel, V., Patel, P. V. and Joshi, D. (2013) 'Analysis of frame using applied element method (AEM)', *Procedia Engineering*, 51(NUiCONE 2012), pp. 176–183. doi: 10.1016/j.proeng.2013.01.026.

Griffith, A. A. (1921) 'The Phenomena of Rupture and Flow in Solids', *Philosophical Transactions of the Royal Society of London. Series A, Containing Papers of a Mathematical or Physical Character*, 221(582–593), pp. 163–198.

Gubinelli, G., Zanelli, S. and Cozzani, V. (2004) 'A simplified model for the assessment of the impact probability of fragments', *Journal of Hazardous Materials*, 116, pp. 175–187.

Harris, R. J., Marshall, M. R. and Moppett, D. J. (1977) 'Response of glass windows to explosion pressures', in *6th Symposium Chemical Process Hazards*. Manchester: Institution of Chemical Engineers Symposium Series.

Henrych, J. (1979) *The Dynamics of Explosion and Its Use*. Amsterdam, New York: Elsevier Scientific Pub. Co.

Hershey, R. L., Higgins, T. H. and Magrab, E. B. (1974) 'Application of the response probability density function technique to predicting the probability of sonic-boom glass breakage', *The Journal of the Acoustical Society of America*, 55(5), pp. 1009–1017.

Hidallana-Gamage, H. D., Thambiratnam, D. P. and Perera, N. J. (2015) 'Influence of Structural Sealant Joints on the Blast Performance of Laminated Glass Panels', *Journal of Performance of Constructed Facilities*, 29(6), p. 04014151: 1-15. doi: 10.1061/(ASCE)CF.1943-5509.0000646.

Hooper, P. A., Sukhram, R. A. M., Blackman, B. R. K. and Dear, J. P. (2012) 'On the blast resistance of laminated glass', *International Journal of Solids and Structures*, 49(6), pp. 899–918.

Huang, P. and Zhang, J. (2015) 'Facts Related to August 12, 2015 Explosion Accident in Tianjin, China', *Process Safety Progress*, 34(4), pp. 313–314.

Johns, R. (2016) *Investigating Annealed Glazing Response to Long-Duration Blast*. PhD Thesis. University of Southampton.

Johns, R. V. and Clubley, S. K. (2015) 'Post-fracture response of blast-loaded monolithic glass', *Proceedings of the Institution of Civil Engineers - Structures and Buildings*, 168(7), pp. 469–478. doi: 10.1680/stbu.13.00099.

Johns, R. V. and Clubley, S. K. (2016) 'The influence of structural arrangement on long-duration blast response of annealed glazing', *International Journal of Solids and Structures*, 97–98, pp. 370–388. doi: 10.1016/j.ijsolstr.2016.07.012.

Johns, R. V. and Clubley, S. K. (2017) 'Experimentally Investigating Annealed Glazing Response to Long-Duration Blast', *Journal of Structural Engineering*, 143(11), p. 04017152: 1-13. doi: 10.1061/(ASCE)ST.1943-541X.0001888.

Keys, R. A. (2016) *Experimental & Computational Structural Analysis of Masonry Panels Subject to Long Duration Blast Loading*. PhD Thesis. University of Southampton.

Kraull, W. R., Siskos, W. R., Stewart, R. A. and Spindler, R. G. (1981) 'The behaviour of float glass under uniform windo loading', in *4th U.S. National Conference on Wind Engineering Research*. University of Washington, Seattle, Washington.

Krauthammer, T. and Altenberg, A. (2000) 'Negative phase blast effects on glass panels', *International Journal of Impact Engineering*, 24(1), pp. 1–17.

Kumar, P. and Shukla, A. (2011) 'Dynamic response of glass panels subjected to shock loading', *Journal of Non-Crystalline Solids*, 357(24), pp. 3917–3923.

Lam, N. T. K., Gad, E. F., Nurhuda, I. and Calderone, I. (2011) 'Impact Resistance of Annealed Glass Panels', *Journal of Performance of Constructed Facilities*, 25(5), pp. 422–432.

Larcher, M. (2007) *Simulation of the Effects of an Air Blast Wave*. Ispra, Italy: Joint Research Centre.

Lilley, S. (2013) 'Kiloton Killer: The collision of the SS Mont-Blanc and the Halifax Explosion', *NASA Safety Centre*, 7(1), pp. 1–5.

Lupoae, M. and Bucur, C. (2009) 'Building demolition - positive aspect of progressive collapse', *MTA Review*, XIX(4), pp. 399–408.

Lusk, B., Salim, H., Perry, K., Nawar, M., Wedding, W. C., Kiger, S. and Ibrahim, A. (2011) 'Modeling and Testing of Laminated Window Systems under Blast Loading', in *Structures Congress*. Las Vagas, Nevada: American Society of Civil Engineers, pp. 1552–1560.

Mallonee, S., Shariat, S., Stennies, G., Waxweiler, R., Hogan, D. and Jordan, F. (1996) 'Physical injuries and fatalities resulting from the Oklahoma City bombing', *Journal of the American Medical Association*, 276(5), pp. 382–387. doi: 10.1001/jama.276.5.382.

Marchand, K. A., Conrath, E. J., Stevens, D. J. and Meyer, S. B. (2006) 'Blast induced glass hazards: a comparison of design approaches and recent research', in *Structures Under Shock and Impact IX*. Southampton, UK: WIT Press (WIT Transactions on The Built Environment, Vol 87), pp. 259–268. doi: 10.2495/SU060261.

McGarry, S. L., Balsari, S., Muqueeth, S. and Leaning, J. (2017) *Preventing the Preventable: The 2015 Tianjin Explosions*. Cambridge, MA: Harvard School of Public Health. Available at: http://www.hkjcdpri.org.hk/download/casestudies/Tianjin_CASE.pdf (Accessed: 17 October 2017).

Meguro, K. and Tagel-Din, H. S. (2002) 'Applied Element Method Used for Large Displacment Structure Analysis', *Journal of Natural Disaster Science*, 24(1), pp. 25–34.

Meyer, B. S., Little, L. and Conrath, E. (2004) *Injury Based Glass Hazard Assessment*. San Antonio, TX USA: Applied Research Associates. Available at: https://apps.dtic.mil/dtic/tr/fulltext/u2/a548169.pdf (Accessed: 19 August 2017).

Morison, C. (2010) 'The resistance of laminated glass to blast pressure loading and the coefficients for single degree of freedom analysis of laminated glass'. Available at: http://dspace.lib.cranfield.ac.uk/handle/1826/4651.

Morse, S. M. and Norville, H. S. (2010) 'Relationship between Probability of Breakage to Maximum Principal Stresses in Window Glass', *Journal of Architectural Engineering*, 16(1), pp. 20–28. doi: 10.1061/(ASCE)1076-0431(2010)16:1(20).

Nawar, M., Salim, H., Lusk, B. and Kiger, S. (2015) 'Modeling and Shock Tube Testing of Architectural Glazing Systems for Blast Resistance', *Journal of Structural Engineering*, 141(7), p. 04014174: 1-9. doi: 10.1061/(ASCE)ST.1943-541X.0001130.

Norville, H. S. and Conrath, E. J. (2006) 'Blast-Resistant Glazing Design', *Journal of Architectural Engineering*, 12(3), pp. 129–136.

Norville, H. S., Harvill, N., Conrath, E. J., Shariat, S. and Mallonee, S. (1999) 'Glass-Related Injuries in

Oklahoma City Bombing', *Journal of Performance of Constructed Facilities*, 13(2), pp. 50–56.

Norville, H. S. and Minor, J. E. (1985) 'Strength of weathered window glass', *American Ceramic Society Bulletin*, 64(11), pp. 1467–1470.

Nurhuda, I., Lam, N. T. K., Gad, E. F. and Calderone, I. (2010) 'Estimation of strengths in large annealed glass panels', *International Journal of Solids and Structures*, 47(18–19), pp. 2591–2599.

Orr, L. E. (1957) *Engineering Properties of Glass*. Publication 48. Washington, D.C.: Building Research Institute, National Academy of Sciences, National Research Council.

Overend, M. and Zammit, K. (2012) 'A computer algorithm for determining the tensile strength of float glass', *Engineering Structures*, 45, pp. 68–77. doi: 10.1016/j.engstruct.2012.05.039.

Pelfrene, J., Kuntsche, J., Van Dam, S., Van Paepegem, W. and Schneider, J. (2016) 'Critical assessment of the post-breakage performance of blast loaded laminated glazing: Experiments and simulations', *International Journal of Impact Engineering*, 88, pp. 61–71.

Pilkington North America Inc (2013) *Technical Bulletin: Properties of Soda-Lime Silica Float Glass*. Toledo, Ohio: NSG Group. Available at: http://www.pilkington.com/en/us/window-manufacturers/technical-bulletins (Accessed: 14 January 2018).

Pittsburgh Plate Glass Industries (1979) *PPG glass thickness recommendations to meet arcitects specified 1-minute wind load*. Pittsburgh: Technical Services/Flar Glass Division, Pittsburgh Plate Glass Industries Inc.

Pritchard, D. K. (1981) 'Breakage of glass windows by explosions', *Journal of Occupational Accidents*, 3(2), pp. 69–85.

Quinn, G. D. (2016) *NIST Recommended Practice Guide Fractography of Ceramics and Glasses*. Gaithersburg, MD: National Institute of Standards and Technology. doi: 10.6028/NIST.SP.960-16e2.

Randall, P. A. (1961) *Damage to Conventional and Special Types of Residences Exposed to Nuclear Effects*. Washington D.C.: United States Atomic Energy Commission. doi: 10.2172/4029823.

Security Facilities Executive Special Services Group - Explosion Protection (1997) *Glazing Hazard Guide RESTRICTED*. Cabinet Office, London.

Seica, M. V., Krynski, M., Walker, M. and Packer, J. A. (2011) 'Analysis of Dynamic Response of Architectural Glazing Subject to Blast Loading', *Journal of Architectural Engineering*, 17(2), pp. 59–74.

Smith, P. and Hetherington, J. (1994) *Blast and Ballistic Loading of Structures*. 6th edn. Oxford: Butterworth-Heinemann.

Spiller, K., Packer, J. A., Seica, M. V. and Yankelevsky, D. Z. (2016) 'Prediction of annealed glass window response to blast loading', *International Journal of Impact Engineering*, 88, pp. 189–200.

Steel Construction Institute (2009) *Buncefield Explosion Mechanism Phase 1*. London: Health and

Safety Executive. Available at: http://www.hse.gov.uk/research/rrpdf/rr718.pdf (Accessed: 5 September 2017).

Tagel-Din, H. and Rahman, N. A. (2006) 'Simulation of the Alfred P. Murrah Federal Building Collapse Due to Blast Loads', in *Architectural Engineering Conference (AEI)*. Omaha, USA: American Society of Civil Engineers. doi: 10.1061/40798(190)32.

Trawinski, E., Fisher, J. W. and Dinan, R. J. (2004) *AFRL-ML-TY-TP-2005-4508 Full Scale Testing of Polymer Reinforced Blast Resistant Windows*. Florida, USA: Air Force Research Laboratory Report.

Tsai, C. R. and Stewart, R. A. (1976) 'Stress analysis of large deflection of glass plates by the finite-element method', *Journal of the American Ceramic Society*, 59(9–10), pp. 445–448.

UFC 3-340-02 (2008) *Structures to resist the effects of accidental explosions.* United States of America: Department of Defense.

UN SaferGuard (2015) *Kingery-Bulmash Blast Parameter Calculator*. Available at: https://www.un.org/disarmament/un-saferguard/kingery-bulmash/ (Accessed: 3 January 2019).

Vallabhan, C. V. G. and Wang, B. Y.-T. (1981) *Nonlinear analysis of rectangular glass plates by finite difference method NTIS Rep. No. PB84-159649*. Lubbock, Tex.: Institute for Disaster Research, Texas Tech Univ.

Veer, F. A., Bos, F. P., Zuidema, J. and Romein, T. (2005) 'Strength and fracture behaviour of annealed and tempered float glass 1', in *11th International Conference on Fracture*. Turin, Italy: Curran Associates, pp. 3055–3060.

Vives, A. A. (2008) *Piezoelectric Transducers and Applications*. 2nd edn. Edited by A. A. Vives. Berlin, Heidelberg: Springer Berlin Heidelberg. doi: 10.1007/978-3-540-77508-9.

Wedding, W. C. and Lusk, B. T. (2012) 'Novel method to determine blast resistant glazing system response to explosive loading', *Measurement: Journal of the International Measurement Confederation*. Elsevier Ltd, 45(6), pp. 1471–1479. doi: 10.1016/j.measurement.2012.03.002.

Wei, J. and Dharani, L. R. (2005) 'Fracture mechanics of laminated glass subjected to blast loading', *Theoretical and Applied Fracture Mechanics*, 44(2), pp. 157–167.

Wei, J., Shetty, M. S. and Dharani, L. R. (2006) 'Failure analysis of architectural glazing subjected to blast loading', *Engineering Failure Analysis*, 13(7), pp. 1029–1043.

Weibull, W. (1939) *A statistical theory of the strength of materials*, *Royal Swedish Institute for Engineering Research*. PhD Thesis. Generalstabens Litografiska Anstalts Förlag, Stockholm, Sweden.

Zhang, X., Zou, Y., Hao, H., Li, X., Ma, G. and Liu, K. (2012) 'Laboratory Test on Dynamic Material Properties of Annealed Float Glass', *International Journal of Protective Structures*, 3(4), pp. 407–430. doi: 10.1260/2041-4196.3.4.407.

Appendix A

Reference Results: ABT Trials 2014

In 2014, a series of 33 full-scale trials were completed in the ABT. Annealed glass, 4mm and 8mm thick, was subjected to a blast environment with P_s 14kPa and t_d 110ms. Thirteen different arrangements were implemented. Glazing support conditions, thickness, aspect ratio and area were all varied and each arrangement was repeated three times. Tables A.1 and A.2 outline the glazing arrangements and recorded break parameters. Break time was calculated from camera data and peak displacement was measured from video footage of a deflection gauge. Tables A.3 to A.8 detail the calculated 90% confidence intervals for each trial measurement. These results were used to benchmark initial AEM models described in section 3.2.

Table A.1: Trial data: rigid arrangements.

	Break Time (ms)	Failure Impulse (kPa.ms)	Failure Displacement (mm)	Window Response
Trial 1 (4mm, 1:1, 0.25m^2)	2.50	65.7	10	Broken
Trial 2 (4mm, 1:1, 0.25m^2)	2.50	59.2	10	Broken
Trial 3 (4mm, 1:1, 0.25m^2)	2.50	63.0	10	Broken
Trial 4 (4mm, 1:1.75, 0.25m^2)	2.00	67.6	10	Broken
Trial 5 (4mm, 1:1.75, 0.25m^2)	2.00	72.6	10	Broken
Trial 6 (4mm, 1:1.75, 0.25m^2)	2.50	86.6	10	Broken
Trial 7 (8mm, 1:1, 0.89m^2)	4.50	130.2	16	Broken
Trial 8 (8mm, 1:1, 0.89m^2)	4.25	122.2	17	Broken
Trial 9 (8mm, 1:1, 0.89m^2)	6.00	193.8	22	Broken
Trial 10 (8mm, 1:1.7, 0.89m^2)	4.50	129.2	17	Broken
Trial 11 (8mm, 1:1.7, 0.89m^2)	3.50	104.9	12	Broken
Trial 12 (8mm, 1:1.7, 0.89m^2)	4.50	137.2	17	Broken
Trial 13 (4mm, 1:1, 0.89m^2)	3.50	84.8	22	Broken
Trial 14 (4mm, 1:1, 0.89m^2)	2.50	64.4	10	Broken
Trial 15 (4mm, 1:1, 0.89m^2)	4.50	120.0	23	Broken

Table A.2: Trial data: elastic arrangements.

	Break Time (ms)	Failure Impulse (kPa.ms)	Failure Displacement (mm)	Window Response
Trial 1 (4mm, 1:1, 0.25m^2)	3.50	88.9	10	Unbroken
Trial 2 (4mm, 1:1, 0.25m^2)	3.25	91.4	10	Broken
Trial 3 (4mm, 1:1, 0.25m^2)	3.00	80.6	10	Broken
Trial 4 (4mm, 1:1.75, 0.25m^2)	3.00	98.4	10	Broken
Trial 5 (4mm, 1:1.75, 0.25m^2)	2.00	75.2	10	Broken
Trial 6 (4mm, 1:1.75, 0.25m^2)	2.50	83.2	10	Unbroken
Trial 7 (8mm, 1:1, 0.89m^2)	3.50	110.6	12	Broken
Trial 8 (8mm, 1:1, 0.89m^2)	3.50	135.1	12	Broken
Trial 9 (8mm, 1:1, 0.89m^2)	4.50	135.0	15	Broken
Trial 10 (8mm, 1:1.7, 0.89m^2)	3.50	106.6	12	Broken
Trial 11 (8mm, 1:1.7, 0.89m^2)	3.50	112.3	12	Broken
Trial 12 (8mm, 1:1.7, 0.89m^2)	3.50	108.2	10	Broken
Trial 13 (4mm, 1:1, 0.89m^2)	3.00	76.8	17	Broken
Trial 14 (4mm, 1:1, 0.89m^2)	4.50	124.4	25	Broken
Trial 15 (4mm, 1:1, 0.89m^2)	4.00	93.3	22	Broken
Trial 16 (4mm, 1:1.7, 0.89m^2)	3.50	92.6	22	Broken
Trial 17 (4mm, 1:1.7, 0.89m^2)	3.00	77.7	17	Broken
Trial 18 (4mm, 1:1.7, 0.89m^2)	3.50	84.7	20	Broken

Table A.3: 90% confidence interval of break time: rigid arrangements.

Arrangement		Mean Break Time (ms)	Standard Deviation	Standard Error	90% Confidence
1	4mm, 1:1, 0.25m^2	2.5	0.0	0.0	0.0
2	4mm, 1:1.75, 0.25m^2	2.2	0.3	0.2	0.5
3	8mm, 1:1, 0.89m^2	4.9	0.9	0.5	1.6
4	8mm, 1:1.7, 0.89m^2	4.2	0.6	0.3	1.0
5	4mm, 1:1, 0.89m^2	3.5	1.0	0.6	1.7

Table A.4: 90% confidence interval of failure impulse: rigid arrangements.

Arrangement		Mean Failure Impulse (kPa.ms)	Standard Deviation	Standard Error	90% Confidence
1	4mm, 1:1, 0.25m^2	62.6	3	2	6
2	4mm, 1:1.75, 0.25m^2	75.6	10	6	17
3	8mm, 1:1, 0.89m^2	148.7	39	23	66
4	8mm, 1:1.7, 0.89m^2	123.8	17	10	28
5	4mm, 1:1, 0.89m^2	89.7	28	16	47

Table A.5: 90% confidence interval of failure displacement: rigid arrangements.

Arrangement		Mean Failure Displacement (mm)	Standard Deviation	Standard Error	90% Confidence
1	4mm, 1:1, 0.25m^2	10	0	0	0
2	4mm, 1:1.75, 0.25m^2	10	0	0	0
3	8mm, 1:1, 0.89m^2	18	3	2	5
4	8mm, 1:1.7, 0.89m^2	15	3	2	5
5	4mm, 1:1, 0.89m^2	18	7	4	12

Table A.6: 90% confidence interval of break time: elastic arrangements.

Arrangement		Mean Break Time (ms)	Standard Deviation	Standard Error	90% Confidence
1	4mm, 1:1, 0.25m^2	3.3	0.3	0.1	0.4
2	4mm, 1:1.75, 0.25m^2	2.5	0.5	0.3	0.8
3	8mm, 1:1, 0.89m^2	3.8	0.6	0.3	1.0
4	8mm, 1:1.7, 0.89m^2	3.5	0.0	0.0	0.0
5	4mm, 1:1, 0.89m^2	3.8	0.8	0.4	1.3
6	4mm, 1:1.7, 0.89m^2	3.3	0.3	0.2	0.5

Table A.7: 90% confidence interval of failure impulse: elastic arrangements.

Arrangement		Mean Failure Impulse (kPa.ms)	Standard Deviation	Standard Error	90% Confidence
1	4mm, 1:1, 0.25m^2	87.0	6	3	10
2	4mm, 1:1.75, 0.25m^2	85.6	12	7	20
3	8mm, 1:1, 0.89m^2	126.9	14	8	24
4	8mm, 1:1.7, 0.89m^2	109.0	3	2	5
5	4mm, 1:1, 0.89m^2	98.2	24	14	41
6	4mm, 1:1.7, 0.89m^2	85.0	7	4	13

Table A.8: 90% confidence interval of failure displacement: elastic arrangements.

Arrangement		Mean Failure Displacement (mm)	Standard Deviation	Standard Error	90% Confidence
1	4mm, 1:1, 0.25m^2	10	0	0	0
2	4mm, 1:1.75, 0.25m^2	10	0	0	0
3	8mm, 1:1, 0.89m^2	13	2	1	3
4	8mm, 1:1.7, 0.89m^2	11	1	1	2
5	4mm, 1:1, 0.89m^2	21	4	2	7
6	4mm, 1:1.7, 0.89m^2	20	3	1	4

Appendix B

Test Specifications

UNIVERSITY OF SOUTHAMPTON

Glazing Trials Specification

Static Phase 1: Evaluation of break detection methods

Static Phase 2: Influence of edge finish and quantifying material strength

Version Number	3	**Author**	Sarah Monk
Date	March 2017	**Supervisors**	Dr Simon Clubley Dr James Robinson Dr John Adams
Status	Final draft		

Contents

Version No.	Changes since previous version
3	Modification of Phase S2 diagnostics and testing rig post completion of Phase S1.

1 Introduction

The following experimental trial specification is for the PhD thesis titled 'Breakage Response of Glass Panels subject to Long-Duration Blast'. These trials will be undertaken in collaboration with AWE and the testing team Spurpark Ltd. Phase Static 1 (S1) should be completed before dynamic trials begin (see separate test specification). Phase Static 2 (S2) should be completed by end of the 2017 calendar year.

Phase S1 will evaluate two methods of detecting window failure. Using a static testing rig, break circuits and triangulation of piezo transducers will be tested and their response times compared. The most effective method will be used in dynamic trials.

Phase S2 will investigate the influence of glass edge finishing using a modified static testing rig. Twenty samples will be tested to failure, enabling quantification of material strength variation.

2 Phase S1

2.1 Overview

The testing box will be designed and constructed by Spurpark Ltd and will consist of an airtight steel container supporting the framed glass specimen (see Figure 1). The frame aperture will be 620mm x 620mm to contain a glass sample size of 700mm x 700mm. Four clamps on each frame edge will provide rigid support conditions. A vacuum pump will reduce the container pressure in small increments, allowing pressure equalisation, until glass failure occurs. The testing box should be capable of withstanding a pressure of 60kPa.

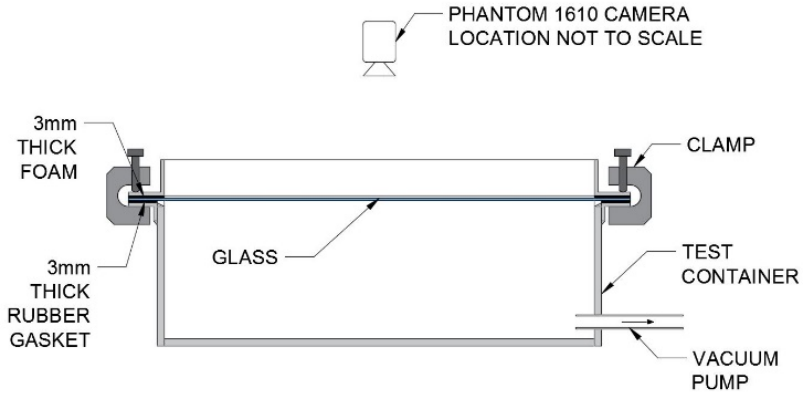

Figure 1: Diagram of static testing rig set-up.

2.2 Diagnostics

Five tests will be undertaken to determine the most effective break detection method. The tests will be designed iteratively, depending on results from the previous trial. The test schedule and diagnostics required for initial trials is outlined in Table 1 and Figure 2.

Table 1: Phase S1 test schedule.

Test No.	Piezo transducers	Conductive Paint
1	2x piezos in unknown locations to test capability.	Single strip along centreline.
2	4x piezos, one in each corner, 100mm from frame edges.	Geometric pattern.
3 **4** **5**	If previous trials successful, test method repeatability.	If previous trials successful, test method repeatability.

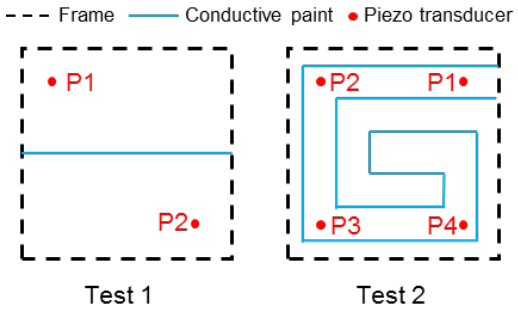

Figure 2: Diagnostics layout for initial Phase S1 tests.

Piezo transducers will be applied to the top surface of the glass in locations specified in Table 1. This will enable calculation of break time and crack location by triangulation of the cracking sound arrival time at each piezo transducer.

Break circuits will be applied to the top surface of the window using a silver based paint (http://uk.rs-online.com/web/p/conductive-adhesives/1015621/). Circuit lines should be 3mm wide. Break circuit resistance should be less than 1Ω, two layers of paint should be adequate for this resistance to be achieved. Circuit resistance should be recorded to determine when the circuit and the glass has broken.

Additional diagnostics required in all tests:

- **Camera:** One high-speed camera viewing the sample from above will record the crack pattern and break time, providing an independent data set (minimum frame rate: 50,000fps).
- **Pressure gauge:** Located inside the testing container, this will provide a pressure history enabling the glazing failure pressure to be recorded.
- **Deflection gauge:** This will record central deflection of glass sample until failure.

Data from all gauges should be recorded using a data logger with a sample rate of 1MHz.

2.3 Materials

All samples will be new annealed glass with dimensions 700mm x 700mm x 4mm. Five samples are required.

The frame and testing box will be constructed from steel grade S355.

3 Phase S2 Modifications (post Phase S1)

3.1 Overview

Twenty glass samples will be tested to failure using a modified static testing rig. All samples will be 4mm thick, new annealed glass. Ten samples will have cut edges with no treatment. The edges of the other ten samples should be ground down after cutting to remove damage. Failure pressures and crack locations will be compared for both groups.

3.2 Testing Rig

The testing rig frame will be modified to closer represent framing used in dynamic trials (outlined in Figure 3). Clamps to restrain the glass will be replaced by bolts beyond the glass extents, preventing stress concentrations in the glass. The aperture will be reduced to 520mm x 520mm to enable this modification. The glazing dimensions will also be reduced to 600mm x 600mm.

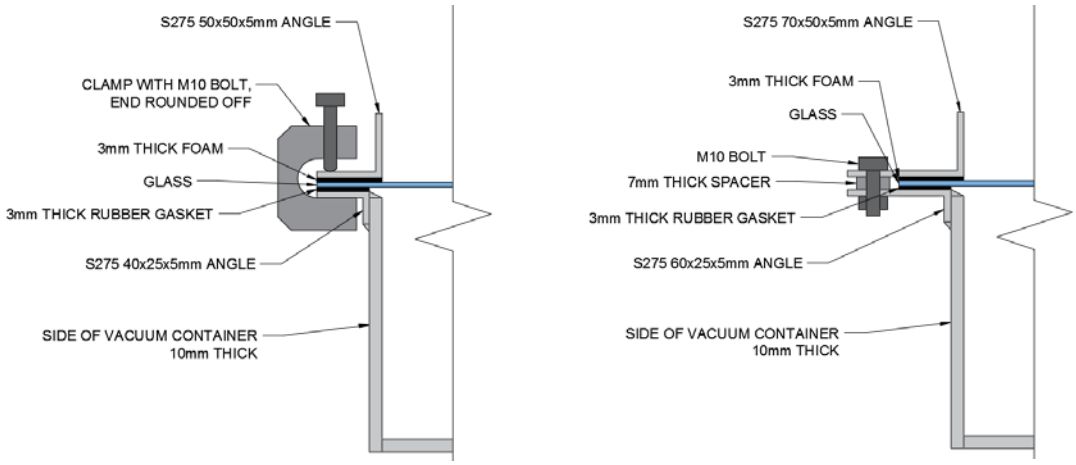

(a) Phase S1. (b) Phase S2.

Figure 3: Comparison of framing details for Phases S1 and S2.

3.3 Diagnostics

The following gauges will be required in all trials.

- **Five piezo transducers:** these will be located in each corner (100mm from edges) and one in the glass centre. See Figure 4 for layout.
- **Camera:** One high-speed camera viewing the sample from above will record the crack pattern and break time, providing an independent data set (minimum frame rate: 50,000fps).
- **Pressure gauge:** Located inside the testing container, this will provide a pressure history enabling the glazing failure pressure to be recorded.
- **Deflection gauge:** This will record central deflection of glass sample until failure.

Data from all gauges should be recorded using a data logger with a sample rate of 1MHz.

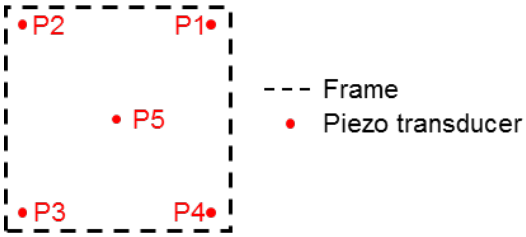

Figure 4: Phase S2 piezo transducer layout.

UNIVERSITY OF SOUTHAMPTON

Glazing Trials Specification

Dynamic Phase 1: Influence of aspect ratio and verification of piezo transducers as diagnostic tools

Dynamic Phase 2: Influence of aspect ratio and overpressure on glazing behaviour

Version Number	9	**Author**	Sarah Monk
Date	January 2017	**Supervisors**	Dr Simon Clubley Dr James Robinson Dr John Adams
Status	Final draft – post Phase S1		

Contents

Version No.	Changes since previous version
9	- Removal of DIC, break circuits and LED scattering - Amendment of piezo locations based on static tests - Amendment of camera spec based on talks with Mike during static testing

1 Introduction

The following experimental trial specification is for the PhD thesis titled 'Breakage Response of Glass Panels subject to Long-Duration Blast'. These trials will be carried out in collaboration with AWE and testing team Spurpark Ltd. Dynamic trials should be undertaken by the end of the 2017 calendar year, after completion of Phase Static 1 (see separate test specification). Phase Dynamic 1 (D1) should be completed before Phase Dynamic 2 (D2).

Phase D1 will investigate the influence of aspect ratio on glass failure at P_s[1] of 14kPa. Triangulation of piezo transducers to detect glazing failure will be further trialled in the ABT[2].

Phase D2 will investigate the influence of structural and blast parameters on glazing behaviour when subjected to long-duration blast loading in the ABT. Parameters to be investigated are aspect ratio, overpressure and support conditions. In 12 firings, six glazing arrangements will be tested in two different blast environments.

2 Trials Description

2.1 Phase D1

Two steel ISO containers, positioned in the 10.2m section of the ABT, will each support one window per trial. Window response will be recorded by high-speed video. Triangulation of piezo transducers as a break detection method will be further investigated in these trials.

Eight trials will be undertaken with window aspect ratios ranging from 1:1 to 1:2. All windows will be 4mm thick, annealed and new. Glazing area will be 0.89m^2 in all trials and all samples will be supported by rigid frames. A trial schedule with required window aspect ratios is outlined in Table 1. The windows in each cubicle should be identical for all trials. Window codes must be visible to all cameras.

Table 1: Trial schedule and glazing arrangements: Phase D1.

Trial	Aspect Ratio	Cubicle 1 Code	Cubicle 2 Code
1	1:1	ABT17-101	ABT17-102
2	1:1.3	ABT17-103	ABT17-104
3	1:1.7	ABT17-105	ABT17-106
4	1:2	ABT17-107	ABT17-108
5	1:1	ABT17-109	ABT17-110
6	1:1.3	ABT17-111	ABT17-112
7	1:1.7	ABT17-113	ABT17-114
8	1:2	ABT17-115	ABT17-116

Expected blast parameters: P_s = 14kPa, t_d[3] = 110ms.

[1] P_s – Peak free-field overpressure
[2] ABT – Air blast tunnel
[3] t_d – Positive phase duration

2.2 Phase D2

ISO container layout will match Phase D1. All glazing will be 4mm thick and annealed with an area of 0.89m^2. All glass will be new. The windows in the cubicles will be identical in all trials. The trial schedule and glazing arrangements are outlined in Table 2. Window codes must be visible to all cameras. In 12 trials, three aspect ratios (1:1, 1:1.3 and 1:2) will be subjected to two blast environments with P_s of 5kPa and 10kPa respectively. All windows will be tested with elastic and rigid support conditions.

Table 2: Trial schedule and glazing arrangements: Phase D2.

Trial	P_s (kPa)	Aspect Ratio	Support Conditions	Cubicle 1 Code	Cubicle 2 Code
1	10	1:1	Rigid	ABT17-201	ABT17-202
2	10	1:1	Elastic	ABT17-203	ABT17-204
3	10	1:1.3	Rigid	ABT17-205	ABT17-206
4	10	1:1.3	Elastic	ABT17-207	ABT17-208
5	10	1:2	Rigid	ABT17-209	ABT17-210
6	10	1:2	Elastic	ABT17-211	ABT17-212
7	5	1:1	Rigid	ABT17-213	ABT17-214
8	5	1:1	Elastic	ABT17-215	ABT17-216
9	5	1:1.3	Rigid	ABT17-217	ABT17-218
10	5	1:1.3	Elastic	ABT17-219	ABT17-220
11	5	1:2	Rigid	ABT17-221	ABT17-222
12	5	1:2	Elastic	ABT17-223	ABT17-224

3 Test Cubicles

Steel ISO containers were constructed by Spurpark Ltd for previous glazing trials trials and will be re-used in this trial series. Modular sub-frames enable each frame to be constructed separately and quickly fitted to the test cubicles. Sub-frames will be bolted to the test cubicle to provide a rigid connection. All window frames will fit in the existing sub-frame aperture so no modification is necessary. The containers will be located in the 10.2m section of the ABT and orientated normal to the blast wave. An elevation of the test cubicles is shown in Figure 1.

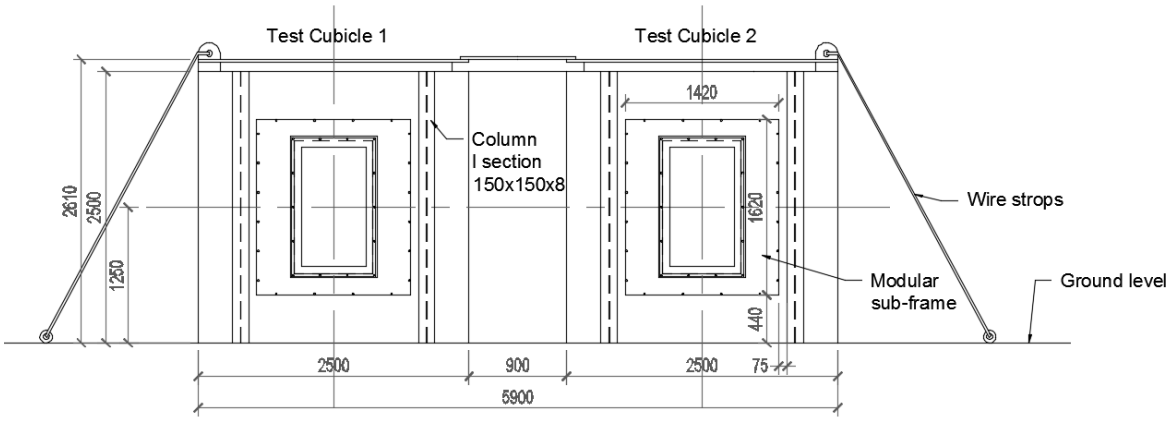

Figure 1: Front elevation of test cubicles. View towards ABT RWE.

4 Diagnostics

4.1 Overview

The diagnostics layout in the ABT are shown in plan in Figure 2.

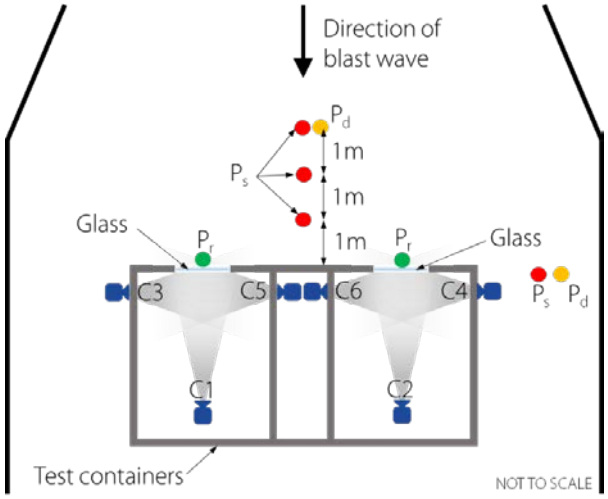

KEY:

P_s – Static overpressure gauge

P_r – Reflected overpressure gauge

P_d – Dynamic overpressure gauge

C – High-speed video camera

Figure 2: ABT plan showing test cubicles and diagnostics layout.

- **Incident static pressure gauges (4)**

  Three will be placed at 1m intervals upstream of test cubicles (see Figure 2). The fourth gauge will be in line with the cubicle front face. All gauges will be 0.5m above ground level.

- **Dynamic pressure gauges (2)**

  One gauge will 3m upstream of the cubicles, the other in line with the cubicle front face. All gauges will be 0.5m above ground level.

- **Surface mounted reflected pressure gauges (2 – one on each cubicle)**

  These will be mounted to the test cubicle beneath the window and in line with the window vertical centreline.

- **Piezo transducers (10 – five on each window)**

  All gauges will be adhered to the inside face of the glass using superglue. Four will be located in each corner, 50mm from the edges. A fifth will be located in the window centre. Piezo transducer locations are shown in Figure 5.

- **High speed cameras (6 –three in each cubicle)**

  Located as shown in Figure 2. Cameras will be fixed to the ABT floor, isolated from the container. See section 3.2 for a detailed camera specification.

- **LED signifying blast arrival (2 – one for each window)**

  This will be mounted to the test cubicle in view of a side camera. The LED will illuminate when the blast wave arrives at the front surface of the test cubicle.

- **Deflection gauges (2 – one on each window)**

  These will be attached to the window centre on the rear face. The gauges will be 100mm long with 10mm intervals marked. Gauges will be fully visible to both side cameras in each cubicle.

- **Still photographs**

  Photographs of windows and frames will be taken before firing. Photographs will be taken after firing of frames and glass fragments.

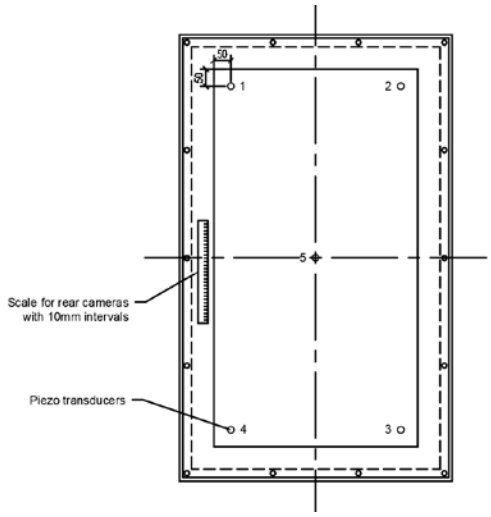

Figure 3: Piezo transducer locations.

Data from all gauges will be recorded by a data logger at a sample rate of 1MHz.

4.2 Camera Set-up

Camera locations are shown in Figure 6, camera numbers correspond to Table 3. All cameras except C5 and C6 will have a minimum resolution of 800 x 600 pixels. Cameras C5 and C6 will have a reduced pixel number to increase frame rate. These cameras should capture full movement of the deflection gauge prior to window failure. Scale with 10mm intervals marked will be attached to the inside of the frame and visible to cameras C1 and C2 to enable crack location measurement.

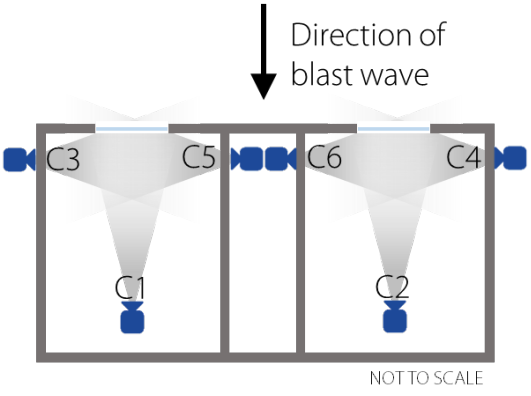

Figure 4: Camera locations in the test cubicles.

Table 3: Descripton of camera views and specifications.

Camera Number	Frame Rate (fps)	Description
1,2	75,000	Rear camera records break time and crack pattern. Whole window to be captured.
3,4	Min 5,000	Side view of whole window. Provides overview of deflection shape.
5,6	75,000	View of deflection gauge only. Number of pixels reduced to increase frame rate.

5 Materials

All windows will be annealed glass, 4mm thick with an area of 0.89m^2. Frames will be constructed of steel grade S355 and be 10mm thick.

6 Expected Responses

Phase D1: All windows are expected to fail. It is anticipated that repeat window arrangements will show some agreement, with some variation to material strength inconsistency. Aspect ratio is expected to affect break time, failure deflection and crack patterns.

Phase D2: All windows are predicted to break. Arrangements one to six should break faster than arrangements seven to 12.

7 Frame dimensions

Frame and glass dimensions for each aspect ratio and framing type are outlined in Table 3 and Table 4. The dimensions are shown in corresponding Figure 4 and Figure 5. For the rigid frame, the glass sample will be restrained by steel frames bolted together against spacers to ensure uniform restraint. 3mm thick foam will be adhered to both sides of the glass to prevent stress concentrations due to uneven frame surfaces. A typical bolt arrangement is shown in Figure 4. Number and layout of bolts will be determined by Spurpark Ltd. Elastic supports will use Sika SG500 to attach the glass to the frames to create pinned support conditions. Specialist contractor Firman Glass will carry out all work with Sika SG500.

Rigid frames with aspect ratios 1:1 and 1:1.7 were built for previous trials and could be reused providing they are undamaged. Rigid frames with aspect ratios 1:1.3 and 1:2 will need to be constructed. These frames will be used in Phases D1 and D2. All elastic frames used in Phase D2 will need to be constructed. These frames will not be reused. Stated glass dimensions are ideal dimensions, glazing should be sized to fit the frame aperture.

Table 4: Glass and frame dimensions: rigid arrangements.

Phase D1 Trial No.	**1, 5**	**2, 6**	**3, 7**	**4, 8**
Phase D2 Trial No.	**1,7**	**3,9**		**5,11**
Glazing Thickness (mm)	4	4	4	4
A_x (mm)	995	877	775	717
A_y (mm)	995	1125	1280	1384
B_x (mm)	815	697	595	537
B_y (mm)	815	945	1100	1204
C (mm)	90	90	90	90
D (mm)	30	30	30	30
E (mm)	65	65	65	65
F (mm)	10	10	10	10
X (mm)	945	827	725	667
Y (mm)	945	1075	1230	1334
X:Y	1:1	1:1.3	1:1.7	1:2
X × Y (Glazing Area) (m^2)	0.89	0.89	0.89	0.89
B_x × B_y (Exposed Area) (m^2)	0.66	0.66	0.65	0.65
Exposed Area / Glazing Area	0.74	0.74	0.73	0.73

Table 5: Glass and frame dimensions: elastic arrangements.

Phase D1 Trial No.			
Phase D2 Trial No.	**2,8**	**4,10**	**6,12**
Glazing Thickness (mm)	4	4	4
A_x (mm)	995	877	717
A_y (mm)	995	1125	1384
B_x (mm)	815	697	537
B_y (mm)	815	945	1204
C (mm)	90	90	90
D (mm) (Bite depth)	60	60	60
E (mm)	30	30	30
F (mm)	65	65	65
G (mm)	10	10	10
H (mm) (Glue line)	12	12	12
X (mm)	945	827	667
Y (mm)	945	1075	1334
X:Y	1:1	1:1.3	1:2
X × Y (Glazing Area) (m^2)	0.89	0.89	0.89
B_x × B_y (Exposed Area) (m^2)	0.66	0.66	0.65
Exposed Area / Glazing Area	0.74	0.74	0.73

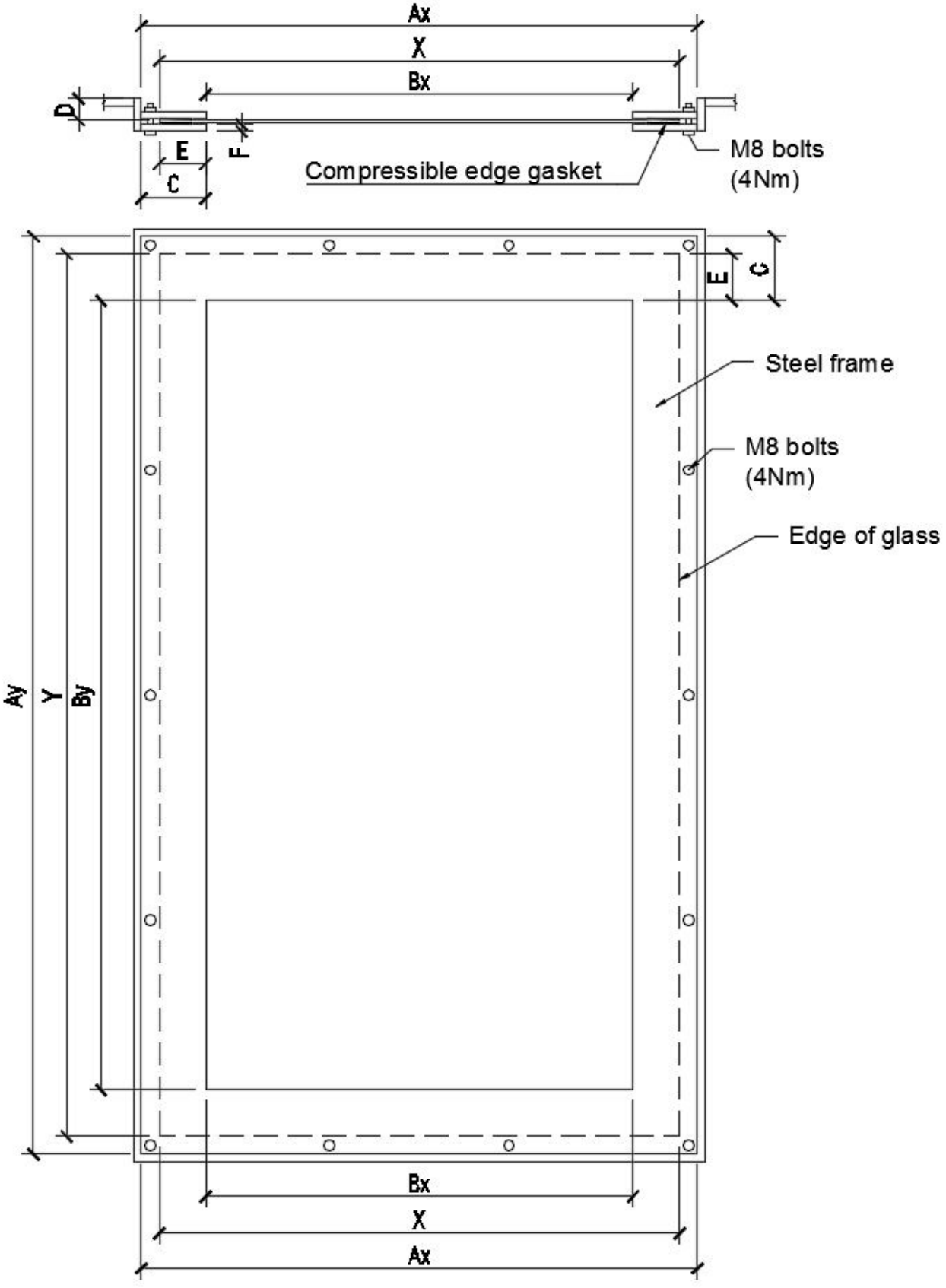

Figure 5: Section and elevation of window and frame: rigid arrangements.

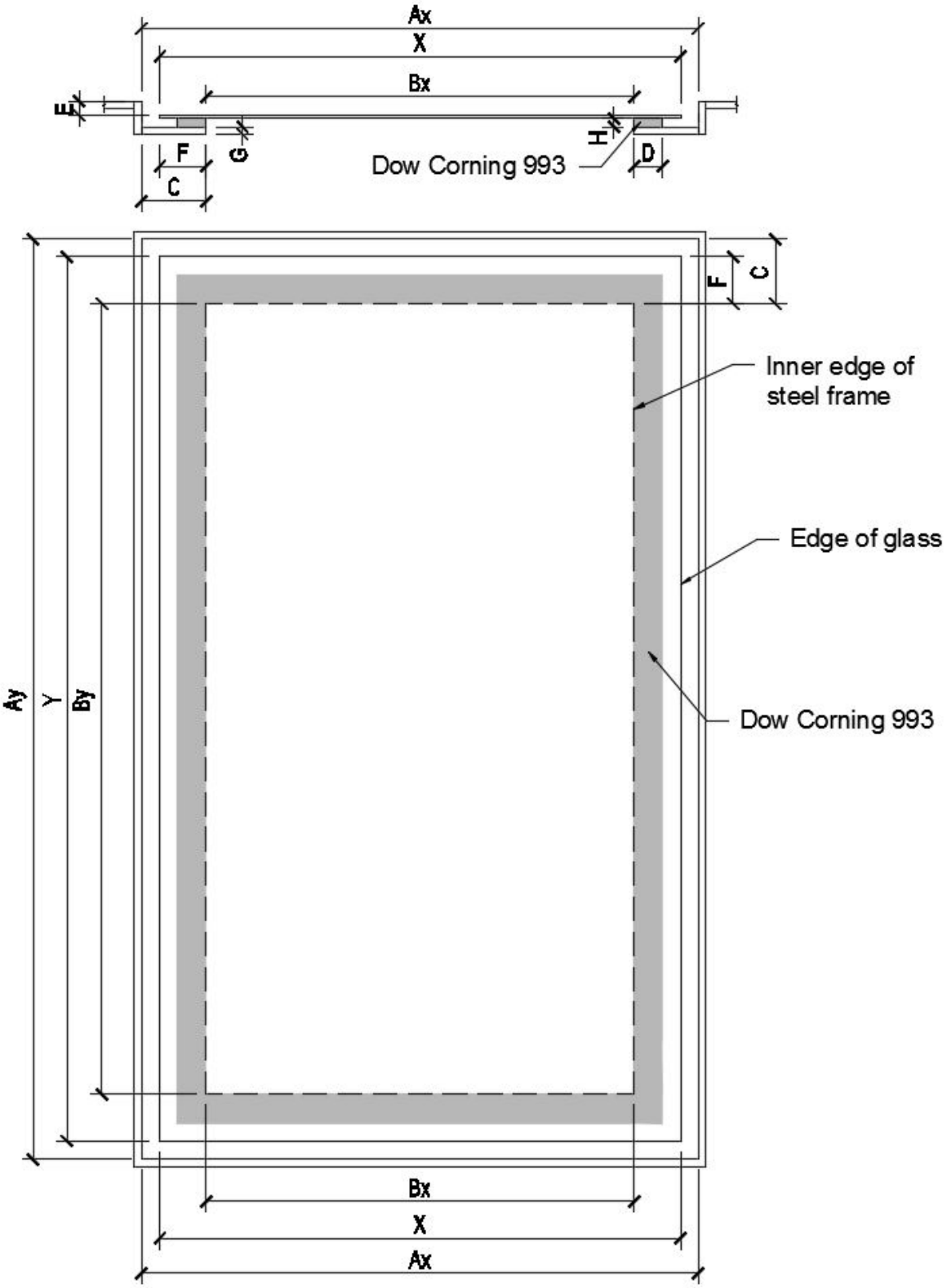

Figure 6: Section and elevation of window and frame: elastic arrangements.

Appendix C

"Alternative Methods of Data Capture for Glass subjected to Long-Duration Blast Loading"

Authors: S. Monk, S.K. Clubley

Conference paper presented at Conference on Fire and Blast (CONFAB) 2017

ALTERNATIVE METHODS OF DATA CAPTURE FOR GLASS SUBJECTED TO LONG-DURATION BLAST LOADING

S. Monk, *University of Southampton, UK*
S. K. Clubley, *University of Southampton, UK*

ABSTRACT

The air blast tunnel (ABT) at MoD Shoeburyness is a unique testing facility capable of simulating pressure regimes recorded in long-duration blast events. Long-duration blasts are typically defined by a positive phase duration greater than 100ms, observed in the far field of large explosions. Due to its highly brittle nature, glass panels require high-speed data capture to provide reliable engineering information about their response to blast loading. The harsh environment of the ABT makes accurate collection of this data very difficult. Current methods of data capture depend on interpretation of high-speed video footage, the accuracy of which is severely affected by shock wave induced camera shake. In a series of five companion static loading tests, two different methods of recording glass failure time were trialled; a circuit of conductive paint on the surface of the glass and a series of piezo transducers to record the acoustic profile at breakage. High-speed photography provided an independent correlation. Experimental results demonstrate that piezo transducers are a low-cost and comparatively accurate method of determining the time of glass failure and crack location in a static testing environment. In February 2017, a series of eight full-scale trials in the ABT demonstrated that piezo transducers were capable of replicating these results in a long-duration blast environment.

1. INTRODUCTION

The air blast tunnel (ABT) at MOD Shoeburyness, UK, was constructed in 1964 and is one of a small number of facilities in the world which are capable of testing full-scale structural response to long-duration blast waves (Figure 1)[1]. Long-duration blasts are typically defined by a positive phase duration greater than 100ms, observed in the far field of large explosions. The 200m long explosively driven shock tube has been used for a number of glass related trials in the past[2]–[4], however the harsh environment makes collecting precise data very challenging. Currently, data capture relies on high-speed photography, however this is susceptible to camera shake, reducing accuracy of the results.

Figure 1. The air blast tunnel (ABT) at MoD Shoeburyness, UK [1].

In this paper, two methods of determining time of glass failure and location of the crack origin are trialled, initially in laboratory conditions and then in the ABT. Break circuits, used by Spiller et al.[5], consist of a 'wire' painted onto the surface of the glass using conductive paint. The circuit then breaks with the glass. Piezoelectric (piezo) transducers convert vibrations, such as the sound of glass breaking, into electrical potential. Difference in time of arrival of the signals between piezo transducers allows the location of the crack to be determined.

2. STATIC TESTING

2.1 EXPERIMENTAL SET-UP

Five tests in the laboratories at MOD Shoeburyness were undertaken in January 2017 to assess piezo transducers and break circuits under static loading conditions. Each specimen of glass was tested to failure by a vacuum chamber (Figure 2) within which the pressure was reduced linearly at a rate of $0.44 kPas^{-1}$. The static testing rig, designed and constructed by the Foulness Trials Group of Spurpark Ltd, consisted of a 10mm thick airtight steel container which supported the framed glass specimen. 700mm x 700mm x 4mm thick basic annealed glass was used in all tests. The aperture of the frame was 620mm x 620mm and the glass was restrained in the frame by four clamps on each edge, providing rigid support conditions.

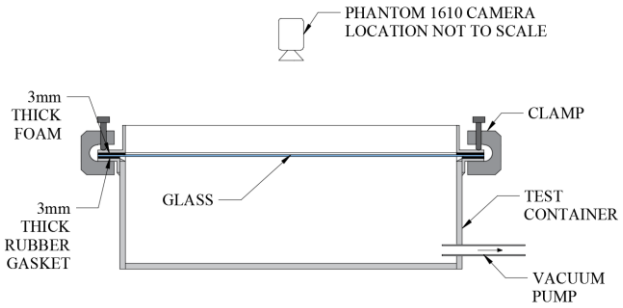

(a) Schematic of full experimental set-up for static testing.

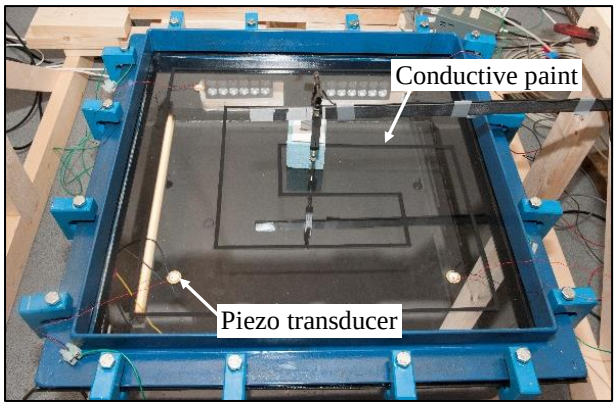

(b) Static testing box with instrumentation for Test 2.

Figure 2. Static testing set-up.

2.2 INSTRUMENTATION

Instrumentation used in each test is shown in Figure 3. Test 1 validated that piezo transducers and conductive paint were capable of recording break time. Piezo transducer locations were not measured and a single strip of conductive paint was applied. In Test 2, four piezo transducers were located 100mm from the edges of the glass, in each corner. A geometric pattern of conductive paint was produced on the glass to ensure the crack met the circuit quickly (Figures 2b and 3). In Tests 3 to 5, repeatability of piezo transducers in recording the break time and location was examined. Four piezo transducers were applied to the glass, one in each corner, 50mm from the edges. No conductive paint was used.

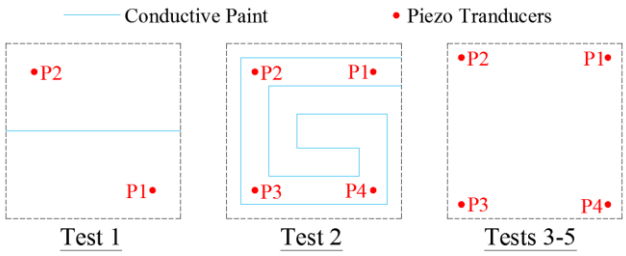

Figure 3. Instrumentation layout on surface of the glass for each test.

The Murata 7BB piezo transducers used were 20mm in diameter and were fixed to the glass using Loctite 496 superglue. The difference in time of arrival method was used iteratively with the minimum sum-of-squares of errors to find crack location. Sound velocity was calculated using the same method. A carbon-based conductive paint was used for the break circuits and was applied as a 5mm thick line. The signal from the piezo transducers and conductive paint was sampled at a rate of 1MHz. A Phantom 1610 camera with a frame rate of 52kHz provided an independent data set for comparison.

2.3 EXPERIMENTAL RESULTS

The initial crack location was calculated for Tests 2 to 5 (Figure 4). This was not possible for Test 1 as only two piezo transducers were used. Good agreement was observed between the piezo transducers and camera with an average difference of 42mm over four tests, and a maximum of 61mm in Test 3. The calculated speed of sound in the glass was 6.0±1.5kms^{-1}. Location of initial failure in the glass and crack pattern was highly variable between samples as it was dependent on the location of the Griffith Flaw [6].

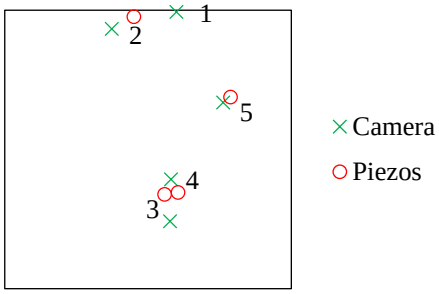

Figure 4. Initial crack locations for each test from the camera and piezo transducers.

Different triggers were used for the camera and gauges, therefore the camera could not be used to compare break times. Piezo transducers accurately located the origin of the cracks in each test, therefore the calculated crack time was reliable. In Test 2, the piezo transducer delay was 0.035ms. Multiple piezo transducers allowed the break time to be calculated, negating this error. In comparison the conductive paint exhibited a delay of 0.312ms (Figure 5a). Figure 5b and Figure 5c show cracking in the glass after these delays. At the time of the piezo transducer response, very slight cracking can be seen. Significant fracturing

had occurred before the paint responded, despite cracks crossing several parts of the circuit.

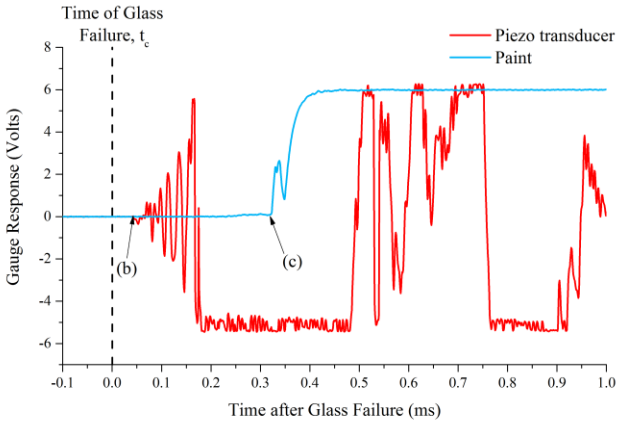

(a) Gauge signal after glass failure for test 2.

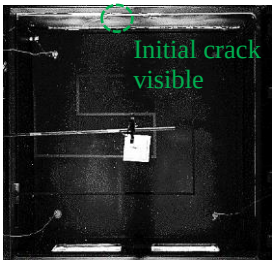

(b) Time of piezo transducer response ($t = t_c + 0.038$ ms).

(c) Time of conductive paint response ($t = t_c + 0.304$ ms).

Figure 5. Delay in gauge response time after glass failure for piezo transducers and conductive paint in test 2.

2.4 DISCUSSION

It was not possible to determine the location of the crack origin using break circuits. When compared to piezo transducers, conductive paint exhibited a response delay of 0.3ms, despite cracks propagating across several parts of the circuit. With break times of approximately 3ms in the ABT, this corresponds to an error of 10% in break time. This delay can be attributed to high resistivity of carbon-based paint. Break circuits required significant preparation time to paint the geometric pattern and allow the paint to dry.

Piezo transducers were able to accurately calculate the location of the crack origin with an average error of 5% of the glass dimensions despite large variation in calculated sound velocity (standard deviation was 24% of the mean). The piezo transducers used had a diameter of 20mm but were assumed to be a point in the calculations which introduced a 10mm error in the crack locations calculated. Due to the crack locations being calculated accurately, the break time of the glass could be determined with confidence. Piezo transducers were easy to use in a time-sensitive trial schedule due to their short preparation time. It was concluded that piezo transducers were the most effective break detection method for use in the ABT.

3. DYNAMIC TESTING

3.1 EXPERIMENTAL SET-UP

Four glass samples with piezo transducers attached were subjected to a blast wave in the ABT with peak overpressure of 14kPa and positive phase duration of 100ms. Two steel test cubicles, designed and constructed by Foulness Trials Group of Spurpark Ltd[2], were fitted in the 10.2m diameter section of the ABT normal to the blast wave (see Figures 6 and 7). 667mm x 1334mm x 4mm annealed glass was supported by a steel frame with an aperture of 1207mm x 537mm. The frame provided rigid support conditions and was fixed by bolts tightened against spacers (Figure 8).

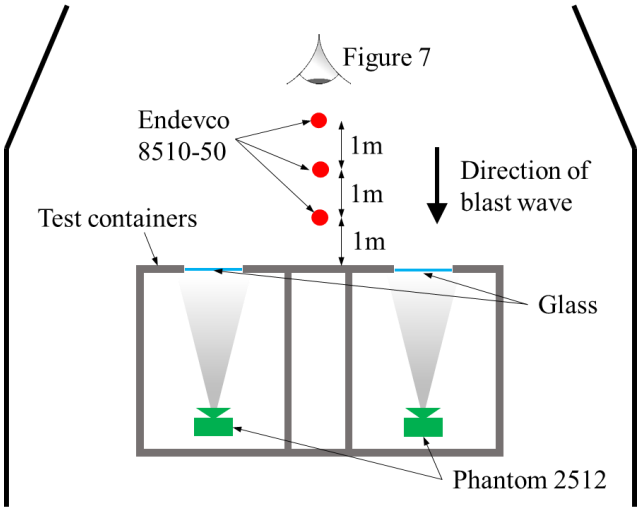

Figure 6. Plan of experimental set-up in the ABT.

Figure 7. Front elevation of test cubicles in ABT.

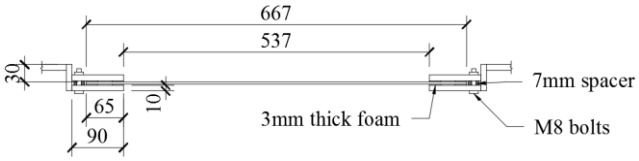

Figure 8. Horizontal section through glass frame.

3.2 INTRUMENTATION

A full free-field pressure history was recorded for each trial using a series of Endevco 8510-50 gauges (shown in Figures 6 and 7). Phantom 2512 cameras, with a frame rate of 75kHz, recorded crack location and break time of the glass. Five 20mm diameter piezo transducers, with a sample rate of 1MHz, were adhered to the rear side of each window (see Figure 9). All instrumentation was triggered at the time of driver detonation to ensure a common time scale.

Figure 9. Piezo transducer numbering.

3.3 EXPERIMENTAL RESULTS

Over the two trials a mean peak overpressure of 13.3kPa was recorded with mean positive phase duration of 100ms (Table 1). While slightly lower than specified, a high level of consistency across the trials was observed with a standard deviation of 0.2kPa. Positive phase duration and maximum impulse demonstrated similar consistency.

Table 1. Blast environment from each trial.

Trial	1	2	Mean
Peak Overpressure (kPa)	13.5	13.1	13.3
Positive Phase Duration (ms)	99	100	100
Maximum Impulse (kPa.ms)	691	683	687

Amplitude sensitivity of the piezo transducers was reduced by a factor of 1000 from the static results to ensure full response was captured (Figure 10). Glass failure was identified by a discontinuity in gauge signal followed by high frequency response. These break times were used to calculate the crack origin for each sample (Figure 11). Very good agreement was seen between the camera and piezo transducers for all tests. The mean difference was 14mm and the maximum was 26mm in sample 2 (see Table 2).

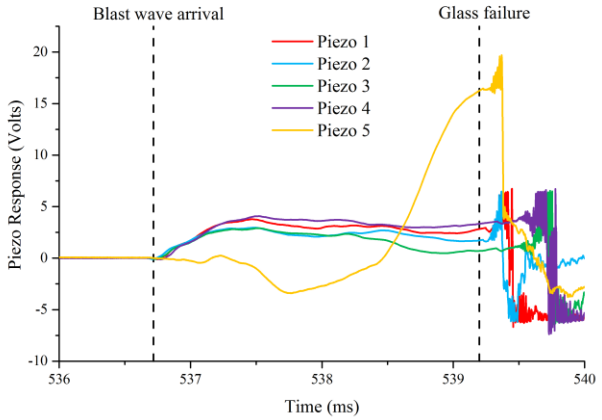

Figure 10. Piezo transducer response for glass sample four.

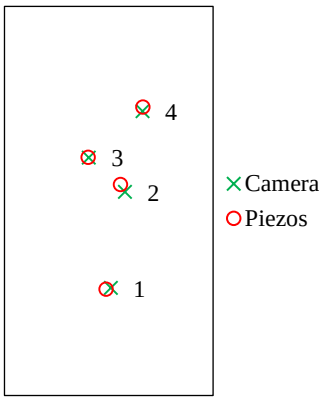

Figure 11. Crack location from camera and piezo transducers.

Table 2. Difference between crack locations from cameras and piezo transducers for each trial.

	1	2	3	4	Mean
Difference (mm)	13	26	3	13	14

Time of glass failure was recorded by cameras and calculated from piezo transducer response. The mean difference in break time between the two methods across four samples was 0.00±0.10ms, this error represents 3% of the mean break time (2.98ms) recorded for the glass panels tested. Calculated sound velocity was 6.0±0.8km/s.

3.4 DISCUSSION

Piezo transducers measured crack locations with high accuracy. The accuracy was greater in the dynamic tests, which could be attributed to the full response being recorded after reduction in sensitivity of the piezo transducers. Spread in calculated sound velocity was low compared to static testing, indicating an improvement in method reliability. Glass break time recorded by piezo transducers was very accurate when compared to the cameras showing that this method is capable of meeting both objectives in the ABT.

4. CONCLUSIONS

Both in the laboratory and the ABT, piezo transducers were capable of measuring both glass failure time and location of the crack origin with very high accuracy. This technique will be used in future experimental work in the ABT.

ACKNOWLEDGEMENTS

The authors would like to express gratitude to the UK Ministry of Defence for allowing use of the blast testing facilities at MOD Shoeburyness. All data obtained whilst using these facilities remains the property of the UK MOD. The permission to utilize these results within this paper is gratefully acknowledged. The authors wish to thank AWE plc for financial support.

REFERENCES

[1] S. K. Clubley, "Non-linear long duration blast loading of cylindrical shell structures," *Eng. Struct.*, vol. 59, pp. 113–126, 2014.

[2] R. Johns and S. K. Clubley, "Experimentally investigating annealed glazing response to long-duration blast," *J. Struct. Eng.*, 2016.

[3] R. Johns and S. K. Clubley, "The influence of structural arrangement on long-duration blast response of annealed glazing," *Int. J. Solids Struct.*, vol. 97–98, 2016.

[4] R. Johns and S. K. Clubley, "Post-fracture response of blast loaded monolithic glass," *Proc. ICE - Struct. Build.*, vol. 168, no. SB1, 2015.

[5] K. Spiller, J. A. Packer, M. V. Seica, and D. Z. Yankelevsky, "Prediction of annealed glass window response to blast loading," *Int. J. Impact Eng.*, vol. 88, pp. 189–200, 2016.

[6] A. A. Griffith, "The Phenomena of Rupture and Flow in Solids," *Philos. Trans. R. Soc. London. Ser. A, Contain. Pap. a Math. or Phys. Character*, vol. 221, no. 582–593, pp. 163–198, 1921.

© British Crown Owned Copyright 2017/AWE

Appendix D

"Quantifying the Influence of Aspect Ratio on Window Failure when subject to Long-Duration Blast Loading"

Authors: S. Monk, S.K. Clubley

Conference paper presented at International Symposium on the Interaction of the Effects of Munitions with Structures (ISIEMS) 2017

Quantifying the Influence of Aspect Ratio on Window Failure when Subject to Long-duration Blast Loading

S. Monk[1*], S.K. Clubley[1†]

[1]Faculty of Engineering and the Environment, Infrastructure Research Group, University of Southampton, United Kingdom

* *PhD researcher, corresponding & presenting author: S.Monk@soton.ac.uk*
† Lecturer in Structural Engineering, co-Author: S.K.Clubley@soton.ac.uk

Abstract
Windows differ vastly in size and shape, even for a single building. Analysis of post-explosion photographs shows that aspect ratio can have a significant effect on the survival of a window. While new constructions use laminated glass to mitigate damage, many older buildings still contain more fragile annealed glass. In the United Kingdom, 4mm-thick annealed glass represents the minimum specification for windows and therefore the worst damage case. This paper reports on the effect of window aspect ratio on the failure characteristics of annealed glass subjected to long-duration planar blast waves. Long-duration blasts are typically defined by a positive phase duration greater than 100ms, observed in the far field of large explosions which produce large impulses. The air blast tunnel (ABT) at MOD Shoeburyness is a unique testing facility capable of simulating pressure regimes observed in long-duration blast events. In a series of eight full-scale trials in the ABT, sixteen 4mm-thick annealed glass windows were examined. Four different aspect ratios, from 1:1 to 1:2, were considered. High-speed photography captured glass response while fibre-optic controlled instrumentation recorded full incident and reflected pressure histories. Results from the experimental study demonstrate that aspect ratio significantly influences the break time and crack propagation in glass panels.

Keywords: Long-duration blast loading; Aspect ratio; Annealed glass

INTRODUCTION

Glass windows are the most vulnerable components of a building and, when exposed to blast loading, produce the largest damage radius. Trawinski estimated that when a blast occurs in an urban environment, 80% of injuries are due to glass failure[1]. While new constructions implement safer laminated glazing, many older building contain annealed glass. At failure, these windows shatter into angular shards that lacerate the skin on impact, causing significant injury. Annealed, 4mm thick glass represents the minimum specification for glazing in the UK and therefore the worst case scenario in terms of damage and injury.

In August 2015, detonation of an estimated 800 tons of ammonium nitrate occurred in Tianjin, China producing two explosions of 15 tons and 430 tons TNT equivalence[2]. Over 17,000 households sustained damage to windows up to five and a half kilometres away from the point of detonation. “Severe damage” resulted in buildings up to two kilometres away[3]. A residential building which incurred partial window failure is shown in Figure 1. It can be assumed that all windows experienced the same blast environment yet only some have failed, implying structural parameters such as glass area and aspect ratio influenced survival. Analysis identified windows with smaller areas and lower aspect ratios as having a higher probability of survival.

A large explosion, such as the Tianjin event, produces a long-duration blast wave in the far-field. This blast environment, which is typically defined by a positive phase duration greater than 100ms, produces large impulses that cause window failure several kilometres away, despite its low overpressure. The air blast tunnel (ABT) at MOD Shoeburyness is capable of replicating this blast environment, allowing full-scale experimental trials to be undertaken (Figure 2)[4]. The 200m long

explosively-driven shock tube was constructed in 1964 and has been used in a number of experiments investigating structural response to long-duration blast loading[5]–[7].

Figure 1. Damage to windows in a residential block near to the Tianjin explosion[8].

Figure 2. The air blast tunnel (ABT) at MOD Shoeburyness, UK [4].

EXPERIMENTAL SET-UP

Two reinforced steel containers, constructed by Spurpark Ltd., were installed in the 10.2m diameter testing section of the ABT, normal to the blast wave. Modular sub-frames containing glass samples were attached to the front of these containers. Each window was subjected to a blast wave with peak free-field static overpressure of 14kPa and positive duration of 100ms. Testing containers were sealed to prevent equalisation behind the glass before failure.

A full pressure history of each trial was recorded using incident and reflected overpressure gauges (locations shown in Figure 3). Three Endevco 8510-50 static gauges were located at 1m intervals upstream of the test cubicles and an Endevco 8510C-50 reflected pressure gauge was adhered to the front of each cubicle, in line with the vertical centreline of the glass. These gauges are labelled in Figure 4. High-speed photography captured glazing response to the blast wave, including break time, deflection at failure and crack patterns. Camera positions are labelled in Figure 3 and Figure 4. Crack patterns were recorded by cameras C1 and C2. These were Phantom 2512 models with a frame rate of 75,000 frames per second (fps). An overall view of glass deflection was provided by Phantom V3.3 cameras at locations C3 and C4. These ran with a frame rate of 5,000fps. Cameras C5 and C6 (Phantom V711 with frame rate 75,000fps) tracked movement of the deflection gauge, allowing central glass deflection to be recorded over time. The deflection gauge is shown in Figure 5.

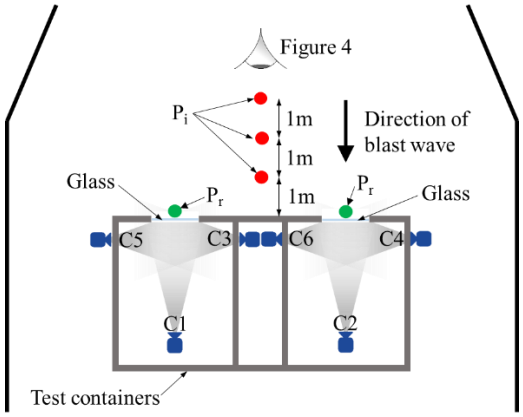

Gauges:
P_i – Incident overpressure (Endevco 8510-50)
P_r – Reflected overpressure (Endevco 8510C-50)

Cameras:
C1, C2 – Phantom 2512 (75,000fps)
C3, C4 – Phantom V3.3 (5,000fps)
C5,C6 – Phantom V711 (75,000fps)

Figure 3. Plan of experimental set-up in the ABT.

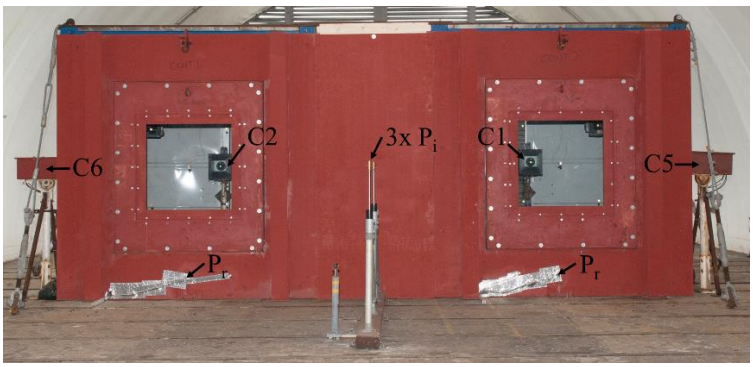

Figure 4. Elevation of test cubicles with instrumentation labelled.

Figure 5. Deflection gauge used to track central deflection.

In this experimental series, eight trials were conducted with 16 pieces of glass. Four glass aspect ratios were investigated; 1:1, 1:1.3, 1:1.7 and 1:2. For each aspect ratio, four glass samples were used. Identical glass samples were tested in each trial. All glass was annealed and had a total area of 0.89m^2 and thickness of 4mm. Glass was restrained by a steel frame bolted against spacers to ensure even stress distribution. This represented "rigid" support conditions. Frame layout and corresponding dimensions for each aspect ratio are presented in Figure 6 and Table 1.

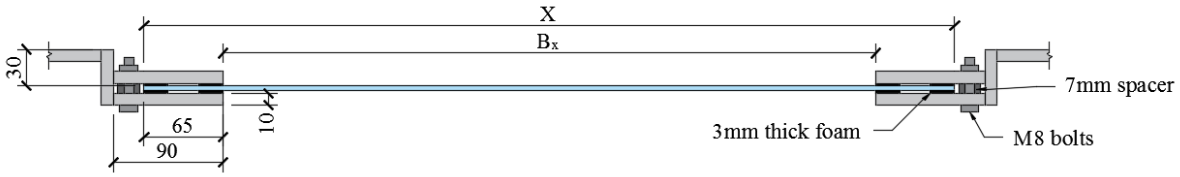

Figure 6. Horizontal section through frame, dimensions listed in Table 1.

Table 1. Frame and glazing dimensions for each trial as detailed in Figure 6.

Trial No.	1-2	3-4	5-6	7-8
Aspect Ratio	1:1	1:1.3	1:1.7	1:2
Area (m^2)	0.89	0.89	0.89	0.89
X (mm)	945	827	725	667
Y (mm)	945	1075	1230	1334
B_x (mm)	815	697	595	537
B_y (mm)	815	945	1100	1204

EXPERIMENTAL RESULTS AND ANALYSIS

Blast Environment

Mean peak free-field static overpressure, recorded 3m upstream of testing cubicles, was 13.4±0.1kPa over the eight trials. Total free-field impulse during the positive phase and positive phase duration were equally consistent, 690±7kPa.ms and 100±1ms respectively. A full pressure and impulse history from this gauge is shown in Figure 7. Very high consistency is observed across all trials, especially in the first 50ms after blast arrival. Slight discrepancies appear towards the end of the positive phase which could be attributed to turbulence behind the blast wave front. The initial rise in overpressure after blast wave arrival was a function of changing light levels on the gauge and has been observed in multiple trials. Large reflections caused by the testing cubicles produced the subsequent peaks in overpressure. This prevented a full free-field pressure history being recorded and an overestimation of total impulse. While a true free-field pressure history was not achieved, consistency between trials was demonstrated.

Reflected overpressure was used to analyse the blast environment that glass samples were subjected to. Very good agreement was observed for both test cubicles across all trials (Figure 8). Mean peak reflected overpressure was 38.8±1.3kPa and mean total reflected impulse was 724±8kPa.ms. All glass samples failed within 4ms of blast wave arrival. Reflected overpressure was approximately constant until after glass failure had occurred.

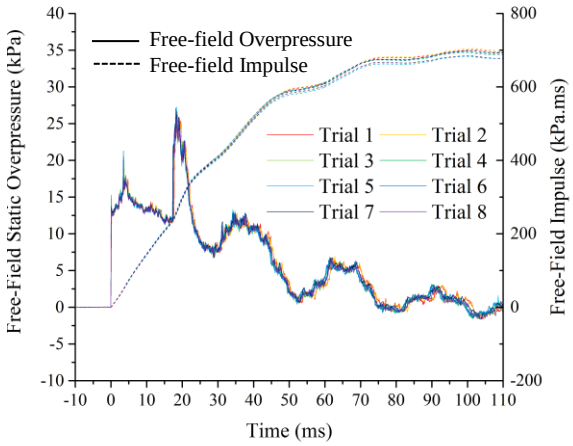

Figure 7. Free-field static overpressure and impulse 3m upstream of test cubicles.

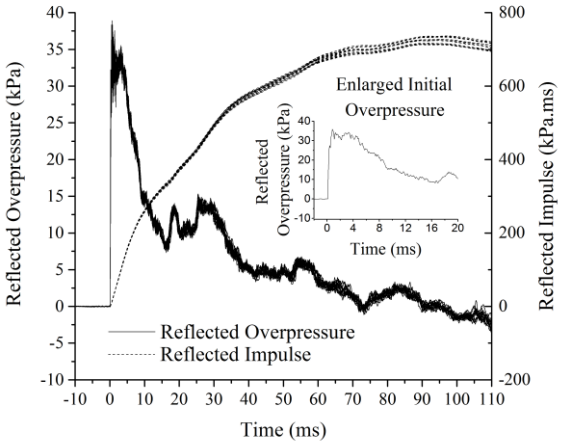

Figure 8. Reflected overpressure and impulse for both test cubicles from all trials.

Break Parameters

Central defection at failure, time to break after blast wave arrival and reflected impulse at break were recorded from camera and gauge data. Deflection was measured using deflection gauges (Figure 5) and cameras C5 and C6. Break time was recorded using cameras C1 and C2 and impulse was calculated from Figure 8 based on break time. Results for each parameter are outlined in Figure 9 and Table 2. Break parameters from Trials 1 and 2 were not recorded due to a gauge fault. This resulted in only two samples for aspect ratios 1:1 and 1:1.3. Mean and individual results are plotted in Figure 9 and 90% confidence intervals were calculated for each parameter and are detailed in Table 2.

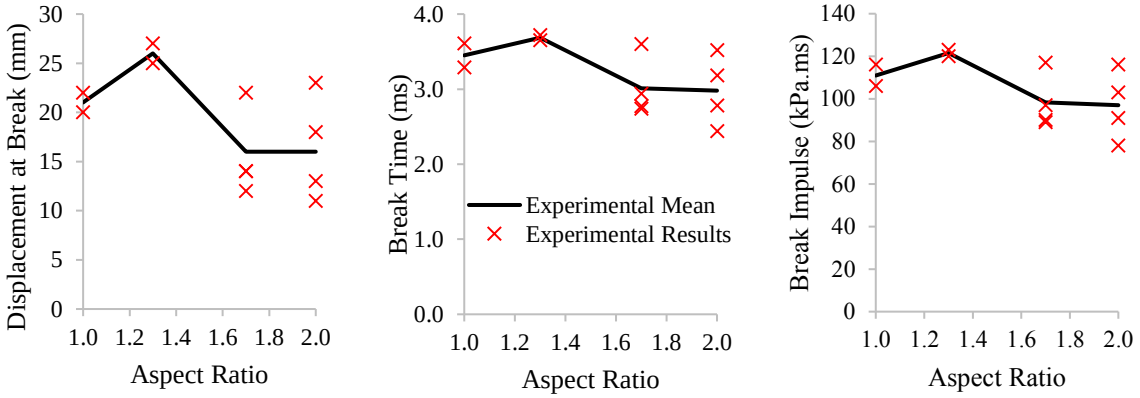

a. Maximum displacement at time of initial crack.

b. Glass failure time.

c. Impulse received at time of initial crack.

Figure 9. Individual and mean break parameters plotted against aspect ratio.

Table 2: Mean break parameters for each aspect ratio with calculated 90% confidence intervals.

		Aspect Ratio			
		1:1	1:1.3	1:1.7	1:2
Displacement at Failure (mm)	Mean	21	26	16	16
	90% CI	±6	±6	±5	±6
Break Time (ms)	Mean	3.45	3.69	3.01	2.98
	90% CI	±1.0	±0.22	±0.47	±0.55
Impulse at Failure (kPa.ms)	Mean	111	122	98	97
	90% CI	±32	±9	±15	±19

When plotted against aspect ratio, all break parameters followed a similar trend with a peak at 1:1.3 and minimum values for aspect ratios 1:1.7 and 1:2. While break time and impulse are inherently linked, this indicates that displacement at break and failure time are also closely related. The trend is most significant for displacement. A decrease in mean displacement at failure of 38% was recorded between 1:1.3 and 1:1.7 compared to decreases of 18% and 20% for mean break time and mean impulse respectively.

High variability was observed between glass samples of the same aspect ratio. This can be seen in the individual results plotted in Figure 9 and the calculated 90% confidence interval. Variation in results is due to high intrinsic variability of the glass itself. This is caused by the random size and location of the Griffith Flaw[9] in samples. In some cases the 90% confidence interval calculated was larger than the observed trend and more repeats are required to determine if the relationship with aspect ratio is significant when compared to variation in glass strength. Experimental errors such as camera rate and pixel size introduced errors of 0.01ms for break time and 0.5mm for central deflection. These errors are minimal compared to glass strength variation.

Crack Patterns

Location of initial failure in the glass and crack pattern was highly variable between samples as it was dependent on the location of the Griffith Flaw. Initiation points for each glass sample are shown in Figure 10. These were measured from video footage with maximum error of 6mm. While there is a large variation in crack locations, there is a clear difference between lower aspect ratios 1:1 and 1:1.3, where crack location is random, and higher aspect ratios 1:1.7 and 1:2 where all cracks initiated along the vertical centreline of the glass. This change in crack location could indicate a transition from two-way spanning conditions to one-way spanning where the glass is governed only by the shortest dimension. A transition in spanning conditions could be the cause of the decreased displacement at

break for higher aspect ratios. These crack patterns and break parameters will provide a benchmark for future computational modelling of glass subjected to long-duration blast.

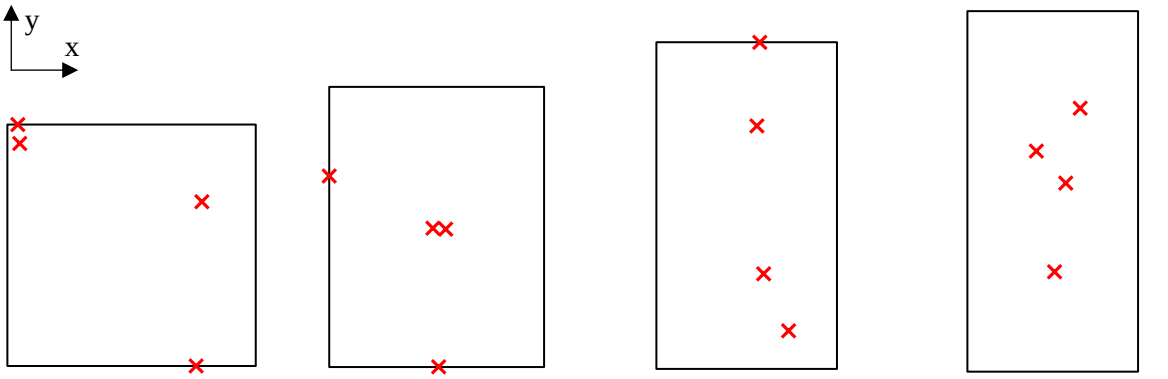

a. Aspect ratio 1:1. **b.** Aspect ratio 1:1.3. **c.** Aspect ratio 1:1.7. **d.** Aspect ratio 1:2.

Figure 10. Initial crack locations from each glass sample.

DISCUSSION

A decrease in displacement at failure, break time and impulse was observed between aspect ratios 1:1.3 and 1:2. This could be attributed to one-way spanning conditions, governed by length of the shortest span. As aspect ratio increased, the shortest side decreased causing an increase in stiffness. This caused a decrease in deflection at failure and an earlier break time. Aspect ratio 1:1 broke with a lower displacement than 1:1.3 despite having longer dimensions. This could be due to two-way spanning conditions increasing stiffness in the glass. While this theory is supported by crack location at high aspect ratios, 1:1.3 demonstrated highly variable cracking, similar to 1:1 indicating two-way spanning. This aspect ratio is at the transition between spanning conditions, producing an increase in resistance to blast pressure due to a large span but additional stiffness from two-way spanning.

Intrinsic variability in the glass was high leading to large confidence intervals being calculated. However break parameters, especially displacement, varied considerably with aspect ratio, indicating that aspect ratio influences failure. More trials are required, especially at lower aspect ratios, to determine if the mean values calculated are representative and confirm that aspect ratio is a significant factor in window failure. All glass samples were subjected to a peak free-field overpressure of 13.4kPa and broke within 4ms. This blast environment was significantly above the threshold of glass failure meaning that structural parameters such as aspect ratio were insignificant compared to the blast. Despite this, a trend between break parameters and aspect ratio was clear. Future trials, with lower overpressures, will investigate the significance of aspect ratio nearer to the threshold of window failure.

CONCLUSIONS

Aspect ratio 1:1.3 exhibited the highest resistance to long-duration blast loading with peak overpressure 13.4kPa. A decrease in displacement and time of break was observed for higher aspect ratios which could be due to additional stiffness as a result of one-way spanning conditions and a span decrease. 1:1 windows were also stiffer than 1:1.3 due to two-way spanning conditions. More data is required to confirm this trend due to large variability in results between repeats. This was attributed to variation in glass strength.

ACKNOWLEDGEMENTS

The authors would like to express gratitude to the UK Ministry of Defence for allowing use of the blast testing facilities at MOD Shoeburyness. All data obtained whilst using these facilities remains the property of the UK MOD. The permission to utilize these results within this paper is gratefully acknowledged. The authors wish to thank AWE plc for financial support.

© British Crown Owned Copyright 2017/AWE

REFERENCES

[1] E. Trawinski, J. W. Fisher, and R. J. Dinan, "AFRL-ML-TY-TP-2005-4508 Full Scale Testing of Polymer Reinforced Blast Resistant Windows," Air Force Research Laboratory Report, Florida, USA, 2004.

[2] G. Fu, J. Wang, and Y. Mingwei, "Anatomy of Tianjin Port Fire and Explosion: Process and Causes," *Process Saf. Prog.*, vol. 35, no. 3, pp. 216–220, 2016.

[3] S. L. Mcgarry, S. Balsari, S. Muqueeth, and J. Leaning, "Preventing the Preventable: The 2015 Tianjin Explosions," Cambridge, MA, 2017.

[4] S. K. Clubley, "Non-linear long duration blast loading of cylindrical shell structures," *Eng. Struct.*, vol. 59, pp. 113–126, 2014.

[5] R. Johns and S. K. Clubley, "Experimentally investigating annealed glazing response to long-duration blast," *J. Struct. Eng.*, 2016.

[6] R. Johns and S. K. Clubley, "The influence of structural arrangement on long-duration blast response of annealed glazing," *Int. J. Solids Struct.*, vol. 97–98, 2016.

[7] J. Denny and S. K. Clubley, "Multi-axis long-duration blast interaction with I-shape steel sections," in *MABS 2016; 24th International Symposium on the Military Aspects of Blast and Shock*, 2016.

[8] BBC News, "China explosions: What we know about what happened in Tianjin," 2015. [Online]. Available: http://www.bbc.co.uk/news/world-asia-china-33844084. [Accessed: 02-Feb-2016].

[9] A. A. Griffith, "The Phenomena of Rupture and Flow in Solids," *Philos. Trans. R. Soc. London. Ser. A, Contain. Pap. a Math. or Phys. Character*, vol. 221, no. 582–593, pp. 163–198, 1921.

© British Crown Owned Copyright 2017/AWE

Appendix E

"Using Sound to Detect Annealed Glass Failure in a Long-Duration Blast Environment"

Authors: S. Monk, S.K. Clubley

Abstract from journal paper submitted to Engineering Failure Analysis, pending acceptance.

USING SOUND TO DETECT ANNEALED GLASS FAILURE IN A LONG-DURATION BLAST ENVIRONMENT.

S. Monk[1*], S.K. Clubley[1†]

1Faculty of Engineering and the Environment, Infrastructure Research Group,

University of Southampton, United Kingdom

** PhD researcher, corresponding author: S.Monk@soton.ac.uk*

† Lecturer in Structural Engineering, co-Author: S.K.Clubley@soton.ac.uk

ABSTRACT

Glass windows are vulnerable components of a building and, in the event of a blast, produce a large damage radius. In the far-field of large explosions, long-duration blast environments can occur, defined by a positive phase duration greater than 40ms. Resulting impulses can cause window failure several kilometres away from the point of detonation. The air blast tunnel (ABT) at MOD Shoeburyness, UK is capable of simulating such blast environments and has been used in a number of experimental trials to quantify annealed glazing response to long-duration blast. Current data capture methods rely heavily on high-speed photography to record glass failure time and location of cracking. Accuracy is limited by camera availability, frame rate and shock-induced camera vibration. In this paper, the use of sound via the triangulation of piezo transducers is proposed as a new method of capturing window response in a rapid and aggressive monitoring environment. Piezo transducers, attached to the surface of the glass, recorded the acoustic emission of glass breaking. An array of sensors in known locations allowed time and location of glass failure to be calculated. The method was tested and refined through two phases of static pressure loading tests then implemented in the ABT under three different long-duration blast environments. Triangulation of piezo transducers was found to be a highly accurate and cost-effective method of capturing window failure in a long-duration blast environment.

Keywords: Long-duration blast, Failure analysis, Glass breakage, Acoustic measurement